ALMA MATER STUDIORUM
UNIVERSITÀ DI BOLOGNA

DOTTORATO DI RICERCA IN

INGEGNERIA BIOMEDICA, ELETTRICA E DEI SISTEMI

Ciclo 36

Settore concorsuale: 09/G2 - BIOINGEGNERIA

Settore Scientifico Disciplinare: ING-INF/06 - BIOINGEGNERIA ELETTRONICA E INFORMATICA

MODELLING THE SINOATRIAL NODE ACROSS THE SCALES: THE ROLE OF HETEROGENEITY IN PACEMAKING AND ATRIAL DRIVING

Presentata da: Eugenio Ricci

Coordinatore dottorato

Michele Monaci

Supervisore

Stefano Severi

Co-supervisore

Chiara Bartolucci

Esame finale anno 2024

"Istruitevi, perché avremo bisogno di tutta la nostra intelligenza.
Agitatevi, perché avremo bisogno di tutto il nostro entusiasmo.
Organizzatevi, perché avremo bisogno di tutta la nostra forza"

Antonio Gramsci, L'Ordine Nuovo, 1 Maggio 1919

Keywords

Electrophysiology
Sinoatrial node
Cardiac Pacemaking
Arrhythmias
Computational Models
Heart Rate Variability

Contents

List of Figures

List of Tables

General abstract

During a human being's life, the heart beats on average 2 to 3 billion times. At each cycle, the primary pacemaker of the heart – the sinoatrial node – automatically depolarizes and excites the atria. The stimulus then travels along the cardiac conduction system and spreads to the ventricles, determining contraction.

Why the sinoatrial node is able to show spontaneous and rhythmic electrical activity, as well as how it manages to drive the surrounding tissue, is still incompletely understood. The contribution of neural control to the physiology and pathology of the sinoatrial node is even less known. All this limits the chances of preventing and treating diseases originating from the disruption of these mechanisms, as it happens during aging.

In this dissertation, the sub-cellular, cellular, tissue and organism levels of cardiac pacemaking are investigated using computational models and heart rate variability analysis. In particular, the aim of this work is that of providing quantitative information about the role of heterogeneity in sinoatrial node functioning.

In summary, the main results show that heterogeneity I) regulates the relative contribution of ion channels and intracellular calcium handling to the beating rate; II) increases the robustness of the sinoatrial node in originating the heartbeat and propagating it to the atrium, in both physiological and pathological conditions and III) vagal nerve stimulation stabilizes spectral heart rate variability metrics and promotes heart rate reduction and variability after myocardial infarction in pigs.

In conclusion, this PhD dissertation represent a step forward in the comprehension of fundamental aspects of cardiac pacemaking.

Introduction & Outline

The overall aim of this PhD dissertation is providing quantitative information about the mechanisms that originate and propagate the heartbeat. This will be mainly achieved thanks to the use of computational models of the primary pacemaker of the heart, the sinoatrial node, from the sub-cellular to the tissue level. An insightful glimpse at the organism level will be made by performing heart rate variability analysis on pig atrial electrograms. In this multi-scale framework, a particular focus is given to heterogeneity, holistically intended as I) biological variability in electrophysiological properties, II) variations in gap junctional coupling and III) presence of non-myocytes inside the sinoatrial node. Detailed mathematical descriptions of the interactions between ionic channels and intracellular calcium handling, as well as between different cellular phenotypes (sinoatrial and atrial myocytes; fibroblasts; connective, fat and scar tissue), have been developed and studied.

The diversity of anatomical and electrophysiological properties shown by this intriguing small piece of cardiac tissue has long been recognized as an outstanding feature that, together with automaticity, distinguishes the node from the working myocardium [1]–[6]. Only the atrio-ventricular node, insofar as it was not investigated as extensively as the sinoatrial node, seems to match this structural and functional variety [2], [4], [7]–[9].

Traditionally, biophysically-detailed electrophysiological models of cardiac myocytes neglected this aspect and reproduced the behaviour of an *"ideal"* cell [10]–[27]. This is obtained by averaging experimental data and by fitting equations on them. However, the paradigm has recently shifted in also considering biological variability, in the wake of a more general effort to personalize medicine by considering intra- and inter-patients differences. Hence, those model parameters that are obtained by averaging experimental data, are randomized to fit not simply an average value, but the experimental range. In this way populations of models [28]–[32] or heterogeneous tissues [33], [34] are built to best reproduce biological variability and to allow the manifestation of a wider array of emerging behaviours.

As mentioned above, heterogeneity assumes a broader meaning when speaking of the sinoatrial node. For clarity's sake, throughout this thesis we will refer to *"heterogeneity"* as biological variability in cellular electrophysiological properties. *"Gradients"* will be used for describing spatial changes in gap junctional conductivity, while *"fibrosis"* will indicate the presence of active fibroblasts connecting via gap junctions to myocytes in the sinoatrial node – if not expressly used as the traditional concept of extracellular matrix deposition.

A comprehensive introduction on the background of this work will be presented in **Chapter 1**. There, all aspects regulating cardiac pacemaker activity are reviewed to the best of the authors' knowledge, with prevailing attention to those works in literature that employed computational methods. Dedicated sections will explain what has been discovered at present about heterogeneity, gradients and fibrosis inside the sinoatrial node, corroborating the purpose of this dissertation.

Chapter 2 provides data on the interplay between membrane and calcium clocks, adding to a decades-long debate on the source of the heartbeat. A spatial model of single rabbit sinoatrial cells is developed, starting from the detailed descriptions of calcium handling by Maltsev and colleagues [35] and of the membrane clock by Severi et al. [24]. Simulations are run to inspect the contribution of local calcium releases in the diastolic depolarization of heterogeneous single or coupled cells.

Coupling and heterogeneity are also the main topics of **Chapter 3**, which is the results of the collaboration with Dr. Chiara Campana and Prof. Eric A. Sobie from the Icahn School of Medicine at Mount Sinai, New York. In this Chapter, advanced computational techniques such as parallel GPU computing are adopted to simulate isolated sinoatrial node tissues. Different levels of intercellular (gap junctional) coupling and heterogeneity (model parameter randomization) in healthy and diseased conditions were tested. This was made to highlight the robustness of the sinoatrial node to changes in its most important parameters (e.g. maximal conductance of the L-type calcium current), as obtained from the logistic regression analyses performed.

Chapter 4 investigates the role of distinct cellular phenotypes in human isolated sinoatrial tissue models. Indeed, different amounts of dormant myocytes, connective/fat/scar tissue and fibroblasts are placed inside the node to evaluate its ability to synchronize and show physiological beating rates when, as it happens in humans, a significant portion of its volume is not composed of spontaneous sinoatrial cells.

The core of this thesis is represented by **Chapter 5**. There, bi-dimensional models of large rabbit and human atrial tissues including the sinoatrial node and the exit pathways are developed. High-performance computing techniques (GPU

parallelization) were again adopted to run the simulations- All the knowledge acquired in the previous Chapters was transferred in this work, with the objective of studying the role of heterogeneity in the context of atrial driving. Thus, simulations with cellular heterogeneity, fibrosis, or the combination of the two, were performed. Their function in pathological conditions such as losses in fundamental ionic currents (reproducing mutations) or atrial tachycardia (determining overdrive suppression) was studied as well. Additionally, perfusion of acetylcholine and isoproterenol was simulated to explore autonomic regulation mechanisms.

The latter aspect is of absolute importance for sinoatrial physiology, given its heart rate generation task. **Chapter 6** uses heart rate variability analysis to investigate the role of vagal nerve stimulation – a cutting edge therapeutic technique – in the recovery from myocardial infarction in pigs. This top-down approach, dealing with real, organism-level data, is the completion of the bottom-up perspective employed in Chapters 2 to 5.

A final Chapter will summarize the main findings and draw the conclusions of this work.

Abbreviations

AC	Adenylyl cyclase
ACh	Acetylcholine
AF	Atrial fibrillation
ANS	Autonomic nervous system
AP	Action potential
APA	Action potential amplitude
APD	Action ptential duration
BR	Beating rate
β-AR	Beta-adrenergic receptor
cAMP	Cyclyc adenosine monophosphate
$Ca_v1.2$	L-type calcium channel α-1C subunit
$Ca_v1.3$	L-type calcium channel α-1D subunit
$Ca_v3.1$	T-type calcium channel α-1G subunit
ChR	Cholinergic receptor
CL	cycle length
CNS	Central nervous system
CPVT	Catecholaminergic polymorphic ventricular tachycardia
CRU	Calcium Release Unit
CV	Conduction velocity
DD	Diastolic depolarization
DDR	Diastolic depolarization rate
EGM	Electrogram
FWS	Fabbri et al. (2017) model [25]
g_{CaL}	Maximal conductance of the L-type calcium current
g_f	Maximal conductance of the funny current
g_{CaL}	Maximal conductance of the L-type calcium current
g_{Kr}	Maximal conductance of the rapid delayed rectifier current
g_{Ks}	Maximal conductance of the slow delayed rectifier current
g_{Na}	Maximal conductance of the sodium current
g_{Ks}	Maximal conductance of the transient outward current

HR	Heart rate
HSMN	Himeno et al. (2008) model [36]
HRV	Heart rate variability
$\mathbf{I_{bNa}}$	Background sodium current
$\mathbf{I_{CaL}}$	L-type calcium current
$\mathbf{I_{CaT}}$	T-type calcium current
ICNS	Intracardiac nervous system
$\mathbf{I_f}$	Hyperpolarization-activated, cyclic-nucleotide-gated (funny) current
$\mathbf{I_{gap}}$	Gap junctional current
$\mathbf{I_{ion}}$	Sum of all sarcolemmal ionic currents
$\mathbf{I_{K,ACh}}$	Acetylcholine-activated potassium current
$\mathbf{I_{Kr}}$	Rapid delayed rectifier potassium current
$\mathbf{I_{Ks}}$	Slow delayed rectifier potassium current
$\mathbf{I_{Kur}}$	Ultra-rapid delayed rectifier potassium current
$\mathbf{I_{Na}}$	Sodium current
$\mathbf{I_{NaCa}}$	Sodium/calcium exchanger current
$\mathbf{I_{NaCa,max}}$	Maximal current of the sodium/calcium exchanger
$\mathbf{I_{NaK}}$	Sodium/potassium pump current
$\mathbf{I_{NaK,max}}$	Maximal current of the sodium/potassium pump
$\mathbf{I_{net}}$	Net membrane current
$\mathbf{I_{sK}}$	Small-conductance calcium-activated potassium current
$\mathbf{I_{sus}}$	Sustained outward current (4-aminopyridine-sensitivecomponent of I_{to}. Alternative definition of I_{Kur})
$\mathbf{I_{to}}$	Transient outward potassium current
K	Koivumäki et al. (2011) model [20]
LCR	Local calcium release
LPM	Leading pacemaker
MBS	Mazhar et al. (2023) model [27]
MDP	Maximum diastolic potential
ML	Maltsev & Lakatta (2009) model [22]
NE	Norepinephrine
ODEs	Ordinary differential equations
OS	Overshoot
$\mathbf{P_{CaL}}$	Maximal permeability of the L-type calcium current
$\mathbf{P_{CaT}}$	Maximal permeability of the T-type calcium current
PDE	Phosphodiesterase
PDEs	Partial differential equations
PKA	Protein kinase A

PLB	Phospholamban
P_{up}	Sarco-endoplasmic reticulum calcium ATPase uptake rate
RA	Right atrium
RAGP	Right atria gnaglionated plexus
R_{gap}	Gap junctional resistance
RyR	Ryanodine receptors
SAC	Stretch-activated channels
SAN	Sinoatrial node
SDiF	Severi et al. (2012) model [24]
SEP	Sinoatrial exit pathway
SERCA	Sarco-endoplasmic reticulum calcium ATPase
SF	Safety factor
SND	Sinus node dysfunction
SR	Sarcoplasmic reticulum
TOP	Take-off potential
V_m	Membrane voltage

Chapter 1

The Sinoatrial Node: Structure, Function and Modelling

The content of this chapter is published in:

"The virtual sinoatrial node: what did computational models tell us about pacemaking?"
Eugenio Ricci[1], Chiara Bartolucci[1], Stefano Severi[1]

[1] Department of Electrical, Electronic and Information Engineering "Guglielmo Marconi", University of Bologna, Cesena, Italy

Progress in Biophysics and Molecular Biology, PBMB 2023, 177(1), 55-79

Abstract

Since its discovery, the sinoatrial node (SAN) has represented a fascinating and complex matter of research. Despite over a century of discoveries, a full comprehension of pacemaking has still to be achieved. Experiments often produced conflicting evidence that was used either in support or against alternative theories, originating intense debates. In this context, mathematical descriptions of the phenomena underlying the heartbeat have grown in importance in the last decades since they helped in gaining insights where experimental evaluation could not reach. This review presents the most updated SAN computational models and discusses their contribution to our understanding of cardiac pacemaking. Electrophysiological, structural and pathological aspects – as well as the autonomic control over the SAN - are taken into consideration to reach a holistic view of SAN activity.

1.1 Introduction

Last decades have seen an extensive multiplication of results elucidating the mechanisms of cardiac pacemaking. Since the discovery of the sinoatrial node (SAN) by Keith and Flack in 1907 [37], many experiments have been carried out, allowing for the functional characterization of this complex tissue, depicted in Figure 1.1. Similarly, since the first attempts of a mathematical description of the cardiac action potential (AP) by Noble [10], many computational models have been implemented to clarify the origin of the heartbeat. Still, many open questions remain, as both experiments (in vitro, ex vivo, and in vivo) and models have sometimes produced conflicting evidence [38]. Ultimately, the SAN is eluding a full and detailed comprehension up to this day [39].

This lack of knowledge represents a major issue since it limits our ability to intervene in clinical practice. SAN disorders are in fact affecting an increasing portion of the (aging) population: sinus node dysfunction (SND), a disease characterized by the inability of the SAN to supply an adequate heart rate (HR) [40], has a prevalence of $1/600$ in subjects 65 years of age or older [40], [41]. Currently, no effective treatment is available for this disease, and the only possibility is the implantation of an electronic pacemaker [41].

Computational models are well-suited tools to overcome these knowledge gaps. The reason is that they avoid the shortcomings of experiments in terms of costs, ethical issues, reproducibility, and control (i.e.: the possibility to change conditions hardly modifiable in vitro, such as intracellular ionic concentrations or selective channel blocks). For this, many research groups and institutions are pushing to extend the use of in silico models in fields such as drug safety (e.g., the CiPA initiative [42], [43]) and cardiology (through "The Digital Twin" [44]).

In line with this, the present work reviews the recently proposed SAN computational models with the aim of understanding what they told – and what they did not tell – about cardiac pacemaking mechanisms. Several reviews on the sinoatrial node can be found in literature, each with particular focus on different SAN aspects: coupled-clock theory [45]–[47]; anatomy and spatial organization [3]–[6], [48], [49]; mechanics [50]–[52]; heterogeneity [1]; genetics [2]; pathology [40], [41], [53], [54]. Mathematical models of cardiac electrophysiology have also been previously reviewed (e.g., [43], [55], [56]), with the SAN being no exception: apart from dedicated chapters in the works listed above, SAN numerical models were reviewed in the works of Li et al. [57], Maltsev et al. [46] and Kohajda et al. [58], although the most comprehensive review still remains the one published by Wilders in 2007 [59]. Consequently, the first section of this paper will be assigned at updating the work by Wilders [59] by enumerating and describing the main features of the recently published models. Differently from

that paper, however, the focus of the following sections will be on the physiology more than on the modelling aspects. Thus, the second section will investigate the results produced by computational models about the origin of the heartbeat. On a higher scale, the third section will discuss the tissue organization of the SAN and its ability to synchronize, while the fourth section will present the current understanding of its pathological mechanisms. A section will be assigned to the role of fibrosis in both physiological and pathological conditions and SAN mechanics, while another important aspect – the autonomic control over the sinoatrial node – will be covered in the sixth section. A final section will summarize the open topics about sinoatrial node activity and draw the conclusions up to this point.

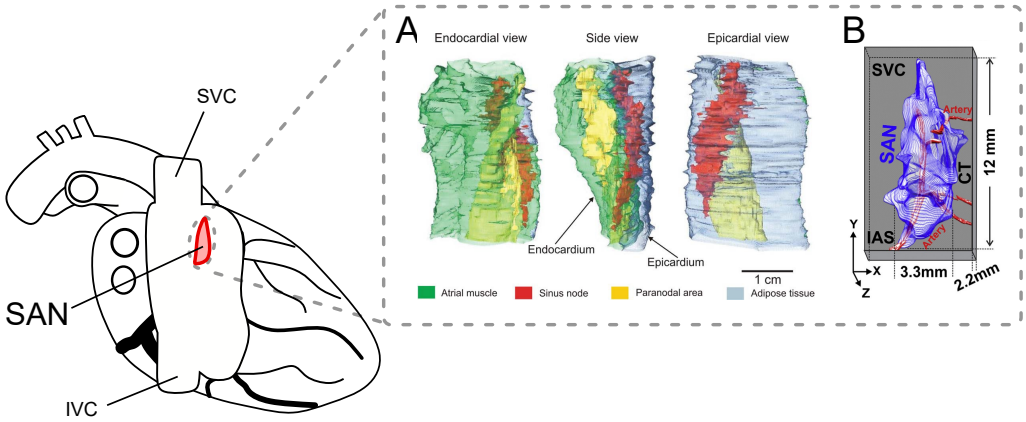

Figure 1.1: ***SAN location (left) and 3D reconstructions (right).*** *A) Different views of a computational 3D reconstruction of the human SAN (red) extracted from Chandler et al. [60], with permissions. Note the intertwining of the SAN with other tissues: atrial (green), adipose (grey) and paranodal area (yellow); B) Computational 3D reconstruction of the human SAN extracted from Csepe et al. [61], with permissions. Note the complex shape of the structure and the presence of the SAN artery through all the SAN. SVC: superior vena cava; IVC: inferior vena cava; IAS: inter-atrial septum; CT: crista terminalis.*

1.2 Recently proposed SAN single cell models

In this section, computational models of SAN single cells will be presented, limiting the analysis to those models proposed after the review by Wilders [59]. While still to be considered as "second generation" models [59], these updated mathematical descriptions of the action potential (see Table 1.1) show refined membrane current formulations and a more detailed intracellular calcium handling, both based on novel experimental data. Figure 1.2 shows a schematization of the cell compartments and ionic channels of such models. Building on evidence

collected in their laboratory in the early 2000*s* (see [62] for review), Maltsev and Lakatta published in 2009 a "coupled-clock" model of the rabbit SAN cell, featuring the interaction ("synergism") between the role of membrane currents (also called "membrane clock", *M*-clock) and calcium handling ("Ca^{2+}-clock") in originating pacemaking (ML model [22]). This conflicted with the consolidated thought that the initiation of the heartbeat was to be found on the membrane surface only. In particular, the behaviour of what had been called the "pacemaker" current, namely the hyperpolarization-activated I_f ("funny") current, had been proposed as the main mechanism driving the diastolic depolarization (*DD*) phase up to the threshold for AP firing ([63] for review). Differently from these ideas, the model by Himeno and coauthors (HSMN model [36]) of guinea pig SAN cell, predicted a central role for the rapid delayed rectifier potassium current (I_{Kr}) decay and for the sustained inward current (I_{st}) in allowing the *DD*. Setting I_f conductance to its value at the maximum diastolic potential (*MDP*) for 275 ms during *DD* did not affect the cycle length (*CL*, [36]). However, neither the ML nor the HSMN models managed to reproduce the reported beating rate (*BR*) reduction upon I_f block in rabbit SAN preparations (median value: 20.3%, range $5.2-30\%$ [64]–[74]). To fill this gap, Severi et al.[24] combined the calcium handling from ML with an updated If description (SDiF model). The resulting rabbit SAN cell model reproduced the available experimental data of the effects of current blocks, autonomic stimulation, and Ca^{2+} transient modifications, showing that a primary role of I_f is fully compatible with the detailed Ca^{2+} handling description proposed as the basis of the Ca^{2+}-clock theory.

Besides rabbit models, mathematical descriptions of the murine AP have also been proposed. This is of note since mice represent a widely used animal model in experiments: a mouse-specific computational tool can therefore be of use not only in basic electrophysiology research, but also in applied fields such as early-stage drug safety assessment. Additionally, gene knock-out is now a well-established technique in mice [75], allowing (with some caution) for comparisons with specific current blocks in models. With these purposes, Kharche et al. [23] published in 2011 a computational model of the mouse SAN cell, using the Kurata [21], [76] and Zhang [77] models as starting points. The efforts of the authors, in addition to fitting current formulations to mouse-specific data when available, were directed towards considering only those currents with a clear molecular determinant. However, formulations for background currents and I_{st} (whose molecular basis has been questioned [22]) are present in the model. In the same year, Tao et al. [78] developed a model of the neuronal control of the rat SAN, considering both the AP of a sympathetic neuron and of the modulated SAN cell. The AP model of the SAN was shown to agree well with the experimental data and reproduced the effects of blocks of the main ionic currents.

In support of the Ca^{2+}-clock theory, Maltsev et al. [79] showed that a 2D

model of the Ca^{2+} handling of a rabbit SAN cell allowed (if coupled to the *M*-clock [80]) for spontaneous depolarizations following synchronization of calcium-release units. These indeed permit local calcium control and thus a more efficient sarco-endoplasmic reticulum calcium ATPase (SERCA) activation. However, the release unit description is based on lumped parameters (e.g., their refractory period) that ignore the underlying mechanisms. To overcome this limitation, the same group [81] considered the 3D spatial organization of ryanodine receptors (RyR) clusters and showed that this – in combination with stochastic RyR gating – allows spontaneous cyclic Ca^{2+} releases with no assumptions on RyR inactivation or different ion diffusion in the subspace (hypothesis on which lumped-parameters models must rely on [36]). Due to the absence of experimental data on the precise RyR distribution and gating scheme, assumptions were necessary also in this case. Finally, a trade-off between a detailed 3D description of Ca^{2+} handling and a lumped-parameter model was recently proposed as a tool for investigating the role of RyR distribution [35].

Recent years have also seen the rise of interest in human-specific SAN models. As reported in [25], some early attempt was made by Seeman et al. [82] and Chandler et al. [83], by including SAN-specific currents or scaling maximal conductances (according to SAN gene expression) in the human atrial model by Courtemanche [17]. In 2016, Pohl et al. [84] updated the rabbit model by Dokos et al. [85] using human data from Verkerk et al. [86]. Being their focus mainly on the mechanism of rate modulation by the parasympathetic branch of the autonomic nervous system (ANS), the model well reproduced the basal *CL* and the response to acetylcholine (ACh), but not the AP shape. A new mathematical description of the human SAN AP was recently given by Fabbri et al. ([25], FWS model). Using again the data from Verkerk et al. [86] to update the SDiF model, they obtained an AP shape and a basal *CL* that closely resembled those of experimental traces. The model was also validated against numerous ion channel mutations and consistently reproduced their effects. Despite the extensive validation of the model, it has to be borne in mind that the human data on which it relies on only comes from three SAN cells of a patient suffering from inappropriate sinus tachycardia [86] highlighting the need for more extensive and reliable human data.

Many of these new AP models – as well as the older ones – have also been updated and ameliorated during the years. Thus, works that did not specifically propose a new AP description, but fitted new data, modified some parameters, or added ANS modulation were included in Table 1.2 as "New versions of previous models". For example, in 2008 Kurata et al. [76] published a development of their 2002 model [21] that considers the different properties of central and peripheral cells, similarly to Zhang et al. [77]. Later on, a modification of the Kurata model was presented by Imtiaz et al. [87] by enhancing the role of intracellular $Ca2+$

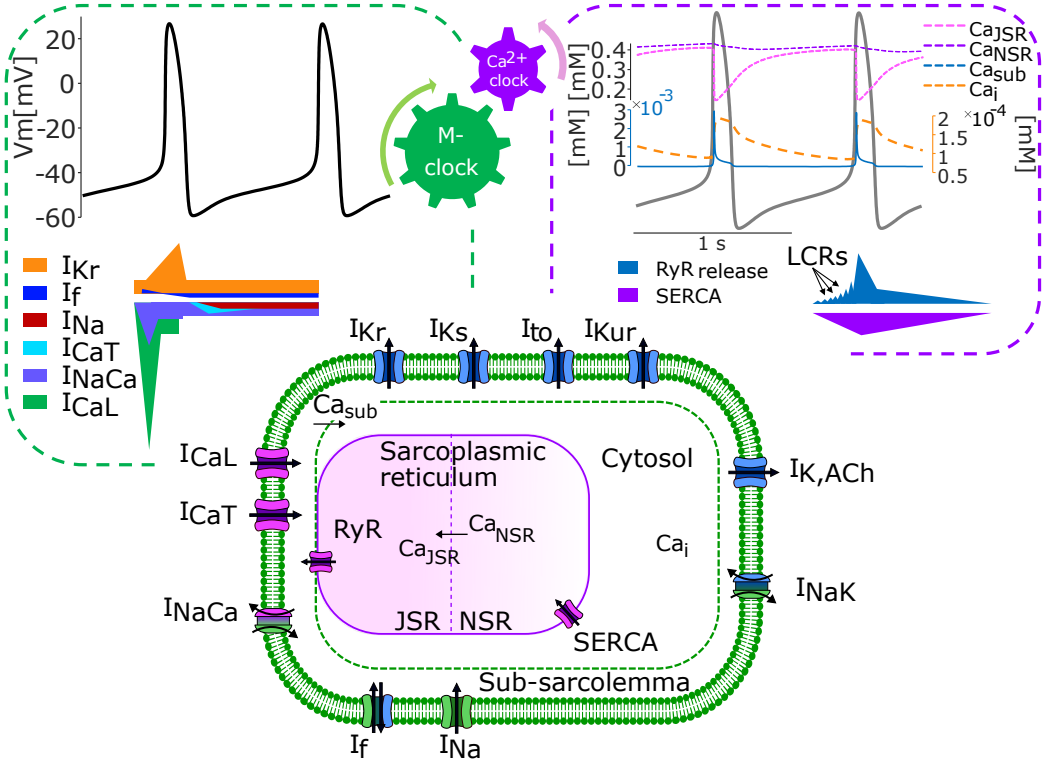

Figure 1.2: ***SAN cell and coupled clock model schematization****. The majority of contemporary models of the SAN featuring calcium handling show four compartments: the cytosol, the sub-sarcolemmal space (which represents the space near the cellular membrane) and the network (NSR) and junctional (JSR) sarcoplasmic reticulum, each with its own Ca^{2+} concentration: Ca_i, Ca_{sub}, Ca_{NSR} and Ca_{JSR}, respectively. Dashed arrows represent fluxes between compartments. Channels depicted in pink transport Ca^{2+}, in blue K^+, in green Na^+. Ionic currents and other abbreviations are reported in Table 1. The membrane clock – depicted in green – is composed by the ionic channels on the cell membrane. The main currents giving rise to the action potential are schematized in the green dashed box on the left. The calcium clock – depicted in purple – is formed by the sarcoplasmic reticulum and its Ca^{2+}-releasing ryanodine channels (RyR) and Ca^{2+}-uptaking SERCA pump. The dashed purple box reports a schematization of local calcium releases (LCRs) from the RyR and the Ca^{2+} concentrations in the different compartments during 2 APs simulated with the FWS model [25].*

stores (as already set in [22] and later discussed in [80]).

Table 1.1: ***Recent computational models of SAN action potential.*** *Different models are listed chronologically and divided by thick black lines. New versions of previous models are grouped chronologically below their parent model and divided by thin black lines. ODEs: ordinary differential equations; PDEs: partial differential equations.*

New models	New versions of previous models	Year	Species	Number of equations	Parent model	Main development
	Kurata [76]	2008	Rabbit	26 ODEs	Kurata et al. [21] Zhang et al. [77]	• Peripheral and central cell models • ACh effect
HSMN [36]		2008	Guinea pig	38 ODEs	Sarai et al. [88]	
ML [22]		2009	Rabbit	29 ODEs	Kurata et al. [21]	
	Maltsev & Lakatta [89]	2010	Rabbit	30 ODEs	Maltsev & Lakatta [22]	ANS modultaion
	Yaniv [90]	2012	Rabbit	27 ODEs	Maltsev & Lakatta [22]	Mitochondrial Ca^{2+} regulation
	Yaniv [91]	2013	Rabbit	27 ODEs	Maltsev & Lakatta [22]	Fitting on new data
	Yaniv [92]	2013	Rabbit	28 ODEs	Maltsev & Lakatta [22]	• No I_{st}/I_{Ks}, reduced I_{hNa}/I_{NaK} • New RyR release kinetics
	Yaniv [93]	2015	Rabbit	37 ODEs	Maltsev & Lakatta [22]	AC-cAMP-PKA signalling in β-adrenergic response
	Behar [94]	2016	Rabbit	34 ODEs	Yaniv et al. [93]	AC-cAMP-PKA signalling in cholinergic response
	Imtiaz [87]	2010	Rabbit	27 ODEs	Kurata [21]	Enhanced intracellular calcium stores' role
Kharche [23]		2011	Mouse	38 ODEs	Zhang et al. [77] Kurata et al. [21]	
	Behar & Yaniv [95]	2017	Mouse	41 ODEs	Kharche et al. [23] Yaniv et al. [93]	• Fitting on new Ca^{2+} data • AC-cAMP-PKA signalling in β-adrenergic and cholinergic response
	Morotti [96]	2021	Mouse	38 ODEs	Kharche et al. [23]	New I_{CaL}, I_{to}, I_{sus}, I_f formulations
Tao [78] Kurata et al. [21]		2011	Rat	39 ODEs	Zhang et al. [77]	
	Alghamdi [97]	2020	Rat	39 ODEs	Tao et al. [78]	Ionic maximal conductances scaling based on aging-induced remodeling
	Christel [98]	2012	Mouse	30 ODEs	Mangoni et al. [99]	Ca^{2+} handling (from Kurata/ML models)
SDiF [24]		2012	Rabbit	33 ODEs	DiFrancesco & Noble [13] (membrane currents) Maltsev & Lakatta [22] (Ca^{2+} handling)	
Stern [81]		2014	Rabbit	• 2 PDEs systems (Ca^{2+} dynamics in RyR couplons and cytosol) • 1 ODEs system (membrane voltage and currents)	Maltsev & Lakatta [22]	3D local calcium releases
Pohl [84]		2016	Human	37 ODEs	Dokos et al. [85]	
FWS [25]		2017	Human	33 ODEs	Severi et al. [24]	
	Loewe [100]	2019	Human	35 ODEs	Fabbri et al. [25]	• Intracellular Na^+/K^+ homeostasis • Addition of I_{sK}
	Hoekstra [101]	2021	Human	33 ODEs	Fabbri et al. [25]	New I_f fitting
	Alghamdi [102]	2020	Rabbit	39 ODEs	Zhang et al. [77]	Neonatal cell action potential
Maltsev [35]		2022	Rabbit		Maltsev et al. [79] (Ca^{2+} handling) Maltsev & Lakatta [22] (membrane currents)	• Updated calcium-release units activation and termination mechanism • Trade-off between common pool and detailed 3D single cell model

Efforts were also designated to include a detailed explanation of the autonomic modulation effects by the description of the AC-cAMP-PKA signalling cascade, intracellular effectors of the ANS activity (AC, adenylyl cyclase; cAMP, cyclic adenosine monophosphate; PKA, protein kinase A). In this regard, additions to

the ML model can be found in [89], [93], [94] and [95] and will be discussed in a specific section.

Other additions to the ML model from the same group assess the role of mitochondria in intracellular Ca^{2+} handling [90] and describe the mechanisms of ivabradine (a selective I_f inhibitor [91]) and caffein administration (which activates RyR and provokes Ca^{2+} releases from the sarcoplasmic reticulum (SR [92]). Behar and Yaniv [95] updated the Kharche model based on their previous works [94] in order to study the effects of aging on mouse SAN; similarly, Alghamdi and colleagues modified the model by Tao et al. [78] to study SND in the aging rat SAN [97]. On the opposite, the same group developed the model by Zhang et al. [77] to describe neonatal rabbit APs [102]. Two additional mouse models are those by Christel et al. [98] and by Morotti et al. [96]. The former updated the model by Mangoni et al. [99] by adding the Ca^{2+} handling from Kurata and ML models. Central to pacemaking, in this case, is the role of L-type Ca^{2+} current, specifically of the $Ca_v1.3$ isoform. The latter added new current formulations to the Kharche model to assess the dependency of pacemaking on intracellular Na^+. Finally, the FWS model was extended with intracellular ion homeostasis by Loewe et al. [100] and with new I_f kinetics by Hoekstra et al. [101].

Table 1.2 summarizes the main AP features of the models as reported in the original papers, divided by species.

Table 1.2: ***Action potential features of SAN models as found in the original papers.*** *Models that did not report AP features are not included. DDR_{100} is defined as the diastolic depolarization rate in the first* 100 ms *of the diastolic phase.*

Model	MDP [mV]	OS [mV]	APA [mV]	CL [ms]	APD_{50} [ms]	APD_{90} [ms]	dV/dt_{max} [V/s]	DDR [V/s]
Mouse								
Kharche [23]	-64.5	22.6		212	35	62	9.2	0.186
Christel [98]				278				
Morotti [96]	-63.2		73.2	147	19.7	61.7	11.1	0.117
Rat								
Tao [78]	-56.3	19.9	76.1	257	77		6.5	
Alghamdi [97]	-56.8	24.6		310	88		10.9	
Aging 1	-45.7	9.5		265	64		2.3	
Aging 2								
Guinea Pig								
HSMN [36]	-64.8	12.9	77.7	455			4.3	0.087
Rabbit								
ML [22]	-62.7		75.9	333	101		4.8	
SDiF [24]	-58	22	80	352	108		7.1	0.092
Yaniv [92]				340				
Behar [94]	-64		86	328			10.2	
Alghamdi [102]	-63	32.2		277			11.9	
Human								
Pohl [84]	-60	15	76	836	40	72 (APD_{100})	15	0.039 (DDR_{100})

Table 1.2: (continued)

FWS [25]	-58.9	26.4		814	136	162	7.4	0.0481 (DDR_{100})
Loewe [100]	-60.9	26.8		828	108	130	6.5	0.0757 (DDR_{100})
Hoekstra [101]				777				

1.3 Origin of pacemaking

Historically, mathematical models of cardiac pacemaking could be mainly divided into three categories, corresponding to the importance of as many currents in originating the diastolic depolarization. Models with a primary role for I_f, I_{Ca}, and for the Ca^{2+}-clock can be found in the literature [57]; however, this categorization is becoming more nuanced and recent models can rely on more than one of them. The first models of pacemaking ascribed the decay of an outward, K^+ current (I_{K2} [10], [11], [103], [104]) that unmasked inward background currents, to be the cause of the slow *DD* phase. However, after about 20 years, these models became outdated for two reasons: first, they regarded the Purkinje fibres; secondly – and most importantly – experimental results showed I_{K2} to be actually due to an inward current carrying both Na^+ and K^+ ions, active at hyperpolarized potentials: what was then called the funny current [63]. Since this discovery, many models have been built relying on the opening of HCN channels (the molecular determinant of I_f) at hyperpolarized potentials to drive the *DD*. Despite this, the reduction of K^+ conductances during diastole and the absence of I_{K1} are still believed to be the premise of cardiac pacemaking [105].

1.3.1 I_f-based pacemaking

In the rabbit SAN, HCN4 is the most expressed isoform of the HCN channels family, representing more than 80% of the total HCN transcriptomics in rabbits, followed by HCN1 (18%) and HCN2 (0.6%, [106], [107]). These proportions were reported to be conserved also in humans [83] and mice [108], [109], even if in the latter case the relative abundance of HCN2 and HCN1 is less clear [107]. In addition to their expression levels, it is important to underscore that HCN channels are tetramers (i.e., they are formed by 4 subunits) and show electrophysiological properties (e.g., half-activation voltage, activation and de-activation kinetics) intermediate between the different isoforms, suggesting that they are composed of different isoforms [110].

Coming to the modelling aspects of I_f, the SDiF single-cell rabbit SAN model [24] includes a realistic formulation for I_f and an accurate revision of all the membrane currents potentially active during the *DD*, allowing it to reproduce both voltage clamp and current block experimental data [65]–[71], [73], [74]. In this model I_f represents the largest current until late *DD*; this has the advantage that the *CL* can be regulated in a fast and energy-efficient manner by only modulating the entity of this current during early *DD* [24]. Another strength of this model is that I_{net} in diastole is the result of the balance between small inward (I_{in}) and outward (I_{out}) currents; thus, I_{net} is only about two times smaller than I_{in}. Other models, such as the ML one, show a similar I_{net}, but the I_{in} and I_{out} determining it are much larger. In particular, I_{in} is almost an order of magnitude bigger than I_{net}, mainly because of the presence of large background currents (Figure 1.3). Smaller inward and outward currents require less subsequent ion movement to ensure ionic gradients, granting a more efficient pacemaking (less energy consumption via sodium-potassium pump [111], [112]). While opposite to this model Ca^{2+}-clock models feature a minor role for I_f (due to its slow dynamics and low half-activation voltage [22]) or even a complete absence [113], other numerical reconstructions have highlighted an intermediate role between the two concepts. This is based on the evidence that both model types detach from experimental data to some extent [114], in particular regarding I_f maximal conductance (too low in the ML model), reversal potential (too depolarized in the SDiF) and gating kinetics (too fast in both models, especially the deactivation ones).

The available experimental data showed that I_f maximal conductance is $3-4$ times smaller, the half activation voltage is $\sim$20 mV more negative and the (de)activation time constant voltage dependence is shifted to more negative values in humans than in rabbits [86]. AP-clamp reconstructions [115] considering these factors obtained a smaller current in humans, which is nevertheless comparable to the total net current (I_{net}) in *DD* [25], [86], claiming for the same importance it has in rabbits [115], even though the ratio between the charge carried by I_f and

I_{net} was later shown to be lower in humans than in rabbits [116]. In the rabbits, dynamic clamp experiments support a primary role for I_f [117]. Indeed, this innovative technique allowed a comparative validation of the ML and SDiF models, highlighting how the injection of a numerically reconstructed I_f restored pacemaking in rabbit SAN cells after block due to ivabradine only if the formulation adopted by the SDiF model was used [117]. A synthesis of all these works is included in the FWS model of human SAN cell, where if on one hand the modulatory role of I_f under β-adrenergic receptor ($\beta - AR$) stimulation was shown to be similar to rabbits, on the other one the sensitivity to I_f block is lower than in the SDiF model (upon 100% If block the model still shows a regular beat, with a CL increase of 28.1% [25]).

Bifurcation analyses (i.e., the systematic assessment of changes in the steady-state model behaviour in response to parameter perturbations) performed by varying the maximal conductance of the funny current in the Kurata and Zhang central and peripheral cell models [119] suggest that I_f is not necessary for pacemaking since it does not contribute to equilibrium point destabilization, differently from I_{CaL} and I_{Na} [76], [120]. On the opposite, an increase in I_f was shown to decrease pacemaking robustness, especially when changes in intracellular Na^+ are considered [121]. For the authors, the explanation is to be found in the voltage dependence of this current: if the membrane voltage V_m depolarizes (due to I_f), then I_f itself decreases, stabilizing that equilibrium point. However, these results are in contrast not only with the evidence reported above, but also with other reports that show how, although limiting the frequency range, I_f increases the model robustness by enlarging the ranges of g_{CaL} (the maximal conductance of the L-type Ca^{2+} current) and P_{up} (the Ca^{2+} uptake rate by the SERCA pump) for which a stable rhythm is obtained [22], [112]. These discrepancies could be explained by incorrect I_f kinetics (too fast compared to [114]) and, as noted by Yaniv and coauthors [92], by incorrect sodium homeostasis in contemporary SAN models. It would be interesting to investigate the response of the SDiF model, where blocking I_f completely stops pacemaking activity, to this kind of analysis. Despite this contradictory result, bifurcation analyses show a beneficial role of I_f to pacemaking under hyperpolarized conditions, such as during ACh administration and electrotonic influence of atrial cells [119], where the presence of I_f prevents cessation of spontaneous activity. Although limited to a specific, hyperpolarized, condition, these results seem to be the most relevant for the role of I_f in vivo. In a physiological setting, the SAN undergoes both the electrotonic influence of the atrium and a relatively high parasympathetic tone. Thus, these results are in agreement with the effects of I_f block and loss of function mutations in HCN4 channels, which both determine bradycardia, as reported below.

Data coming from the evaluation of the effects of mutations in the HCN4 channel support indeed a key role for I_f in DD ([122] for review, updated in [123]),

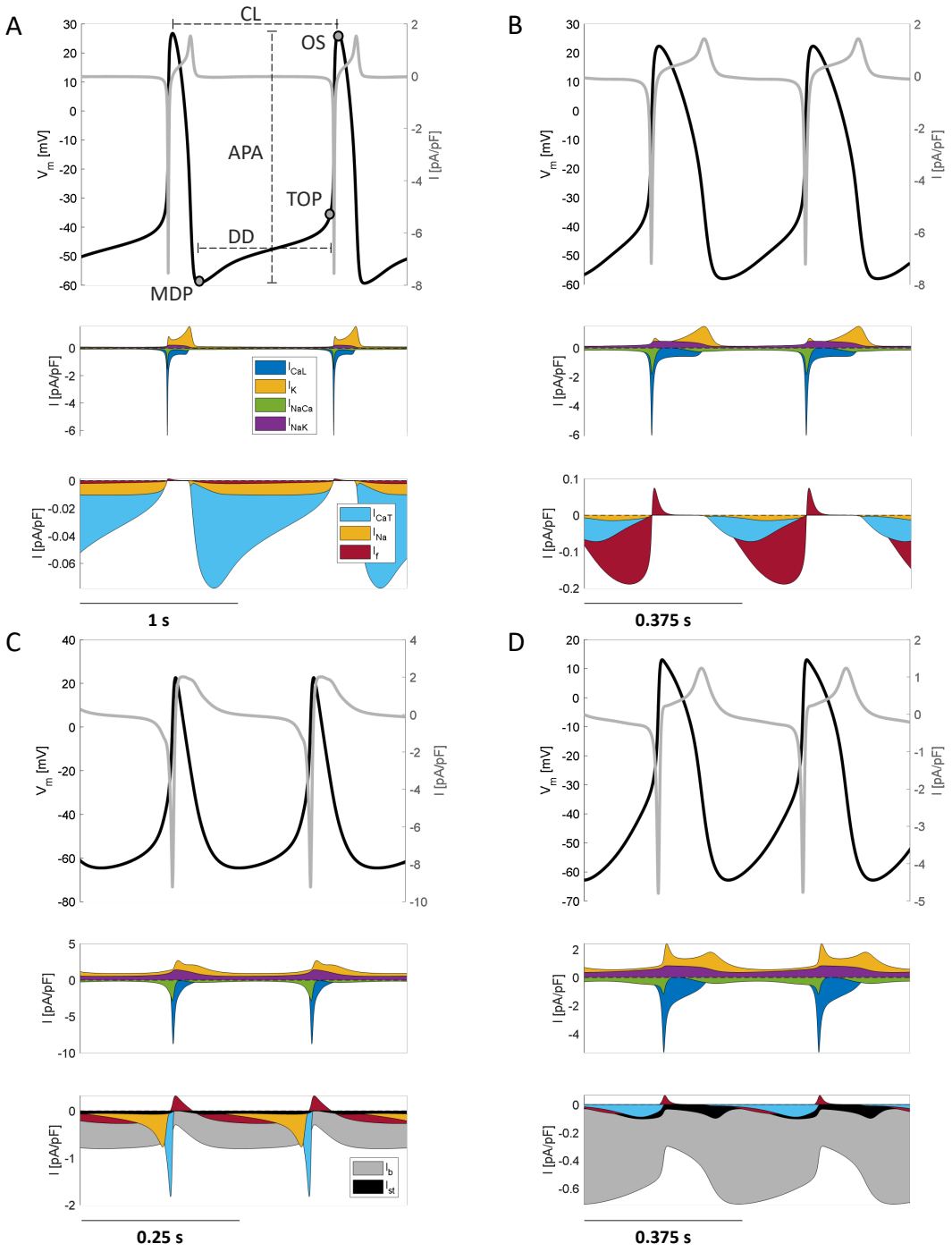

Figure 1.3: (Caption in next page).

Figure 1.3: ▲ ***Examples of action potentials and ionic currents***. *SAN AP (TOP) and main currents (middle and bottom) at steady state (*500 s*) for A) human (FWS model [25]), B) rabbit (SDiF model [24]), C) mouse (Kharche model [23]) and D) rabbit (ML model [22]. Action potentials are depicted in black, total current in grey.* I_K *is the sum of all* K^+ *currents:* I_{Kr}, I_{Ks}, I_{Kur}, I_{to}. I_{K1} *(inwardly rectifying* K^+ *current) is included in the Kharche model, where additionally* I_{CaL} *and* I_{Na} *are each the sum of two distinct current components:* $Ca_v1.2$, $Cav_1.3$ *for* I_{CaL} *and* $Na_v1.1$, $Na_v1.5$ *for* I_{Na} *(respectively the neuronal tetrodotoxin-sensitive and cardiac tetrodotoxin-resistant components of the sodium current).* Na^+, K^+ *and* Ca^{2+} *background currents are present in the Kharche model,* Na^+ *and* Ca^{2+} *in the ML one. MDP: maximum diastolic potential, defined as the most negative value of the membrane potential in one cycle; TOP: take-off potential, defined as the membrane voltage at the first time instant during diastolic depolarization when the second derivative of the membrane potential reaches* 15% *of its peak [118]; OS: overshoot, defined as the most positive value in membrane voltage during one cycle; DD: diastolic depolarization, defined as the time interval between MDP and TOP; APA: action potential amplitude, defined as the voltage difference between OS and MDP.*

since almost all the patients carrying a loss of function mutations show bradycardia. The FWS model qualitatively reproduces this behaviour, with the *CL* prolongation being milder than that seen clinically [25]. As the authors note however, the comparison between single cell and clinical data is hazardous, since many levels of complexity (source-sink relationship with the atrium, ionic remodelling due to adaptation to the mutation, experimental conditions of electrophysiological data) can influence it [25].

Another important aspect of I_f is its ability to regulate the *HR* in response to autonomic modulation. Here, dynamic clamp experiments [117] used as benchmark of alternative funny current computational models [22], [24], showed that the funny current is the main effector of both an acceleration or a deceleration of the heartbeat in response to isoprotenerol (ISO, a sympathomimetic drug) and to the neurotransmitter ACh, respectively. The recent data and simulations by Hoekstra et al. [101] report of a small fully-activated HCN4-specific current, insufficient by itself to drive the membrane voltage from the *MDP* to the take-off potential (TOP): the estimated carried charge is 57% of that required for such depolarization. However, there is a relevant HCN4 current increase (the charge becomes 73% of the total required to reach the TOP) after administration of forskolin, an adenylyl cyclase activator [124] that mimics $\beta - AR$ stimulation. Similarly, hyperpolarized conditions determine a larger current [101]. This supports the ideas of I_f contributing to the sympathetic response and serving as a backup mechanism protecting the SAN from excessive bradycardia. Also, the time constant of deactivation was found to be larger than usually considered and determined an

incomplete current deactivation during the AP phase, further slowed by forskolin [101]. A similar result was obtained by Peters et al. [125] for mouse SAN cells, where the slow dynamics of the HCN4 channel in the model – with respect to the high beating rate of mice – determine a persistent I_f activation throughout a cycle. On one hand, this allows for a larger portion of current to be immediately available at the beginning of the *DD*; on the other, it highlights the under-appreciated role of I_f as an outward current, contributing to early repolarization (at least in mice, whose *HR* is $550-620$ bpm [126]). This would also explain why HCN4, despite its slow kinetics [108], is the most abundant isoform also in mouse SAN in place of a faster isoform such as HCN1.

In summary, a realistic current reconstruction in normal conditions, with HCN4 channels mutations and under autonomic modulation show that I_f is an important *DD* driver in many species including humans. Given its pivotal role to reproduce experimental data, future models must not overlook I_f contribution to the net current balance during diastole.

1.3.2 Spontaneous calcium release-based pacemaking

While the "membrane clock" theory bases itself on the activity of currents located on the cell membrane, the "calcium clock" looks for an explanation to pacemaking inside the cell. Following this idea, the *DD* (particularly the late phase) of SAN myocytes is mainly determined by spontaneous Ca^{2+} releases from the SR. This in turn activates the sodium-calcium exchanger which, extruding $1Ca^{2+}$ and intruding $3Na^{+}$ ions, raises V_m up to the threshold for AP firing (that is, I_{CaL} activation voltage which is typically between $-30\,/-50\,\mathrm{mV}$ [2], as better explained in section 1.3.4). The *M*-clock is relegated to a "refilling" role, providing the cell – through I_{CaL} – with the Ca^{2+} needed to restart a cycle. Central to this whole idea is the presence of Ca^{2+} oscillations when V_m is clamped: the first numerical reproduction for this phenomenon comes from the ML model. However, periodic Ca^{2+} oscillations are only obtained when P_{up} is high ($40\,\mathrm{mM\,s^{-1}}$) compared to control ($12\,\mathrm{mM\,s^{-1}}$ for the ML and SDiF models, $5\,\mathrm{mM\,s^{-1}}$ for the Tao and FWS ones, $4\,\mathrm{mM\,s^{-1}}$ for Kharche) – a value for which the SDiF model is also able to show damped oscillations [24]. Bifurcation analysis [127] found no rhythmic spontaneous release from the SR at any clamped voltage, even with large P_{up}. Only few damped oscillations were obtained, in agreement with the SDiF model. As already presented in section 1.2, finer descriptions of functional and structural properties of intracellular Ca^{2+} handling allow the reproduction of these oscillations [35], [79]–[81], showing that these phenomena are reproducible with detailed models.

The other most important component of the Ca^{2+}-clock is the sodium-calcium exchanger current (I_{NaCa}), which couples the membrane and Ca^{2+}-clock together by influencing V_m ([58] for review). Minor in vivo *BR* changes in mice with in-

complete (∼80%) NCX (the gene encoding for I_{NaCa}) knock-out would point to a minor contribution of this current to pacemaking [128], in opposition to another experimental report showing absence of pacemaking with complete I_{NaCa} knock-out [129]. This discrepancy could be due to the large reserve of this current: simulations have indeed shown that even little amounts of this current are functional [24], [80], limiting the effects of blocks on the basal *CL*. This is because a block in I_{NaCa} determines Ca^{2+} accumulation inside the cell, increasing I_{NaCa} itself and thus compensating for the block. Very strong reductions ($> 75/80\%$) result nevertheless in arrhythmia or loss of pacemaking since, despite the increase in intracellular calcium, there is not enough I_{NaCa} available to sustain this negative feedback [24], [81], [96], [112]. Symmetrically, a rise in I_{NaCa} has been shown to prolong the *CL* by reducing the intracellular calcium concentration [130] and to compensate for reduced I_{CaL}, providing a possible explanation for the inverse correlation between *BR* and I_{CaL} density found in rabbit SAN cells in vitro [113]. Other computational works about I_{NaCa} report a similar role between rabbits and humans [116], and an earlier activation with respect to I_f [112]. A large reserve was also shown for local calcium releases formation depending on P_{up} [131], but it seems unlikely that these mechanisms can explain an unaltered *BR* following SR inhibition, such as Ca^{2+} chelation [132]. This result, together with the absence of Ca^{2+} oscillations when the membrane voltage is clamped, represent strong evidence against a primary role for the Ca^{2+}-clock in originating pacemaking. Thus, its role would be that of a "forced oscillator" [127], entrained by the *M*-clock, with the ability to accelerate the *BR*.

It is indeed generally accepted that the Ca^{2+}-clock provides flexibility to pacemaking, allowing the *HR* to vary in a wide range of frequencies [39]. Maltsev and Lakatta showed that models based on the Ca^{2+}-clock had a larger *HR* range with respect to *M*-clock based models, which were, in turn, more robust [112]. That is mainly achieved thanks to the modulation of cAMP and PKA levels that phosphorylate phospholamban (PLB), which controls P_{up} and RyR release [89]. A faster (slower) uptake results in earlier (later) and stronger (weaker) local calcium releases that determine, following this concept, the next *CL*. Models indeed suggest that the AC-cAMP-PKA signalling pathway to have the same kinetics (∼20 s) of *HR* increases during $\beta - AR$ stimulation [93] and to be implicated also during cholinergic receptor (ChR) response [94]. However, this second messenger cascade also involves the *M*-clock by modulating I_f, I_{CaL}, I_{Ks} among other currents [133], highlighting how sarcolemmal currents are involved in *HR* modulation, too. This data show that, in order to understand how pacemaking works, the two mechanisms cannot be considered as separated.

1.3.3 Coupled-clock pacemaking

Recent understanding points therefore toward an integrated action of the two clocks, both in basal conditions and under ANS stimulation during all the *DD* [87]. This "coupled-clock" theory ([46] for review on first coupled-clock models) was able to explain the effect of I_f block due to ivabradine (if additionally taking into consideration an indirect effect of ivabradine on the SERCA pump) and an HCN4 gain of function mutation taking into account the feedback mechanisms connecting the two clocks [91], [134]. Plus, a combination of Ca^{2+}-clock-based models with a subset of membrane currents provides the best trade-off in terms of both robustness and flexibility, achieved by neither clock alone [112]. Thus, after years of vivid debate over which mechanism prevailed [38], the consensus has recently shifted on this unified view [39], [93]. In this context, the AC-cAMP-PKA and Ca^{2+} signalling would act as a bridge [95], as also Na^{+} and Ca^{2+} electrochemical gradients were shown to behave [135]. Kim et al. [136] analysed guinea pig SAN cells with irregular – or without at all – electrical activity and proposed that this phenomenon was due to partial – or complete – clock uncoupling. The models showing this behaviour were indeed those with both lower P_{up} and g_{CaL}. $\beta - AR$ stimulation, simultaneously increasing the rate of SERCA uptake and the availability of membrane currents, reinforces the feedbacks between the clocks allowing these cells to show rhythmic APs. Finally, I_{NaCa} and I_f can "cooperate", representing a reciprocal depolarization reserve in case of block of one of the two [118].

1.3.4 Ca^{2+} currents-based pacemaking

The last category of SAN computational models focuses its attention on the role of calcium currents. I_{CaL} is considered as the main SAN current in all the model types since – in the absence of a large I_{Na} – it determines the (relatively slow) upstroke phase. This current is formed by two components mediated by two different channels isoforms: $Ca_v1.2$ and $Ca_v1.3$, with the latter activating at potentials (-50 mV) more negative than $Ca_v1.2$ (-30 mV) [137]. $Ca_v3.1$ channels, mediating I_{CaT}, are active at even more negative potentials (-55 mV) [99]. Thus, $Ca_v1.3$ and $Cav_3.1$ show properties suitable for a role during diastole.

Based on experimental data [137], Kharche and coauthors were the first to include a $Ca_v1.3$ component in their model. The simulations showed a major role for $Ca_v1.3$ since a 100% block resulted in absence of pacemaking [23]. Integration of experimental data on colocalization of $Ca_v1.3$ channels with ryanodine receptors (RyR) and voltage-dependent facilitation, a mechanism by which depolarization and Ca^{2+} influx facilitate the opening of the channel at hyperpolarized potentials through the transition from a "reluctant" to a "willing" state, allow

for an increased $Ca_v1.3$ contribution in diastole [98]. In computational models, $Ca_v1.2$ current could have a role in late diastole too due to a "technical" reason: little changes in the slope factor k of its Boltzmann curve (made to best fit the activation curve around $-40\,\text{mV}$) determine little percentage changes in $Ca_v1.2$ activation gate. Given the large maximal conductance of this component, these variations have a strong impact on the fine current balance during the diastolic phase. The high *CL* sensitivity over the $Ca_v1.2$ component of I_{CaL} and its importance to pacemaking as reported by sensitivity analyses [112], [120], could also be due to this dependence.

I_{CaT} was suggested to be essential in allowing the sufficient Ca^{2+} release from the SR that guarantees the high *BR* of small mammals [87]: its low activation threshold allows to accelerate the *DD* by determining calcium-induced calcium releases [138]. Therefore, if I_{CaT} was first suggested to contribute to the diastole of cat atrial subsidiary pacemaker cells [139], its role in pacemaking seems to be important also in the context of SAN Ca^{2+}-clock based models [138], [140]. In models based on the *M*-clock theory, the contribution of I_{CaT} is similarly important for its direct effect as an inward current in *DD* [24], [25]. This evidence confirms – as explained at the beginning of this section – that the categorization of these models is not sealed. On the opposite, experimental data show that $Ca_v1.3$ channels induce local calcium releases and promote their synchronization upon $\beta - AR$ stimulation, modulating – if not directly controlling – Ca^{2+} clock activity [141]–[143]. In this perspective, $Ca_v1.3$-mediated L-type Ca^{2+} current would be a direct link between the two clocks, acting in addition to I_{NaCa} activity in determining clocks interaction. The direction of the feedback is however opposite to I_{NaCa}: if the latter influences the membrane voltage depending on spontaneous calcium releases, $Ca_v1.3$ channels influence the Ca^{2+}-clock depending on the membrane voltage.

Another source of data giving hints on pacemaking mechanisms is the difference between the SAN and the atrium both in terms of genetic (mRNA) and protein expression. Chandler et al. [83] managed to obtain a SAN-like AP by modifying the maximal conductances of a human atrial model according to the respective mRNA levels found in the two tissues. Similar results were more recently obtained by Linscheid et al. [109] for the mouse SAN: scaling the maximal conductances of the Kharche SAN model and of an atrial mouse model [144] according to mRNA expression levels, they obtained an atrial-like and a SAN-like AP, respectively. The interesting part of these works is that Ca^{2+}-handling protein expressions were found to be conserved between SAN and atrium; $Ca_v3.1$ expression was instead higher and HCN4 almost exclusive to the SAN, reinforcing the idea of a leading role for the *M*-clock. Despite this, Ca^{2+}-cycling proteins' activity was both measured [145] and predicted by modelling [93] to be higher

in SAN than in ventricles, highlighting a possible increased contribution of the Ca^{2+}-clock. Also, as already reported in section 1.2, spatial organization seems to have an important role in Ca^{2+}-clock activity [81], with RyR distribution influencing pacemaking robustness with respect to simulated I_{CaL} losses [35]. Thus, the importance of intracellular calcium store to pacemaking cannot be completely ruled out relying on this data, especially considering the exceptional heterogeneity found in this tissue [1], [113] and the possible different roles of Ca^{2+} and M-clock in different clusters inside the SAN [49]. Despite this, the balance of the evidence reported above does not advocate for a primary role of the Ca^{2+}-clock in originating cardiac action potentials.

In conclusion, pacemaking can be thought as an emergent property, synthesis of many complex and deeply interconnected processes. Feedback and backup mechanisms should restrain from conceptualizing the heartbeat as the straightforward outcome of a single factor. None of these is indeed essential for pacemaking on its own, and any schematization, if useful to test a specific hypothesis, becomes a limitation when attempting a comprehensive explanation. Rather, each actor has its importance and its specific role – not fixed in time but adaptive (e.g.: in pathological conditions) – that allows the mammalian SAN to beat from about one billion of times [146] in most mammals to $2-3$ billion of times in humans [39] with a flexible frequency (due to intrinsic variability and physiological needs). Still, many aspects are preventing a satisfying, shared understanding of SAN activity. Among them, the just mentioned pathological remodelling but also differences between species and tissue (e.g.: central vs. peripheral SAN). All these were shown to affect pacemaking in terms of prominence of the mechanisms originating it and will consequently be discussed in the next sections.

1.4 Cellular synchronization and tissue structure

1.4.1 Entrainment

Computational evaluations of the ability of sinoatrial cells to synchronize their beating frequency (Figure 1.4) date back to the 80s [147], [148], taking inspiration from mutual entrainment theory thanks to the intuition that SAN cells could behave as coupled oscillators [149], [150]. Being electrically connected by gap junctions, the self-oscillating SAN cells are in fact able to "entrain", *i.e.*, show the same *BR* (frequency synchronization). In this condition, cells can additionally show simultaneous firing (phase synchronization) or not [151], [152]. This ability was investigated by coupling model cells in pairs or inside tissues, stimulating them with brief current pulses or by giving signals generated by a computational model in input to in vitro cells (model clamp technique [152], [153]). Using these

methods, it was possible to reveal that SAN cells (and in general pacemaking cells such as atrioventricular ones [154]) can show different patterns of frequency entrainment depending on many factors, including the strength of electrical coupling, the timing of the stimulus, the difference in intrinsic *CL* and the influence of the nervous system. The result is a frequency within the range of individual intrinsic rates of the cells, thought to be obtained through a "democratic" process and not simply given by the fastest cell [147]. The value of gap junctional conductance determines the nature of the interaction [151]: phasic (*i.e.*, synchronization is obtained thanks to the action potential of the fastest cell that depolarizes the neighbouring ones) when the coupling is poor, tonic (*i.e.*, continuous current exchange during *DD*) when it is high [147], [152]. The synchronization process is a peculiar aspect of the SAN, firstly because it enables it to deliver a unique stimulus to the heart at every beat. Secondly, synchronization results in an "apparent propagation", where cells discharge progressively in space not because of an input (stimulus current), but as a consequence of entrainment [148]. This is true even with tens of thousands of cells, as shown by simulations of a 3D mesh of biophysically detailed models [155]. As one would expect, lower couplings and fewer connections between cells increased the time necessary for synchronization. However, a certain degree of uncoupling appears to be beneficial for pacemaking in heterogeneous tissues, as indicated by 2D models in which heterogeneity was achieved by randomizing the ion channel maximal conductances and permeabilities of the single cell models [33], [34]. Notably, low intercellular coupling values of 0.25-1.1 nS allow pacemaking in a tissue where only the 3.4% of cells (FWS model) show spontaneous depolarization following parameter randomization and a 50% I_{CaL} block mimicking a diseased condition [34]. Sensitivity analyses on the Kurata model [156] revealed that the influence of I_{CaL} on *CL* and diastolic depolarization rate (*DDR*) diminished upon coupling, whereas the one of I_{Kr} increased. Furthermore, specific intercellular coupling intervals ($0.00014-0.00033\,\Omega^{-1}\,\mathrm{cm}^{-1}$) promoted arrhythmic activity (spiral waves in the absence of anatomical obstacles), whereas higher coupling values ($>10^{-3}\,\Omega^{-1}\,\mathrm{cm}^{-1}$) increased the portion of SAN tissue showing phase synchronization (*i.e.*, with simultaneous firing) in addition to frequency synchronization (*i.e.*, firing with the same *CL*). Cellular heterogeneity has a similar effect, but at the same time results in shorter *CL* [155], [157], [158]. In addition to this rate-modulatory effect, heterogeneity seems to play a key role in determining pacemaking robustness: 2D models composed of identical ML single cell models (not showing spontaneous depolarizations due to a $P_{up} - g_{CaL}$ combination preventing APs) do not show electrical activity. However, when P_{up} and g_{CaL} are randomized to reproduce cellular heterogeneity starting from the same values that did not allow depolarizations, pacemaking in the tissue is rescued [33]. Besides coupling and heterogeneity, spontaneous cell clustering [33], [34] and uniformly random RyR distributions [35] could represent other

mechanisms strengthening SAN activity.

Besides investigation of the steady-state behaviour, the assessment of dynamical properties of SAN tissue can provide information about the entrainment process. For example, this can be done by applying current pulses of different amplitudes at different phases of the *CL* to evaluate how the next *CL* is affected (phase response) [147], [159]. Combinations of stimulus duration, amplitude and timing were shown to be capable of terminating pacemaking in Zhang central and peripheral cell models [160] as well as in the ML one [161]. At the same time cell coupling, stimulus site [162] and $[Na^+]_i$ [163] deeply influence the phase response behaviour of the models, with low coupling being protective with respect to annihilation in 1D [161]. Elevated $[Na^+]_i$ instead promoted irregular pacemaking activity in Kharche model [163], with normal activity interrupted by quiescent periods due to $[Na^+]_i$ accumulation. On one hand, this highlights the importance of Na^+ homeostasis, which will be discussed in section 1.5.5, and its poor description in contemporary SAN models. On the other, the simulated AP traces obtained in this condition [163] – are interestingly similar to those recorded by Fenske et al. [164] in SAN cells from mice with mutant HCN4 channels lacking cAMP regulation. This possibly suggests a similar modulation of the *CL* by both $[Na^+]_i$ and cAMP regulation of HCN4 channels (whose slow kinetics, as reported above, appear to have a central role in pacemaking).

1.4.2 Heart rate variability

Intercellular coupling determines a reduction in intrinsic (*i.e.*, not due to ANS modulation) heart rate variability (HRV) caused by stochastic single-cell current fluctuations, with this reduction being equal to $\sqrt{(1/N)}$, where N is the number of coupled cells [165]. An increased single-cell membrane current stochasticity determines nevertheless a monotonic shortening of *CL* in the SDiF model (through an increase in *DDR*, [165]). Under this point of view, a better coupling acts to lower the *BR* by reducing the membrane current stochasticity. 2D simulations by Ponard et al. [166] show that long-term cellular phenomena, such as a change in the expression of ion channels, also have a role in HRV. Particularly, this mechanism describes the power-law behaviour of HRV of cell cultures better than current stochastic fluctuations [166].

Despite the evidence of intrinsic variability mechanisms in denervated animal models, explanted hearts, single cells (e.g. see [167] for the evaluation of the relative contribution of *M*- and Ca^{2+}-clocks to the intrinsic variability in guinea pig SAN cells), and also computational models here reported, HRV is generally believed to be mostly determined by extracardiac factors, such as autonomic modulation. However, by adding a stochastic component to the total membrane current (with uniform distribution and a maximal amplitude of 20 pA) to the Zhang model

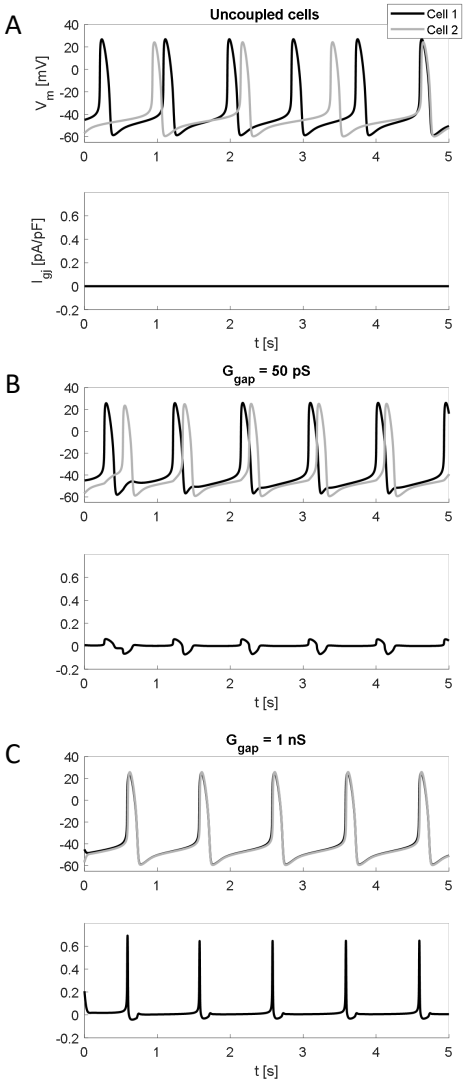

Figure 1.4: ***SAN cells entrainment.*** *Synchronization of two heterogeneous SAN cells (FWS model) at different intercellular coupling conductance (G_{gap}) values, starting from different initial conditions. Heterogeneous cells were obtained by randomization of the main ion channels permeabilities and maximal conductances using a log-normal distribution ($\sigma = 0.2$; Cell 1: $P_{CaL} = 0.3652\,nA\,mM^{-1}$, $P_{CaT} = 0.0444\,\mathrm{nA\,mM^{-1}}$, $g_{Kr} = 0.0042\,\mu\mathrm{S}$, $g_{Ks} = 5.7032 \cdot 10^{-4}\,\mu\mathrm{S}$, $g_{Kur} = 1.4737 \cdot 10^{-4}\,\mu\mathrm{S}$, $g_{Na} = 0.0231\,\mu\mathrm{S}$, $g_f = 4.8857\,\mu\mathrm{S}$, $g_{to} = 0.0046\,\mu\mathrm{S}$, $i_{NaKmax} = 0.0708\,\mathrm{nA}$, $K_{NaCa} = 4.5284\,\mathrm{nA}$, $P_{up} = 5.3762\,\mathrm{mM\,s^{-1}}$; Cell 2: $P_{CaL} = 0.4549\,\mathrm{nA\,mM^{-1}}$, $P_{CaT} = 0.042\,\mathrm{nA\,mM^{-1}}$, $g_{Kr} = 0.0044\,\mu\mathrm{S}$, $g_{Ks} = 6.4198 \cdot 10^{-4}\,\mu\mathrm{S}$, $g_{Kur} = 1.7862 \cdot 10^{-4}\,\mu\mathrm{S}$, $g_{Na} = 0.0257\,\mu\mathrm{S}$, $g_f = 3.9361 \cdot 10^{-4}\,\mu\mathrm{S}$, $g_{to} = 0.0037\,\mu\mathrm{S}$, $i_{NaKmax} = 0.0718\,\mathrm{nA}$, $K_{NaCa} = 3.5916\,\mathrm{nA}$, $P_{up} = 5.8853\,\mathrm{mM\,s^{-1}}$). I_{gap} is considered positive when flowing out from Cell 1 which is faster, thus it depolarizes Cell 2. When uncoupled (panel A), cells are prevented from exchanging current and thus beat at their intrinsic rates. When coupled with low conductances, the cells are able to synchronize their frequency – i.e., beat with the same CL – but not their phase (panel B, TOP: the AP of Cell 2 occurs during the repolarization phase of Cell 1). Higher gap junctional conductances (panel C), lead to faster synchronization and more overlapping voltage traces, allowing both frequency and phase synchronization.*

it was possible to fully explain changes in HRV in terms of changes in *HR*, without any ANS contribution [168]. Even if experimental evidence tells of a more complex behaviour (since – opposite to the model – *HR* does not fully explain HRV by itself) a hyperbolic relationship between the standard deviation of the inter-beat interval and *HR* was found [168], which is due to a "geometric effect", first pointed out by Zaza and colleagues [169], [170]. In short, this geometric effect consists in the fact that same perturbations have a major impact on longer *DD* phases since these are due to a smaller net current; thus, stochastic current fluctuations will affect a low *HR* (*i.e.*, longer *CL* due to longer *DD*) more than a high *HR*. Consequently, total HRV cannot be straightforwardly adopted as a metric for ANS activity (either normal or pathological), which can be instead quantified using normalized values such as the ratio between powers in the high and low frequency bands [170]–[172].

1.4.3 The role of cellular heterogeneity in cardiac pacemaking

Cellular heterogeneity, as disclosed above, plays a significant role in determining the heart rate. Some research groups have proposed that two distinct cellular phenotypes constitute the SAN: a central and a peripheral one, each with different morphology, genetic expression, electrophysiology, and consequently with a different function [1], [2]. Assuming peripheral cells as bigger than central ones ($\sim$60 pF vs. 20/30 pF in membrane capacitance – a measure of cell size), Zhang et al. [77] developed mathematical models of these two cell types (later improved by Boyett and coauthors [173] and Kurata et al. [76] with the inclusion of Ca^{2+} handling) and of a transitional phenotype with intermediate characteristics. Under this assumption, peripheral (bigger) cells show larger currents densities such as I_{Na}, I_f, I_{to}, I_{Kr} and the model obtained by fitting on this data shows shorter *CL* and action potential duration (*APD*), more negative *TOP* and *MDP*, and more positive overshoot (*OS*) with a consequent higher action potential amplitude (*APA*) as well as faster upstroke and repolarization phases, compared to central cells. A gradient in cellular properties going from the centre to the periphery (as a function of membrane capacitance) in a 1D model consisting of central, peripheral, and atrial cells was able to reproduce the experimental evidence of earliest activation from the central SAN [77]. However, single-cell properties far from experimental values (too low upstroke velocity in peripheral cells), were required to obtain this result [174]. Increasing conductivity values going towards the periphery was necessary, in the same 1D model, to "protect" central cells from the faster rate of SAN periphery, which is instead slowed down by atrial load [174]. This result agrees with the classic study by Joyner and van Capelle [175] showing that a gradient in intercellular coupling is necessary for a small SAN region (of central phenotype only) to successfully depolarize the atrium.

Gradient vs. mosaic model

The hypothesis underlying the studies by Zhang and Garny [77], [174] is that, to achieve frequency entrainment and atrial driving (with the correct activation pattern), spatial gradients in cellular ionic properties and coupling conductance are necessary. This idea, referred to as the "gradient model", was nevertheless questioned by another theory, called the "mosaic model", stating that a specific peripheral phenotype cannot be found inside the SAN (see Figure 1.5 for a graphical schematization and examples of simulated AP traces obtained with models based on these two different conceptions). Thus, the transition in AP morphology from the centre to the periphery seen experimentally [176]–[179] would exclusively be caused by the electrotonic influence of interspersed atrial cells, whose number grows distally from the SAN ([5], [6], [48] for review of the two conceptions). In support of a central role for gradients in pacemaking is the evidence that frequency entrainment is more easily achieved, and the AP variation is smoother with the gradient model [180]; at the same time, specific cell numbers and arrangements – such as tree nets mimicking cellular interdigitations – allow the SAN to efficiently drive atrial cells, supporting the consistency of the mosaic model [181]. Contradictory results have been obtained regarding the ability of the gradient model to reproduce physiological earliest activations in central SAN. If some group showed that this can be achieved [182], [183], others pointed out the incompatibility of gradients in cellular properties with central activation [184] or the need for extrinsic factors such as ANS stimulation [185]. About this last point, it has to be remembered that the SAN is under relevant parasympathetic tone in vivo. Therefore, simulations showing only a transient central activation in the absence of ChR stimulation to a 2D gradient model (composed of central and peripheral cells obtained from the SDiF model [185]) don't necessarily rule against this type of cellular organization. Backing a major role for gradients in the SAN is the work by Inada and coauthors [186] (Figure 1.5B) which showed that removing either a gradient in ionic properties or in cellular coupling from 1D and 2D models of SAN-atrial coupling results in the absence of atrial driving or even of pacemaking. This is different from another report showing that a gradient in diffusion coefficients alone allowed for the activation to start in the centre [187]. Plus, intercellular conductance values in periphery (up to 4000 nS) and atrium (4000 nS) used by Inada and colleagues were much higher than the experimental ones (average 175 nS in rabbit atrium [188]) in order to obtain physiological conduction velocities and central activation. However, the comparison with experimental data must be cautious for two reasons. First, compared to a real 3D tissue, cells in 1D and 2D models have less connections with their neighbours for geometric reasons. To compensate these, larger gap junctional conductance values have to be set [174]. Second, experimental values were obtained from laterally

coupled cells that had undergone enzymatic dissociation [188], likely representing an underestimate of the real coupling conductance in rabbit atrium.

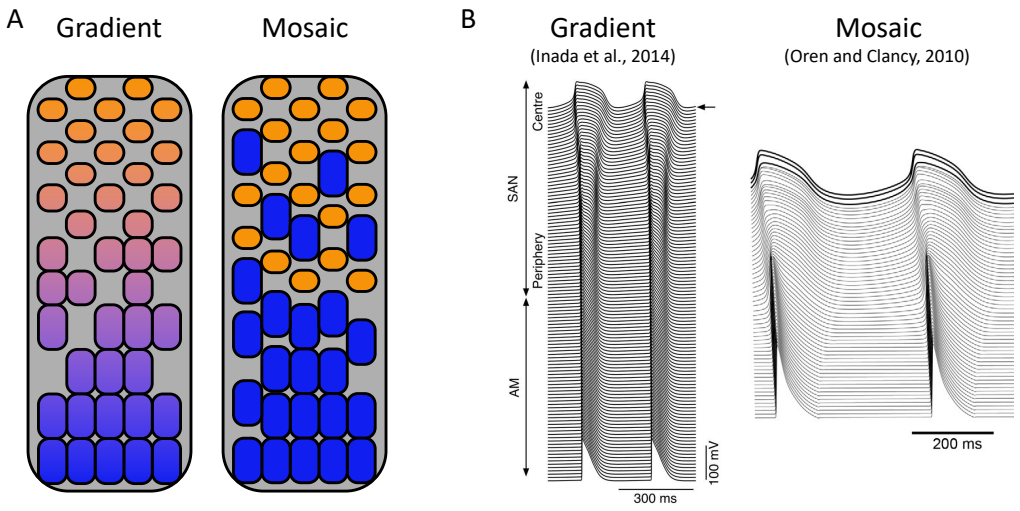

Figure 1.5: ***Gradient vs. Mosaic model.*** *A) Graphical representation of gradient and mosaic models. Left: gradient model schematization. Transition from central cells (orange) through peripheral cells (purple) to atrial cells (blue). Right: mosaic model schematization. Atrial cells (blue) are interspersed between central cells (orange). B) Illustrative results of gradient and mosaic models simulations. Left: simulated AP traces along a line obtained with a 2D gradient model of the rabbit SAN [186]. Kurata [21] and Lindblad [189] models were used for the SAN and atrial cells respectively. SAN cells membrane capacitance was increased from 20 pF in the centre to 60 pF in the periphery; gap junctional conductivity was increased from 25 nS in the centre to 4000 nS in the periphery [186]. The black arrow indicates earliest activation point. Right: simulated AP traces along a line obtained with a 2D mosaic model of the rabbit SAN [184]. Atrial cells (Lindblad model [189]) presence was increased from 22% in the centre to 63% in the periphery; gap junctional conductivity was set homogeneous in the tissue and equal to 7.5 nS. Kurata model [21] was used for SAN cells. The simulated traces indicate that both models can show both earliest activation in central SAN and atrial driving.*

In summary, both a gradient and a mosaic SAN organization were shown to be compatible with pacemaking and atrial driving. The main limitation of the "full" gradient model (considering a gradient in both intercellular coupling and cellular electrophysiological properties) is that it relies on the hypothesis that bigger cells, showing a peripheral phenotype, are located in the SAN periphery. However, "peripheral" cells have not actually been isolated from the periphery of the SAN. They have been identified as bigger cells with an electrical activity similar to that of peripheral tissue balls [1]; therefore, there is no direct correspondence between this phenotype and its location. Plus, some studies did not identify a correlation

between cell size and current density [113], a fact that questions the existence of such cell type in favour of a remarkable SAN heterogeneity. About gradients in gap junctional conductance, different connexin expressions can be found between SAN regions, although their distributions and the ratio between coupling values in centre and periphery, to the best of the authors' knowledge, have not been experimentally validated yet.

Anatomically detailed simulations show that intercellular coupling gradients (implemented as spatial changes in the monodomain model diffusion coefficient) can explain central activation [187], supporting the idea that such arrangement is found inside the SAN. However, the contradictory computational evidence collected so far does not allow for an exclusive adoption of either the gradient or mosaic models. Conversely, these two architectures could be both present in the SAN, as suggested by mixed gradient-mosaic models combining an increase in intercellular coupling conductance with an increase of atrial cells presence towards the periphery. This type of setup has in fact been shown to be able to reproduce A) central activation and leading pacemaker (LPM) migration following ACh administration (also thanks to the presence of fibroblasts) in a 2D SAN-atrial tissue [190] and B) physiological *CL* and conduction velocity (*CV*) in a human 3D SAN-atrial model featuring sinoatrial exit pathways (SEP [191]).

Electrophysiological regional differences

In support of the presence of a gradient in electrophysiological properties comes the evidence that different SAN regions seem to show different intrinsic ionic properties: experiments have shown that HCN4 channels are for example more expressed in the centre than in periphery [107], [192]. However, being I_f more activated at more negative potentials it is actually larger in a hyperpolarized peripheral environment (as discussed in section 1.3.1 and in [101], [119], [121]). I_{Na} is a more peculiar case: it is believed to be absent from the central zone, but it is fundamental for propagation in the peripheral one. Indeed, if on one hand I_{CaL} does not suffer from overdrive suppression as much as I_{Na}, on the other one an upstroke solely based on I_{CaL} would not be strong enough to drive the atrium [186], [193]. Experimental evidence against a functional role of I_{Na} in central SAN under physiological conditions, at least in adult dogs, is given by its low density and its steady-state voltage dependence (hyperpolarized with respect to the physiological V_m range [194]). In this case, I_{Na} could likely have a function similar to that conceived for I_f by Kurata and colleagues [119], [121], protecting from excessive hyperpolarization (especially in the periphery). Simulations run with the Kurata model – enriched with a canine-specific I_{Na} formulation – suggest that this mechanism is significant only in young subjects, in which I_{Na} would be more active because of the hyperpolarization coming from the increasing atrial

load and predominant parasympathetic tone [194]. A similar more prominent impact of I_{Na} on pacemaking in the first stages of life was also found to account for the higher heart rate seen in models of young rabbits SAN cell compared to older ones [102].

While only few data are available to determine the relative importance of the sodium current in the human SAN [195], evidence for this importance comes from numerous simulation studies showing that an impairment in I_{Na}, following a loss of function mutation in the *SCN5A* gene, can lead to SND. In particular, simulating a loss of I_{Na} lead to slowing of conduction and to *CL* prolongation [196], [197] up to the absence of beat [198] or exit block [199] in presence of ACh. A sum of *SCN5A* mutation and ACh release was seen to stop conduction along SAN exit pathways in a human SAN-SEP-atrial model, thus preventing the delivery of the stimulus to the atrium [200]. This combination of effects determines indeed the biggest drop in the safety factor (SF, a dimensionless parameter that indicates the margin of safety with which the action potential propagates relative to the minimum requirements for sustained conduction [201]; if SF$\geq$1, then electrical propagation in cardiac tissue is possible), since ACh disables the compensatory role of I_f [202], especially under heart failure and in presence of fibrosis [200].

Besides a major role for I_{Na}, other currents were also shown to be important for the SAN to drive the atrium. A decreased I_{CaL} and an impaired release from RyR led to a SF reduction in both a SAN-atrial cell pair and 1D string (built with the SDiF and Lindblad model [189] for the SAN and atrium, respectively [203]), setting the stage for atrial fibrillation (AF). On the opposite, reducing K^+ currents (I_{Kr} and I_{Ks}) increased the SF. Autonomic modulation can alter the SF as well, with the sympathetic branch (NE, norepinephrine) increasing it and the parasympathetic one (ACh) reducing it [203]. Other factors contributing to a successful atrial driving are the strength of the source – the SAN in this case – and of the sink: the atrium. In this regard, a higher number of SAN cells was reported to broaden the interval of coupling conductivities showing a pace-and-drive behaviour [175], [204]. On the opposite, increasing the number of atrial cells (Courtemanche model [17]) paced by a constant number of SAN cells (FWS model) in a 1D string results in a negligible effect on the SF of conduction [204]. This would suggest that a large atrium does not necessarily result in a bigger electrical sink, confirming the hypothesis that distant atrial regions do not interact electrotonically with the SAN [175]. In this way, the SAN would be able to excite the most proximal portion of the crista terminalis despite the disproportion in sizes between SAN and right atrium [175].

1.4.4 Sinoatrial exit pathways

The ability of the SAN to drive the atrium also depends on the interface between the two tissues. Based on experimental evidence, some research groups have promoted the idea that the SAN is surrounded by a border of adipose and fibrotic tissue, insulating and protecting the SAN from mechanical and electrical stress [61], [205]. The excitation would therefore be delivered to the right atrium exclusively through specialized structures, often referred to as sinoatrial conduction pathways or sinoatrial exit pathways (SEP). Instead, others proposed that such structures cannot be found inside the SAN, which would be consequently connected to the atrium thanks to diffuse interdigitations [1], [181]. Kharche and coauthors [187] developed a detailed 3D model of the human SAN and atrium and evaluated the effects of different anatomical configurations such as the presence of an insulating border with SEP. The simulations indicated that the addition of such structures does not affect the primary pacemaker location but in turn modulates the *BR*. Interestingly, in the presence of fibrosis and induced arrhythmia, the border sustained both micro and macro re-entry, with a complex SAN-atrial behaviour due to both the shielding action of the border and the presence of SEP. These indeed allowed the excitations to travel from and to the SAN, but at the same time protecting it from excessive tachycardia coming from the atrium, resulting in a longer period of activation and reduced overdrive suppression [187]. A modulatory effect of SEP on SAN rate was also suggested to be given by both conductivity and SEP width [206]. Specifically, narrow SEP allowed for a wider interval of diffusion coefficients showing a pace-and-drive behaviour and were therefore deemed necessary for the human SAN to overcome the electrotonic influence of the atrium. This seems to find confirmation in a recent study [191] which underscores how insufficient widths ($<$0.45 mm vs. experimental 1.75$-$2.2 mm [61] and lengths ($<$2 mm, compared to experimental measures of 2$-$3 mm [61]) of the SEP prevent pacing in a 3D human SAN-SEP-atrial model. In these conditions indeed the SEP did not have a sufficient volume or a sufficiently smooth transition in electrical properties, respectively, to overcome the hyperpolarizing effect of the crista terminalis. The same held for widths $>$0.75 mm, given the larger contact surface between SEP and atrium, whereas increased lengths ($>$2 mm) were shown to decrease the *CL* only slightly [191]. This would suggest the existence of an optimal geometrical setup for the SEP to robustly pace the atrium.

Similar to unphysiological SEP width or length, Li et al. [200] showed that a combination of I_{Na} removal and hyperpolarization reduces the SF for conduction along the SEP, leading to SAN exit blocks in both basal and especially heart failure models of human SAN-SEP-atrium. In this condition, the SF was also shown to be direction-dependent and, being higher for entrance conduction, allowed for the stabilization of re-entry in the SAN.

In these studies, the number of SEP was set to $3-5$, based on histological reconstructions and optical mapping studies [61], [205]. Even if more work is needed to elucidate the role and structure of exit pathways, these investigations highlight their deep influence on pacemaking and their protective role over the atrial load.

1.4.5 SAN within multiscale cardiac models

1D, 2D and anatomically detailed 3D models of the right atrium including sinoatrial and atrioventricular node provided hints on times and patterns of activation in physiological [183], [207] and in pathological conditions such as atrioventricular nodal tachycardia [208] or AF [182], [187], [209]. At baseline, the stimulus was shown to originate in the centre of the SAN, travel through the periphery and reach the crista terminalis from which it spreads radially in the whole right atrium (Figure 1.6). At the same time, excitation propagates around the block zone to reach the interatrial septum and the atrioventricular node, which is also reached by the stimulus travelling from the crista terminalis (right panel of Figure 1.6, [209]).

The main drawback of whole-atrium or even whole-heart models is the approximations they must introduce either in the electrophysiological description or in the anatomical detail. Hopefully, recent advances in computational power and techniques (especially through parallelization) will allow the combination of discrete models (which have the advantage of providing punctual, single-cell, information) with accurate geometries.

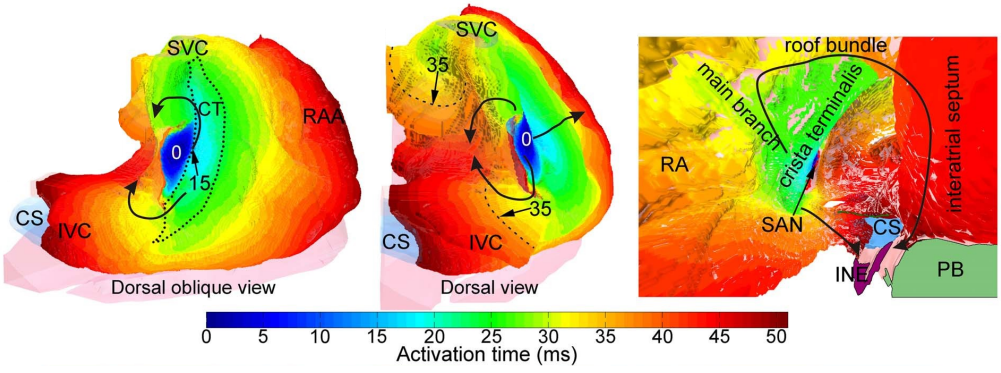

Figure 1.6: ***Impulse conduction from the SAN to the atria****. Different views (left: dorsal oblique; centre: dorsal; right: internal) of simulated 3D propagation from the SAN (extracted from Li et al. [209]). SVC: superior vena cava; IVC: inferior vena cava; CT: crista terminalis; CS: coronary sinus; RA: right atrium; RAA: right atrial appendage; INE: inferior nodal extension; PB: penetrating bundle.*

Notably, 3D reconstructions of the SAN alone or with the surrounding atrium can be found in [210] for the rabbit and in [60], [61], [211], [212] for the human one (Figure 1.1).

1.5 Pathogenesis in the sinoatrial node

Sinoatrial node disfunction (SND) is a collection of SAN disorders manifesting as arrhythmias comprising bradycardia, pauses, or even arrest [40], [213]. In general, it refers to a condition in which the SAN does not manage to supply a *HR* that meets systemic needs. There can be several causes for this condition – Figure 1.7 reports the ones that have been investigated with mathematical models – but all eventually lead to abnormal impulse formation and conduction. SND can be congenital or acquired: mutations constitute the first category, whereas the second one is due to aging or other associated pathologies such as heart failure and AF.

1.5.1 Mutations

Even if familial forms (*i.e.*, caused by mutations) of SND are rare, several computational works have elucidated the mechanisms underlying them. Investigation over the consequences of mutations in the *SCN5A* gene – encoding for cardiac I_{Na} – were discussed in section 1.4.3. There, the importance of this current for SAN function was highlighted by the correlation between its impairment and SND. However, mutations affecting other genes reveal the significance of the corresponding currents. For instance, Verkerk and Wilders [123] built an atlas of the HCN4 mutations associated with SND, providing current reconstructions under AP clamp for each of them. While these are most commonly loss-of-function mutations leading to bradycardia, gain-of-function mutations have been discovered and studied as well. Concerning HCN4 channels, the *R524Q* mutation first reported by Baruscotti and coauthors in 2015 [232], was shown to cause tachycardia in patients carrying the mutation due to the increased sensitivity of I_f to cAMP found in patch clamp experiments [232]. Analysis of this effect in the single cell rabbit model by Yaniv et al. [93] proposed that this higher sensitivity determines a larger I_f which, by decreasing the *CL*, raises the SR calcium content and the phosphorylation levels of the AC-cAMP-PKA system, increasing I_f and I_{CaL} in feedback [134] and resulting in a higher beating rate [134]. Opposite to this, gain of function mutations in the *KCNQ1* gene cause an increased and persistently active I_{Ks}, leading to reduced *APD* and slower *HR* [215]–[217]. These effects determine an increased probability of ectopic beats and of re-entry stabilization, whose combination forms the substrate for AF [215]. To avoid this, in silico pop-

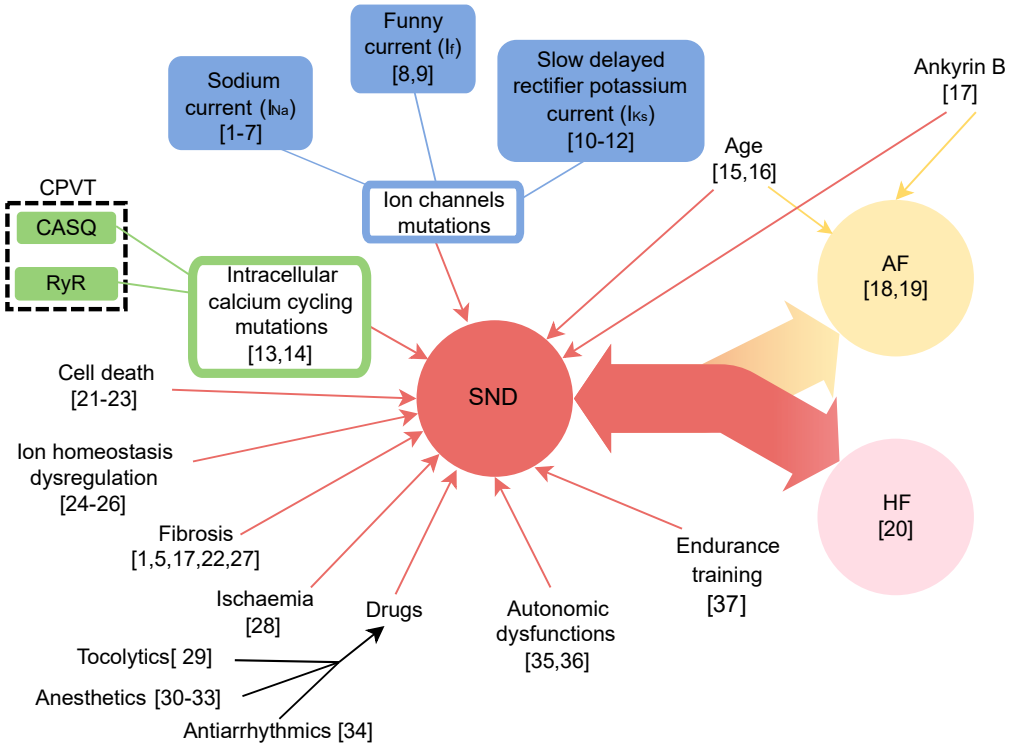

Figure 1.7: ***Sinus node dysfunction causes and related pathologies investigated in computational studies****. Mutations affecting the intracellular calcium handling and membrane ion proteins are depicted in green and blue, respectively. Catecholaminergic polymorphic ventricular tachycardia (CPVT, black dashed line) is given by mutations in both calsequestrin (CASQ) and RyR. Diseases are represented in circles: sinus node dysfunction (SND, red); atrial fibrillation (AF, yellow); heart failure (HF, pink). Numbers in square brackets indicate bibliographic references: [1] [196], [2] [197], [3] [198], [4] [199], [5] [200], [6] [202], [7] [214], [8] [123], [9] [134], [10] [215], [11] [216], [12] [217], [13] [87], [14] [218], [15] [95], [16] [97], [17] [219], [18] [182], [19] [220], [20] [200], [21] [221], [22] [222], [23] [193], [24] [96], [25] [100], [26] [223], [27] [187], [28] [224], [29] [225], [30] [226], [31] [227], [32] [228], [33] [229], [34] [230], [35] [218], [36] [78], [37] [231].*

ulations of models [217] and multiscale modelling [216] suggest that an increase in I_{CaL} and quinidine (an anti-arrhythmic drug), are beneficial in increasing SAN robustness and in reducing the risk of AF, respectively.

1.5.2 Relationship between sinus node dysfunction and other pathologies

Preventing the onset of atrial fibrillation is of utter importance, in order to preserve SAN function. Nevertheless, while AF is known to be strictly related to SND, the cause-effect relationship between the two diseases is still not clear [41], [54], [233]. Hints come from simulations showing that an imbalanced autonomic modulation (large ACh concentration) can force the SAN to promote AF due to hyperpolarization and heterogeneous response to ACh [182]. These two conditions can in fact both originate and sustain the arrhythmia. Preliminary work suggests that inclusion in the FWS model of remodelling due to AF (reduction in I_f, I_{CaL}, I_{CaT}, I_{Ks} and in the release and uptake fluxes of the SR) leads to a *BR* reduction [220]. To make things even more complex, SND and AF can have a common origin. Ankyrin-B dysfunction determines a loss of I_{CaL} (Ankyrin-B is responsible for its membrane localization), I_{NaCa} and I_{NaK} that lead to a reduced *BR* as well as an increased *BR* variability in the single cell Kharche model [219]. At the tissue level, shifts in the leading pacemaker location, exit blocks and SAN failure were found to be consequences of the single cell effects and of fibrosis as well [219]. Similar results were obtained for ischemia [224]: inclusion of electrophysiological remodelling due to this disease (I_{CaL}, I_f, $[K^+]_o$, $[Na^+]_i$ increase, I_{CaT}, I_{Kr}, I_{Ks}, I_{NaCa}, I_{Na} reduction) in the Zhang central and peripheral cell models resulted in longer *CL*s (more pronounced in the central cell model compared to the peripheral one). In 2D, this led to a lower tissue *HR* and *CV*. Administration of ACh amplified ischemia effects causing exit blocks and complete SAN arrest [224].

Incorporating the experimentally measured *M*- and Ca^{2+}-clock remodelling due to heart failure with preserved ejection fraction in the FWS model, Mesquita et al. [234] reproduced the chronotropic incompetence associated with this disease. Simulations of single SAN cells showed an impaired response to $\beta - AR$ stimulation (lower maximal *BR* and slower dynamics), which could be brought back to normal by restoring control values of the *M*- but not of the Ca^{2+}-clock.

Another disease in strict relationship with SND is Catecholaminergic Polymorphic Ventricular Tachycardia (CPVT). This pathological phenotype is characterized by ventricular tachycardia under stress conditions but also by bradycardia at rest, mainly caused by RyR and calsequestrin (a sarcoplasmic buffer) mutations that determine a leaky reticulum. These mutations deplete the SR with consequent reduced *BR*, a condition exacerbated by $\beta - AR$ stimulation (e.g., under stress [87]). Interestingly, simulations revealed that while RyR and calsequestrin mutations result in the same phenotype (SAN pauses), they do so through different mechanisms in response to $\beta - AR$ stimulation: either through the involvement of I_{NaCa} or not, respectively [218]. In addition, a simulated increase in cAMP/PKA

activity is sufficient to amend the effects of the mutations and restore a physiologic *BR* [218]. Besides CPVT, increased sensitivity to $\beta - AR$ stimulation was also related to hypertension [78], as described in more detail in section 1.7.1.

Cell death is another major contributor to SND, since it imbalances the source-sink relationship between SAN and atrium. Simulation of a 2D anatomically detailed SAN model showed that 25% cell loss determine a prolongation of the diastolic phase with a consequent drop in the heart rate and exit blocks [221]. Slightly lower amounts of apoptosis (19%) still lead to reduced *HR*s but additionally determine shifts in the leading pacemaker site towards the periphery [222]. Similarly, the threshold for complete SAN arrest was found to be 15%, while sinoatrial conduction time was unaltered up to 10% apoptosis in another study [193]. The effect was however worsened by a concomitant loss of I_{Na} and by an increase in the contact surface between SAN and atrium [193].

1.5.3 Drugs

In the context of secondary SND (*i.e.*, associated with other systemic diseases) drugs can be beneficial – as discussed above for quinidine – but also detrimental. Amiodarone, which is used as an anti-arrhythmic treatment for AF, was indeed found to further depress SAN function in simulations with the FWS model when the reduction in SAN ionic currents caused by amiodarone was considered on *TOP* of the ionic remodelling due to SND [230]. The authors of this study consequently suggest using dysopiramide, another anti-arrhythmic drug, to avoid exacerbation of SND, since simulations showed its ability to raise the *HR*. Anaesthetic drugs were also shown to induce acute bradycardia, posing a risk of arrhythmia during surgical interventions [226], [227], [229] ([229] for review). Tocolytics (*i.e.*, labor-suppressing drugs) were reported to have negative cardiac effects. Many of these drugs block L-type Ca^{2+} current in order to avoid contraction in the uterus, affecting SAN activity as a side effect. Simulations with uterine, SAN and ventricular computational models showed that combinations of L- and T-type calcium currents blocks prevented a uterine AP while leaving the SAN and ventricular ones unaffected [225].

To conclude, clinical studies and case reports [235], [236] suggested that ivabradine is a safe and effective therapy for inappropriate sinus tachycardia (a disease associated with SND) thanks to its *HR*-lowering effect. Being this drug a specific blocker of the funny current, these results stress the importance of I_f in regulating the *HR* also in humans and validate model predictions of a *BR* reduction after I_f block [23]–[25].

1.5.4 Aging

While the effect of drugs is often temporary and reversible, other processes like aging and endurance training can irreversibly favour the onset of SND. This was reproduced in a model of the aged mouse SAN, obtained by reducing the activity of calcium cycling proteins – as well as reducing the conductances of the main sarcolemmal channels – according to experimental data [95]. Simulations showed that age remodelling leads to lowered intrinsic beating rates (associated with increased HRV) and reduced sensitivity to autonomic stimulation. However, simulated pharmacological increase of AC activity or phosphodiesterase (PDE) inhibition was shown to restore physiological SAN function by preserving cAMP/PKA activity [95] as in the case of CPVT discussed above. Again, similarly to CPVT, different types of remodelling (coming from different experimental datasets) were found to determine similar SND phenotypes [97]. This agrees with the idiopathic nature of this disease and represents the main challenge in its diagnosis and treatment. Despite this, I_{CaL} (typically down-regulated but also up-regulated with aging) was identified as the main cause of bradycardia in the Tao model, with little I_f or RyR involvement [97].

The role of reduced HCN4 expression is in turn believed to be central in training-induced bradycardia. Simulations by Bidaud and colleagues show that I_f downregulation in mice accounts for 15% of training-induced HR reduction, I_{CaT} for 13% and I_{CaL} for less than 1% (given the balance between prolonged DD and shortened APD), with an overall 38% BR drop [231]. However, consensus is still to be achieved on this topic [237], [238]. In fact, the idea of a predominant involvement of ionic remodelling in determining training-induced bradycardia (first suggested in mice [239]) contrasts with the traditional belief of an increased parasympathetic activity in mediating the observed HR reduction in athletes. Also, experiments on dogs suggested an ANS-mediated mechanism as the cause of HR reduction after training programmes [240].

1.5.5 Ion homeostasis

One final mechanism of SND onset is ion homeostasis dysregulation. The recent modification of the Kharche model by Morotti and colleagues showed that, while mild reductions of I_{NaCa} and I_{NaK} both slightly increase SAN cell BR, strong blocks ($> 70/80\%$) led to bursting activity and absence of APs [96]. Despite the opposite actions of these two currents (mainly inward and depolarizing I_{NaCa}, outward and repolarizing I_{NaK}), the effect of block of these currents is the same due to the feedbacks between Ca^{2+} and M-clocks mediated by Na^{+} and Ca^{2+} ionic concentrations. Computational studies also suggested that changes in extracellular ionic concentration underlie bradycardia and sudden cardiac death in

patients suffering from ischemia [224], diabetes [241] or renal diseases requiring hemodialysis [100], [241]. Simulations with the updated FWS model by Loewe et al. [100] predicted negligible ($0.15\,\mathrm{bpm\,mM^{-1}}$) or mild ($8\,\mathrm{bpm\,mM^{-1}}$) effects for $[Na^+]_o$ and $[K^+]_o$ reductions, respectively, but loss of extracellular calcium alone caused severe bradycardia ($-46\,\mathrm{bpm\,mM^{-1}}$). Specifically, the diminished driving force for I_{CaL} explained 83% of the resulting bradycardia by determining a chain of effects that depressed the HR: reduced I_{CaL}, reduced $[Ca^{2+}]_i$, reduced I_{NaCa} amplitude, reduced $[Na^+]_i$. However, simulations testing the combined action of hypoglicaemia and hypokalemia show a reduction in $\beta - AR$ response and an increased sensitivity to ChR stimulation in the FWS model [241]. The consequent higher influence of parasympathetic tone leads to CL prolongation up to loss of pacemaking, a mechanism which could provide a possible explanation to bradycardia and sudden cardiac death in diabetic patients [241]. In these conditions, being the CL increases mainly due to a prolongation of the late DD phase, such mechanisms seem specific to human SAN cells, considering that smaller mammals lack this phase [223].

Finally, ischemia contributes to a reduction in HR by modulating ionic channel conductances, activating the ATP-sensitive K^+ channel and elevating intracellular Na^+ and extracellular K^+ concentrations. Of note, reversing the last effect (simulating control values of $[Na^+]_i$ and $[K^+]_o$) helped to obtain an attenuated bradycardic effect in the rabbit Zhang central and peripheral models [224].

Ion regulation has been often overlooked in modelling works (many models consider fixed ionic concentrations) because little attention has been given to non-electrogenic ion flows. These are not directly involved in the generation of the AP, but contribute to ionic balance which, as reported above, is determinant to sinoatrial function. Hence, there is a need for biophysically detailed models to accurately reproduce these mechanisms.

1.6 Problem or advantage? Contribution of fibrosis to cardiac pacemaking

When dealing with the SAN, fibrosis deserves a section on its own. The presence of connective tissue in or around the SAN is in fact traditionally thought to underlie or at least contribute to the occurrence of arrhythmia [187], [196], [200], [219], [222]. However, the role of fibrosis has perhaps to be richer than that of a mere non-conductive, arrhythmogenic, barrier. As depicted in Figure 1.8A, experimental data shows how the rabbit and mouse SAN has larger fibrotic content than atria or ventricles [242], [243], up to 50% of the total volume in healthy human subjects [244]. Plus, fibroblasts express ionic channels and are able to establish electrical

connections with myocytes through gap junctions [245] (see [246], [247] for reviews of computational studies investigating the role of fibroblast in the heart and in arrhythmogenesis). This evidence suggests the involvement of such cells in the electrical activity of the SAN not only in pathogenesis, but also under physiologic conditions. Panel B and C of Figure 1.8 show two different ways of considering fibrosis in computational models [247], [248]: as resistive barriers, or as "active" models (featuring voltage-dependent ionic currents even if they do not fire APs) connecting to SAN cells. A third possibility is treating them as a passive load (resistive-capacitive element). Finally, "activated" fibroblasts, i.e. *myofibroblasts* express ionic channels and are able to fire APs when stimulated [249]

Fibroblasts were found to modulate the *DD* phase and the *CV* in a 2D SAN-atrium model depending on their density, distribution, and coupling strength [184]. In the case fibroblasts were modelled as conduction barriers, they determined a hyperpolarization of the SAN (less SAN cells, thus weaker source), whereas treating them as passive loads further increased the electrical load seen by SAN myocytes. In both conditions, the result was a slowing of the *BR* and a reduction of the *CV*. In addition, simulations revealed that fibroblast could differently modulate central and peripheral rabbit SAN cells models: the firsts are deeply influenced by fibroblasts, showing substantial *CL* shortening (-30.7%) and *APA* reduction (-27 mV) when only one fibroblast is connected to one central cell model [190]. Two fibroblasts are enough to prevent any spontaneous electrical activity, differently from the peripheral phenotype model that is almost unaffected even with four fibroblasts attached ($+2.7\%$ in the *CL*). In a 2D mixed gradient-mosaic model, these phenotype-specific effects allow for a physiological earliest activation in central SAN [190]. The slight increase in peripheral *CL* was indeed suggested to be enough to shift the LPM location from the periphery to the centre, with only minor effect on the *HR*. A biphasic relationship between *CL* and number of active fibroblasts (MacCannel ventricular fibroblast model [250]) was instead obtained in preliminary work by Greisas and Zlochiver [251], with the *CL* first decreasing and then increasing depending on the number of fibroblasts connected to a single SDiF SAN cell model. Fibroblast also monotonically reduced the *APA*, depolarized the *MDP* and exponentially increased the *BR* variability since they would act as amplifiers of stochastic current fluctuations. However, the gap junctional conductance employed in this study ($0-5\,\mu$S) might appear to be too high compared to both experimental values ($\sim$1 nS [252], which were nevertheless obtained from pairs of cultured neonatal rat cells following dissociation) as well as to the above [184], [190] and previous computational works [253], which used intercellular gap junctional conductivities of few nS. Finally, recent preliminary computational work from our lab [254] highlighted the dual influence of active fibroblasts (Morgan atrial fibroblast model [255]) on SAN activity: acceleration of the *DD* but also slowing of the upstroke phase because of their depolarized resting

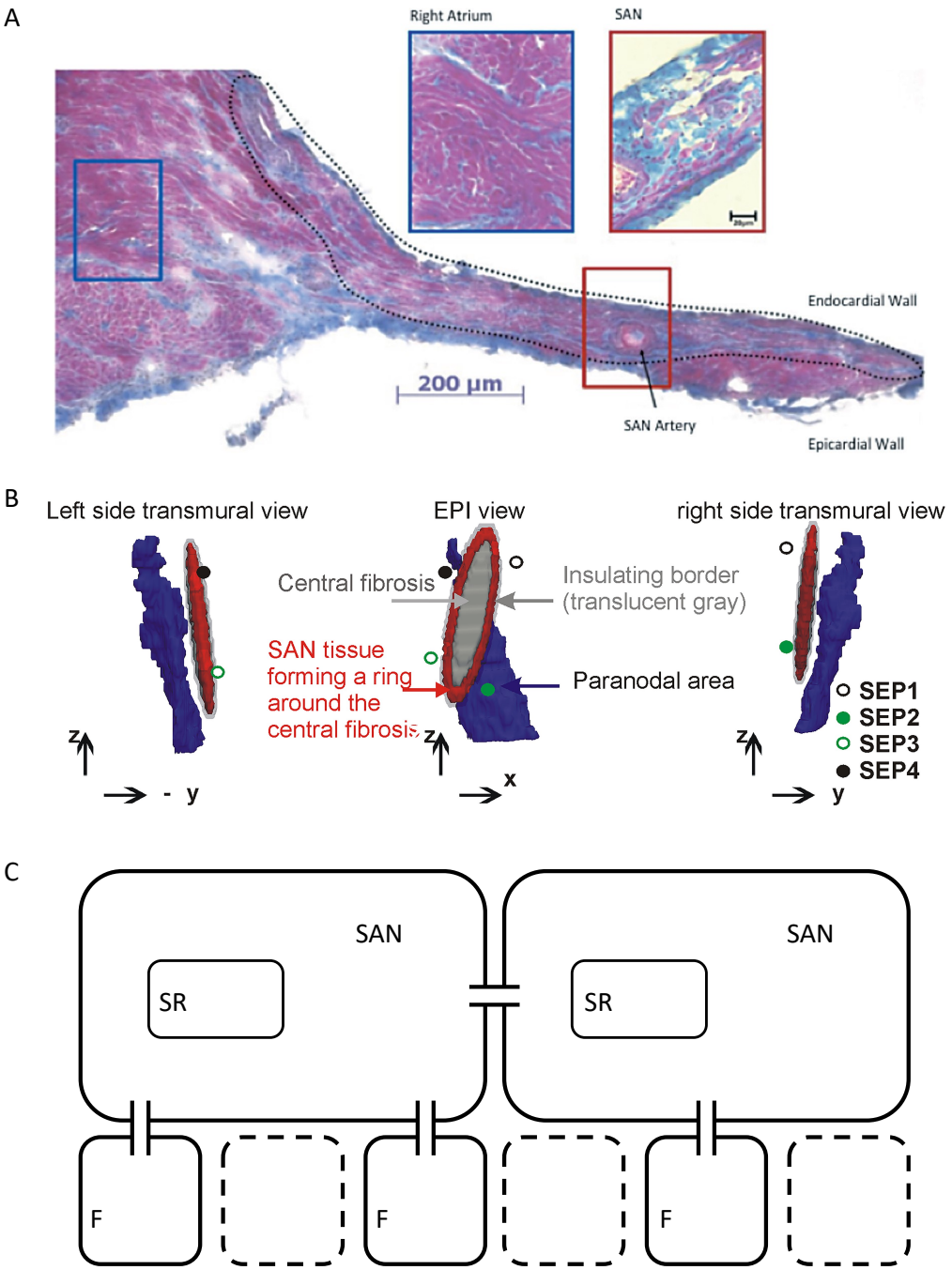

Figure 1.8: (Caption in next page).

Figure 1.8: ▲ ***SAN fibrosis and its modelling****. A) Histological section of rat SAN (encircled by black dotted line) and surrounding atrium (adapted from Doris et al. [243]). Of note, the two magnified boxes show a lower presence and organization of myocytes (in purple) in the SAN (red box) than in the atrium (blue box). B) Anatomically detailed 3D reconstruction of a human SAN (adapted from Kharche et al. [187]). Fibrosis is simulated as inactive cells in the central part of the mesh. C) SAN cell model schematization of the spatial organization used by Karpaev et al. [190]: fibrosis is simulated as 1 to 3 active fibroblasts (small rectangles, bottom) connected to each SAN cell (TOP) through gap junctions.*

potential (around -40 mV). A similar result was previously shown in fibroblast-SAN rat cell pairs during simulated atrial stretch [253], thanks to the ability of fibroblasts to act as current sources.

Overall, these studies demonstrate that, in the SAN, fibrosis does not simply mean loss of conduction, but likely exerts a profound modulatory role on pacemaking also in physiological conditions. While more data are needed to clarify if this action is beneficial – e.g., protecting the SAN from excessive hyperpolarization – or harmful (or when and where it becomes so), computational studies should not simply model fibrosis as a loss of cells or presence of conduction blocks, but should take into consideration active models able to account for the complex behaviours reported in this section. For this purpose, the development of a SAN-specific active fibroblast model would be highly beneficial.

1.6.1 Mechanical regulation

Another neglected aspect of the SAN is mechanical feedback. Fibroblasts likely play a major role in this since they are believed to protect the SAN from excessive stretch. In addition, they express stretch-activated channels (SACs) that generate currents in response to mechanical stimuli. Coupled fibroblast-SAN cell model simulations suggested that this feature would allow fibroblast to contribute to an acceleration of the *HR* following right atrial stretch [253] thanks to their depolarized resting potential (-20 mV). In a 3D SAN-atrial model featuring Zhang central and peripheral models, inclusion of fibroblasts in both SAN and atrium resulted in a prolonged *CL* [256]. However, when SAN spontaneous activity was impeded by decreasing cell to cell coupling, a 4 µm simulated fibroblast stretch was able to reinitiate spontaneous electrical activity thanks to the depolarizing current flowing through SACs [256]. Again, this action was possible thanks to the reversal potential (16 mV) of such channels.

In addition, SAN cells have a mechanical response on their own. In this context, besides stretch magnitude and reversal potential, another factor possibly in-

fluencing the stretch response of the SAN is the shape of the AP. This last aspect was proposed to explain the species-dependent response to stretch in rabbit vs. mice [257], with the former showing an acceleration and the latter a deceleration of the *HR* following stretch. The simulations show indeed that depending on the AP phase, SACs can have an accelerating (during diastole) or decelerating (during late repolarization) effect. It remains unanswered if this double role of SACs would hold in the case of cyclic diastolic stretch, therefore there could be other factors determining the experimentally observed reduction of *HR* in mice.

Extensive reviews of current understanding of SAN mechanical feedback can be found in [52], [258], [259].

1.7 Autonomic control

We have already partially discussed the role of the autonomic nervous system in modulating the heart rate and in eliciting arrhythmias. In this section, emphasis will be given on the mechanisms of action of sympathetic and parasympathetic tone, as well as on LPM shifts.

1.7.1 Sympathetic and parasympathetic modulation

The response to ACh and NE is often used as a validation benchmark for the developed computational models. In this case, experimental data on the overall effect of the two chemicals – such as channel conductance reduction/increase and positive/negative shifts in the steady-state voltage dependence – are included into the models. This allows to reproduce the single cell *BR* changes obtained with cholinergic and adrenergic stimulation in patch-clamp. Nevertheless, being this a phenomenological approach, it neglects the concentration-dependent effects and the specific mechanisms of the second messenger cascades. Starting from early investigations in the late 90s to describe the mechanisms of vagal and sympathetic stimulation [260], [261], later extended to account for regional differences [262], researchers have tried to fill this gap by including equations describing the changes in ionic currents depending on intracellular signalling (Figure 1.9). Himeno et al. [36] added this dependence for the main ionic currents of their guinea pig SAN cell model for both sympathetic and parasympathetic responses. Hence, I_{CaL} and I_{Ks} fully-activated currents and voltage dependences vary with active [PKA], whereas I_f voltage dependence is directly modulated by [cAMP]. The results showed a sigmoidal dependence of *BR* increase with respect to ISO concentration, with saturation at high levels (1 µM) due to I_{NaK} increase upon $[Na]_i$ accumulation. Similar curves were obtained by Zhang et al. [133] which found a primary role for I_{Kr} in $\beta - AR$ stimulation in evolutions of Zhang SAN models of

central and peripheral SAN by Boyett et al. and Kurata et al. [76], [173]. The dependence of I_{Kr} deactivation time constant (τ_{Kr}) on ISO concentration determined a faster inactivating potassium current that allowed for a faster diastolic phase. If τ_{Kr} did not show this dependence, the ISO-determined fully-activated I_{Kr} increase actually reduced the *BR*.

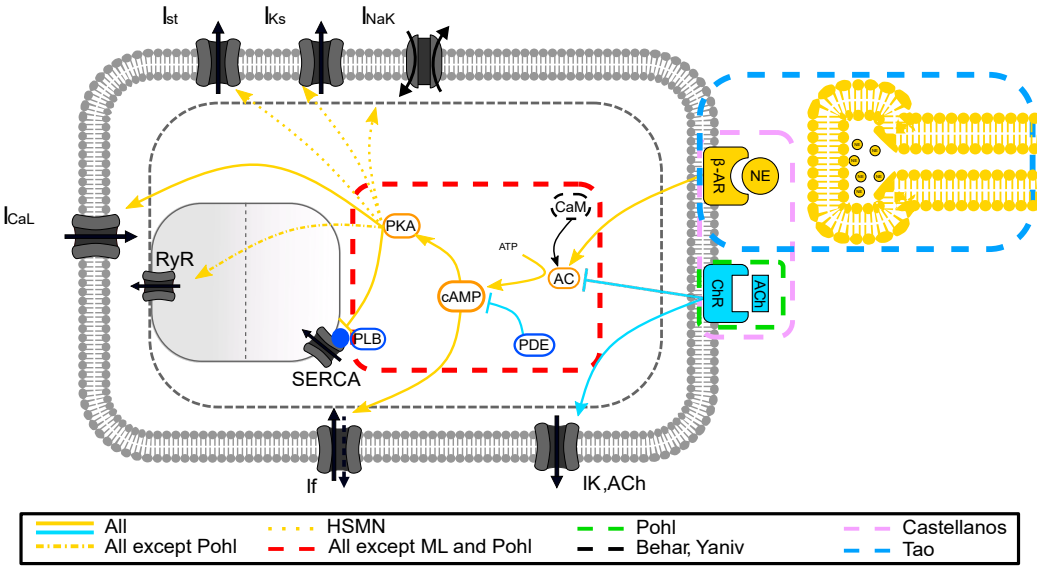

Figure 1.9: ***Autonomic signalling cascades****. Schematization of stimulating neuron (yellow), SAN cell (grey), intracellular signalling cascade and main affected ionic currents. NE: norepinephrine; CaM: calmodulin; ATP: adenosine triphosphate; refer to Table 1 for other abbreviations. HMSN: Himeno et al. [36]; Pohl: Pohl et al. [84]; Castellanos: Castellanos et al. [263]; ML: Maltsev & Lakatta [89]; Behar: Behar et al. [94]; Yaniv: Yaniv et al. [93]; Tao: Tao et al. [78].*

Regarding parasympathetic stimulation mechanisms, Maltsev and Lakatta [89] considered the dependence of the single cell *BR* on [ACh]. Targets of the stimulation, in this model, are: I) $I_{K,ACh}$ (which becomes increasingly activated), II) I_f (negative shift in the voltage-dependent activation curve), III) I_{CaL} (partial block), IV) SERCA pump. Regarding the latter, ACh determines dephosphorylation of PLB that in turn decreases the uptake rate by SERCA pump as much as it decreases I_{CaL}. Considering this dependence, the simulations show that at high (100 nM) ACh concentrations, $I_{K,ACh}$ is the main effector of *BR* slowing, accounting for almost half of the reduction. This was found to be the case also at lower concentrations (30 nM) by running simulations of a markovian model of $I_{K,ACh}$ featuring the voltage dependence of the muscarinic receptor [264]. Indeed, hyperpolarization promotes the ACh affinity to the receptor, thus incrementing the available K^+ current in early diastole with a consequent *BR* slowing in the FWS

model [264].

Building on the work by Maltsev and Lakatta [89], Yaniv et al. [93] modelled the AC-cAMP-PKA signalling network in rabbit SAN cells for the $\beta - AR$ response and, in a later work, extended the description to the ChR response [94]. In these models, a set of differential equations describes the changes in AC-cAMP-PKA concentrations, similarly to what was done by Himeno and coauthors [36]. In the model, the activation of AC is given by the sum of $\beta - AR$ and ChR stimulation (whose effect is actually not additive because of the non-linear dependence of the *BR* on cAMP [94]) and by calmodulin. AC transforms ATP into cAMP, which is further converted into PKA or degraded by PDE. cAMP and PKA phosphorylate I_f and I_{CaL}, PLB (hence SERCA), and RyR respectively. NE acts on increasing AC activity and therefore influences active cAMP and PKA concentrations, whereas ACh reduces it, besides activating $I_{K,ACh}$. Simulations run with such models suggest that PLB phosphorylation is the main mechanism of *BR* increase at either high or very low cAMP levels, whereas I_f and I_{CaL} contribute at intermediate levels [93]. Without PLB phosphorylation the models do not show $\beta - AR$ response and the ChR one leads to higher *BR*s (instead of lower ones) and instability [94]. I_{CaL} phosphorylation was instead suggested to contribute to both a deceleration (through calcium-dependent inactivation [94]) and an acceleration [24] of the *BR* in simulations of ISO administration. Pharmacological I_{CaL} enhancement supports the second mechanism [265]. As already discussed in section 1.5.4, aging reduces the sensitivity of SAN cells to ANS stimulation, leading to a disruption of these processes. Simulations on a aged mouse SAN cell model predicted that this deleterious effect involves a reduced sensitivity of I_f to cAMP and of PLB to PKA [95]. Therefore, both these changes have to be reversed (through either maximal concentration of ISO or cAMP or PDE inhibitors) to obtain the same response to $\beta - AR$ and ChR stimulation as in non-aged cell models [95].

While the AC-cAMP-PKA signalling can explain the link between autonomic modulation and beating rate change at the single cell level [93], the models by Tao et al. [78], Pohl et al. [84] and Castellanos and Godinez [263] describe the mechanisms of autonomic modulation from the neurotransmitter release to the resulting frequency variation. The complete messenger cascade sequentially includes: I) neurotransmitter release; II) receptor binding; III) G-protein activation; IV) AC activation; V) PDE cAMP hydrolysis; VI) PKA activation; VII) Ionic current changes (see Figure 1.9 for schematization and comparison on how these mechanisms have been modelled). The simulations involving neuronal stimulation showed *BR* variations in agreement with experimental data in response to adrenergic modulation in rats [78], and cholinergic modulation in humans [84] and in rabbits [263]. For example, high frequency parasympathetic stimulation (50 ms bursts at 200 Hz applied after every AP) determined a progressive *CL* prolongation in the human SAN cell model by Pohl and coauthors [84], whereas com-

bined adrenergic and cholinergic neurotransmitter release reproduced the HRV at different stimulation frequencies ($0-10$ Hz) in the SDiF rabbit model combined with a second messenger cascade model [266], in accordance with experimental data [263]. The study by Tao et al. [78] considered – even if only for $\beta - AR$ stimulation – the additional step of neural excitation (AP) determining the Ca^{2+} influx and the consequent neurotransmitter (NE) release. According to their own experimental data, a 40% increase in calcium current maximal conductance and a 26% decrease in PDE activity were included in the neuron and SAN model, respectively. This reflected the effect of reduced cyclic guanosine monophosphate levels as found in hypertensive rats. The results showed an 80% higher NE release with a 12% *BR* increase in basal conditions. Moreover, under adrenergic stimulation the *BR* in the hypertensive model was more sensitive to stimuli of increasing frequency, and the relative contribution of the two parameters changes showed a clear frequency dependence, with the *BR* increase being more sensitive to an upregulation of Ca^{2+} conductance at higher frequencies.

1.7.2 Shifts of the leading pacemaker location

The effect of a shift in the leading pacemaker site following autonomic modulation (Figure 1.10) was reproduced by mathematical models already long ago. Brief ACh pulses in a portion of cells forming a tissue were shown to be able to reversibly affect the LPM location by perturbing the cells' entrainment process [148]. The LPM site (and/or the number of stable LPMs) also depended on the coupling conductance [148]. Recent computational work [187] has indeed highlighted that changes in SAN intercellular coupling can account for this phenomenon, with the LPM migrating towards the site with lower coupling. Cellular heterogeneity within the SAN is also believed to play a critical role in determining the shift. Gradients in ionic properties and gap junctional coupling (modelling the different properties of central and peripheral SAN, Figure 1.10) could explain the LPM shifts under $\beta - AR$ [186] and ChR [190] stimulation. Under basal conditions, P_{up} was proposed to be the main factor in determining the pacemaker site [140]. Simulations also indicated a dependence of the LPM position on the distribution of g_{CaL}, the maximal conductance of L-type Ca^{2+} current, with the site of earliest activation colocalizing with an increased g_{CaL} [182] or moving away from a region with reduced g_{CaL} [140]. While this theoretically complies with the primary role of I_{CaL} in cardiac pacemaking, it also agrees with the Ankyrin B syndrome model by Wolf et al. [219], which showed an LPM shift towards the periphery after loss of I_{CaL}.

In physiological conditions, ACh could be the main actor of the LPM shift because of 1) the higher sensitivity to ACh ([262], again due to the geometric effect explained in section 1.4.2) and 2) the higher innervation and number of choliner-

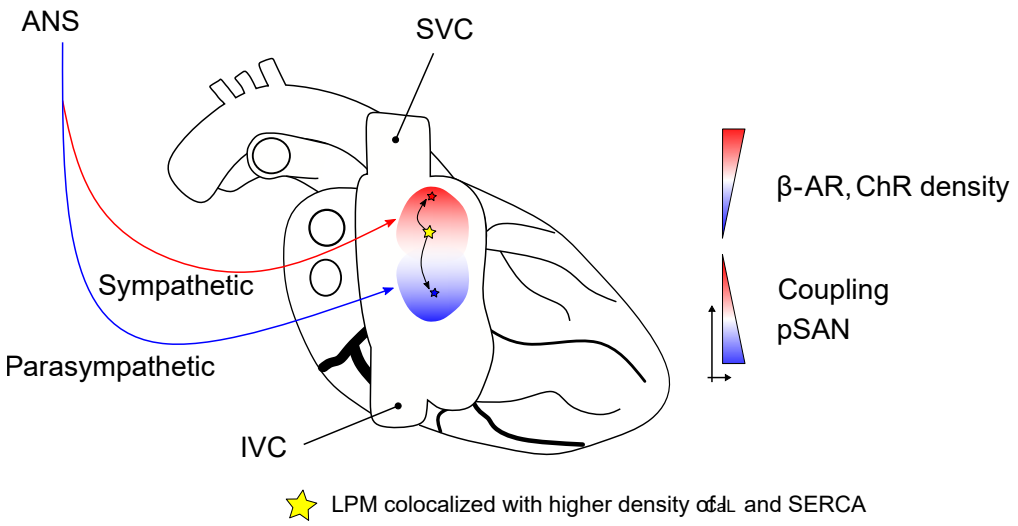

Figure 1.10: ***Leading pacemaker (LPM) site shifts due to autonomic stimulation****. LPM colocalizes with I_{CaL} [140], [182] and SERCA uptake rate [140]. Sympathetic stimulation (red arrow) shifts the LPM superiorly (red star); parasympathetic stimulation (blue arrow) shifts the LPM inferiorly (blue star). Right: summary of possible causes of the shift in the LPM following ANS stimulation: different densities of β-adrenergic and cholinergic receptors [267], coupling [187], [190] and cellular phenotypes [182], [186], [262] between superior and inferior SAN. pSAN: peripheral SAN.*

gic receptors in central SAN cells with respect to peripheral ones [182]. Hence, the *CL*-prolonging effect of ACh is more pronounced in the centre [1], and upon cholinergic stimulation the earliest site of activation shifts towards the periphery. The addition of linear gradients of $\beta - AR$ sensitivity and $g_{K,ACh}$ (maximal conductance of the acetylcholine-activated K^+ current) in a 2D rabbit model, shows indeed superior and inferior shifts of the LPM site during sympathetic and vagal stimulation, respectively, in agreement with optical mapping data [267]. Plus, in the model larger gradients lead to larger shifts and faster dynamics, with an earlier stabilization of the new LPM location in case of ACh compared to ISO response [267].

Recent experimental data on humans show that different portions of the SAN could be linked to different *HR*s, with the superior SAN preferentially showing high rates and the inferior portion correlating with lower rates [268]. This behaviour – conserved across species – is determined by the hierarchical organization of the SAN ([49] for review). In other words, it could be due to an intrinsic dominance of either the *M*- or the Ca^{2+}-clock in different SAN regions [39], together with the deep control exerted by the nervous system [269]. More studies – both experimental and computational – are needed to elucidate these tissue levels

mechanisms of neural modulation of the *HR*, especially in humans.

1.8 Open issues

Evolution has shaped the SAN to guarantee the onset of the heartbeat for billions of times during a human being's life, despite ever-changing conditions (physical activity, sleep, arising of diseases). Considering that this is achieved through different mechanisms that cooperate to deliver the heartbeat and to serve as back-up for one another, a conclusion can be that every aspect of the SAN matters for its functioning, from intracellular mechanisms to fibrosis, from tissue-level structure to innervation. Sub-cellular organization is also believed to play a determinant role [270].

Computational models have helped to unravel many of the processes underlying SAN activity. The previous sections showed that several simulations were run to elucidate, for example, how SAN cells synchronize or how their behaviour is affected by diseases. Despite these precious contributions, however, certain aspects remain not fully explained, among which the origin of pacemaking stands out. As discussed in section 1.3.3, nowadays consensus takes the coupled-clock theory as the best compromise between spontaneous Ca^{2+} releases and funny current activity, with the underlying idea that these mechanisms ("clocks") are interacting ("coupled") but remain anyway distinct. This conception represents a simplification of the actual complexity of pacemaking mechanisms, and it is the consequence of two different but related aspects. On one hand, there is a time gap between experimental results and modelling works. As a relevant example, reported in section 1.3.4, in recent years there has been an accumulation of evidence showing the triggering and modulation of local calcium releases by $Ca_v1.3$ current, yet no computational model has tried to reproduce this phenomenon. On the other hand, experiments are intrinsically limited to hypothesis isolation and testing, and cannot address the nature of the phenomenon as a whole. This is particularly limiting while studying cardiac pacemaking, since this could be seen as an example of emergent property, result of the coordination between several interacting processes, more than just the action of single players.

Another controversy is whether gradients in cellular properties and intercellular coupling are the correct description of the SAN heterogeneity or if a mosaic structure is the case. This debate has provided computational evidence supporting both hypotheses, showing their compatibility with pacemaking and atrial driving. Experimental data on connexin and ionic channels expression and on conduction velocities let the gradient hypothesis appear hard to be rejected [4], but at the same time, it is not excluded that atrial myocytes locate among SAN myocytes and regulate their function. Once again, the complexity of the SAN makes it difficult

to classify it under rigid categories and therefore it appears more constructive to consider these theories as complementary rather than opposite [190], [191]. Else, species differences may explain different SAN organization [6].

A specific limitation of contemporary SAN models is represented by the accurate description of Na^+ homeostasis: few models consider Na^+ concentration as a state variable despite its influence on the sodium-potassium pump and therefore its role on the current balance in diastole. More generally, ionic balances should be taken into account given their importance for the correct functioning of pacemaking.

The astonishing complexity of the sinoatrial node from a structural, cellular, and molecular point of view, all of them strictly related to heterogeneity, stands out as a peculiar aspect that needs to be considered to gain a complete understanding of SAN function. Indeed, the broad range of cellular phenotypes, spatial organizations, and intracellular mechanisms making up the SAN are not matched by any working cardiac tissue. Recently, two experimental works have highlighted how the SAN shares functional and transcriptional features of neurons [271]–[273]. A previous computational study showed that SAN and pyramidal cells produce similar responses following mutations in Na^+ and hyperpolarization-activated channels (even though Ca^{2+} channel mutations had opposite effects [274]). It is well known that the autonomic nervous system innervates and controls the SAN [275], as also discussed in this review. Nevertheless, the fact that the SAN itself shares properties with neural structures is a new discovery that opens new scenarios in our understanding, especially on heart rate regulation.

As discussed in section 1.6, the role of fibrosis needs further study: despite its large presence inside the SAN, it has not received proportional attention yet. Fibroblasts participate in SAN activity and can modulate it, but further work is necessary to elucidate the mechanism and thus the purpose of fibrosis in basal conditions. Similarly, SAN mechanics is a generally neglected aspect, consequently if and how SAN automaticity is regulated by a "mechanics-clock" [50], [258] is still an open question. What is instead emerging as a reality is the presence of conduction pathways connecting the otherwise insulated SAN to the atrium. The resolution of contemporary experimental techniques has allowed to obtain robust evidence for sinoatrial exit pathways [61], [200], [212] while, as discussed, their mechanistic behaviour is starting to be assessed thanks to models.

Other aspects that need clarification are the relative contributions of intrinsic variability and of autonomic control on heart rate variability, the relationship between sinus node dysfunction and atrial fibrillation [41], [54], [233] as well as the cause of the leading pacemaker shift. All these topics require further investigation in order to achieve a better understanding of SAN functioning and consequent broader possibilities of preventing and treating disorders. This can be best achieved thanks to the cooperation between experimental and computational

works, where simulations would take experimental data as input, to give in output model predictions that can be verified by additional experiments. In this setting, all the standardization efforts and open-source initiatives are warmly welcomed since they allow researchers to focus on experiments and simulations and encourage the comparison between results. Many of these have already become virtuous realities: CellML [276], OpenCARP [277], Myokit [278] and ParamAP [279], to name a few.

To conclude, despite all the data in silico models provided us with, sinus node dysfunction still lacks a satisfying treatment, primarily because of a limited comprehension of SAN functioning. The increasing computational power and growing body of evidence now available suggest that computational models will have a lot to tell about the origin of the heartbeat: the history of cardiac pacemaking is far from being over.

Chapter 2

Local Calcium Releases Contribution to Diastole and Cell Synchronization

Part of the content of this chapter is published in:

"Quantification of Local Calcium Releases Contribution to Diastolic Depolarization in a 3D Model of Single Rabbit Sinoatrial Node Cell"
Eugenio Ricci[1], Chiara Bartolucci[1], Stefano Severi[1]

[1] Department of Electrical, Electronic and Information Engineering "Guglielmo Marconi", University of Bologna, Cesena, Italy

Computing in Cardiology 2023, Atlanta (GA), USA

Abstract

This Chapter aims at investigating the role of local calcium releases (LCRs) in cardiac pacemaking. This is achieved by developing a 3D model of a single rabbit sinoatrial node cell featuring detailed membrane and calcium-clock descriptions. Secondly, single cell simulations where LCRs were prevented during the diastolic period are run to assess their effect on the cell's cycle length. Finally, two heterogeneous model cells were coupled together to study the influence of LCRs on the synchronization process.

The simulations show that this model reproduces both experimental and previous models' basal rabbit sinoatrial cell action potential features. Comparing simulations in control conditions with simulations where LCRs are prevented below a membrane voltage of $-30\,\mathrm{mV}$ shows that their effect depends on the parameter randomization of heterogeneous cells. Coupled cells simulations at different gap junctional resistance values show that, below a specific inter-cellular coupling value ($R_{gap} < 10^4\,\mathrm{M\Omega}$), spontaneous cells drive dormant ones regardless of the presence of LCRs. The latters hamper the driving process at lower coupling strengths ($R_{gap} = 10^4\,\mathrm{M\Omega}$), but provide larger heart rate dynamics.

Overall, this work provides a useful tool to study pacemaking and gives quantitative hints on its mechanisms.

2.1 Introduction

Sinoatrial node physiology has been extensively investigated since the discovery of this fundamental cardiac tissue. Especially for small mammals (e.g., mice, rabbits, guinea pigs), lots of data have been accumulated and allowed the understanding of the role and functioning of the SAN. Computational models have also greatly contributed in elucidating the mechanisms that determine the heartbeat. However, as underlined in Chapter 1, a comprehensive description of cardiac pacemaking is lacking, and in particular the quantitative role of different actors involved is still not consolidated (Section 1.3), limiting the possibility of acting effectively in case of disease.

In the SAN, intracellular calcium cycling does not have a role in contraction, but participates to homeostasis and electrophysiology through sodium-calcium exchanger activity. In particular, supposedly stochastic openings of ryanodine receptors (RyRs) determine local calcium releases (LCRs) from the sarcoplasmic reticulum (SR). The increased local Ca^{2+} concentration inside the cell activates the exchanger which, extruding 1 Ca^{2+} ion and intruding 3 Na^{+} ions, generates a depolarizing current. While experimental evidence [141] has questioned the spontaneity of RyRs opening (and therefore the presence of an independent "calcium-clock"), this process remains crucial for AP onset [58].

Consequently, in order to provide additional quantitative information about the contribution of LCRs to diastolic depolarization, this work aims at: 1) developing a detailed, 3-dimensional single SAN cell rabbit model combining state-of-the-art membrane and calcium-clock descriptions; 2) comparing AP features of the updated model in control conditions and when LCRs are disabled and 3) investigate the contribution of LCRs to the synchronization process between 2 model cells.

2.2 Methods

Membrane current formulations were taken from the SDiF model [24]. The main model development in this work is represented by the adoption of the 3D detailed intracellular calcium handling description of the recent Maltsev et al. model [35]. In that work, the inside of the cell is divided in voxels of increasing size going from the membrane to the cell core. In the subsarcolemmal space just below the membrane, where the spatial resolution of the model is higher, the change of Ca^{2+} concentration is described according to the following equation:

$$\frac{\partial Ca_{sub}}{\partial t} = D\nabla^2 Ca_{sub} - J_{ring} + J_{CRU} - J_{Ca} - J_{CM}$$

where D is the diffusion coefficient, J_{ring} is the Ca^{2+} flux to the central part

of the cell, J_{CRU} is the Ca^{2+} flux due to release from the CRUs, J_{CM} is the Ca^{2+} flux due to calmodulin binding and J_{Ca} is the Ca^{2+} flux due to membrane Ca^{2+} currents:

$$J_{Ca} = \frac{I_{CaL} + I_{CaT} + I_{bCa} - 2 \cdot I_{NaCa}}{2 \cdot F \cdot v}$$

where in turn F is the Faraday constant and v is the volume of the voxel.

The parameters P_{CaT} (maximum permeability of T-type calcium current) and Km_{fCa} (dissociation constant of Ca^{2+}-dependent I_{CaL} inactivation) were scaled by a factor 0.8 and 6, respectively, compared to the original SDiF model. The latter modification was necessary to account for the greatly increased Ca^{2+} concentration seen by the I_{CaL} Ca^{2+}-dependent gate following the co-localization of $Ca_v1.2$ with RyR and sodium-calcium exchanger channels, compared to the concentration in the subspace of the original lumped-parameters SDiF model. All other cell parameters (dimension, compartmentalization, etc) were the same as in [35].

Table 2.1: ***Comparison between models and experimental AP features****. Cycle Length (CL), Maximum Diastolic Potential (MDP), Action Potential Amplitude (APA), Overshoot (OS), Action Potential Duration at 50% repolarization (APD_{50}), Maximum Upstroke Velocity (dV/dt_{max}). Data is shown as mean ± standard deviation for the present model (values averaged on the last 2 s of 20 s baseline simulation) and as mean ± standard deviation and range [lower bound, upper bound] for experimental values.*

Feature	Present model	SDiF model [24]	Experimental values [24]
CL[**ms**]	379±1	352	325±42 [247, 389]
MDP[**mV**]	-61±0.1	-58	-56±6 [-66, -52]
APA[**mV**]	78.4±0.8	80	87±6 [78, 98]
OS[**mV**]	19±0.7	22	27±5 [20, 32]
APD_{50}[**ms**]	131±0.4	108	93±12 [73, 111]
dV/dt_{max}[**V/s**]	6.4±0.2	7.1	11.3±6.5 [4.8, 27]

Different types of simulations were run with n = 5 heterogeneous cells, obtained by randomization of the maximal conductances, currents and permeabilities (P_{CaL}, P_{CaT}, g_{Kr}, K_{NaCa}, i_{NaKmax}, g_{Na}, g_{Ks}, g_f, g_{to}) of the SDiF model via log-normal distribution ($\sigma = 0.2$) sampling [34]. In addition, P_{up}, the maximal uptake rate of the SERCA pump was also randomized to take into account Ca^{2+}-clock heterogeneity (Table A.1).

In the first set of simulations, control conditions were tested (20 s to reach steady-state) with both the baseline and the 5 models obtained by parameter randomization. Secondly, 1 s simulations where LCRs were disabled or not during

diastole, were performed. When LCRs were disabled, CRUs were allowed to open only when the cell membrane voltage (V_m) reached a threshold of -30 mV (more positive than the take-off potential, $TOP = -34.9$ mV, computed as in [118]). Still, they could release Ca^{2+} when the cell membrane reached this threshold, in order to produce the AP-induced calcium transient. These simulations started from the last *MDP* of the control simulations. Thirdly, 1 s coupled cells simulations with and without LCRs were run. Coupling was obtained by adding the gap junctional current at different R_{gap} values (gap junctional resistance = $10^1, 10^2, 10^3, 10^4, \infty$ MΩ) to the cells' current balance, as previously done [34]:

$$\frac{dV_m}{dt} = \frac{-(I_{ion} + I_{gap})}{C_m}$$

where V_m is the membrane voltage of one cell, C_m its membrane capacitance, I_{ion} is the sum of all the sarcolemmal ionic currents produced by the cells and I_{gap} is in fact the gap junctional current computed according to the following equation, where V_{m1} and V_{m2} are the membrane voltages of the two cells:

$$I_{gap} = \frac{V_{m1} - V_{m2}}{R_{gap}}$$

One of the two cells was made "dormant" (i.e., it did not show spontaneous depolarizations, see again Chapter 3) by reducing I_f maximal conductance and I_{CaT} maximal permeability to 10% of their original values. The presence of a dormant cell and the disabling of LCRs were implemented to study the effect of LCRs on inter-cellular synchronization. Steady-state conditions at 20 s and $R_{gap} = \infty$ MΩ were used as initial conditions.

To gain quantitative information in the relative contribution to diastolic depolarization, the charges transported by I_f, I_{NaCa} and I_{tot} were computed as the integral of the respective currents during diastole (from the first *MDP*, to the first TOP). The first diastolic depolarization duration (*DD*) was computed as the time difference between the occurrence of the first *MDP* and the first TOP. Other AP features were computed as in [34]. All simulations used uniformly random distributed calcium release units (CRUs [35]).

The model was developed in MATLAB R2021a and integrated using an explicit Euler scheme (step = 7.5 µs) together with first order finite differences. 1 s of simulation took approximately 20 minutes on an Intel(R) Core(TM) i7-8565U CPU @1.80 GHz machine with 8 GB of RAM.

2.3 Results

The present model reproduces rabbit SAN cell physiology by showing AP features similar to previous models and compatible with experimental values (Table 2.1). Another important experimental validation is the simulation of funny current block by ivabradine: 66% I_f block led to a 19% rate reduction ($CL = 470 \pm 4$ ms, +24%). These results are similar to the SDiF model and experimental data [24]. Figure 2.1 shows the model APs and the calcium concentration in the subspace at (1) the beginning of the late diastolic phase; (2) the AP onset and (3) during the AP. As shown, LCRs appear in late diastole, grow in number before the AP upstroke (contributing to the exponential voltage rise) and finally merge into a global AP-induced calcium transient.

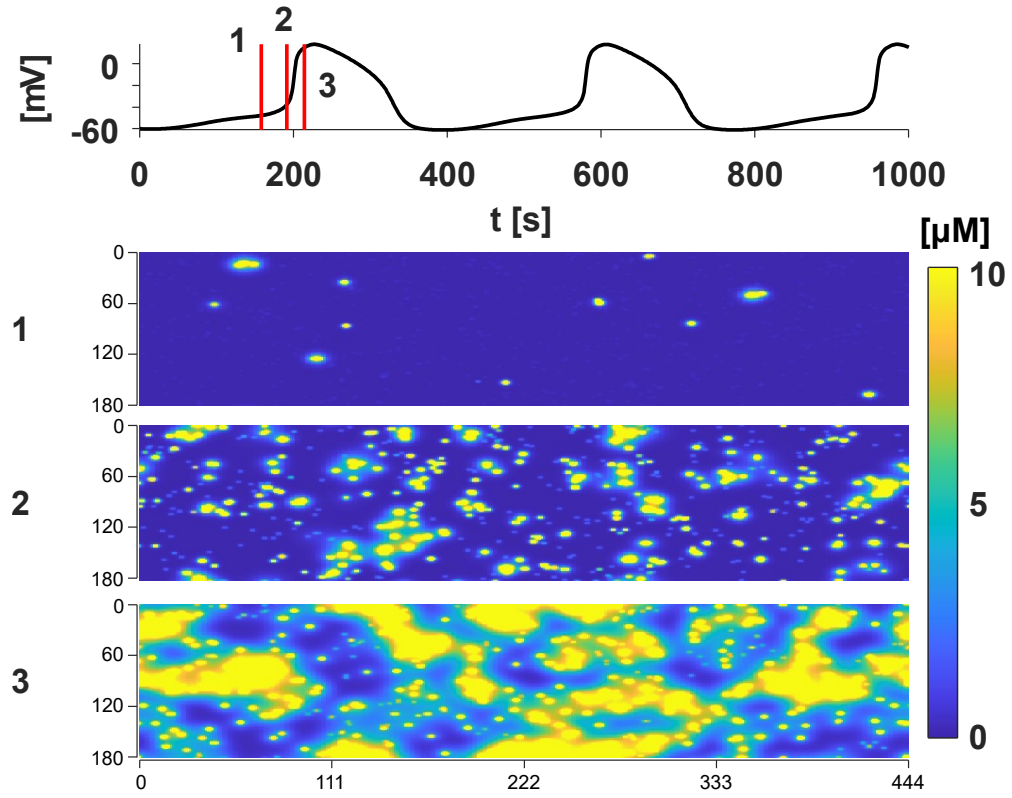

Figure 2.1: ***Baseline model action potential and calcium handling****. Action potential (top) and calcium concentration in the subspace (bottom three panels) in a steady-state (20 s) baseline simulation. Red vertical lines indicate the times at which the calcium concentration in the bottom panels is plotted. In the bottom panels, the whole cylindrical subspace was unfolded to allow its visualization in 2D: all 180x444 voxels are displayed.*

2.3.1 Disabling LCRs has different effects in baseline and heterogeneous models

Figure 2.2 shows the results of disabling LCRs during the diastolic depolarization of a single cell. As explained in the methods section 2.2, in this simulations CRUs could open only when the membrane voltage was above −30 mV, a value at which I_{CaL} activation threshold is already reached and the AP is triggered. In this condition, the first diastolic period lasted 308 ms, representing an average +60% increase compared to baseline (193 ms).

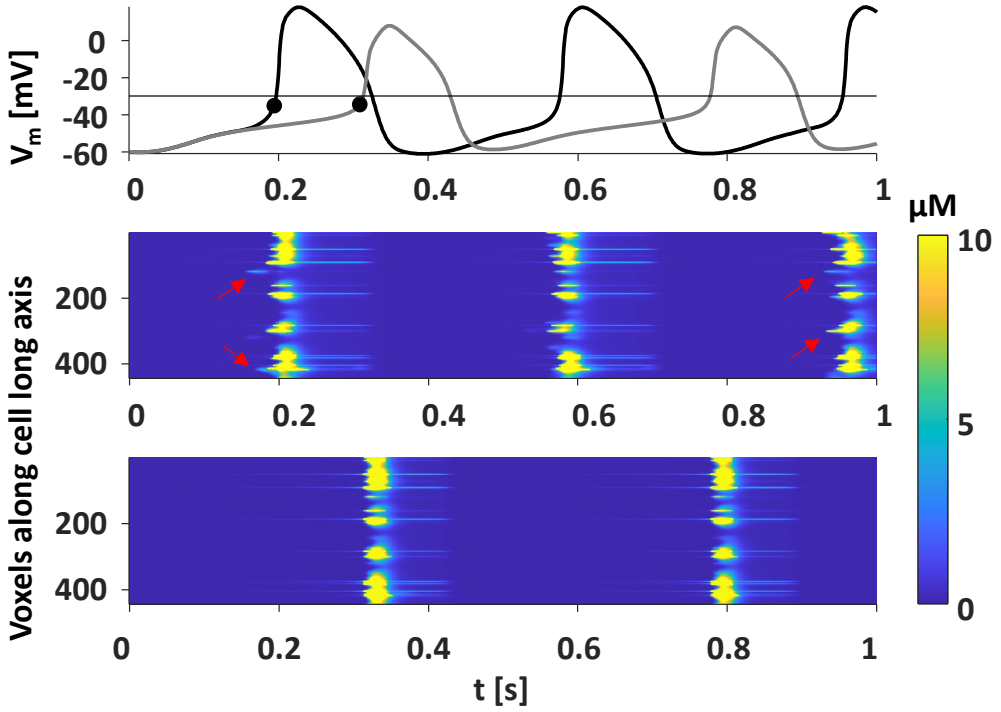

Figure 2.2: ***LCRs contribution in the baseline model****. Comparison between AP traces (top panel) of control (black) and no LCRs (gray) conditions in the present model. Black dots indicate the TOP, horizontal black line the −30 mV LCRs activation threshold. Line-scan along the cell long axis in control conditions (middle panel) and when LCRs are disabled during diastole (bottom) are reported, with red arrows marking LCRs.*

In comparison, preventing Ca^{2+} release below −30 mV in the original SDiF model leads to a milder *DD* prolongation (243 vs. 179 ms in control, +36%). Of note, the AP occurrence in the present model is delayed due to the fact that the diastolic depolarization slope in the late exponential phase is lower than in control conditions (Figure 2.2). This is a direct consequence of the reduced I_{NaCa} (Table

2.2) caused by the absence of LCRs (compare Figure 2.2 middle and bottom panels), which however seems not to affect the AP firing threshold ($TOP = -34.9$ mV in control vs. -34.2 mV when LCRs are disabled). However, the analysis on 5 heterogeneous cells provides different results: the first diastolic period lasted 166 ± 14 ms in the absence of LCRs, representing an average $-15 \pm 76\%$ decrease compared to when LCRs are present (181 ± 68 ms, $p > 0.68$). The huge variability is due to the fact that cells #3 and #4 shorten their *CL*, cell #5 is only slightly affected (+11 ms) while cells #1 and #2 see a *CL* prolongation (Table A.2). This happens despite the average reduction in Q_{NaCa} (Table 2.2, $p = 0.02$ for Q_{NaCa}/Q_{tot}). Also, the *TOP*s are significantly depolarized:-31.3 mV with respect to -34.2 mV in baseline ($p = 0.024$).

2.3.2 LCRs cut cell synchronization capacity but provide pacemaking flexibility in coupled cells

Figure 2.3 reports the results of the coupled cells simulations at different coupling values in the presence or absence of LCRs in diastole. If $R_{gap} < 10^4$ MΩ, the spontaneous cell is able to depolarize the dormant one whether LCRs are allowed or not. For $R_{gap} = 10^4$ MΩ however, in the presence of LCRs only 1 dormant cell over 5 is effectively driven to fire an AP. When LCRs are prevented, this number grows to 4, even if the *DD*s are prolonged (average +19.4% for the spontaneous cell and +32.4% for the driven one).

Interestingly, the DD duration range is enlarged by the presence of LCRs when $R_{gap} < 10^4$ MΩ, coupling values at which all pairs of heterogeneous cells are completely synchronized. For example, *DD* = 196 ms vs. 24 ms without LCRs with $R_{gap} = 10^3$ MΩ, +717%).

Table 2.2: ***Comparison of charge influx ratios during the first diastole in control and no LCRs conditions****. Q_{NaCa}, sodium-calcium exchanger charge; Q_f, funny current charge; Q_{tot}, total charge during diastole. For each condition, the first line refers to the baseline model, while the second one report the results of the 5 heterogeneous cells.*

Condition	DD [ms]	Q_{NaCa}/Q_{tot}	Q_{NaCa}/Q_f	Q_f/Q_{tot}
Control	193	111%	87.2%	127.3%
	181±68	99.2±13%	80.6±46.4%	145±51.9%
No LCRs	308	111.3%	55%	202.3%
	166±14	56.6±14.6%	39±10.3%	145.4±9.3%

2.4 Discussion

In this Chapter, we merged detailed calcium [35] and membrane clock [24] formulations to develop a tool for future investigations, which we also started to address here. First of all, the model showed a physiological behaviour for a single rabbit sinoatrial node cell in terms of AP features values (Table 2.1).

Simulations in which CRUs are prevented from opening during the diastolic phase show that LCRs are important in determining the late diastolic phase. If they are absent indeed, the action potential is substantially delayed because of the reduction in positive charge influx by the sodium-calcium exchanger. Interestingly, this effect is more pronounced in the present 3D model (+60% acute diastole prolongation) than in the original SDiF (+34%), highlighting an increased importance for Ca^{2+} cycling with the detailed description adopted. When considering 5 heterogeneous model cells however, variable results are obtained, with an average *DD* shortening ($-15 \pm 76\%$) following LCRs deactivation. This happens despite the general reduction in I_{NaCa} contribution in diastole (Table 2.2). This may suggest that LCRs contribution is dependent on the balance between calcium and membrane clocks achieved by the parameter randomization in both the membrane (e.g., g_f and P_{CaL}) and calcium-clock (P_{up}).

Concerning the coupled cell simulations (Figure 2.3), it can be noted that in conditions of extremely low coupling ($R_{gap} = 10^4\,\mathrm{M\Omega}$), the LCRs presence reduces the chances of the spontaneous cell to drive the dormant one. At the same time however, the interaction between the heterogeneized Ca^{2+} (when LCRs are allowed to happen) and membrane clocks allows to achieve larger beating rate dynamics. This supports the idea [39] that the membrane clock acts as a limit-cycle oscillator, providing robustness to pacemaking, while the calcium clock, acting through criticality mechanisms, adds flexibility to pacemaking. A similar behaviour was found regarding the origin of beat-to-beat variability in guinea pig SAN cells, with the calcium clock being the main source of it [167]. Thus, the Ca^{2+}-clock helps to achieve the range of physiological heart rates seen in mammals *in vivo*. Imagining that the interaction between the two clocks may differ in cells located in different portions of the SAN, creating clusters with different intrinsic properties, one could think that the autonomic nervous system would select one of these clusters to generate the required heart rate from time to time [280].

A limitation of the model is represented by the slightly prolonged APD_{50} values, which provide a *CL* at the upper limit of experimental values. However, further possible model developments - in particular regarding the membrane clock description - such as the inclusion of small-conductance calcium-activated potassium channels (I_{sK}) [281], may resolve this issue by shortening the *APD*, consequently allowing higher beating rates. Additionally, 100% I_f block leads to the

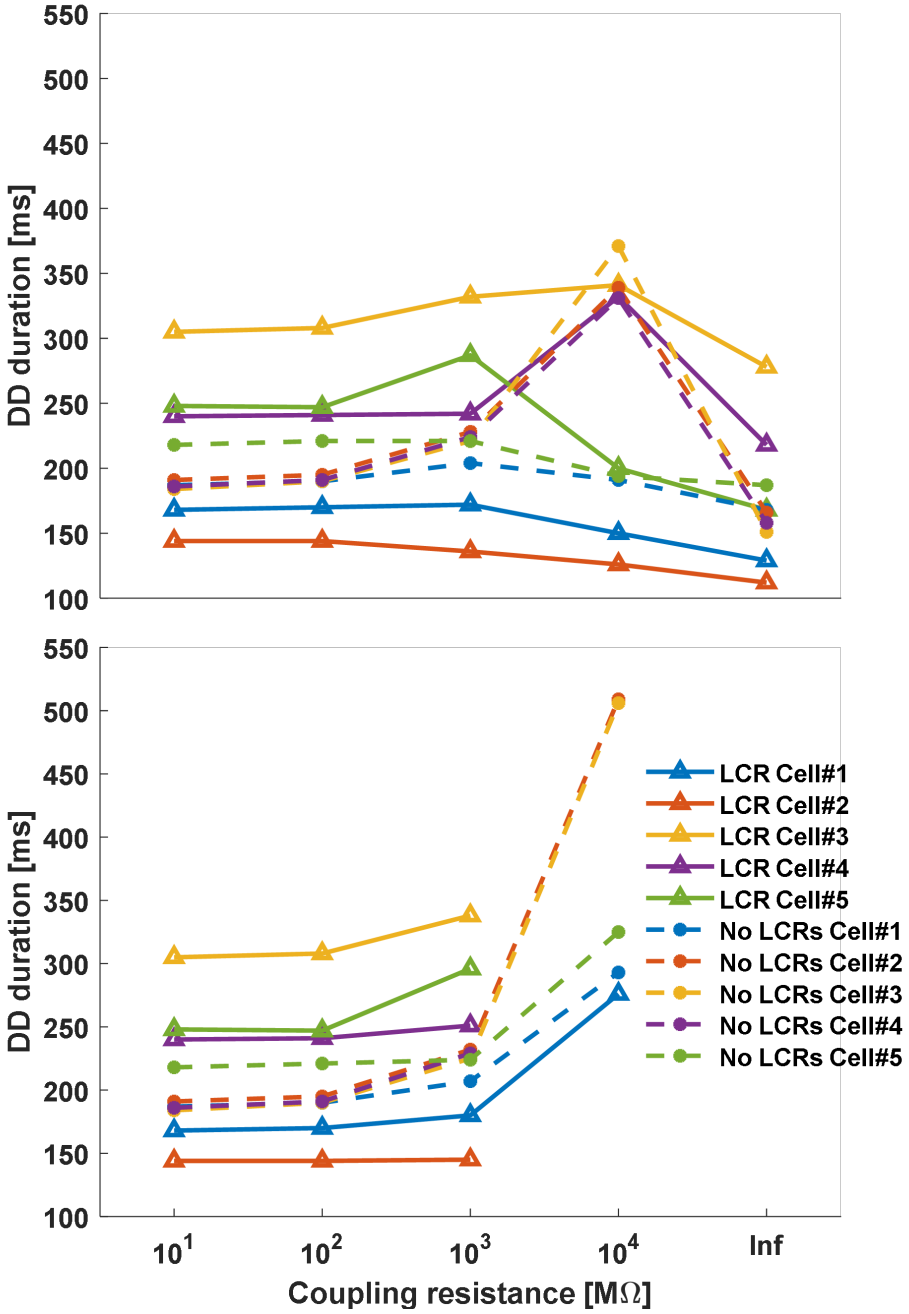

Figure 2.3: ***LCRs contribution to coupled cells synchronization****. Diastolic depolarization durations of coupled cells with (solid line) or without (dashed line) LCRs during diastole at different coupling values. Top: spontaneous cell; bottom: dormant cell.*

cessation of spontaneous beating and to model instability, highlighting the possibility of improvement in the description of the fine current balance during early diastole. Finally, the mechanisms behind the behaviour of LCRs in determining a lengthening or a shortening of the diastolic period must be further inspected.

2.5 Conclusions

In conclusion, this model constitutes a valuable tool to investigate pacemaking mechanisms with a high detail of membrane and calcium clock dynamics. Preliminary evidence here reported 1) suggests that the importance of local calcium releases for late diastolic depolarization depends on ionic channel expression and 2) supports the idea that the calcium clock adds flexibility but cuts robustness of pacemaking in coupled cells. The development of small tissues of such detailed SAN cellular models represent promising future developments that will allow to investigate the role LCRs have in SAN tissue entrainment .

Chapter 3

Importance of Coupling and Heterogeneity in the Isolated Sinoatrial Node

The content of this chapter is published in:

"Coupling and heterogeneity modulate pacemaking capability in healthy and diseased two-dimensional sinoatrial node tissue models"
Chiara Campana[1*], Eugenio Ricci[2*], Chiara Bartolucci[2], Stefano Severi[2], Eric A. Sobie[1]

[1] Department of Pharmacological Sciences, Icahn School of Medicine at Mount Sinai, New York, New York, United States of America
[2] Department of Electrical, Electronic and Information Engineering "Guglielmo Marconi", University of Bologna, Cesena, Italy

[*] These authors contributed equally to this work

PLOS Computational Biology, PloS Comp Bio 2022, 18(11), 1-21

Abstract

Both experimental and modelling studies have attempted to determine mechanisms by which a small anatomical region, such as the sinoatrial node (SAN), can robustly drive electrical activity in the human heart. However, despite many advances from prior research, important questions remain unanswered. This study aimed to investigate, through mathematical modelling, the roles of intercellular coupling and cellular heterogeneity in synchronization and pacemaking within the healthy and diseased SAN. In a multicellular computational model of a monolayer of either human or rabbit SAN cells, simulations revealed that heterogenous cells synchronize their discharge frequency into a unique beating rhythm across a wide range of heterogeneity and intercellular coupling values. However, an unanticipated behavior appeared under pathological conditions where perturbation of ionic currents led to reduced excitability. Under these conditions, an intermediate range of intercellular coupling ($900-4000\,\mathrm{M\Omega}$) was beneficial to SAN automaticity, enabling a very small portion of tissue (3.4%) to drive propagation, with propagation failure occurring at both lower and higher resistances. This protective effect of intercellular coupling and heterogeneity, seen in both human and rabbit tissues, highlights the remarkable resilience of the SAN. Overall, the model presented in this work allowed insight into how spontaneous beating of the SAN tissue may be preserved in the face of perturbations that can cause individual cells to lose automaticity. The simulations suggest that certain degrees of gap junctional coupling protect the SAN from ionic perturbations that can be caused by drugs or mutations.

3.1 Introduction

Understanding the mechanisms that coordinate the spontaneous firing of the sinoatrial node (SAN) has long been an issue of great interest in cardiac electrophysiology. After early studies believed that a single pacemaker region drives the entire SAN, more recent research has shown that the heartbeat originates from the coordination of a complex structure [268]. Many studies have worked to unravel the basis of this coordination, through both experiments [152], [282], [283] and mathematical modelling [148], [155], [156]. Despite the many insights obtained by these studies, important questions remain unresolved, particularly with respect to how heterogeneity between SAN myocytes and inter-cellular coupling combine to influence coordinated beating in tissue. For example, although it has recently been shown experimentally that not all SAN cells fire spontaneously when they are enzymatically isolated [136], [143], [284], we do not know how non-firing cells behave when they are electrically coupled in tissue, nor how the percentage of non-firing cells influences the overall electrical activity of the SAN.

Multiple mathematical models exist in the literature that describe the electrophysiology of isolated SA nodal myocytes [46], [59]. Most of these have been developed on the basis of data obtained in animal models, especially rabbits [22], [24], but a model based on human data has been published more recently [25]. Although it is obviously helpful to have multiple tools available for computational analyses, a question that commonly arises in such circumstances is the extent to which the behavior observed in a particular model is generalizable. On the other hand, when similar trends are seen across multiple mathematical representations, this can provide confidence in the model predictions [285]–[287].

In this investigation, we performed cellular and tissue simulations to examine how heterogeneity between SAN myocytes and intercellular coupling influence the coordination of beating within the SA node. The main goals were to: i) assess the effect of cellular heterogeneity in isolated SAN cells; ii) gain mechanistic insight into how electrical coupling between SAN cells modulates pacemaker activity at different levels of heterogeneity; and iii) investigate how simulated Sinus Node Disease (SND) influences SAN automaticity. Heterogeneous populations of SAN myocytes were generated at several levels of variability, and physiological behavior was simulated in both isolated cells and 2-dimensional tissue. Major results of the simulations were: i) cellular heterogeneity increases AP frequency and duration as well as the percentage of “dormant” cells, with remarkable consistency between three SAN myocyte models [13–15]; ii) intercellular coupling allows the cells to synchronize the beating rate in all conditions, except when heterogeneity is large and coupling between myocytes is weak; and iii) blockade of particular ionic currents leads to a loss of robustness in which coordinated beating

of the tissue fails at high and low coupling but can be maintained within a narrow range of intermediate coupling values. Overall, these simulations provide insight into the conditions that promote synchronized beating in the SAN, and how this can be maintained in the presence of heterogeneity.

3.2 Methods

3.2.1 Study Design

The goal of our study was to analyze, through mechanistic simulations, how heterogeneity between cells and gap junctional coupling influence the automaticity of the sinoatrial node and entrainment of the Action Potential (AP). As schematically shown in Figure 3.1, a two-dimensional tissue model was developed using, as the building block, models of the isolated SAN cell of different species (human and rabbit). For human SAN, the recent Fabbri et al. [25] model was used, whereas for rabbit SAN, both the Maltsev-Lakatta [22] and Severi et al. [24] models were considered. As shown in the expanded section of the center panel, each myocyte is electrically connected to its neighbors through gap junctional resistances. These connections may result from connexin 43 or connexin 45 isoforms, or both, with the composition of SAN gap junctions still a topic of active debate [109], [288]. This tissue model can then be used to simulate normal beating in the well-coupled SAN and to determine the effect of structural remodeling due to conditions such as reduced coupling (mimicking diffuse fibrosis [61], [289]) and clusters of non-spontaneous ("dormant") cells [136], [143], [284].

3.2.2 modelling heterogeneous populations of SAN cells

Heterogeneity between myocytes was simulated in each model by varying the maximal conductances of the ionic currents such that each current's baseline conductance was multiplied by a random scale factor chosen from a lognormal distribution [290], [291]. Five different values of the lognormal distribution shape factor (σ; from 0.1 to 0.5) were used to account for different levels of heterogeneity. Measurements from relatively large numbers of SAN myocytes ($30-130$) have revealed considerable heterogeneity in ionic current magnitudes, up to a 10-fold difference between cells with the largest and those with the smallest ionic currents [113]. As a lognormally-distributed random variable with $\sigma = 0.5$ shows a ratio of approximately 5 between the 95th and the 5th percentiles, these simulations may in fact underestimate true biological variability.

The purpose of creating heterogeneous populations of cells was three-fold. First, we used these populations to run a sensitivity analysis where the contribu-

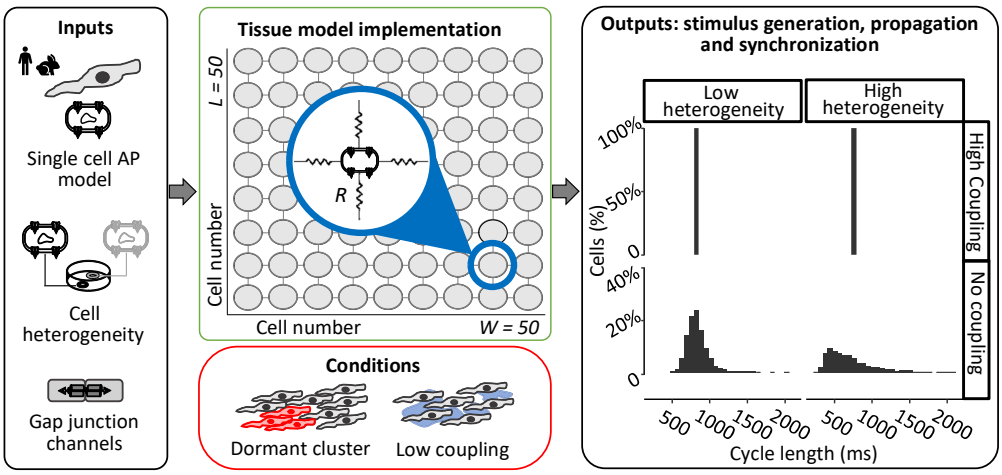

Figure 3.1: ***Schematic of multicellular study design****. A multiscale mathematical modelling approach was employed to study the mechanisms of sinoatrial node excitability. The effect of cell-to-cell coupling and cellular heterogeneity on tissue synchronization were evaluated in both healthy sinoatrial nodes and those that mimicked Sinus Node Disease. Blue inset in central top panel shows that cells were connected to 4 neighbors using ohmic resistances that modeled gap junctions between adjacent myocytes.*

tions of individual ionic currents on the cell's automaticity were evaluated with a logistic regression model [292], [293]. Second, isolated cell simulations were performed to assess the effects of σ on the AP parameters and on each model's robustness (that is, how many cells showed spontaneous beating after parameter randomization). Third, the cellular populations were used to create the two-dimensional propagation model in an attempt to recapitulate a small part of the complexity characteristic of the SAN structure. In particular, we aim to compare the behavior of isolated and coupled cells to gain a mechanistic understanding of how coupling modulates the effects of heterogeneity.

3.2.3 Logistic regression analysis of isolated cell results

When heterogeneity was imposed in isolated SAN myocyte simulations, spontaneous APs stopped in a percentage of cells. To evaluate which parameters influenced this transition, we developed a logistical regression model that could be used to predict the cellular state (e.g., "spontaneous" or "dormant") from a cell's set of randomly-varied parameters, similar to previous studies on Ca^{2+} spark probability [292] or arrhythmic behavior [293]. In this statistical model, a logistic relationship is derived to relate the heterogeneous ionic conductances, placed in

an input matrix, to the vector of cellular states, consisting of 1's and 0's for spontaneous and dormant cells, respectively. Each regression coefficient quantifies by how much, and in which direction, a model parameter needs to change to move a myocyte from the spontaneous to the dormant category.

3.2.4 Mathematical modelling of electrical propagation throughout the SAN

We implemented a tissue model by connecting individual SAN cells through an intercellular resistance that represents the gap junctional channels. In this model, each cell is described by a system of ordinary differential equations that, integrated over time, yields the values of ionic concentrations and gating variables (state vector). In addition, the membrane potential is calculated through a partial differential equation since its value depends both on the individual cell and the neighboring cells in the tissue. Thus, the updating of the membrane potential is described by the following equation:

$$\frac{dV_m}{dt} = \frac{-(I_{ion} + I_{gap})}{C_m} \tag{3.1}$$

where V_m is the membrane potential, C_m is the cellular capacitance, I_{ion} is the sum of all the ionic currents (dependent on the model), and I_{gap} is the sum of the currents exchanged with the four neighboring cells. We define the sign of I_{gap} such that negative I_{gap} represents current flowing into a particular cell from its neighbors, which will depolarize that cell. To speed computation time, V_m, which depends on V_m in neighboring cells, and the remaining state variables, which are specific to each cell, were updated separately. This allowed the updates to be computed in a massively parallel fashion using Graphical Processing Units, as described in more detail elsewhere [157]. Hardware and software specifications are provided in Table 3.1; model code is available at `https://github.com/Eugenio95/2D_hetero_SAN_parallel_models.git`.

3.2.5 Simulation protocols and conventions for model outputs

We considered a tissue formed of 2500 cells of equal size, arranged in a $50x50$ matrix. Simulations were executed for a duration of 20 s. In addition to different amounts of cellular heterogeneity, we tested multiple levels of intercellular coupling from a resistance value of 10^1 MΩ (10^2 nS; strongly coupled cells) to 10^4 MΩ (0.1 nS; weakly coupled cells) [179], [186]. The outputs of these simulations for each cell in the tissue were: membrane potential (V_m), ionic current of

Table 3.1: ***Hardware and software specification for model reproducibility.***

	Workstation 1	**Workstation 2**
Hardware		
Operating system	Ubuntu 19.04	Windows 10
RAM	64.0 GB	16.0 GB
CPU	16-core AMD Ryzen threadripper 2950x	Intel® Core™ i7-8700K
GPU	Nvidia Titan V 12 GB	Nvidia Geforce GTX 1060 6 GB
Software		
Simulation	MATLAB R2019b MATLAB GPU coder	MATLAB2020a CUDA 8.0 Visual Studio 2015
Integration	Euler method fixed step (10 µs)	Euler method fixed step (10 µs)
Analysis	MATLAB R2019b Pyhton 3.7	MATLAB 2020a R 4.0.3

each SAN cell (I_{ion}), and gap junctional current (I_{gap}). Additionally, I_{net} is defined as the sum of I_{gap} and I_{ion}, reflecting the total net current of each cell. A negative I_{net} depolarizes the membrane, whereas a positive I_{net} hyperpolarizes it.

From the AP trace (Figure3.2) we defined maximum diastolic potential (MDP; in mV) as the minimum value of voltage during the cycle; overshoot (OS; mV) as the peak membrane voltage during the AP; and take-off potential (TOP; mV), as the voltage at the first time step during diastolic depolarization when exceeds 15% of the maximum [118]. These three outputs were then used to compute the metrics on which our analysis relied: DD (ms), or diastolic depolarization, is the phase of the AP between MDP and TOP; APD (ms), or action potential duration, is the time difference between TOP and the following MDP; CL (ms), or cycle length, is the time difference between two consecutive peaks; APA (mV), or action potential amplitude, is the difference in voltage between OS and MDP. Cells were classified as spontaneously beating when the following criteria were satisfied: (1) $OS \geq 0$ mV; (2) $MDP \leq -40$ mV; (3) at least 3 peaks in the final 5 s of simulation.

3.2.6 Categorization of cells inside the tissue

To better describe their behavior, the cells forming the 2D tissue were divided into categories. Initially, cells were defined as "spontaneous" or "dormant" depending on whether they showed rhythmic electrical activity when simulated in an uncou-

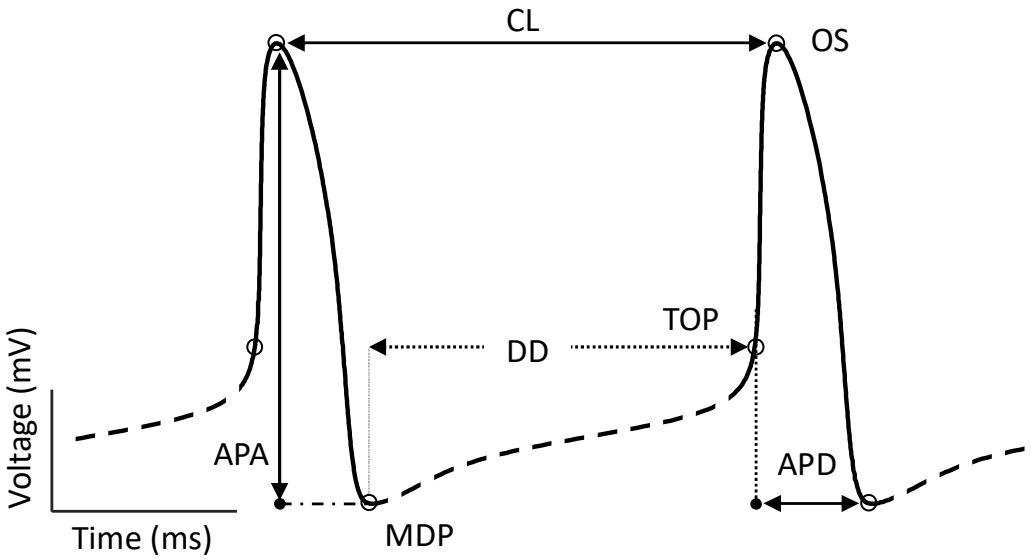

Figure 3.2: ***Features extracted from sinoatrial node AP simulations.*** *A schematic AP trace is annotated with characteristic features. The full waveform is divided into the AP phase (solid line) and diastolic phase (dashed line) based on the criteria described. Critical voltages and durations are defined as labeled. Abbreviations: APA, action potential amplitude (mV); APD, action potential duration (ms); CL, cycle length (ms); DD, diastolic depolarization (ms); MDP, maximum diastolic potential (mV); OS, overshoot (mV); TOP, take off potential (mV).*

pled condition ($R_{gap} = \infty$ MΩ). When a mixture of spontaneous and dormant cells is coupled in tissue, conditions may allow the dormant cells to exhibit action potentials. Understanding this concept requires the definition of subcategories, as illustrated in Figure 3.3, that capture different types of cellular behavior.

As schematized in Figure 3.3, based on their behavior when coupled within the tissue, "spontaneous" isolated cells could be further classified into: (1) "driving" if they continued to show rhythmic APs and had a positive (outward) I_{gap} at TOP, indicating that they reached threshold before adjacent cells and delivered current to their neighbors; (2) "followers" if, in spite of their spontaneous activity when uncoupled, they had a negative inward I_{gap} at TOP in the coupled condition, meaning that adjacent cells supplied current to assist their depolarization; (3) "stopped" if they did not show APs. On the other hand, "dormant" cells showed two different behaviors when coupled: (1) isolated dormant cells that started to beat thanks to coupling were called "driven", whereas (2) cells that remained silent

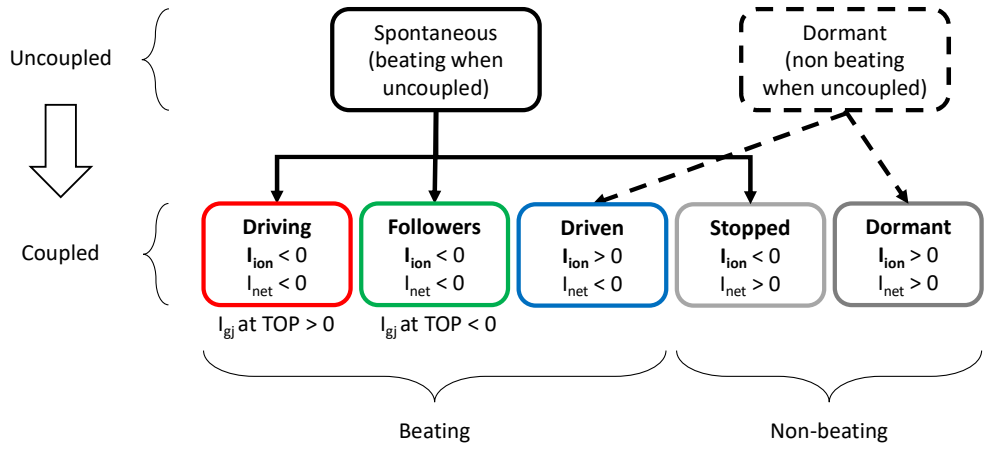

Figure 3.3: ***Cell categorization.*** *Cells forming the tissue have been divided into different categories, depending on whether they exhibited action potentials, or not, under both coupled and uncoupled conditions. Alterations in intercellular coupling can cause an individual cell to switch categories, for instance from dormant at one value of coupling to driven at another value.*

were termed "unexcitable". Note that since "unexcitable" cells do not show APs under any condition, features such as TOP and DD are undefined for these cells. For "stopped" cells we calculated DD and TOP based on simulations performed in the uncoupled condition. This procedure allowed us to investigate the current generated and exchanged at corresponding time points when they were coupled.

3.3 Results

3.3.1 Increased heterogeneity causes failure of spontaneous beating in a fraction of isolated SAN cells

Following the approach described in the Methods, we introduced heterogeneity in the ionic currents underlying the APs of the 3 models studied [22], [24], [25]. Figure 3.4 illustrates the impact of heterogeneity on the excitability and electrical properties of the isolated SAN cells. It is evident from Figure 3.4A that at increasing levels of the heterogeneity factor σ, some cells within the population lose their automaticity. The percentage of dormant cells depends on the model, with the Severi model more resistant, and the Fabbri and Maltsev models more

susceptible to increased variability in parameter values. In Figure 3.4B the AP metrics are summarized for the cells that retain their automaticity throughout various levels of heterogeneity. Across all models, there is a positive relationship between the level of heterogeneity and variability in AP amplitude, duration and frequency. Additionally, the Fabbri model shows a substantial decrease in the mean value of cycle length at increasing heterogeneity (-20% for $\sigma = 0.5$ vs. $\sigma = 0.1$), while only much smaller decreases are seen in the other two models (-3% for Maltsev and -0.2% for Severi model). In Figure 3.4C, we examined which specific ionic currents were responsible for the automaticity. The results of the logistic regression analysis shown in this panel indicate how much each parameter needs to be altered to move the cell from the spontaneously beating to the silent group [96], [292]. One notable difference between the 3 models is the background Na^+ current I_{bNa}, a current that is not even present in the Severi or Fabbri models, but which ranks as the third most important current in the Maltsev model. Despite this key difference, what is more notable is the consistency between the 3 models in terms of the relative importance of different currents in maintaining spontaneous activity. In all 3 cases, the L-type Ca^{2+} current, $Na^+ - K^+$ pump, and rapid delayed rectifier K^+ current I_{Kr} ranked as 3 of the most important parameters. Also notable is the relatively small regression coefficient corresponding to the "funny" current I_f in all 3 models. Considering that they were developed for different species (human vs. rabbit), from different data, and based on different hypotheses (Membrane clock vs. Ca^{2+}-clock), this is not an obvious result.

3.3.2 Well-coupled SAN tissues synchronize their behavior despite intercellular heterogeneity

Next we sought to investigate how variability between SAN myocytes influenced spontaneous beating at the tissue level. Since heterogeneity is known to be an important feature of the sinus node [3], [136], we expected cells in well-coupled tissue to coordinate their beating and fire at a common rate. Figure 3.5 shows that this occurs in human tissue, which confirms previous findings obtained in rabbit multicellular simulations [156]. When cells are coupled in tissue, the percentage of dormant cells drops to near zero at all levels of heterogeneity (Figure 3.5A), and the CL shifts to a single value throughout the tissue (Figure 3.5B), which we define as tissue synchronization. Coupled SA nodal cells also mostly synchronize their action potential amplitudes (Figure 3.5C) and durations (Figure 3.5D), although some residual variability is observed when heterogeneity between cells is high ($\sigma = 0.5$). Thus intercellular coupling can act as a powerful synchronization mechanism in human SA node, as previously demonstrated in rabbit [156].

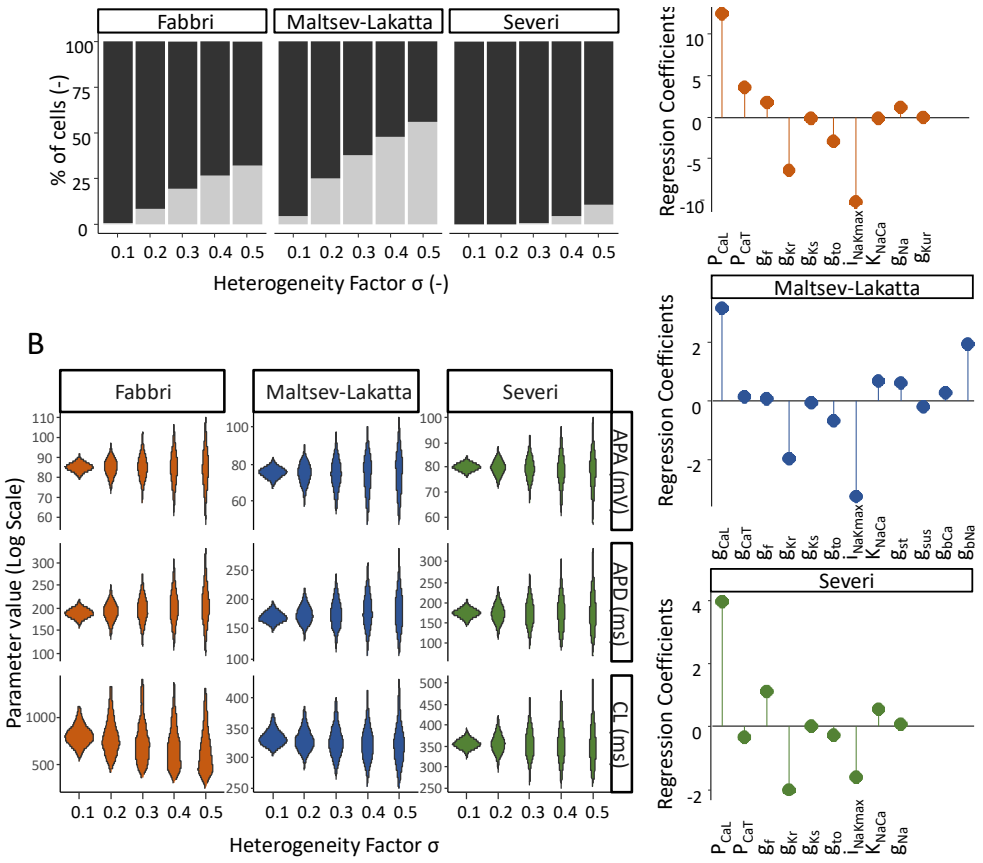

Figure 3.4: ***modelling conductance heterogeneity using virtual populations of isolated SAN cells.*** *(A) The effect of heterogeneous ionic channel expression on the automaticity of SAN cells was compared across models. In all three models the percentage of dormant cells rose with increasing levels of heterogeneity. (B) The effect of heterogeneity on the SA node AP properties was evaluated in spontaneously beating cells, by measuring cycle length (CL), AP amplitude (APA) and AP duration (APD) at varying σ levels. Outliers (values more than three median absolute deviations) were removed from distributions. (C) Logistic regression analysis was utilized to deduce which specific ionic currents across the three models are responsible for SA node cell's automaticity. Positive values indicate that an increase in the parameter increases the probability of the cell to be spontaneously beating.*

3.3.3 Ionic current perturbations alter the relationship between gap junctional coupling and SAN automaticity

The previous simulations suggested that strong intercellular coupling favors synchronization of SAN cells, since, for high levels of heterogeneity between isolated

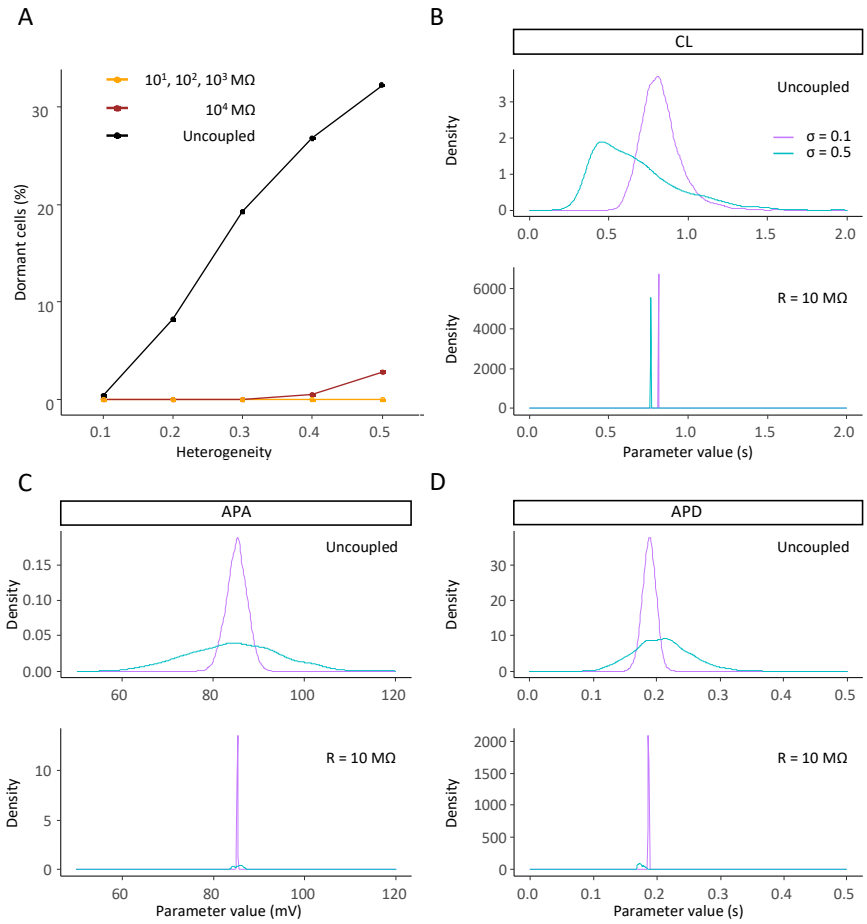

Figure 3.5: ***SAN cells synchronize their electrical properties when coupled in a tissue.*** *(A) When coupled together heterogeneous SAN cells give rise to a spontaneously beating tissue. The only exception occurs at very high values of heterogeneity (σ equal to 0.4 and 0.5, with 0.5% and 2.8% of dormant cells respectively) and very high levels of intercellular resistance (R_{gap} =10^4 MΩ). (B-D) The population of cells synchronizes its AP metrics: cycle length (CL), action potential amplitude (APA) and action potential duration (APD) when well-connected in tissue.*

SAN myocytes, previously dormant cells exhibited synchronized beating in tissues. Next we explored the combined effects of heterogeneity and perturbations that inhibit spontaneous beating and are potential causes of SND. Figure 3.6A shows the impact of diminished I_{CaL} on the single cell AP of the Fabbri model. Blocking P_{CaL}, the permeability controlling I_{CaL}, by 10% or 25% causes a reduction in beating frequency and AP amplitude, and spontaneous beating stops at 50% block. Next, we analyzed the consequences of the same perturbations in het-

erogeneous tissue, which implies a shift in the distribution of P_{CaL} (Figure 3.6B). Unexpected results were seen, however, when these heterogeneous cells with reduced P_{CaL} were coupled in tissue. Figure 3.6C, for example, compares results at different levels of coupling in heterogeneous tissue ($\sigma = 0.1$), before (left) and after (right) 50% reduction of P_{CaL} in all cells. With normal P_{CaL}, Cell #1120 exhibited spontaneous beating when uncoupled, and beat synchronously with the remainder of the tissue with both high and intermediate levels of intercellular coupling (left panels). The same cell, however, lost its ability to spontaneously beat when P_{CaL} was reduced by 50%. Surprisingly, however, this cell recovered its ability to beat at intermediate, but not at high, levels of intercellular coupling - *i.e.* certain levels of intermediate coupling encouraged SAN tissue automaticity. Generalizing to the whole tissue, Figure 3.6D shows that although the vast majority of cells (96.6%) did not beat spontaneously when electrically isolated, a middle range of coupling values (900 MΩ to 4000 MΩ), allowed these cells and the entire tissue to beat synchronously. The electrical properties of the tissue at different levels of P_{CaL} reduction and at intermediate coupling resistance (R_{gap} =10^3 MΩ) are quantified in Figure 3.6E. Blockade of I_{CaL} up to 25% caused the monolayer of SAN cells to beat at a lower frequency, but then at a higher rate when I_{CaL} is inhibited by 50% due to micro-reentry within the tissue (see S1 Movie).

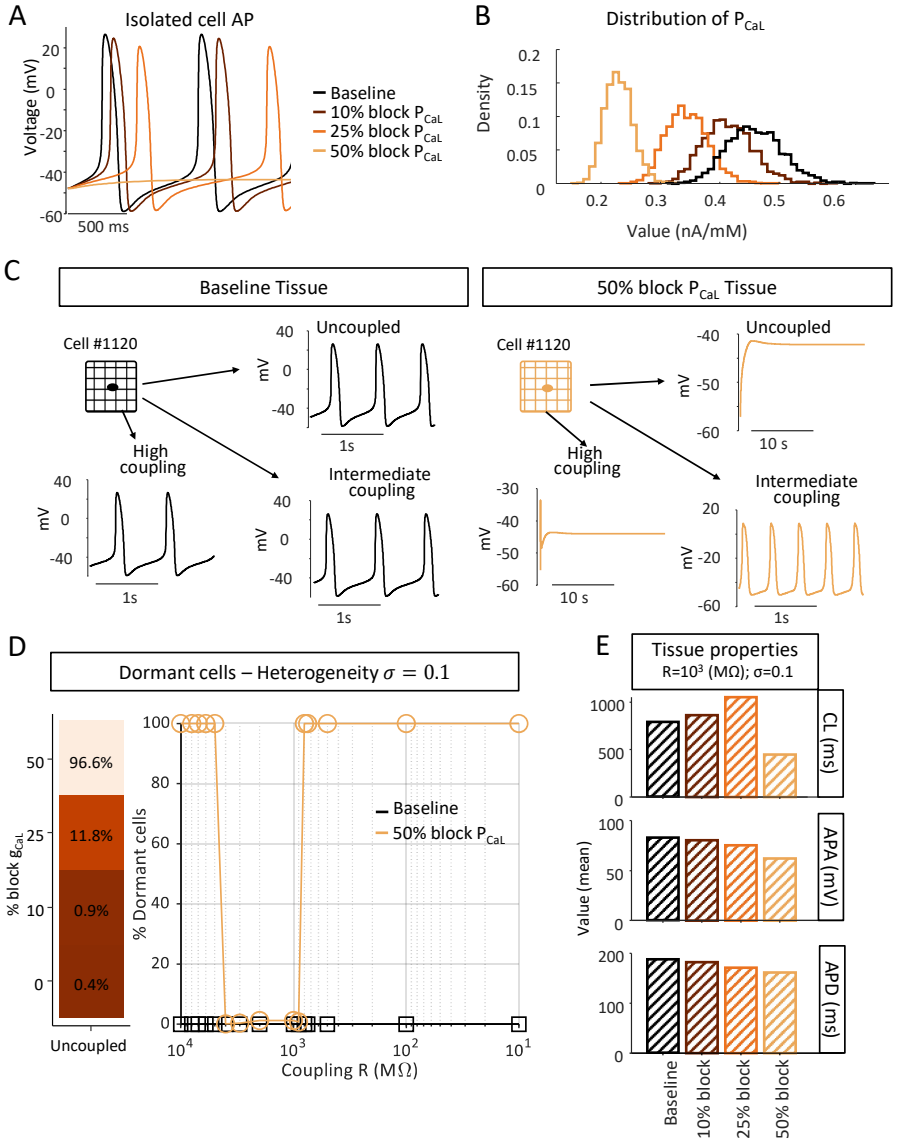

Figure 3.6: ***Certain coupling conditions restore automaticity to a prevalently dormant SA node tissue.*** *(A) Effect of Ca^{2+} blockade in the Fabbri model with published parameters. (B) Distribution of P_{CaL} in the tissue at varying degrees of Ca^{2+} blockade (cellular heterogeneity factor σ equals 0.1). (C) Comparison of the electrical activity of a cell within the tissue (σ equals 0.1) before and after blockade of Ca^{2+} by 50%. (D) Dormant cells within the tissue beat at intermediate values of coupling. (E) Quantification of the average tissue CL, APA and APD at varying degrees of Ca^{2+} blockade.*

Next we asked whether the protective effects of intermediate intercellular coupling were specific to the Fabbri model at 50% I_{CaL} reduction, or if this was a more general phenomenon. Figure 3.7 shows example results obtained in all 3 models where particular combinations of heterogeneity and ionic current perturbation led to synchronization of SA nodal tissue only at intermediate values of coupling. For example, when combined with heterogeneity, a 50% reduction of I_{CaL} in the Fabbri model (Figure 3.7A), either an increase in I_{NaK} or a decrease in I_{CaL} in the Maltsev model (Figure 3.7B), or a combination of 3 parameter changes in the Severi model (Figure 3.7C), all led to failure of spontaneous beating with strong intercellular coupling, successful propagation through the tissue at intermediate levels of coupling, and a substantial percentage of non-beating myocytes ($> 60\%$) when cells were completely uncoupled. These results therefore suggest that intermediate coupling may enable the SA nodal tissue to beat spontaneously under a range of conditions that will lead to failure when coupling between myocytes is strong. S2 and S3 Movies show the patterns of electrical activity in representative simulations from the Maltsev-Lakatta and Severi tissue models, respectively.

3.3.4 Clusters of beating cells can drive AP propagation over a range of coupling strengths

The results shown in Figure 3.6 demonstrated that a small number of spontaneously beating SAN myocytes could, at certain coupling strengths, drive propagation in the entire tissue. In that case, however, cells were distributed randomly throughout the tissue, whereas anatomical studies suggest clustering of similar cells in different regions of the SA node [4], [294]. We therefore tested the effects of placing all spontaneously-beating SA nodal cells within a defined cluster (Figure 3.8A). Results show that the clustered myocytes can drive propagation through the rest of the tissue over a wider range of coupling strengths, compared with the randomly-distributed, spontaneously-beating cells (Figure 3.8B). These results therefore suggest that pacemaker cells, when co-localized in a subregion of the node, may be protected from the influences of neighboring cells of a different type [210].

3.3.5 Intermediate coupling encourages tissue beating due to interactions between driving cells and dormant cells

Results presented thus far suggest that to understand the mechanisms of excitability in the overall tissue, we need to take a closer look at what occurs in the vicinity of the few pacemaker cells present in the tissue. In particular, we are interested in uncovering how, under conditions when a majority of cells do not exhibit spon-

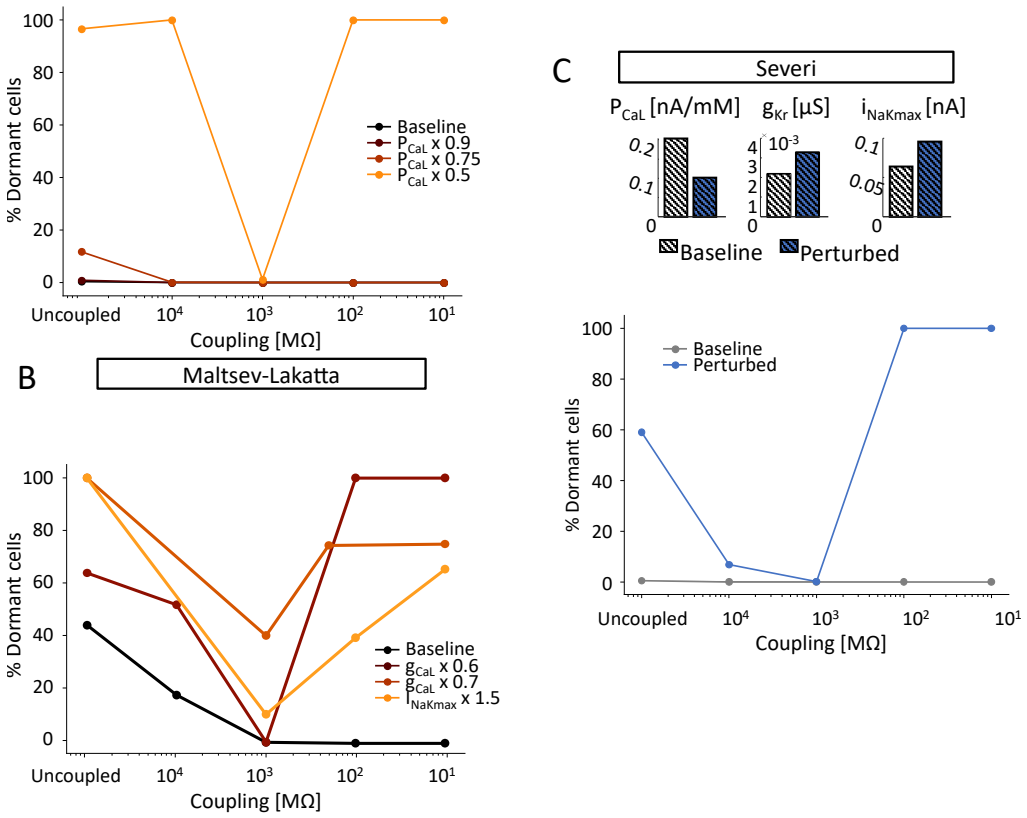

Figure 3.7: ***Pathophysiological changes in ionic currents lead to a pattern of tissue automaticity dependent on the degree of intercellular coupling.*** *(A) Effect of L-type Ca^{2+} current (I_{CaL}) perturbation in the Fabbri tissue model (σ equal to 0.1). (B) Effect of perturbation in I_{CaL} and Na^{+}/K^{+} pump (I_{NaK}) in the Maltsev-Lakatta tissue model (σ equal to 0.4). (C) Effect of combined I_{CaL}, rapid delayed rectifier K^{+} current (I_{Kr}), and I_{NaK} perturbation in the Severi tissue model (σ equal to 0.2).*

taneous beating, a small percentage of cells is able to drive tissue depolarization within a narrow range of intercellular coupling.

To investigate this question, we performed simulations with a spontaneously beating and a dormant cell (both extracted from tissue with $\sigma = 0.3$, 50% P_{CaL} reduction). From the simulation results of the two cells, we computed the average I_{net} during the central portion of the DD and, when action potentials occurred, I_{net} at the TOP (Figure 3.9A). Plots of these quantities over a range of coupling resistances (Figure 3.9B) help to explain why the spontaneously beating cell (Cell 1) is only able to drive the dormant cell (Cell 2) at intermediate coupling values.

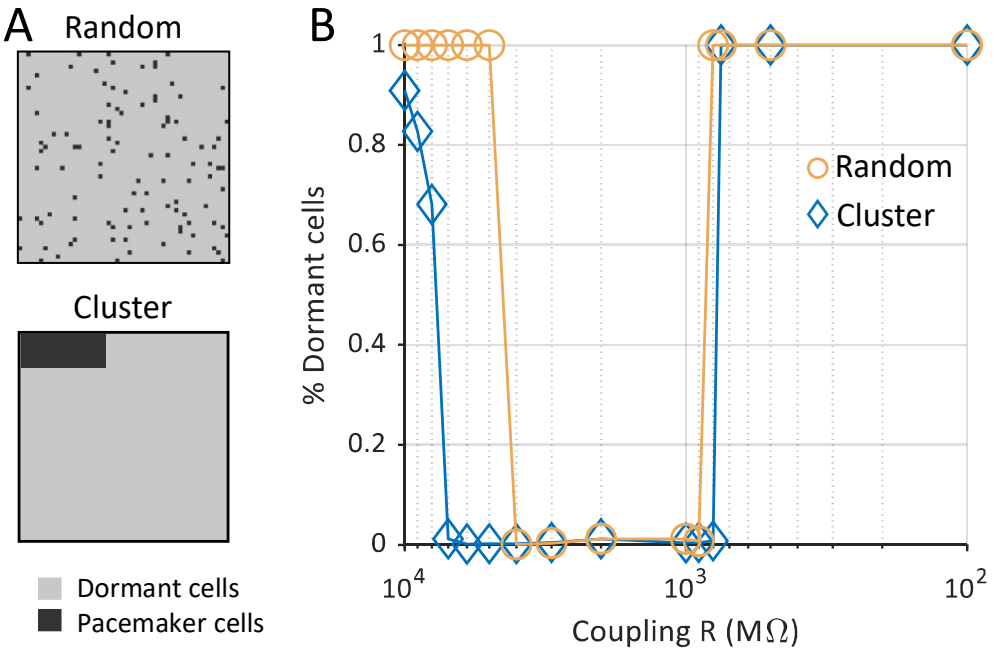

Figure 3.8: ***A small cluster of pacemaker cells can drive a prevalently dormant tissue.*** *(A-top) (A) In the random tissue configuration dormant and pacemaker cells are interspersed in the matrix. (A-bottom) In the cluster configuration pacemaker cells are confined to a small portion of the matrix surrounded by dormant cells. Here dormant cells are cells that fail to depolarize after inhibition of I_{CaL} by 50%. (B) The range of intercellular coupling compatible with AP generation and entrainment, i.e. reduced percentage of dormant cells, is wider in the cluster tissue configuration compared to the random. Results shown here were obtained with Fabbri human model (σ equal to 0.1).*

When the coupling between the two cells is strong (R_{gap} =10^1 MΩ), the dormant cell can suppress action potentials in the cell that would otherwise beat spontaneously (Figure 3.9C, right). This occurs because the large gap junctional current through the low resistance junction results in a small magnitude of diastolic I_{net} in the spontaneous cell. Under these conditions, TOP I_{net} is undefined since neither cell reaches TOP. With reduced coupling between the two cells (R_{gap} =10^3 MΩ) gap junctional current between the two cells is reduced, which allows a larger magnitude of diastolic Inet in Cell 1 (Figure 3.9B, top). This enables Cell 1 to reach its TOP and fully activate its inward current, thereby supplying enough current to Cell 2 for it to reach its TOP (Figure 3.9B, bottom) and fire an AP (Figure 3.9C, middle). Finally, when the coupling between the cells is reduced further (R_{gap} =10^4 MΩ and higher), a large inward diastolic I_{net} in Cell 1 is able to bring this cell to TOP, but the small magnitude of coupling current means that Cell 1 is

unable to drive beating in Cell 2. Thus, intermediate values of coupling represent a "sweet spot" at which the spontaneously beating cell and the dormant cell can be synchronized.

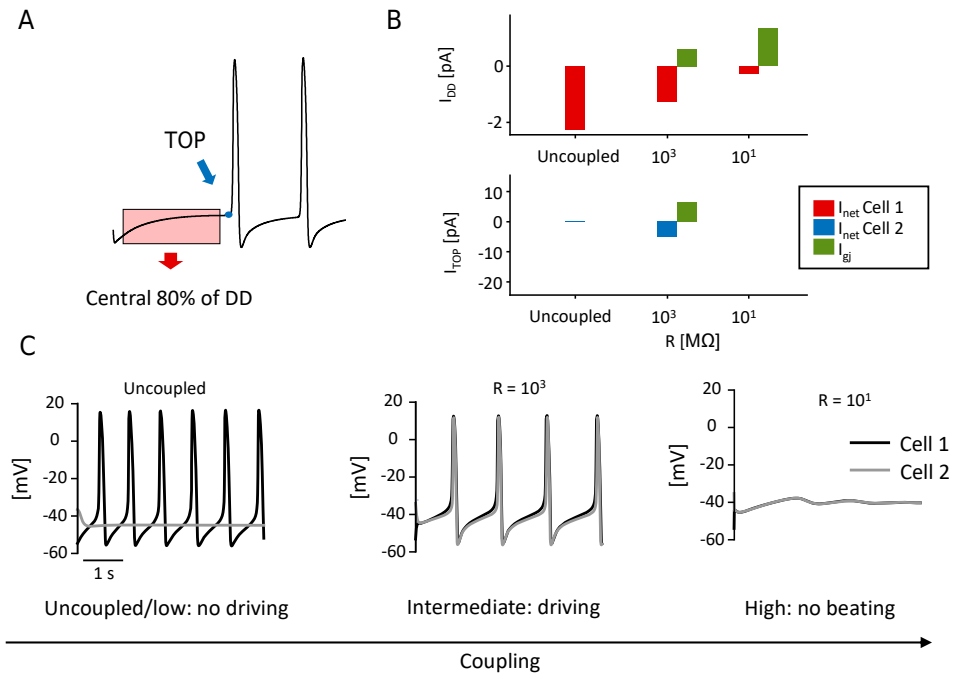

Figure 3.9: ***Coupling between a spontaneous cell and a dormant cell.*** *(A) Average I_{net} and I_{gap} were extracted from the central 80% portion of the first occurrence of DD (from the beginning of the simulation to the first TOP); TOP I_{net} and I_{gap} were sampled at the time of the TOP. (B) I_{net} and I_{gap} trends during diastole (top) for Cell 1 (spontaneous) and at TOP (bottom) for Cell 2 (dormant) with respect to different degrees of cellular coupling. I_{gap} is plotted in green for Cell 1 in both panels (the positive sign indicates an outward current, supplied to Cell 2). (C) Behavior of the two cells depending on coupling: both cells are beating periodically only for intermediate coupling values.*

To further support this view, the same analysis of I_{net} was applied to the whole 2D tissue ($\sigma = 0.3$, 50% P_{CaL} reduction). To understand this significantly more complex situation, cells were divided into categories based on their behavior, as explained in the Methods section. In these simulations, the initial condition for each spontaneous cell was set as state vector at the *MDP* in the uncoupled condition, and initial conditions for dormant cells were set at those of the spontaneous cell with the most depolarized *MDP*. As with the cell pair, strong coupling (R_{gap} =10^1-10^2 MΩ) allows dormant cells to suppress electrical activity in spontaneous

cells (Figure 3.10C, right) by draining current during the diastolic phase. Thus, TOP is not reached and the entirety of the tissue becomes "stopped" or "dormant" (right side of Figure 3.10A). With reduced coupling (R_{gap} =10^2 MΩ), spontaneous cells retain a larger fraction of diastolic I_{net} which allows them to reach the TOP. The first cells to reach TOP are classified as "driving," since they supply current to the other cells in the tissue, which are either "followers," if they beat spontaneously, or "driven," if they are otherwise dormant. A further reduction in the coupling (R_{gap} =10^4 MΩ and higher, left part of Figure 3.10A) allows more cells to reach the TOP on their own, but these spontaneously-beating cells are able to only drive a small percentage of the remainder of the tissue, due to reduced gap junctional currents between myocytes. Thus, under conditions of reduced excitability, the magnitudes of currents flowing between spontaneous and dormant cells determine whether the tissue can become entrained.

3.4 Discussion

In the present study, we investigated how different levels of cellular heterogeneity and intercellular coupling influenced human and rabbit SAN pacemaking. We simulated both healthy tissue and conditions of reduced excitability that were meant to approximate SND arising from diverse causes. Results showed that although increased cellular heterogeneity leads to a growing fraction of cells losing automaticity, intercellular coupling allows for synchronous and rhythmic activity in the whole tissue. Of note, this remained true for nearly all combinations of heterogeneity and coupling, highlighting the robustness of beating in nodal tissue. When we simulated diseased conditions by increasing or decreasing levels of fundamental ionic currents, the SAN tissue could fail to depolarize spontaneously. However, even under these extreme conditions, intermediate values of gap junctional resistance could rescue SAN electrical activity, and simulations provided mechanistic insight into this unusual phenomenon. This behavior was seen in all 3 models that we examined [22], [24], [25], and with different causes of reduced cellular excitability, suggesting that it may be a general property of SAN entrainment rather than specific to particular circumstances.

3.4.1 Comparison with previous computational SAN studies

Mathematical modelling has been employed as a tool to understand the mechanisms of SAN coupling and entrainment for more than two decades. Early studies [148], [175] demonstrated how simulations of SAN pacemaker activity in models of coupled cells can provide insights and encourage new hypotheses about cardiac electrical conduction. Combined with animal experiments, modelling has

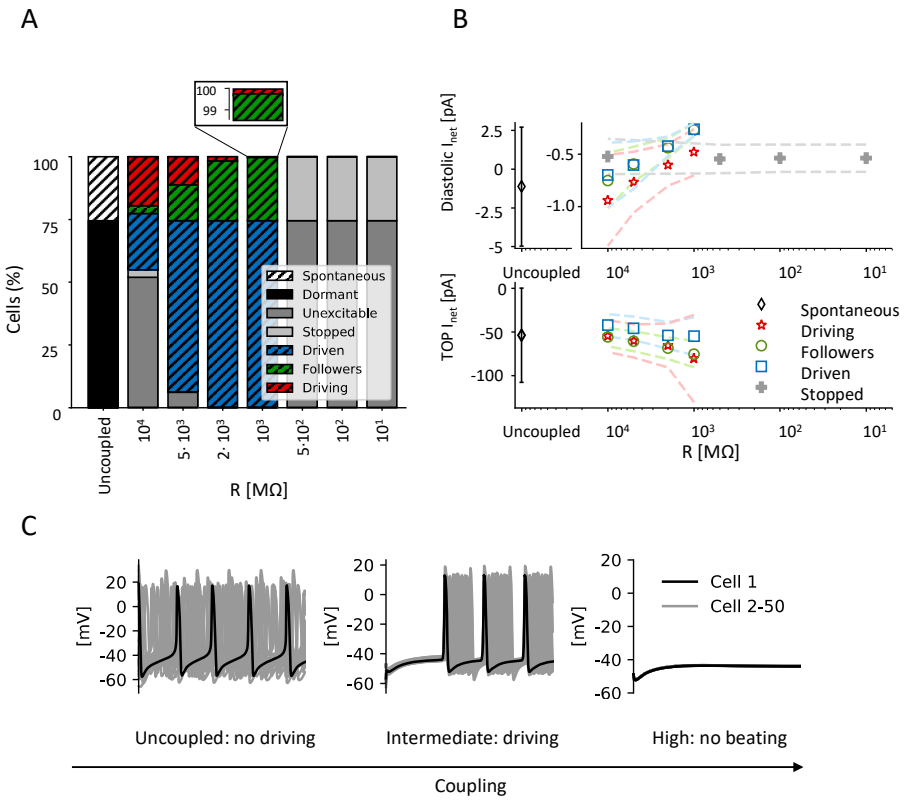

Figure 3.10: ***Coupling spontaneous cells with dormant cells inside a tissue.*** *(A) Percentages of cells composing each category at different degrees of intercellular coupling. (B) Inet trends during diastole (top) and at TOP (bottom) with respect to different degrees of intercellular coupling for every cell category. Average value (symbol) ± standard deviation (dashed line). (C) Electrical activity of 50 cells (4^{th} column of the 2D tissue matrix) when they are coupled with different intercellular resistances.*

been instrumental in developing our understanding that the heartbeat is likely to be dictated by the mutual entrainment of multiple spontaneously beating cells that synchronize their activity. Over the years, many investigators developed models to further describe the role of mutual entrainment of heterogeneous cells in the generation of the pacemaker activity. For instance, Oren and Clancy [184] showed that connections between the SAN and the atrium might be sufficient to impart the different features of peripheral SAN compared with central SAN APs. Conversely, Inada and colleagues [186] argued for the necessity of gradual changes in cell size, ionic current densities, and intercellular coupling from center to pe-

riphery. In particular, they suggested that the expression of $Na_v1.5$ and $Cx43$ in the periphery of the SAN might be fundamental for driving propagation to the atrium. Additional relevant insights were obtained by Gratz et al. [156], who studied interactions between ion channel conductances and intercellular coupling and found that the factors determining synchrony depended on whether this was defined by a metric based on activation times or one based on peak voltages. This study [156] is especially relevant to our work, as these authors examined synchronization of heterogeneous SAN tissue over a range of coupling strengths. Also pertinent is a recent study by Maltsev et al. [33], who examined tissue under conditions where the average cell was close to the border between spontaneously beating and dormant, finding that heterogeneity between myocytes enhanced the firing stability of the tissue. Our work builds on this prior research by perturbing myocytes in a heterogeneous population and demonstrating that a small percentage of spontaneously-excitable cells can sometimes be sufficient to drive the remainder of the tissue.

3.4.2 Modelling insights into the physiology and pathophysiology of the SAN

We simulated the effects on SAN automaticity of both physiological heterogeneity in ionic current densities and pathological changes to these currents. The results showed that this heterogeneity is compatible with synchronization of a large monolayer of either human or rabbit SAN cells. Moreover, we suggest that under conditions of reduced coupling between nodal cells, this heterogeneity helps to impart remarkable resilience that allows for AP entrainment even in the presence of pathological changes in the cellular electrical properties.

Sinus Node Disease (SND), also referred to as Sick Sinus Syndrome, is a general term that encompasses SA nodal dysfunction resulting from a wide variety of causes. Most cases of SND are acquired and associated with aging [53], but several congenital forms caused by mutations in ion channels or associated proteins have also been described [202], [294]. Normal aging, which frequently produces a reduction in heart rate, is also associated with decreases in expression of peripheral Na^+ channels [295], [296] and Cx43 [297]. Heart failure (HF), chronic atrial fibrillation and cell apoptosis [221] can also contribute to structural and electrical remodeling of the node and SAN dysfunction. Given the complexity involved in different types of SND, our goal was to broadly study conditions that caused some cells to lose automaticity, rather than any particular pathological state. Accordingly, we inhibited automaticity by altering different ionic currents in the 3 models (see Figure 3.7).

Whatever the cause of dysfunction, our results show that heterogeneity and

intercellular coupling are important factors in allowing SAN tissue to continue to exhibit spontaneous beating in the face of potentially pathological perturbations. Our simulations revealed that specific coupling strengths, falling in the range 900-4000 MΩ, or 0.25-1.1 nS when expressed as conductances (Figure 3.6D), allow the tissue to beat even under conditions where many cells no longer spontaneously fire. Comparing this range of coupling strengths to the existing literature, we find that it sits at the low end of previously reported values. For instance, experimental studies on rabbit SAN suggested that 0.5 nS would allow for frequency entrainment and 10 nS for waveform entrainment [152], while a previous computational work had predicted these thresholds to be 220 pS and 50 nS [151]. Other computational investigations have employed intercellular resistances of 7.5 nS [184] and 25 nS [186], whereas experiments have estimated values such as 0.6-25 nS [179] and 2.6±0.6 nS [298]. In pacemaking AVN cells, Spitzer et al. managed to achieve frequency synchronization at 2 nS. Values of intercellular coupling may be non-uniform across the SAN if different connexin isoforms are expressed in different SAN regions. Thus, the protective range of coupling that our simulations identified, which became relevant under simulated pathological conditions, is consistent with the fibrosis observed under pathological conditions [61], [289], which is likely to be associated with reduced coupling between SAN cells. One could even speculate that fibrosis, remodeling of gap junctions, and decreased connexin expression in SND may help to protect the SAN from failure.

Naively, one might expect that stronger coupling between SA nodal myocytes will be beneficial, since this will lead to faster propagation and enhanced synchronization of the cells within the node. Although our results are consistent with this idea under normal conditions, our findings also highlight a potential advantage of reduced coupling–namely that this can impart the tissue with greater resilience under conditions that impair spontaneous beating in individual myocytes. Indeed, it is remarkable that under particular conditions, fewer than 10% of the cells in the tissue can drive electrical activity in the remaining 90% of myocytes that do not.

3.4.3 The protection provided by intermediate coupling: AP vs. DD intercellular interactions

To attempt to explain the protective range of coupling strengths under pathological conditions, (Figures 3.6 and 3.7), we formulated a hypothesis based on the concepts of tonic and phasic entrainment that are well-established in the SAN literature [147], [151], [152], [154]. What differentiates our results from these previous ideas is that in our simulations these two types of interaction not only regulate SAN synchronization, but also determine the presence of spontaneous beating inside the tissue. In other words, spontaneous cells manage to drive dormant cells

only if two conditions are satisfied. First, spontaneous cells have to reach the take-off potential. Second, they have to supply enough current to the neighboring dormant cells. In this scenario, coupling resistance becomes the most critical parameter, since deviations in either direction can cause spontaneous firing of the tissue to fail. If resistance is too low, dormant cells will hyperpolarize the spontaneous ones during the DD phase, preventing them from reaching the threshold for AP firing. On the other hand, if coupling resistance is too high, spontaneous cells will not supply enough current to depolarize dormant cells. However, intermediate values of coupling guarantee that both conditions are satisfied. During diastole, when the voltage difference is low, I_{gap} is negligible, whereas during the upstroke, I_{gap} increases and allows dormant cells to depolarize (Figures 3.9 and 3.10). Although the cell types are different, this general phenomenon resembles the propagation of ectopic beats in ventricular tissue, where reduced coupling encourages propagation by inhibiting dissipation of depolarizing current [299], [300].

3.4.4 Are dormant cells present inside the sinoatrial node?

Given the numerous mechanisms that interact to produce SA nodal pacemaking at the cellular level [47], [301], it was not especially surprising that heterogeneity in ionic current properties caused a percentage of cells to cease beating spontaneously. Although it seems reasonable to ask whether this behavior is realistic or an artifact of the modelling, recent studies strongly suggest that dormant cells do indeed exist, both in isolated cell studies and within intact SA nodal tissue. A combined experimental and computational work published in 2018 [136] reported that about half of SAN cells isolated from guinea pig hearts did not exhibit spontaneous APs, although many of these cells recovered spontaneous beating when β-adrenergic signaling was stimulated with isoproterenol. A limitation of that study, however, is that results could have been influenced by the enzymatic dissociation procedure used to isolate individual cells. More recent studies, from that group and others [164], [271], [284], have confirmed the existence of dormant SA nodal cells in tissue under a variety of conditions. Our results, along with similar recent modelling studies [33], demonstrate that when dormant cells are coupled with a minority of spontaneous cells, the tissue can exhibit stable electrical activity even in the absence of sympathetic stimulation. Our results also suggest that relatively large percentages of dormant cells can indeed be consistent with normal pacemaker function at the tissue level due to the protective effects of heterogeneity and intercellular coupling. An excessive presence of dormant cells nevertheless poses a threat to SAN function, since these conditions restrict the coupling range in which rhythmic electrical activity can be generated. This highlights the perils of pathologies such as SND that depress SAN cellular excitability.

3.4.5 Limitations and future developments

Although the modelling strategy we used in this study allowed us to investigate tissue automaticity under a wide range of conditions, several limitations of our approach should be mentioned. First, the cellular heterogeneity was represented as random differences in ion channel expression between cells, and we did not consider gradients across the tissue in cell type, size, or shape. Several different types of myocytes have been proposed to exist within the SA node [61], [294], and non-myocyte cell types such as fibroblasts, atrial cells and adipocytes have been hypothesized to play important roles [4], [289], [302], and we did not examine these possibilities. Another structural simplification is the idealized geometry represented by a square sheet, far from the 3D banana-shaped anatomy of the SAN [4], [61]. Our tissue, which comprised 2500 cells, is comparable in size to the rabbit SAN (about 5000 cells [176]), but represents only a fraction of the human SAN. An additional limitation is that the isolated cell models we used are appropriate for for tissue simulations of electrical propagation, but not well-suited for local calcium release events that contribute to normal pacemaking and can appear even in dormant cells [136], [303]. More complex cellular models that consider stochastic gating of intracellular release channels [81] are required to simulate these local phenomena. These limitations can be addressed in future work to shed additional light on mechanisms of SAN pacemaking.

3.5 Conclusions

In conclusion, we have shown how multiscale mathematical modelling can be used to gain insight into the importance of cellular heterogeneity and intercellular coupling for efficacious cardiac entrainment. Previous multicellular studies have shown that synchronization of heterogenous cells is responsible for the SAN pacemaker function in rabbits [33], [156]. Our data confirmed that the same phenomenon occurs in a two-dimensional model of the human sinoatrial node. In addition, our study suggests that certain degrees of intercellular coupling make the sinoatrial node resistant to ionic perturbations that might be provoked by mutations and/or drug therapies.

3.6 Supporting information

Supplemental videos S1, S2 and S3 can be found at `https://doi.org/10.1371/journal.pcbi.1010098`.

Chapter 4

Effects of Different Cell Phenotypes in the Sinoatrial Node

Part of the content of this chapter is published in:

"Effects of Density and Distribution of Non-Spontaneous Myocytes, Scars and Fibroblasts Inside the Human Sinoatrial Node"
Eugenio Ricci[1], Chiara Bartolucci[1], Stefano Severi[1]

[1] Department of Electrical, Electronic and Information Engineering "Guglielmo Marconi", University of Bologna, Cesena, Italy

Computing in Cardiology 2021, Brno, Czech Republic

Abstract

In Chapter 1 we reported how recent works have highlighted a substantial presence of fibrosis inside the human sinoatrial node (SAN). However, it is not clear what the physiological purpose of such a high fibrotic content is. Also, its contribution to SAN pathology is largely unknown.

Here, building on the work presented in Chapter 3, we aim to elucidate the effects of structural and functional heterogeneity within the sinoatrial node tissue on its synchronization process. This is obtained by positioning either randomly or in clusters different densities of three cellular phenotypes: dormant cells, unexcitable tissue or fibroblasts. For each condition, four levels of heterogeneity ($\sigma = 0.1, 0.2, 0.3$ and 0.4) in SAN cellular electrophysiological properties are examined.

The results show that the presence of dormant cells does not avoid frequency entrainment. The cycle length (CL) of the tissue shortens with higher σ and with cluster distributions of the dormant myocytes. Opposite to this, randomly distributed unexcitable cells prevent the tissue from synchronizing its frequency (the standard deviation of the CL increases with σ and density). Moderate presence of fibroblasts (up to 40%) supply physiologic rates ($CL \sim 800$ ms), whereas high rates ($CL < 500$ ms) are obtained at up-regulated levels (60%) of fibrosis distributed in clusters. Specific configurations (e.g., $D = 60\%$, $\sigma = 0.1$ in presence dormant cells) lead to arrhythmic behaviours with high frequency ($CL = 438$ ms) and spiral wave-like patterns due to functional reentry.

In conclusion, the SAN is robust to the presence of substantial amounts of non-myocytes populations. However, high densities of randomly-distributed unexcitable cells and dormant cells (at low SAN cellular heterogeneity) and cluster-distributed fibroblasts may represent SAN pathological conditions.

4.1 Introduction

The fundamental role of the SAN as the physiological source of the heart beat is achieved thanks to many electrophysiological, anatomical and mechanical characteristics (Chapter 1). Thus, the properties of the cells composing the SAN and their distribution inside this complex structure are of uttermost importance in determining its function.

Recent works have highlighted the surprising heterogeneity of cells inside the SAN: e.g., more than 40% of the tissue was estimated to be fibrotic in healthy, adult human males [244], a value much higher than in the neighbouring atrium. This relevant amount of fibrosis inside the SAN could represent a protection mechanism: in order to avoid excessive hyperpolarization and stretch coming from the atrium, fibrosis provides electrical and mechanical shielding. This fact is supported by evidence of a continuous border (except for specific exit pathways) of fibrosis and fat around the SAN [61] and by the fact that fibrotic content increases with age and animal species size, quantities positively correlated with heart dimensions (and thus to electrical load and mechanical strain).

Additionally, it has been proven that fibroblasts can establish connections with cardiac myocytes both *in vitro* [51], [304] and recently *in vivo*, too [305]. Thus, being an electrically active cell phenotype, able to connect to SAN myocytes [245], they are supposed to directly participate to the rhythmic activity of the SAN, as shown by computational studies on rabbit SAN models [184], [190].

Fibrosis is however also thought to have a role in pathogenesis, and has been implicated in sinus node dysfunction (SND). By limiting the interconnections between myocytes indeed, fibrosis could prevent them from reaching an entrained condition, possibly leading to arrhythmias. The mechanism is however still not fully understood, since a correlation between the amount of fibrotic tissue and SND has not been demonstrated yet [61].

In this work, three different conditions were investigated sing bi-dimensional human SAN computational models. Namely, 1) dormant cells (reported in Chapter 1, 2 and 3) to reproduce silent SAN tissue; 2) unexcitable myocytes (mimicking a fatty, collagen or scar tissue) and 3) active fibroblasts to model fibrosis were included in SAN tissues. Different densities (D, range 0-60%), heterogeneity levels ($\sigma = 0.1, 0.2, 0.3, 0.4$) and distributions (random, to model diffuse fibrosis, or cluster, to model patchy fibrosis) were tested in each case.

The cycle length (CL), action potential amplitude (APA) and action potential duration (APD), as well as the number of beating cells in the tissue were computed. The objective of this work was that of estimating the effects of these cellular phenotypes on the beating rate and entrainment capability of the sinoatrial tissue.

4.2 Methods

4.2.1 Cellular Coupling and Heterogeneity

A 2D discrete tissue featuring the FWS model [25] for human single SAN cells, as described in Chapter 3, was used in the simulations. A value of R_{gap} of 1 GΩ was adopted from the physiological range of coupling found in literature [186] and following our sensitivity analysis in Chapter 3 [34]. The model consisted of 50x50 central SAN cells, an estimate of the number of cells ($\sim$ 5000) from which the stimulus is seen to originate [176] in the rabbit SAN. No flux boundary conditions were applied.

To account for SAN cellular heterogeneity [1], the Ca^{2+} currents permeabilities (P_{CaL}, P_{CaT}), the maximal conductances (g_{Kr}, g_{Ks}, g_{Kur}, g_{Na}, g_f, g_{to}), the maximal activity of the Na^+/K^+ pump and of the Na^+/Ca^{2+} exchanger (I_{NaKmax}, K_{NaCa}) of the Fabbri model were randomized as done in Chapter 3. Four levels of σ, the width of the log-normal distribution used to randomize the parameters, were considered (0.1, 0.2, 0.3, 0.4). Simulations lasted 20 s to reach steady state and AP features (*CL*, *APA* and *APD*) were computed on the last 5 s as in [34].

4.2.2 Cell type density and distribution

Simulations with $R_{gap} = \infty$ (uncoupled cells) were run in order to investigate how many cells did not show spontaneous electrical activity (i.e., the were dormant) following parameter randomization. For every σ, two additional levels of density D were tested:

- 40% : an approximation of the amount of fibrotic tissue found in adult human subjects under physiological conditions [244];
- 60% : reflecting a condition of upregulated fibrosis.

Being dormant cells in the uncoupled condition less than 40% and 60% for each σ (Table 4.1), the same cell parameters were used multiple times to reach a total amount of 1000 and 1500 dormant cells in the tissue, respectively. To evaluate the effects of diffuse vs. patchy fibrosis, random and cluster distribution of cells inside the tissue were tested. The latter was considered only in the $D = 40\%$ and 60% cases, so that to obtain randomly-distributed, non-overlapping clusters of 10x10 cells. The cell position was fixed across different simulations in order to exclude the effects of different distributions. The same workflow was adopted to simulate the effect of unexcitable tissue - modeled as cells that did not show any

connection with their neighbours ($R_{gap} = \infty$) and consequently acting as conduction barriers - and of fibroblasts, for which the atrial fibroblast active model by Morgan et al. [255] was used.

4.3 Results

As obtained in Chapter 3, in an uncoupled condition the increase of σ leads to a growing number of dormant cells (Table 4.1).

Table 4.1: ***Results of the uncoupled cells simulation.*** *The number of dormant cells in the tissue grows with σ (width of the log-normal distribution).*

σ	**0.1**	**0.2**	**0.3**	**0.4**
Dormant cells	1 (0%)	126 (5.0%)	357 (14.3%)	584 (23.4%)

Despite this, when the cells are coupled with $R_{gap} = 1\,\text{G}\Omega$, all of them show rhythmic electrical activity, even with D = 40% and 60% (Figure 4.1). The only exception is $D = 60\%$ and $\sigma = 0.1$, where 18 cells do not beat. From the bottom left panel (*CL* of non-spontaneous myocytes, D = 60%) of Figure 4.1, it can be seen that the *CL* of this condition, being 438 ms, is substantially shorter than the *CL* of the uncoupled condition (829 ms). This is due to the behaviour of two irregularly-beating cell clusters, circled in red in Figure 4.3. In fact, some of these cells show a sub-threshold and irregular electrical activity (Figure 4.2), that let them act as functional blocks around which a double spiral wave can form and be sustained (Figure 4.3). Despite this, the cells manage to synchronize their frequency as in all other coupled conditions, as shown by the negligible dispersion of the *CL* (Figure 4.1, first column).

In general, the results in Figure 4.1 show how the average *CL* is reduced with an increase in cellular heterogeneity, being almost halved from $\sigma = 0.1$ to $\sigma = 0.4$ (e.g., $D = 40\%$ condition: from 936 ms to 473 ms). A similar but weaker trend is shown by the *APA* (except with $\sigma = 0.1$, Figure B.1), whereas the average *APD* does not show a dependence on σ. The standard deviation of the *APA* and *APD* tends to increase with cellular heterogeneity. The density of non-spontaneous cells tends to prolong the average *CL* (when $\sigma = 0.2$, $CL = 646$ ms vs. 752 ms vs. 788 ms with $D = 5\%$, 40% and 60%, respectively), while it slightly reduces the average *APA* and *APD*. The partitioning of non-spontaneous cells into clusters produces a shortening in the mean *CL* but has negligible effects on the average

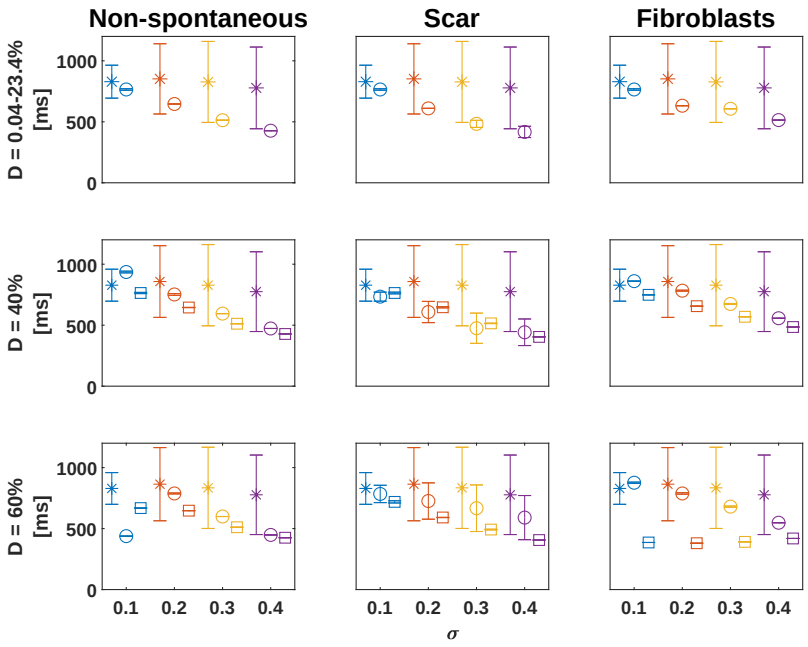

Figure 4.1: CLs ***in the tissue containing dormant cells, scar tissue and fibroblasts at different densities*** *(D)* ***and SAN heterogeneity levels*** *(σ). Asterisks (∗) identify simulations with uncoupled cells, whereas circles (∘) and squares (□) identify simulations with random and cluster distributions, respectively. Mean±std.*

APA and *APD* when compared to the random distribution configuration (Figure 4.1 and B.1).

Regarding the presence of fat, collagen or scars in the tissue, the central column in Figure 4.1 shows that all excitable cells are beating regardless of the heterogeneity level of the tissue and of the type of cell distribution. However, when unexcitable cells are randomly distributed, the tissue fails to fully synchronize its frequency: the *CL* sees a growing dispersion with an increase in D and σ (Figure 4.1). This is due to the fact that unexcitable cells prevent connections between SAN myocytes, determining isolated cluster of SAN cells with different intrinsic frequencies. Indeed, this does not happen when the scar tissue is grouped in clusters that allow all SAN myocytes to entrain one with another. Similar to the presence of dormant cells, the average *CL* is shorter with higher σ and cluster distribution (the latter only when $D = 60\%$). Furthermore, D prolongs the *CL* (e.g., when $\sigma = 0.1$, from $D = 0\%$ to 60%, *CL* changes from 765 ms to 784 ms). Compared to the previous condition, similar trends for the *APA* and *APD* can be appreciated, if not for a reduction in *APA* with $D = 60\%$ and cluster configuration, with respect to the random distribution (Figure B.2).

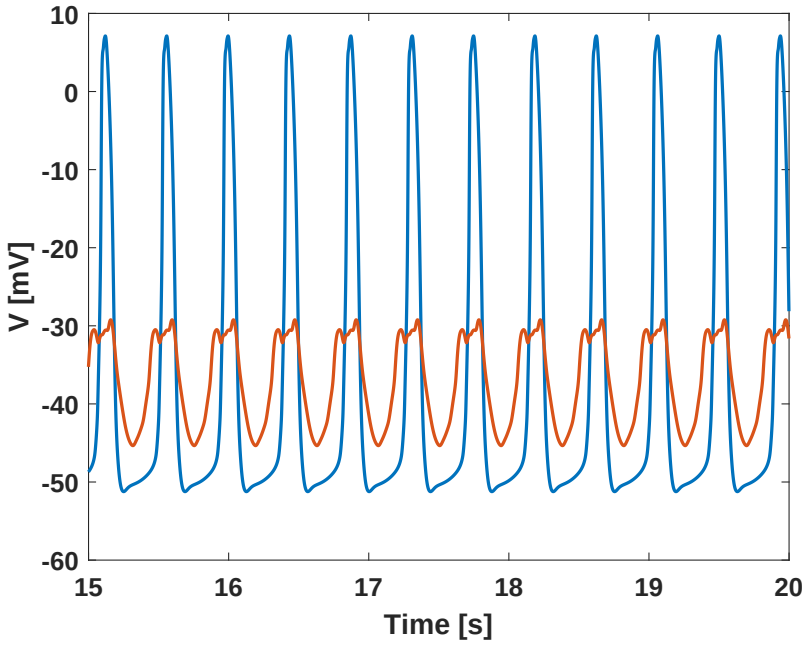

Figure 4.2: ***Examples of membrane voltage traces from the D = 60%, σ = 0.1 simulation with dormant cells****. The blue trace represents a SAN cell showing normal activity, while the orange line shows the behaviour of one irregularly-beating cell composing the clusters that act as functional blocks in the tissue.*

The presence of fibroblasts determines similar *CL* trends as in the previous conditions with respect to σ, but in this case the dependence on the fibroblasts' density is stronger with randomly-distributed fibrosis (when $\sigma = 0.2$, $CL = 632$ ms vs. 783 ms vs. 788 ms with $D = 5\%$, 40% and 60%, respectively). With the cluster distribution, $D = 60\%$ and $\sigma = 0.1 - 0.3$ cases however, the *CL*s are substantially shorter (of more than > 300 ms) than those of the random ones, as will be discussed in Section 4.4. *APA*s are substantially reduced by both fibroblasts distributions, whereas only the random distribution determines a marked prolongation of the *APD* (+48% with $\sigma = 0.2$, $D = 60\%$, Figure B.3). Figure 4.4 shows that when fibroblasts are distributed in clusters, a large amount of cells is not showing rhythmic activity. This is because SAN myocytes do not manage to drive the cores of the fibroblast clusters, since these represent an electrical sink too big for the weak upstroke of SAN cells. Only the most external fibroblasts are driven by SAN cells (Figure B.4), but do not propagate the excitation wave.

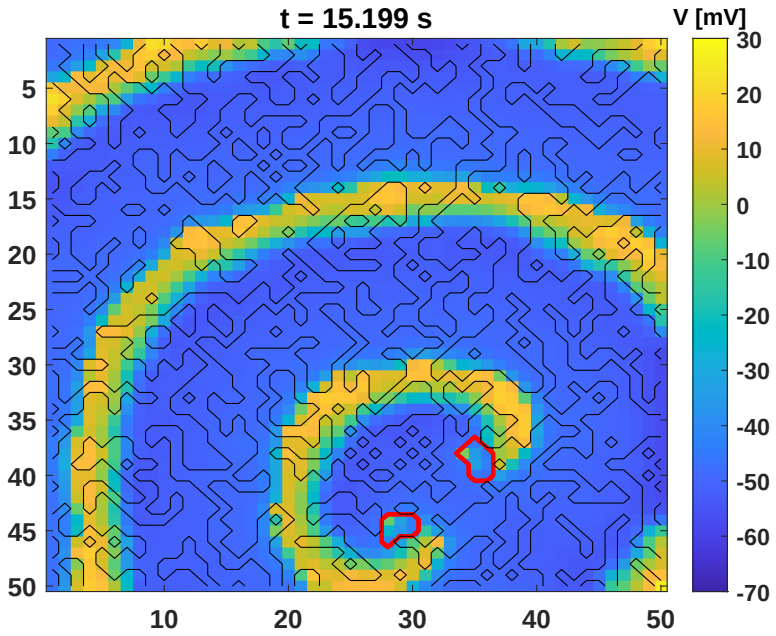

Figure 4.3: ***Voltage map showing the electrical activity of the 2D tissue with randomly-distributed dormant cells (circled in black): D = 60%, σ = 0.1****. The spiral wave-like pattern is established around the two clusters of the irregularly-beating cells (in red).*

4.4 Discussion

The results reported above allow to draw some conclusions about the cross-talk of different cellular phenotypes inside the human sinus node. First of all, increasing the density of the three phenotypes investigated (dormant cells, scar tissue and fibroblasts) determines a prolongation of the average *CL*. Considering that the maximal prolongation is 24% (random fibroblasts distribution, $\sigma = 0.2$, $D = 60\%$) even when consistently different densities (5% vs. 60%) are compared, it can be stated that the SAN is overall robust to a high presence of non-spontaneous cells and manages to supply a physiologic and synchronized rate despite the reduction in SAN myocytes. Indeed, besides fibroblasts, dormant cells – i.e. those cells not showing a spontaneous AP when isolated – have been identified inside the SAN, and are believed to participate in the entrainment process (Chapters 1-3 and [136], [143], [164], [306]). Indeed, as shown in Figure 4.4, all cells – dormant ones included – are beating inside the tissue, if not for the $D = 60\%$, $\sigma = 0.1$ case where two clusters of cells are not able to show an action potential. Considering that re-entry-like waves around these clusters are elicited, this functional blocks formation could represent a possible mechanism of sinus tachycardia onset (*CL* is

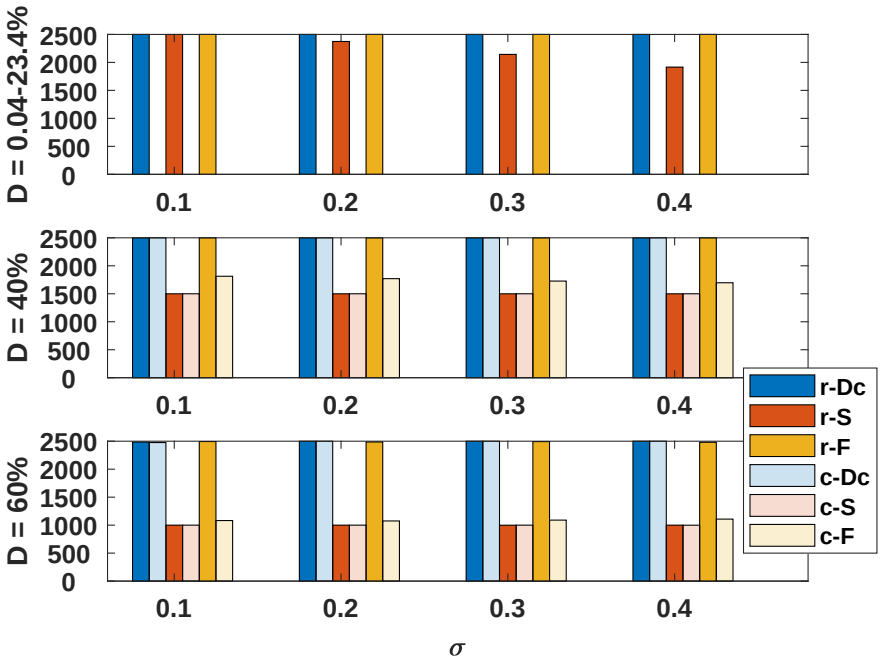

Figure 4.4: ***Number of beating cells inside the tissue at different heterogeneities (σ) and densities (D).*** *r-: random distribution; c-: cluster distribution; Dc = dormant cells; S = scar tissue; F = fibroblasts.*

438 ms, equal to 137 bpm). However, this condition is strongly dependent on the specific distribution of dormant cells and randomized SAN ionic properties.

The type of cell distribution has a stronger effect on the *CL*. Grouping dormant cells in clusters determines a shortening of the *CL*, with respect to the random distribution condition. When scars are considered, the cluster distribution leads to a lengthening of the average *CL*. These effects can be explained in terms of source-sink relationship: with cluster distribution, spontaneous cells establish less connections with electrical loads (dormant cells) that would prolong their diastolic depolarization phase. With unexcitable cells instead, the clusters determine a condition in which faster cells show on average more connections with their neighbours. As a consequence, they are slowed down with respect to the random distribution condition, where they face more electrical barriers ($R_{gap} = \infty$) that protect them from being slowed. However, when $D = 60\%$, some clusters can fall near the border of the tissue, shielding fast-pacing cells that are thus able to deliver higher rates.

An interesting role is played by the fibroblasts: being their resting potential more depolarized (around -50 mV) than the SAN *MDP*, they act as current

sources, speeding up the initial *DD* phase. However, they prolong the rest of the diastolic phase while simultaneously reducing the *OS* because of their sink action when the SAN membrane voltage overcomes their resting potential. Indeed, Figure 4.1 reports a *CL* prolongation with increasing fibroblasts densities, in accordance with experimental and computational data [61], [184], [190], [289]. Similarly, Figure B.3 shows a progressive *APA* reduction and an *APD* prolongation with diffused fibrosis, due to the fibroblasts' slow repolarization (Figure B.3). Thus, the overall effects of fibroblasts on heterogeneous isolated SAN tissue are bradycardia (for both *DD* and *APD* prolongation) and AP upstroke hampering, in accordance with simulations where 1 fibroblast was coupled to 1 SAN cell (Figure B.5). This would suggest that fibroblasts are detrimental to SAN ability to self-depolarize and electrically drive the atrium. However, these results do not rule out a protective action of the fibroblasts during early *DD* towards the hyperpolarization exerted by atrial tissue.

An additional results is that *CL* synchronization is reached in almost every condition, confirming the robustness of the SAN in delivering a rhythmic and stable depolarization even when the beating myocytes are only a fraction of the tissue, as was obtained in Chapter 3. However, this is not true in the presence of randomly-distributed unexcitable cells, where there is a high *CL* dispersion (Figure 4.1, central column). This may reflect the fact that the condition modelling a diffuse fatty, collagen or scar tissue represents a pathological condition in which SAN cell clusters are isolated with respect to each other, consequently failing to deliver a synchronized rate.

Finally, the bottom right panel of Figure 4.1 ($D = 60\%$ of clustered fibroblasts), suggests an additional sinus tachycardia mechanism. As exemplified by Figure B.4, when many clusters are present inside the tissue and SAN cells are not enough to drive the clusters cores to a full AP, these act as functional blocks. The electrical waves slowly propagate around them and break in many different wavelets, determining tachycardia. A similar process was shown to sustain re-entrant activity, determining AF in a 3D atrial model [255]. Because of a border effect in the model (see yellow dashed arrow in Figure B.4), SAN cells may be isolated enough from the rest of the tissue but connected enough to fibroblasts to receive substantial current in diastole, determining a marked increase in the tissue beating rate (155 vs. 76 bpm of the diffuse fibrosis configuration, +108% when $\sigma = 0.2$).

The present study includes several limitations. First of all, the sinoatrial node was modelled as a bi-dimensional single layer of cells, neglecting the complex anatomy of this cardiac structure [1], [60], [61]. Secondly, only the membrane clock parameters of SAN cells were randomized to obtain an heterogeneous model population. Thirdly, only one occurrence of both random and cluster distributions were investigated, limiting the generalizability of the results. Fourth, the fibrob-

last model adopted [255] was developed to model atrial and not sinoatrial node fibroblasts. Finally, atrial tissue was not taken into account. This is of uttermost importance since the presence of a large electrical load would deeply influence the physiological (and pathological) activity of the SAN. Furthermore, considering the SAN connection to atrial tissue would allow the investigation of the specific role of fibroblasts in protecting the SAN from hyperpolarization. Therefore, the next Chapter will present a 2D sinoatrial tissue model connected to the atrium.

4.5 Conclusions

The purpose of this Chapter was to elucidate the effects of the presence of different cellular phenotypes inside the sinoatrial node. In summary, the simulations highlight the robustness of the SAN with respect to substantial amounts of non-spontaneous myocytes in terms of *CL*, *APA* and *APD* changes. However, a combination of low cellular heterogeneity and high densities of dormant cells or clustered fibroblasts favour conditions in which functional blocks form inside the tissue, representing a possible mechanism of tachycardia onset.

Chapter 5

The Role of Sinoatrial Heterogeneity and Fibroblasts in Atrial Driving

Part of the content of this chapter is published in:

"Computational Investigation of Atrial Driving: How Sinoatrial Node Heterogeneity Affects the Heart Rate"
Eugenio Ricci[1], Chiara Bartolucci[1], Moreno Marolla [2], Stefano Severi[1]

[1] Department of Electrical, Electronic and Information Engineering "Guglielmo Marconi", University of Bologna, Cesena, Italy
[2] Department of Computer Science and Engineering, University of Bologna, Cesena, Italy

Computing in Cardiology 2023, Atlanta (GA), USA

and is currently under review for the special issue "The Architecture of the Human Sinus Node" in Frontiers in Physiology.

Abstract

Cardiac pacemaking remains an unsolved matter under many points of view. Extensive experimental and computational research has been performed to describe sinoatrial physiology across different scales, from the molecular to the clinical level. Nevertheless, how the heartbeat arises inside the sinoatrial node and propagates to the working myocardium is, at present, not fully understood.

This work aims at providing quantitative information about this fascinating phenomenon, especially regarding the contribution of cellular heterogeneity and fibrosis to sinoatrial node automaticity and atrial driving.

This is achieved by developing bi-dimensional computational models of rabbit and human right atrial tissue including the sinoatrial node. State-of-the-art knowledge of anatomical and physiological aspects was adopted during the design of the control tissue models. The novelty of this study is the presence of cellular heterogeneity and fibrosis inside the sinoatrial node to investigate how they tune the robustness of stimulus formation and conduction under different conditions (baseline, ionic current blocks, autonomic modulation, external high frequency pacing).

The simulations show that both heterogeneity and fibrosis significantly increase the safety factor for conduction by more than 10% in almost all the conditions tested and shorten the sinus node recovery time after overdrive suppression up to 60%. In the human model, especially in challenging conditions, fibrosis helps the heterogeneous myocytes to synchronize their rate (e.g., -82% in σ_{CL} under 25 nM acetylcholine administration) and to capture the atrium (with 25% L-type calcium current block). However, anatomical and gap junctional coupling aspects remain the most important model parameters to allow an effective atrial excitation.

In conclusion, despite the limitations of the models, this work suggests a quantitative explanation to the astonishing overall heterogeneity shown by the sinoatrial node.

5.1 Introduction

As outlined in Chapter 1, the mechanisms by which the sinoatrial node is able to excite the atrium, thus starting the cardiac cycle, are still incompletely understood. Starting from the study by Joyner and van Capelle [175], several computational works have investigated driving mechanisms in animal (mostly rabbit) models [174], [184], [186], [187], [190], [191]. As reported above, these explored the role of gradient and mosaic configurations, the presence of transitional phenotypes in the SAN periphery and the presence of specialized conduction pathways (Sections 1.4.3 and 1.4.4).

Specific to humans, Kharche and colleagues [187] used a detailed 3D anatomy combined with a simplified electrophysiological description to study the mechanisms of micro and macro-re-entry onset and how they were modulated by the SEPs. Cellular heterogeneity was considered phenomenologically as randomly distributed SAN cells having different *CL*s, while fibrosis (extracellular matrix deposition) was included as an unexcitable patch in the centre of the SAN. Zyantekorov et al. [206] investigated the effects of SEP width and gap junctional coupling in a 2D SAN-SEP-RA model. They found that 1) narrower SEPs provide stronger conduction and 2) an insulating border is necessary to allow a pace and drive behaviour. Li et al. [200] showed the importance of the sodium current I_{Na} in determining conduction to the atrium. SAN and SEP cells had different I_{Na}, I_{CaL}, I_f and I_{K1} maximal conductances and patchy fibrosis was considered in the context of heart failure simulations, again modeled as unexcitable, resistive barriers. Amsaleg and coauthors developed a 3D model of the SAN and adjacent atrium [191] and used it to extensively investigate combined configurations of the gradient and mosaic models as well as SEP features (number, length and width). The sensitivity analysis carried out on reduced models yielded a set of parameters that achieved atrial excitation and physiological activation sequences in the full-scale 3D model. Recently, Zhao and colleagues proposed an anatomically detailed 2D model based on histological sections [307]. The inclusion of heterogeneous properties (e.g. intrinsic rate and parasympathetic sensitivity) in different SAN compartments (head, center and tail) allowed the reproduction of important experimental observations such as shifts in the leading pacemaker location by autonomic stimulation or remodelling due to heart failure. While all these works provided lots of data and useful information about atrial excitation mechanisms, none of them took into consideration randomized electrophysiological properties or fibroblast-myocyte interactions, despite the influence that coupled non-excitable cells were shown to have on pacemaking activity [154].

Therefore, the behaviour of cellular heterogeneity and active fibroblasts – as modelled in the previous Chapters – is still unexplored with respect to atrial driv-

ing. Up to this point, this thesis focused on investigating their role in pacemaking, considering exclusively the SAN itself and neglecting its "boundary conditions". In this Chapter, the two aspects will be merged by developing bi-dimensional computational models of SAN-SEP-RA tissue featuring heterogeneity and fibrosis. State-of-the-art knowledge about the anatomy and physiology of the SAN will be implemented with the aim of gaining quantitative information about atrial driving mechanisms by the SAN but also on SAN modulation by the atrium in physiological and pathological conditions. The role of cellular heterogeneity – in the form of 1) presence of different cellular phenotypes (e.g., active fibroblasts) inside the SAN and 2) of different ionic electrophysiological properties among SAN cells – will be the core of this work. The previous chapters indeed highlighted a primary role for moderated levels of heterogeneity in SAN ionic properties in modulating the relative weights of membrane and Ca^{2+}-clocks (Chapter 2) and in granting pacemaking robustness in pathological conditions (Chapter 3).

The hypothesis here is that cellular heterogeneity increases the robustness of driving capability, in terms of safety factor for conduction and of a larger parameter space for which atrial excitation is achieved in physiological and pathological conditions. About fibrosis, if Chapter 4 showed that physiological amounts (40%) of fibroblast density in the SAN is compatible with its synchronization and rhythmical depolarization, the hypothesis investigated in this study is that its presence helps the SAN pacing the atrium. Therefore, we hypothesize that heterogeneity and fibrosis specifically contribute to 1) overcome hyperpolarization from the atrium, 2) provide a current source in case of ionic current blocks in the SAN and 3) protect the SAN from overdrive suppression in the case of high-frequency stimulation. The next section will illustrate the methodology adopted to investigate these phenomena.

5.2 Methods

The models used in this study were built starting from the knowledge and techniques acquired in the previous Chapters, in particular 3 and 4. Two different species were taken into account - rabbit and human – which required different parameter choices. Therefore, they will be presented separately.

5.2.1 Rabbit model

The rabbit model consisted of a square matrix of 200x200 cells, representing the discrete, simplified Kirchhoff network model framework [308]. The sinoatrial node is located at the center of the tissue and is modelled as an ellipse having semi-major and semi-minor axes of 75 and 11 cells, respectively. The SAN is

surrounded by an insulating border ($R_{gap} = \infty$MΩ) which prevents the interaction with atrial tissue if not for 5 specific exit pathways (SEPs). These are 10x10 cells in dimensions and uniquely include a SAN phenotype (Figure 5.1).

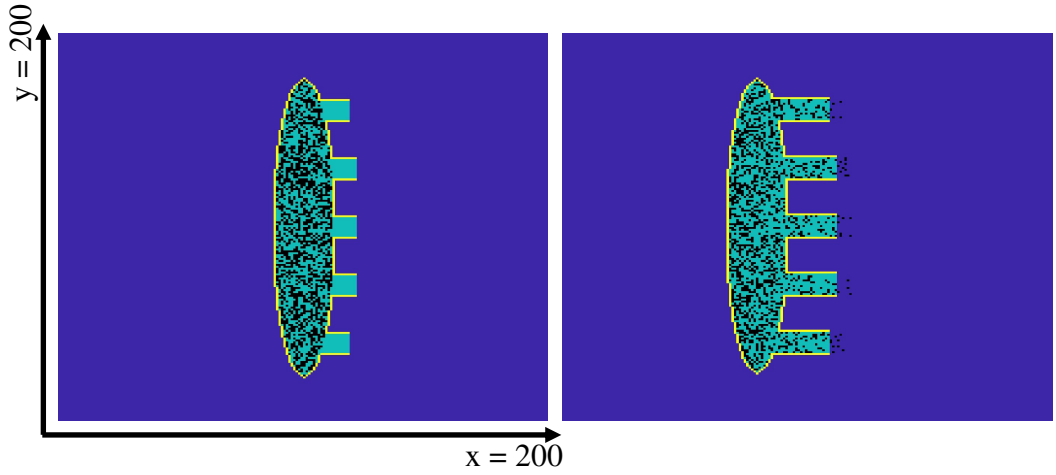

Figure 5.1: ***Geometry of the 2D SAN-SEP-RA model****, for rabbit (left) and human (right). The yellow contour line shows the insulating border, while dark blue indicates atrial tissue. SAN tissue is reported in green while fibroblasts are represented in black. Note that the latter fall uniquely inside the SAN ellipse for rabbit but can fall inside atrial tissue in the human model. SEPs have been numbered #1-5 from top to bottom.*

As single cell electrophysiological models, the SDiF one [24] was chosen for the SAN, the Lindblad et al. 1996 one [189] was used for the atrium and finally the active (human atrial) fibroblast model by Morgan and colleagues [255] was adopted to model fibroblasts. Indeed, certain simulations included the presence of 40% fibrosis in the SAN excluding the SEPs, by substituting SAN cells as done above (Chapter 4). In addition, SAN cellular heterogeneity was considered as previously done in Chapters 3 and 4. A value of 0.2 was used for the width σ of the log-normal distribution and the parameters P_{CaL}, P_{CaT}, g_{Kr}, K_{NaCa}, $i_{NaK,max}$, g_{Na}, g_{Ks}, g_f were randomized. Five different occurrences of both heterogeneous SAN properties and fibroblasts distribution were investigated to perform statistics and improve the generalizability of the results. No cellular heterogeneity or fibrosis was considered in the atrium.

Cellular coupling was achieved by 4-neighbours connectivity (left, top, right, bottom) with gap junctional resistance values of 10 MΩ in the atrium [309], [310] and 10 GΩ in the SAN and fibroblasts [34], [179], [186]. These values were chosen in order to: 1) obtain a physiological conduction velocity in the atrium (26.9 $cm\,s^{-1}$ vs. experimental values: 49.7±10.2 $cm\,s^{-1}$ [311], 51.7±5.0 $cm\,s^{-1}$ [312], 80±9 $cm\,s^{-1}$ for longitudinal and 49±10 $cm\,s^{-1}$ for transverse [313] or other computational works: 60 $cm\,s^{-1}$ and 20 $cm\,s^{-1}$ for longitudinal and trans-

verse velocity, respectively [310]); 2) allow frequency and phase synchronization inside the isolated uniform SAN. A sigmoidal gradient in gap junctional conductance was implemented, similar to [191]:

$$S = \frac{1}{R_{RA}} + (\frac{1}{R_{SAN}} - \frac{1}{R_{RA}}) \frac{1}{1 + e^{-\alpha x + \beta}}$$

where R_{RA} and R_{SAN} are the gap junctional resistances for atrial and SAN tissue, $\alpha = 0.5$ and $\beta = 60$ in order to have the half maximal value in the middle of the SEPs. This configuration was dubbed low-coupling (*lc*) in the following. SAN cells did not show a dependence of the ionic properties with respect to space.

Simulations were run starting from 500 s single cell steady-state conditions and lasted 20 s. The last 2 s were saved and analyzed. To simulate arrhythmia, and investigate the response of the SAN, a high-frequency (5 Hz) pacing protocol was performed. A 5x5 cell cluster of atrial cells in the top-right corner of the tissue was stimulated with 2 nA for 1 ms from second 6 to second 16, then the pacing was stopped. In this case, the last 5 s of the simulations were exported and analysed.

To investigate the robustness of atrial driving with respect to loss of ionic currents, I_{CaL} and I_f blocks were tested. These were obtained by reducing the maximal permeability P_{CaL} and maximal conductance g_f of 25% and 50%, respectively.

To explore the model parameter space, coupling values of 5 and 2 MΩ for the atrium and a slope factor of 10 for the sigmoidal gradient (which results in SAN central R_{gap} values of 40 MΩ) were investigated. The latter value was chosen since it allowed phase synchronization on top of frequency synchronization inside the SAN when cellular heterogeneity is considered. This gradient configuration was dubbed high-coupling (*hc*) in the following.

Finally, the number of SEPs was varied between 1 and 7 in the absence of heterogeneity and fibrosis.

5.2.2 Human model

Geometry and electrophysiological models

The human model geometry is based on the rabbit model one. However, to better reproduce experimental data on the human SAN, some modifications were performed. About SAN dimensions [60], [61], the semi-minor axis of the ellipse was enlarged to 12 cells and the SEPs were prolonged to reach a dimension of 20×11 cells (Figure 5.1). Considering the FWS model cell length (67 µm [25]), this corresponds to 1.34 mm, a value compatible with experimental reports [61] and with previous computational investigations [191]. Besides the FWS model, we adopted

the Koivumäki et al. 2011 model [20] for atrial cells (dubbed "K model" in the following) and the Morgan 2016 [255] for fibroblasts. In addition, the behaviour of the Mazhar, Bartolucci and Severi ("MBS") atrial model [27] recently developed in our group was tested. In this work, the latter was simplified by removing the equations describing the mechano-electric feedback and calmodulin-kinase II activity, reducing it to 29 ordinary differential equations for the description of the atrial AP.

Heterogeneity and fibrosis

Instead of a fixed amount of fibrosis in the SAN as done above for rabbit, in the human model a linear gradient in fibroblast density was implemented, from the left part of the SAN to atrial tissue. In particular, central SAN saw a 45.7% presence of fibroblasts [314]–[317] substituting SAN cells. The gradient allowed the SEP to have lower fibroblast densities than the central SAN, as recently reported (45.7±10.9 vs. 27.7±16.3% [317]). The probability that a fibroblast would substitute a SAN cell depended on the gradient and on a random number extracted between 0 and 100 from a uniform distribution. If the sum of these two terms exceeded 50, then the SAN cell was replaced with a fibroblast. The linear gradient fell to zero 10 cells to the right of the SEPs' exit and fibroblasts were allowed to replace atrial cells in these areas. However, the rest of atrial tissue was considered to be completely free of fibrosis. Concerning cellular heterogeneity, in addition to the parameters randomized in the SDiF model, the maximal conductance of the potassium transient outward current and ultra-rapid delayed rectifier, and the maximal uptake rate of the SERCA pump (g_{to}, g_{Kur}, $P_{up,basal}$) were also randomized. Again, no heterogeneity was considered in the atrium. To improve the generalizability of the results of each set-up, 5 models (dubbed tissue #1-5 in the following) with different distributions of heterogeneity, fibroblasts or both, were generated by using 5 different random seeds for sampling the log-normal and uniform distributions.

Gap-junctional coupling

Coupling resistance values of 1 GΩ [298], [309] and 3 GΩ [184], [190], [252] were chosen for SAN cells and fibroblasts, according to experimental measures and previous computational works (see also Section 3.4.2). In the atrium, R_{gap} was set to 1 MΩ to allow conduction velocities of 70 $cm\,s^{-1}$ [211], [318], [319]. However, we doubled g_{Na} [191] (the maximal conductance of the fast sodium current) in the Koivumäki model in all atrial tissue to achieve conduction velocities of 100 $cm\,s^{-1}$, typical of crista terminalis tissue [191], [320]. In addition, a sigmoidal gradient in coupling conductivity was again implemented, but this time it

was necessary to spread it outside of the SEPs in the atrium with a semicircular shape [191] to achieve driving (Figure 5.2). If the change in conductivity was confined in the SAN and SEPs, no parameter configuration (R_{gap} in SAN and atrium, α and β of the sigmoidal gradient) allowed the atrium to be excited.

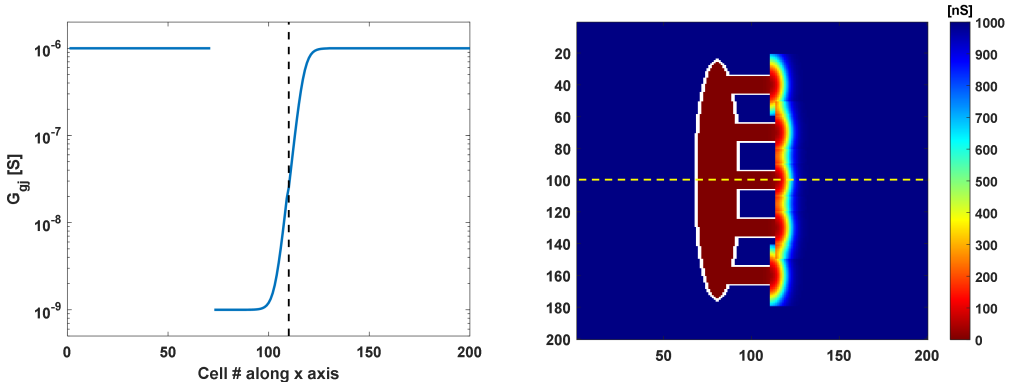

Figure 5.2: ***Coupling conductance profiles of the 2D SAN-SEP-RA model****. (Left) Sigmoidal gradient in gap junctional conductance along the central SEP (yellow dashed line in right panel). The vertical dashed black line indicates the interface between the SEP and the atrium. (Right) Gap junctional conductance values visualized in the tissue. Bidimensional gradients with circular shape were implemented in the atrium around the SEPs to allow stimulus propagation in the crista terminalis.*

Simulation protocols

Simulations were run starting from 500 s single cell steady-state conditions and lasted 50 s. The last 5 s were saved and analyzed. To simulate atrial tachicardia, and investigate the response to overdrive suppression of the SAN, a high-frequency pacing protocol was performed to overdrive suppress the SAN [200]. A 15x15 cell cluster of atrial cells in the top-right corner of the tissue was stimulated at 2 Hz with a current of 5 nA for 1 ms from second 32 to second 42, then the pacing was stopped. In this case, the last 10 s of the simulations were exported in order to compute the sinus node recovery time (*SNRT*) and the *CL*. To asses the effects of autonomic control over atrial driving capability, and to test SAN responses to challenging conditions, the effects of 25 nM acetylcholine (ACh) and 1 µM isoproterenol (ISO) continuous infusion were assessed in both baseline and stimulated conditions. Moreover, 50% and 25% blocks in I_f and I_{CaL} of SAN cells were tested to investigate the robustness of atrial propagation with respect to loss of key diastolic and action potential ionic currents, respectively. Finally, additional SEP widths of 7, 15 and 19 cells were investigated, similar to what was done for rabbit.

For clarity, we define for both rabbit and human "U" as the uniform condition (no heterogeneity or fibrosis), "H" as the condition with SAN heterogeneity, "UF" as the condition with fibrosis but no heterogeneity and "HF" as the condition in which both SAN heterogeneity and fibrosis are included.

5.2.3 Analysis

Cycle lengths (*CL*) were computed as the time difference between two consecutive maximum points of the first derivative of the membrane voltage for the atrium or two consecutive overshoots for the SAN, as the two methods proved more robust in the two cases. For the SAN, the last *CL* value was averaged between cells to inform on SAN synchronization at the end of the simulation. For the atrium, the *CL*s were first averaged in time and then between cells. The safety factor for conduction (*SF*) was computed as the ratio between the net charge received by the neighbouring cells and the charge required to obtain a full upstroke in single-cell simulations, as done in [321]:

$$SF = \frac{C_m \Delta V_m - Q_{ion} - Q_{stim}}{Q_{thr}} = \frac{Q_{gap}}{Q_{thr}}$$

where Q_{gap} is computed as

$$Q_{gap} = \int_{t_a} I_{gap}\, dt$$

Here, I_{gap} is the net current exchanged with neighbours (a negative current to the cell is considered to be depolarizing) and t_a is the time interval over which I_{gap} is negative, computed from the time instant in which I_{gap} is 1% of its negative peak to when I_{gap} changes sign). For simplicity, in the rabbit model Q_{thr} was not considered to depend on the stimulus duration as in [321], but was fixed to the value obtained with a 2 ms stimulus for the Lindblad model. For the human one, the computation was refined and Q_{thr} was made stimulus-dependent. However, owing to the fact that atrial cells could be stimulated by SAN cells very slowly, the linear dependence of Q_{thr} with respect to t_a was saturated at 4 ms. In that condition indeed, a non-negligible charge used for depolarization would fall below the 1% I_{gap} threshold and thus Q_{net} would result smaller than Q_{thr} despite the cell reaching the threshold for AP firing. The SF values were computed only for the cells at the leading SEP interface, averaged and compared across different conditions, since Li et al. [200] showed that in that point the lowest *SF* values are obtained. If the SAN excited the atrium across all SEPs (as it happened in the absence of cellular heterogeneity and fibrosis), the values were averaged between all SEPs.

In externally paced model tissues, the sinus node recovery time (*SNRT*) was computed as the time difference between the first atrial action potential occurring after the last stimulus and the time instant of the last stimulus [200], [212].

In order to allow comparisons with clinical-level and experimental data, and to improve the multiscale framework developed in this thesis work, simulated electrograms (EGMs) were obtained for the human simulations. These were computed as previously done in 2D in our group [322] according to Shillieto et al. [323]:

$$EGM_{unipolar} = \sum_i \frac{0.5D_x \frac{\partial^2 V_{mi}}{\partial x^2} + 0.5D_y \frac{\partial^2 V_{mi}}{\partial y^2}}{\sqrt{d_i^2 + z_0^2}}$$

where D_x and D_y are the diffusion coefficients along x and y; V_{mi} is the membrane potential for each cell i; d_i is the euclidean distance of each cell from the electrode and z_0 is the distance of the electrode from the tissue along the z axis. A 7-french bipolar sensing catheter with 3.5 mm tip and 2-5-2 mm inter-electrode distances, as used in [212], was implemented. Considering a 100 µm cell length for the Koivumäki model, this converted to 20-50-20 cell distances in the discrete model (Figure 5.3).

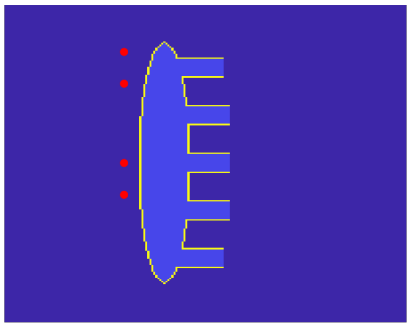

Figure 5.3: ***EGM catheter position inside the tissue model.*** *The red dots indicate the single electrode positions with the 2-5-2 mm spacing, numbered #1-4 from top to bottom.*

Activation time maps were built by color-coding the time difference in the occurrence of the peak of the membrane voltage first derivative. The atrial cells at the SEP frontiers which first showed an AP were taken as zero-reference.

Statistical differences in the *CL*, *SF* or *SNRT* obtained with the different set-ups (H, UF and HF, n = 5) were assessed via one-sample or paired t-tests or via one-sample t-tests when comparing them with the U set-up (n = 1). All the statistical analyses were performed in Matlab R2019b using built-in functions and P-values of 0.05 or lower were deemed significant. The statistics were performed to

quantify the consistency of the results across the different set-ups (U, H, UF, HF) and experimental conditions (ACh, ISO, external pacing and ion current blocks) but significance was not inferred to be physiologically relevant given its dependence on the model parameters.

5.2.4 Simulation code

The simulation was initially developed as a C++ implementation of a fixed-step Euler integration algorithm. However, the serial program proved to be too slow and therefore we modified the implementation to make use of GPU parallelism to speed up the critical part, i.e., the state variables update. This is possible because the state variables update for each cell at each time step is an "embarrassingly parallel" problem for which GPU architecture is well suited. Input files specifying 1) the simulation parameters (e.g., duration), 2) the geometry (position of cells inside the tissue), 3) the randomized conductances and 4) the gap junctional conductance values (4 for each cells) are generated in Matlab as .txt files and given in input to the CUDA/C code. Zero-flux boundary condition are applied. Table 5.1 reports the pseudo-code for the C functions and CUDA kernels.

Table 5.1: ***CUDA/C pseudo code for the SAN-SEP-RA tissue model.*** *Operations performed on the GPU are expressed in italic.*

function 2D tissue main
1 Load initial conditions
2 Load input files
3 Allocate output files (t, V_m)
4 Copy data from host to device
5 cudaCheckError();
6 **for i = 0:sim_steps**
7 *Update state variables*
8 *Compute gap junctional current*
9 *Update membrane potential*
10 cudaCheckError();
11 Copy data from device to host
12 cudaCheckError();
13 Save undersampled time step on disk
14 **end for**
15 Free memory
end

The resultant CUDA/C program running on a Linux workstation with a 12 GB Nvidia Titan V GPU with 5120 cores is ∼150 times faster (∼20 minutes vs. >2 days) than the equivalent serial program running on an AMD Rhyzen Threadripper 2950x CPU at 3.5 GHz. A time step of 5 µs was adopted and data were undersampled at 0.2 ms. Smaller time steps (1 µs) did not provide different results.

5.3 Results

5.3.1 Rabbit model

The simulations with the rabbit model show that atrial driving can be achieved in different conditions: in the *lc* uniform and in the *hc* (both uniform and with heterogeneity) ones, the atrium is excited by all the 5 SEPs at the same time. In the heterogeneous *lc* configuration or in presence of fibrosis, specific SEPs become dominant depending on the leading pacemaker sites location (Figure 5.4). Phase synchronization is not achieved throughout the SAN and even frequency synchronization is not complete due to the formation of cell clusters with slightly different cycle lengths (e.g., $CL = 341 \pm 9.1$ and 341 ± 13.9 ms for the H and HF simulations in middle and right panels of Figure 5.4, see Figure C.1 for the *CL* distributions). Simulations including fibrosis intriguingly show larger standard deviations of SAN *CLs*.

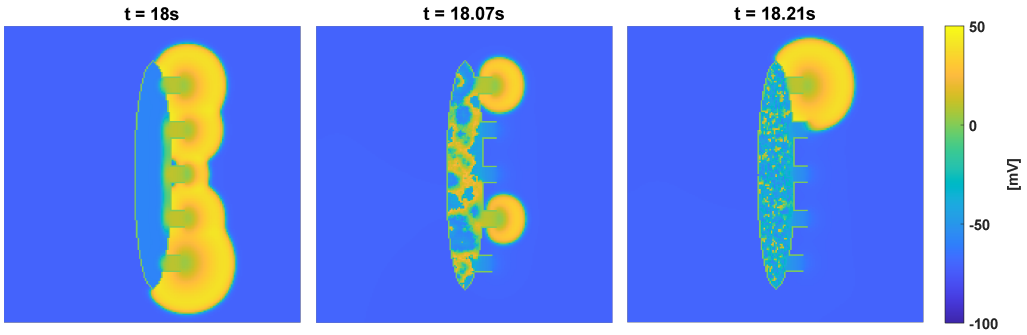

Figure 5.4: ***Voltage maps showing atrial driving by the SAN in lc conditions****. Left: uniform; middle: SAN heterogeneity; right: SAN heterogeneity and fibrosis conditions.*

Figure 5.5 reports the results of the *CL* and *SF* computations. As it can be seen, the presence of inter-cellular heterogeneity in the *lc* condition significantly affects the average *CL* (339 ± 2.5 vs. 355 ms, $p = 0.00013$) and the robustness of atrial driving ($SF = 2.94 \pm 0.13$ vs. 2.77, $p = 0.043$). The latter effect is also the

case in the *hc* condition (*SF* = 2.34±0.02 vs. 2.29, p = 0.0062). Interestingly, fibrosis on one hand prevents atrial propagation in the *hc* condition, but at the same time increases the *SF* in the *lc* one (*SF* = 2.94±0.06 vs. 2.77, p = 0.0037). However, the combination of inter-cellular heterogeneity and fibrosis did not result in a significant change of average *CL* or *SF* due to the large variability in the results.

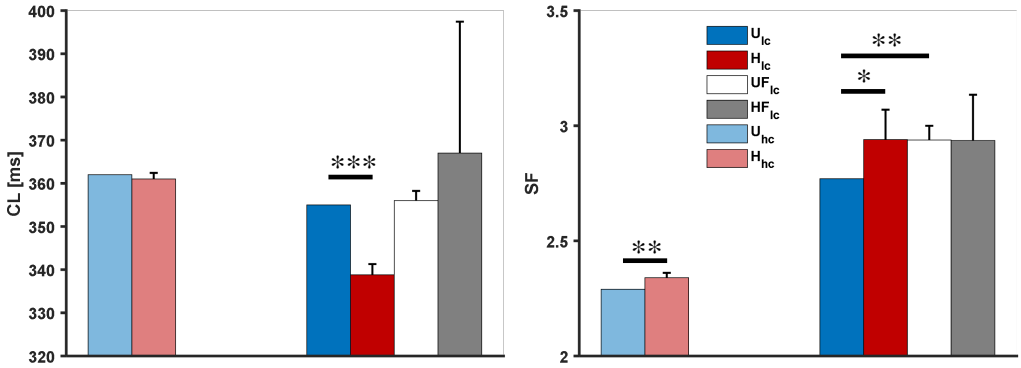

Figure 5.5: ***Cycle lengths and safety factor results for the rabbit model in different conditions****: U (uniform tissue), H (SAN heterogeneity), UF (uniform tissue with 40% fibrosis) and HF (SAN heterogeneity with 40% fibrosis) in the low-coupling (lc) and high-coupling (hc) SAN configurations. No beating is obtained in the* UF_{hc} *and* HF_{hc} *conditions. *p<0.05, **p<0.01, ***p<0.001.*

Simulations with high-frequency stimulation in the atrium show suppression of spontaneous activity in the SAN in all conditions. However, when the stimulation is stopped, the *lc* and *hc* conditions show different behaviours: the latter is affected by re-entrant activity through the SEPs which tends to last less when heterogeneity is considered (Figure 5.6, 1.45±0.61 vs. 1.89 s, p = 0.18). The *lc* condition does not show re-entry onset at all.

The results of simulations with ionic current blocks show that, while the *hc* condition is more robust with respect to 25% I_{CaL} block (since atrial driving is not achieved with the *lc* one), in the *lc* configuration the presence of heterogeneity seems to be protecting the SAN from bradycardia when a 50% I_f block is tested (Table 5.2).

Finally, the number of SEPs (1-7) in the uniform *lc* configuration does not seem to affect the average *CL* or the *SF* at all, while it slightly modulates both in the *hc* one (*CL* = 356 ms and *SF* = 2.19 with 1 SEPs vs. *CL* = 366 ms and *SF* = 2.31 with 7 SEPs).

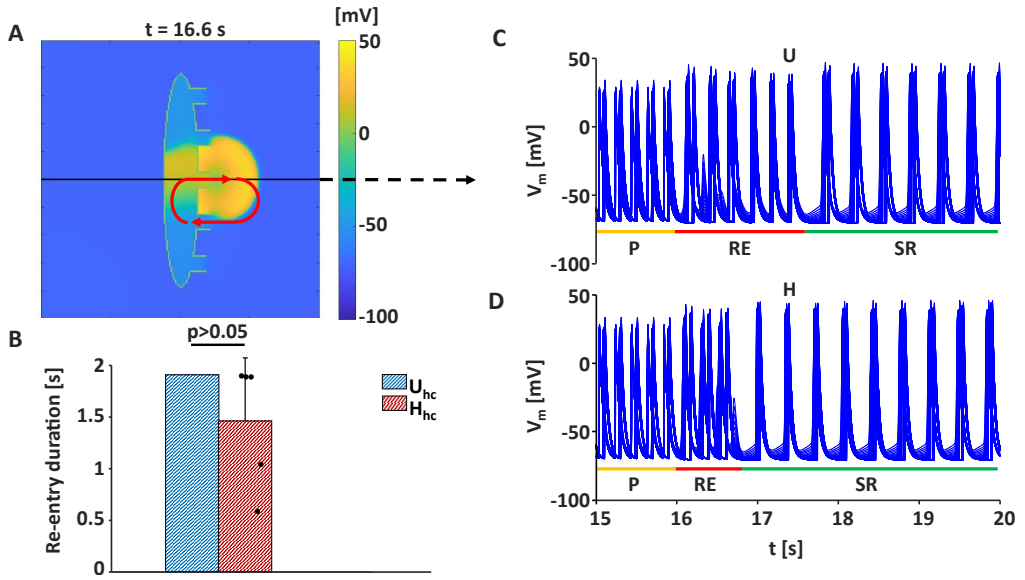

Figure 5.6: ***Re-entrant circuit formation after high-frequency stimulation in the rabbit hc model****. A) Voltage map showing the mechanism for re-entry: the stimulus exits from the central SEP and enters back from SEP #4, as highlighted by the red arrows. Uniform high-coupling condition (U_{hc}). B) Comparison of re-entry durations without (U_{hc}) and with SAN heterogeneity (H_{hc}, n = 5). No re-entry was seen in the lc condition with or without the addition of heterogeneity and/or fibrosis, while in the hc condition the presence of fibrosis prevented beating. C) and D) Action potential traces along the black line in panel A in the U_{hc} condition and in the H_{hc} one (showing shorter re-entry duration), respectively. P: paced, RE: re-entry, SR: sinus rhythm*

5.3.2 Human model

Control conditions

In first place, the behaviour of the model in control conditions was tested to explore the role of heterogeneity and fibrosis in the absence of extrinsic modifications. Figure 5.7 shows the *CL* and *SF* results of the human tissue model: the presence of fibrosis (UF condition) significantly prolongs the average atrial *CL* compared to the uniform condition (817±1 ms vs. 814 ms, p = 0.005), despite the little influence that different spatial distribution of fibroblast have on the *CL*. Notably however, the random fibroblasts distributions determine a negligible atrial σ_{CL}, while different cellular heterogeneity instances produce widely variable *CL*s (817±181 ms). The combination of heterogeneity and fibrosis determines a marked reduction of the *CL* (666±55 ms) compared to the uniform tissue and to the presence of fibrosis alone (p = 0.004 and p = 0.003), but also show a

Table 5.2: ***Rabbit model sensitivity on gap junctional coupling and current blocks.*** *Different random heterogeneity distributions (n = 5) were used for R_{gap} = 10 MΩ (mean±std); for every other condition only 1 distribution was tested. hc, high-coupling; lc low-coupling conditions.*

			Uniform	***SAN heterogeneity***
hc	*R_{gap} in atrium*	10 MΩ	CL = 362 ms	CL = 361±1.4 ms
		5 MΩ	No driving	CL = 375 ms
		2 MΩ	No driving	No driving
	Blocks	25% I_{CaL}	CL = 381 ms	CL = 376 ms
		50% I_f	CL = 424 ms	CL = 420 ms
lc	*R_{gap} in atrium*	10 MΩ	CL = 355 ms	CL = 339±2.5 ms
		5 MΩ	No driving	No driving
		2 MΩ	No driving	No driving
	Blocks	25% I_{CaL}	No driving	No driving
		50% I_f	CL = 410 ms	CL = 387 ms

lower *CL* variability than heterogeneity alone. The huge variability seen in presence of heterogeneity (see Figure C.2A for the standard deviations of the *CL*s, σ_{CL}) is due to the fact that exit blocks occur in the SEPs, with consequent alternation in the leading SEP and delay in atrial activation. The presence of fibrosis completely abolished this phenomenon, allowing atrial tissue to be paced at a constant steady-state rate ($\sigma_{CL} = 0$, Figure C.2A). This can be ascribed to two main reasons. Firstly, opposite to the rabbit model, fibrosis in the human SAN helps the myocytes to achieve better CL synchronization (lower σ_{CL} in the SAN), by blunting the intrinsic rate differences among cells given by cellular heterogeneity (Figure C.2A). Secondly, fibroblasts act on the pace and drive ability of the SAN by increasing the *SF* with respect to a uniform tissue condition (1.62±0.02 vs. 1.45, $p = 2 \cdot 10^{-5}$). Figure 5.7 also shows that heterogeneity by itself significantly increases the *SF* (1.58±0.06 vs. 1.45, p = 0.009) but its combination with fibrosis provides a raise in the *SF* slightly higher than heterogeneity alone (1.60±0.05, p = 0.002 vs. uniform; p > 0.05 vs. fibrosis), even if lower than fibrosis alone (not significant).

Overdrive suppression of the SAN

Next, we sought to investigate the ability of the SAN model to recover from external high frequency pacing. Stimuli were delivered at 2 Hz, to allow comparisons with experiments [200], [212] Excitation of atrial tissue at this rate resulted in overdrive suppression of the SAN, with all paced stimuli entering the SAN from all of the 5 SEPs. After the pacing was stopped, the tissue showed *CL*s and σ_{CL}

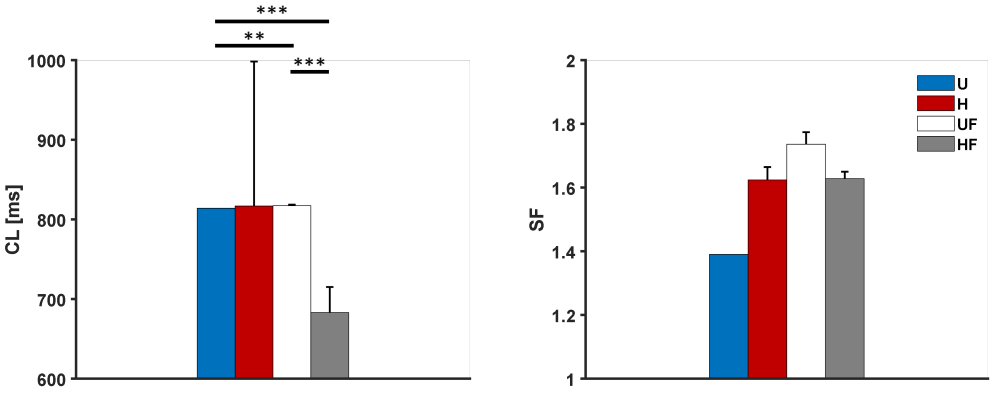

Figure 5.7: ***Cycle lengths and safety factor results for the human model in different conditions****: U (uniform tissue), H (SAN heterogeneity), UF (uniform tissue with fibrosis) and HF (SAN heterogeneity and fibrosis). *p<0.05, **p<0.01, ***p<0.001.*

similar to the control condition (Figure 5.8), if not for the HF condition showing tachycardia (*CL* = 588±51 ms) compared to the uniform (815 ms, $p = 6 \cdot 10^{-4}$), heterogeneous (820±218, $p \geq 0.05$) and fibrosis (813±1 ms, $p = 7 \cdot 10^{-4}$) simulations. Due to its very small standard deviation, the UF set-up resulted significantly shorter than the U one (p = 0.009), opposite to the control condition where it was slightly longer. The right panel shows instead the *SNRT* values after pacing, with the heterogeneity condition showing a slightly lower – even if significant – value than the uniform set-up (1047±18 ms vs. 1102, p = 0.002). However, in these conditions the first recovered beat originates from the SEPs and then re-entry circuits with complex patterns (e.g., 2:1 exit block in the SEPs) are formed. These, together with the fact that the *CL*s have not yet reached a steady state value after pacing, explains the obtained *CL* dispersion (Figure 5.8 and C.2B). Exit blocks do not happen in the UF UF (124±9 ms, p = 0.005 vs. U and $p = 9 \cdot 10^{-4}$ vs. H) and HF conditions (1009±164 ms, $p > 0.05$ with respect to any condition), but all 5 tissues show re-entrant activity in both cases. Tissue #1 shows a shorter *SNRT* (718 ms) since the last paced beat determines a stable re-entry across 2 contiguous SEPs. This explains the lower average *SNRT* value and the increased standard deviation of the HF set-up.

Acetylcholine administration

To study the effects of parasympathetic stimulation on the model, we simulated the administration of 25 nM ACh to the SAN. The results in Figure 5.9 show a profound bradycardia in both the uniform (1448 ms vs. 814 ms without ACh, +78% as in single cells), heterogeneous (1489±287 ms vs. 817±181 ms, p =

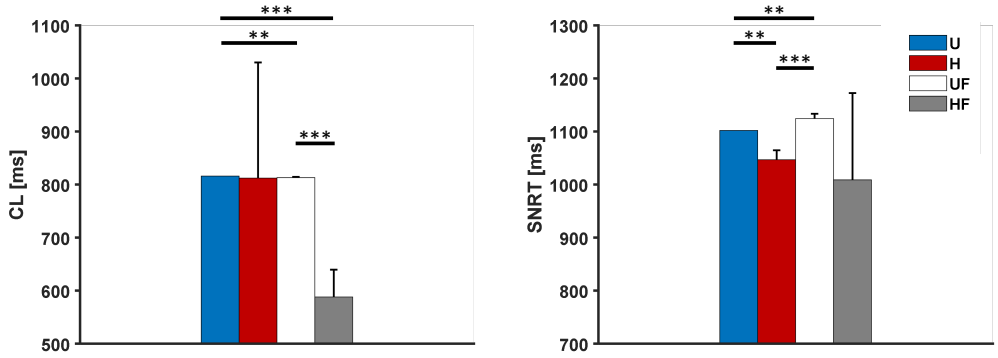

Figure 5.8: ***Cycle lengths and sinus node recovery time results for the human model after pacing in different conditions****: U (uniform tissue), H (SAN heterogeneity) and HF (SAN heterogeneity and fibrosis). *p<0.05, **p<0.01, ***p<0.001.*

0.02) and fibroblasts (1277±197 ms vs. 817±1 ms, p = 0.006) conditions. The combination of heterogeneity and fibroblasts provides *CL*s closer to physiological resting values (991±76 ms, equal to an average rate of 61 bpm; p = 0.01 vs. H and $p = 2 \cdot 10^{-4}$ vs. U conditions). However, this is still much longer than the control conditions (666±55 ms, $p = 4 \cdot 10^{-4}$). Also in this case heterogeneity and fibrosis provide strength to atrial driving (*SF* = 1.60±0.05, 1.76±0.08 and 1.54±0.09 for the H and HF conditions vs. 1.44 of the uniform one, p = 0.002, $p = 9 \cdot 10^{-4}$ and p > 0.05) even if the HF set-up did not provide significantly higher values, as obtained in control condition. Here, atrial σ_{CL} in the H condition is still high due to the occurrence of exit blocks and leading SEP alternation (Figure C.2C).

Overdrive suppression of the SAN with acetylcholine administration

Then, we tested challenging conditions in which the SAN underwent simultaneous 25 nM infusion and external 2 Hz pacing, as was done in *ex-vivo* human hearts [200], [212]. In these settings, the cycle lengths show values of 2102 ms, 1333±152 ms, 1169±71 ms and 952±176 ms in the U, H, UF and HF conditions ($p = 3 \cdot 10^{-4}$ for H vs. U; $p = 8 \cdot 10^{-6}$ for UF vs. U; $p = 1 \cdot 10^{-4}$ for HF vs. U; p = 0.02 for HF vs. H). The SAN was once again completely suppressed from the depolarizations travelling through all SEPs. Concerning the *SNRT*, Figure 5.10 interestingly shows that the H, UF and HF set-ups determine a significantly faster recovery of pacemaking: 1923±325 ms for the heterogeneous tissue, 1440±269 ms with fibroblasts and 1206±141 ms in presence of heterogeneity and fibrosis vs. 3020 ms of the uniform model (p = 0.002, $p = 2 \cdot 10^{-4}$ and $p = 2 \cdot 10^{-5}$, respectively). The decrease in *SNRT* given by the addition of fibroblasts in the tissue resulted significant also with respect to the presence of cellular heterogeneity

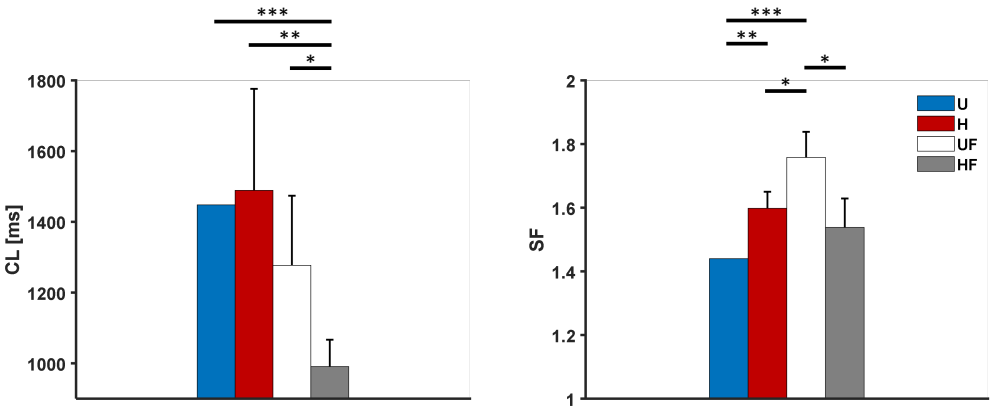

Figure 5.9: ***Cycle lengths and safety factor results for the human model with 25 nM acetylcholine administration in different conditions****: U (uniform tissue), H (SAN heterogeneity) and HF (SAN heterogeneity and fibrosis). *p<0.05, **p<0.01, ***p<0.001.*

alone (UF vs. H: p = 0.03, HF vs. H: p = 0.01). Compared to results without ACh administration, the uniform condition sees a *SNRT* prolongation of $+174\%$. In this condition, SAN depolarization originates in the middle of the SEPs as before but no re-entry is established even though 2:1 exit blocks occur for the first two beats (Figure C.4, $\sigma_{CL} = 950$ ms). In presence of heterogeneity, re-entrant circuits are formed in all tissues, but the administration of ACh increases the number of exit blocks after the cessation of pacing. Being the *CL* longer, there are clusters of spontaneous cells that fire APs before the arrival of the re-entrant stimulus, which then merge with it at the entrance of the leading SEP. This happens in the presence of fibroblasts as well, but only model #3 of the HF conditions shows exit blocks from the SEPs. Figure C.2D shows indeed a really high atrial σ_{CL} in the H condition, while it is substantially lower for the UF condition and almost zero for the HF one. Again, this suggests that fibrosis helps the SEPs in capturing the atrium (Figure C.4).

Isoproterenol administration

After the experiments with ACh infusion, we evaluated the model responses to sympathetic stimulation. In this case, given the on/off behaviour of the FWS model with respect to adrenergic activation (calibrated to 1 µM release), it was not possible to use other concentrations, as found in experiments (e.g., 1 nM [200]. We consequently simulated the infusion of 1 µM ISO, which shortens the *CL* in all conditions with respect to control: U = -21% (639 vs. 814 ms), H = -30% (531±13 ms vs. 764±183 ms, p = 0.04), UF = -19% (663±2 ms vs. 817±1 ms,

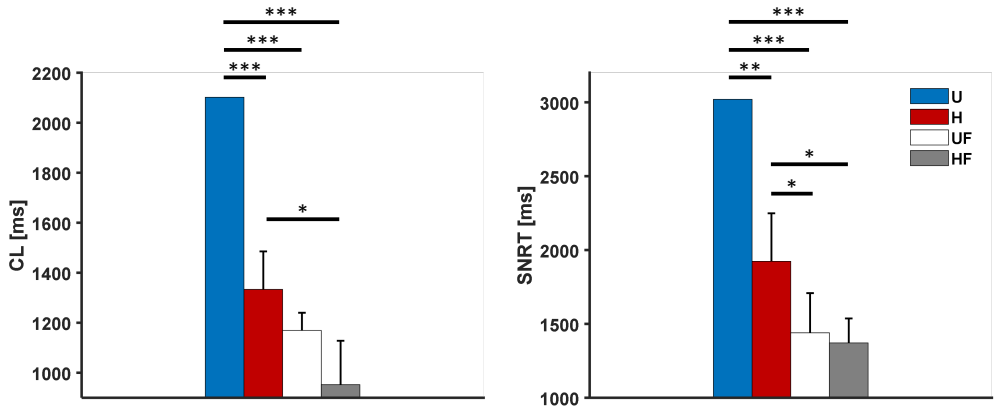

Figure 5.10: ***Cycle lengths and sinus node recovery time results for the human model with 25 nM acetylcholine administration after pacing in different conditions****: U (uniform tissue), H (SAN heterogeneity) and HF (SAN heterogeneity and fibrosis). *p<0.05, **p<0.01, ***p<0.001.*

p $<1 \cdot 10^{-5}$) and HF = -18% (548±16 ms vs. 665±55 ms, p = 0.009). Now the H condition does not show any exit block, with a consequent reduced *CL* and *CL* variability (Figure 5.11 and C.2E). This is due to the remarkable increase (>20%) in the *SF* in both H and HF conditions compared to the uniform one (1.88±0.08 and 1.86±0.08 vs. 1.53, p = $5 \cdot 10^{-4}$ and p = $7 \cdot 10^{-4}$). The UF set-up showed a milder *SF* increase to 1.63±0.07, but still showed no exit blocks.

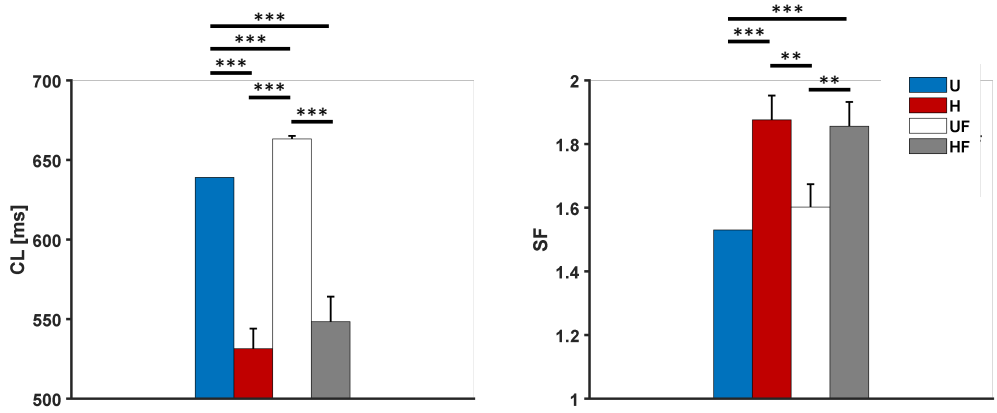

Figure 5.11: ***Cycle lengths and safety factor results results for the human model with 1 µM isoproterenol administration in different conditions****: U (uniform tissue), H (SAN heterogeneity) and HF (SAN heterogeneity and fibrosis). *p<0.05, **p<0.01, ***p<0.001.*

Overdrive suppression of the SAN with isoproterenol administration

Then we added external 2 Hz pacing to 1 µM ISO infusion. The models show average *CL* values similar to the unpaced condition (Figure 5.12). Despite the *SNRT* in the U condition being shorter than without ISO (841 ms vs. 1102 ms, -24%), the H and HF ones provide an even faster recovery (*SNRT* = 775±18 ms and 790±31 ms, respectively p = 0.001 and p = 0.02 vs. U) also compared to their control values ($p = 4 \cdot 10^{-6}$ and p = 0.047). The UF condition shows the longest *SNRTs* values (862±4 ms; $p = 3 \cdot 10^{-4}$ vs. U, $p = 6 \cdot 10^{-6}$ vs. H, $p = 8 \cdot 10^{-6}$ vs HF), but these are nevertheless still shorter than without ISO ($p = 2 \cdot 10^{-7}$).

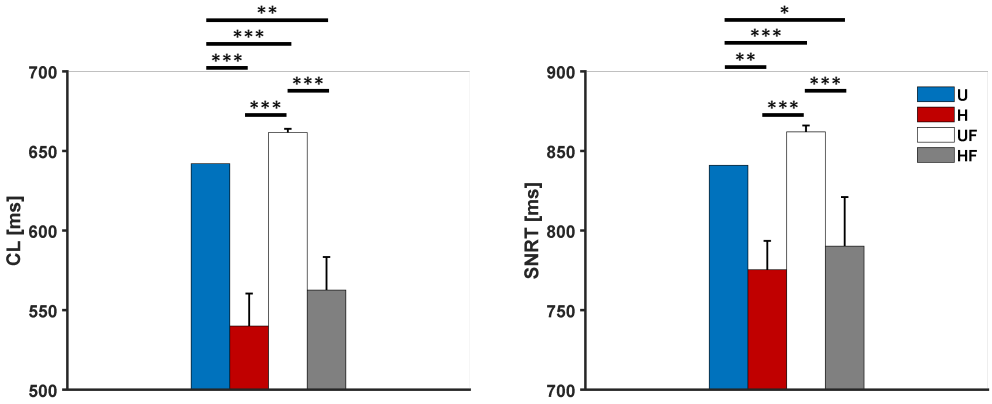

Figure 5.12: ***Cycle lengths and sinus node recovery time results for the human model with 1 µM isoproterenol administration after pacing in different conditions****: U (uniform tissue), H (SAN heterogeneity) and HF (SAN heterogeneity and fibrosis). *p<0.05, **p<0.01, ***p<0.001.*

Funny current block in the SAN

To check if the model was robust with respect to the loss of depolarizing current in diastole, and if heterogeneity and fibrosis contributed to its strength, the funny current I_f is blocked by 50% in the SAN (Figure 5.13). As a consequence, a 12% *CL* prolongation is obtained in the uniform tissue compared to the control tissue (912 ms vs. 814 ms), just as in single cell simulations of the FWS model (not shown). A similar value is obtained in the HF case (average +10.7%, 745±27 ms vs. 665±55 ms with no block, p = 0.021); however, a counter-intuitive average *CL* shortening is achieved in the H condition (−3%, 741±25 ms vs. 817±181 ms, $p \geq 0.05$). This is actually explained by the presence of exit blocks in the control H conditions which determine a longer average *CL* in the atrium despite the fact that, inside the SAN, the CL is longer with I_f block, as expected (741±25 ms vs.

662±26 ms). Both conditions show lower *CL*s ((741±25 ms and 745±27 ms vs. 912 ms, p = $1 \cdot 10^{-4}$ and p = $2 \cdot 10^{-4}$ respectively) and higher *SF*s compared to the uniform SAN case (1.62±0.04 and 1.63±0.02 vs. 1.39, p = $2 \cdot 10^{-4}$ and p = $2 \cdot 10^{-5}$). With the UF set-up, only 3 tissues achieved atrial driving. These show *CL*s similar to the U case (907±2 ms, p = 0.01 vs. U and +11% prolongation compared to control) but with slightly higher *SF*s (1.58±0.13, p > 0.05).

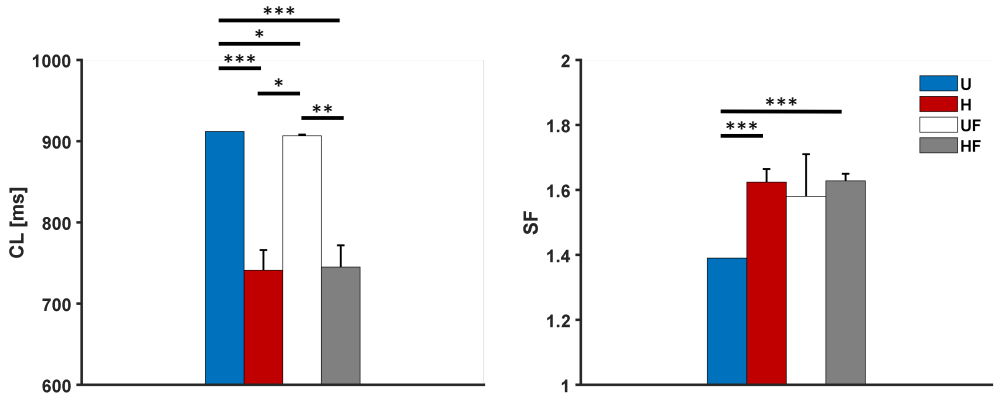

Figure 5.13: ***Cycle lengths and safety factor results for the human model with 50% funny current block in different conditions****: U (uniform tissue), H (SAN heterogeneity) and HF (SAN heterogeneity and fibrosis). *p<0.05, **p<0.01, ***p<0.001.*

L-type calcium current block in the SAN

Similar to I_f block, we also simulated a 25% reduction in I_{CaL} to assess the tissue robustness during the upstroke phase, being this current the main responsible for the slow SAN action potential. This block leads to loss of driving in the U and in all H models. Intriguingly, 3 models out of 5 of the UF condition and 4 out of 5 of the HF one show a pace and drive behaviour. UF tissue #1 and HF tissues #3 and #4 show however 2:1, 3:1 and 2:1 exit blocks with consequent extreme atrial bradycardia (*CL* = 2209 ms or 27 bpm, showing only 2 APs in 5 s, 2583 ms or 23 bpm and *CL* = 1797±0 ms or 33 bpm). HF tissue #5 has a complex electrical activity as well, with re-entrant excitation showing 1 exit block in the last 5 second of the simulation, with a resultant *CL* of 1142±463 ms. Only model #2 shows a regular and physiological rate (*CL* = 806±0 ms), but the activation starts from the center of SEP #2 (Figure C.5). UF tissues #2 and #4 show stable driving but at a slightly bradycardic pace (*CL* = 1073±0 ms and 1076±0 ms both equal to 56 bpm). For this 4 models, the SF appears to be slightly reduced compared to the HF model in other conditions (Figure C.3), even if not significantly.

Similarly, the H configuration does not show significant differences in the *SF* across conditions. Only the administration of 1 μM ISO significantly increases the *SF* compared to any other condition with both H and HF set-ups (Figure C.3). With only fibroblasts, the results are more complex since the highest SF are obtained with ACh administration and I_f block, showing a significant difference with respect to control and ISO (ACh: p = 0.02 and 0.009; I_f block: p = 0.004 and 0.003, respectively). Interestingly, SAN frequency synchronization is worse in the HF than H condition with both I_f and I_{CaL} current blocks (Figure C.2, panels G and H). In all other cases, the combination of heterogeneity and fibroblasts determines a lower or equal σ_{CL} inside the SAN, opposite to what happens in the rabbit model (Figure C.1).

Effects of SEP width and mosaic configuration on atrial driving

To gain additional understanding of driving mechanisms, two additional model parameters were investigated: the width of the exit pathways and the cellular organization at their interface. Table 5.3 reports the effects of SEP width on the driving capability of the SAN, showing that there is an inferior limit (width = 11 cells) for propagation. The results are similar for both the K and MBS model, with no modulation of the *CL* with respect to SEP width. However, conduction velocity along the leading SEP shows an increase proportional to the width, with a corresponding decrease in conduction time. The MBS model needed a mosaic configuration on top of the set-up described in the Methods, to be able to pace the atrium. This consisted in a gradient of atrial cells interspersed in the SEPs. Without it, it was not possible to obtain propagation in a uniform SAN condition. When heterogeneity was considered (without mosaic), only 1 model out of 5 achieved very poor driving, with 3:1 exit blocks and consequent pronounced bradycardia (*CL* = 1932 ms). However, even with the mosaic (uniform) configuration, only in 3 occurrences out of 5 the atrium was effectively activated (*CL* = 814±0 ms).

Combining heterogeneity, fibrosis and neural modulation

A final simulation including heterogeneity, fibrosis (HF tissue #3 with K model) and simultaneous administration of 25 nM ACh and 1 μM ISO (named "full" model), was run to model a condition as close as possible to SAN physiology. To reproduce a physiological activation sequence, the R_{gap} was lowered to 10 and 100 MΩ for SAN cells and fibroblasts, respectively. In addition, the mosaic model was implemented as with the MBS model simulations and the FWS model was modified to account for simultaneous adrenergic and cholinergic effects in an additive way (see Section). This setting provides a *CL* of 1192 ms, with the activation starting from the left central part of the SAN and exciting the atrium through SEP #3 after

Table 5.3: ***Effect of SEP width on pacing and driving*** *with K and MBS models. P but no D: pace but no drive; CV: conduction velocity; CT: conduction time.*

SEP width [# of cells]	7	11	15	19
K model				
CL [ms]	P but no D	814±0	814±0	814±0
SEP CV [cm s^{-1}]	-	0.35	0.41	0.52
SEP CT [ms]	-	380	320	250
SF	-	1.45±0.03	1.48±0.01	1.63±0.08
MBS model				
CL [ms]	P but no D	814±0	814±0	814±0
SEP CV [cm s^{-1}]	-	0.27	0.38	0.49
SEP CT [ms]	-	490	350	270
SF	-	1.38±0.15	1.45±0.23	1.31±0.09

roughly 80 ms (Figure 5.14). The propagation wave then re-enters the SAN from SEP #1 and #5 where it collides with the depolarization coming from the SAN's head and tail. The *SF* results to be equal to 1.56.

If the fibroblasts' R_{gap} was left to its original value of 1 GΩ, a more physiological *CL* of 961 ms and a higher *SF* (1.75) were achieved, but atrial excitation was achieved after ∼120 ms through SEP #5 and the slow CV inside the SAN allowed the depolarization to enter from the other SEPs (Figure C.6). Interestingly, in the absence of fibroblasts, pacemaking activity was completely suppressed.

5.4 Discussion

The results reported above show that atrial driving can be achieved in different conditions in both the rabbit and human models, with cross-species agreement on the beneficial contribution of heterogeneity. The simulations also show that fibrosis increases human SAN robustness in different conditions, but seems less advantageous for the rabbit SAN, as discussed in detail below.

5.4.1 Heterogeneity and fibrosis increase robustness of atrial driving

An important and novel role of heterogeneity and fibrosis is that of increasing the ability of the rabbit and human SAN to drive the atrium (Figure 5.5, 5.7, 5.9, 5.11 and 5.13). In all conditions, the H configuration show significantly higher *SF* values in both rabbit and humans ($> +10\%$). This is likely due to

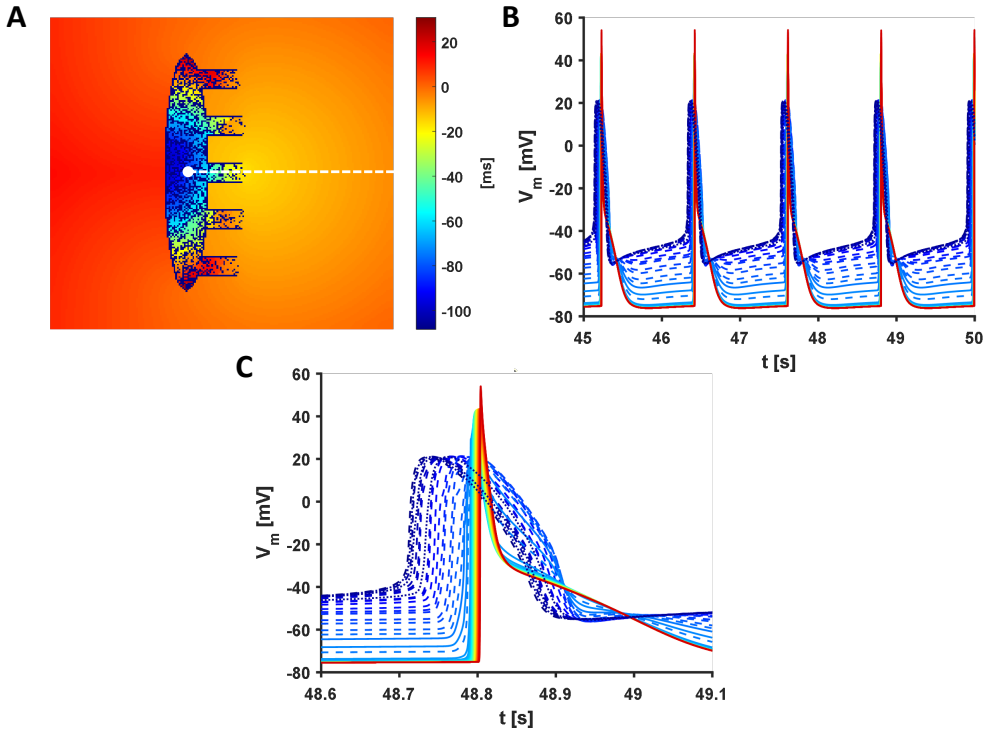

Figure 5.14: ***Propagation in the "full" model with heterogeneity and fibrosis plus 25 nM acetylcholine and 1 µM isoproterenol administration.*** *A) Activation time map. B) EGMs obtained from the four electrodes of Figure 5.3 in the unipolar configuration. C) Action potentials along the dashed black line of panel A. D) Conduction along the dashed black line of panel A.*

the presence of "stronger" cells (i.e. expressing for example more I_{CaL}) that deliver more current at the SEP interface. UF and HF conditions have a similar behaviour, since as further described below (section 5.4.4) fibroblasts act as current sources and allow SAN cells to provide more charge to atrial tissue. Table C.2 supports this mechanism by reporting how heterogeneity and fibrosis determine depolarized *MDP*s and higher upstroke velocities especially in the leading SEP, compared to when they are absent. The contribution of heterogeneity in ionic properties has long been deemed central to pacemaking robustness [1]. Regarding fibroblasts, experimental and computational works on ventricular tissue [289], [324] allowed to hypothesize that they are able to influence the source-sink relationship for an effective stimulus propagation in the SAN as well [314]. Indeed, a possible first validation of the present results comes from co-cultures of fibroblasts and ventricular myocytes [325]: in these experiments, the percentage of myocytes preparations showing spontaneous activity was above zero only when a minimum amount of fibroblasts (20%) was present and it reached a maximum

(>80%) with 50% fibroblast density. Considering that fibroblast-myocyte coupling was recently demonstrated *in vivo* (at least in mouse infarcted ventricular tissue) [305], our simulations and these previous report point towards a role of the fibroblasts' depolarized resting potential in providing pacemaking robustness.

Exceptions to this general *SF* increase are represented by the rabbit HF_{lc} condition – probably because of the limitations concerning fibroblasts, see below (section 5.4.9) – and by the human HF models with 25 nM acetylcholine administration. On the opposite, 1 µM isoproterenol showed a synergistic effect with the H and HF configurations, showing a raise in *SF* bigger than the one it determines in the uniform one (Figure C.3). In fact, only ISO provided *SF* values higher than the other conditions (control, ACh, current blocks) for the same configuration (H or HF, Figure C.3).

The "full" model showed a *SF* value (1.56) closer to the average obtained with ACh administration (1.54±0.09) than the one with ISO infusion (1.86±0.08). When a weaker coupling of the fibroblasts is considered (original R_{gap} value of 1 GΩ), this is enough to substantially raise the *SF* towards the ISO values (1.75). This is consistent with results from coupled rabbit SAN and atrial cell models, which showed a substantial dependence of the SF on R_{gap} [203]. A further beneficial consequence of increased R_{gap} in the "full" model is that of avoiding bradycardia (62 vs 50 bpm). Both effects nevertheless come at the cost of losing phase synchronization inside the SAN (lower apparent conduction velocity, Figure C.6), a fact that may facilitate re-entry onset. Most interestingly, when the fibroblasts are removed from the "full" model, the SAN tissue loses automaticity. This supports their importance in mitigating atrial hyperpolarization, thus protecting SAN myocytes depolarization and allowing atrial driving.

5.4.2 Heterogeneity and fibrosis provide protection from key ion currents reductions

The simulations show that heterogeneity protects the SAN from loss of key ionic currents (I_f and I_{CaL}) also when it is coupled to the atrium (Table 5.2, Figures 5.13 and 5.9), confirming its beneficial action found in isolated pacemaker tissues [33], [34]. When fibroblasts are also considered, a stronger beneficial effect is appreciated, allowing the SAN to pace the atrium despite a 25% I_{CaL} block in the UF and HF human set-ups, while all U and H tissues remained quiescent. As for the raise in the *SF*, this is due to the depolarization of the MDPs and especially to the increase in the dV/dt_{max} of SAN cells in the leading SEPs given by the synergism of heterogeneity and fibroblasts (Table SC.3).

Particularly, with both I_f and especially I_{CaL} block, the HF condition shows higher σ_{CL} values in the SAN than the H one, opposite to what happens in the

other cases. This could be due to the fact that a portion of SAN cells loses the strength (i.e. a large enough diastolic current) to depolarize at a rate set by the fibroblasts' resting potential. Possibly to a larger extent, the increased sink effect would also differently slow SAN cells according to their intrinsic properties and to the fibroblasts' distribution.

5.4.3 Heterogeneity and fibrosis improve recovery from overdrive suppression

In this work, the *indirect SNRT*, measuring the time interval between the first atrial AP and the last paced beat [200], [212], was implemented to quantify the ability of the SAN to recover driving capability after it was overdrive suppressed.

In the heterogeneous tissue in control conditions, the first spontaneous beat propagates from the middle of the SEP slightly – but significantly – before than it does in the uniform tissue. After this beat, re-entry are formed in all 5 models, but they do not stabilize on specific SEPs, as it happens with fibrosis. The latter configuration sees the absence of exit blocks, in line with the observation by [307] which saw lower exit blocks occurrences upon sodium current block or ACh administration compared to when fibrosis was not considered in remodelling due to heart failure. While this suggests again that fibrosis provides strength to atrial driving, at the same time it leads in the present model to macro re-entry stabilization. All conditions show SNRT values after pacing at 2 Hz similar to those obtained in two explanted human hearts: U = 1102 ms, H = 1047$\pm$18 ms, UF = 1124$\pm$9 ms and HF = 1063$\pm$163 ms vs. 1020 and 1459 ms [200]. When corrected for the basal *CL*, the *SNRT* value of the uniform condition (288 ms) is in agreement with computational reports (167 ms with pacing at 950 ms [200]). However, after external pacing no exit blocks were observed in the experiments [200] and in the computational model by [307]. In both cases, the exit blocks were obtained only with reduced sodium current and ACh administration or in heart failure remodelling conditions, which also lead to re-entry.

Further, the simulations with administration of 25 nM ACh show that fibroblasts greatly reduce the *SNRT* compared to heterogeneous tissues (-37%), which in turn recovered much earlier than a uniform one (-36%, Figure 5.10). In particular, the *SNRT* in the UF and HF set-ups with ACh administration are much closer to the values without ACh (1479$\pm$223 ms vs. 1124$\pm$9 ms and 1371$\pm$165 ms vs. 1007$\pm$163 ms, p = 0.03 and p = 0.01) than the H condition (1923$\pm$325 ms vs. 1047$\pm$18 ms, p = 0.004), even if they are still significantly longer. Our result of SNRT = 3020 ms in the U condition, evidencing nodal dysfunction (corrected indirect $SNRT > 525$ ms), is in line with *ex-vivo* experiments on dogs [326], [327] and humans [200]. Modelling work on humans [200] congruently obtained atrial

pauses of > 5 s seconds due to exit blocks happening at the SEP exits upon ACh application, when the fast sodium current was blocked by 20%. However, in the rabbit model by[190], the pauses duration was proportional to the number of fibroblasts connected to SAN cells. No pauses were reported in the model by [307]. During pacing, none of the models showed filtering of the paced stimulus through the SEPs, as it was instead previously demonstrated in optical mapping experiments in human hearts at frequencies lower or equal to 2 Hz [212].

The bigger strength shown by the HF condition can however also translate in a more stable re-entry onset compared to the H one, where exit blocks could give the SAN the chance to restore spontaneous activity. Nevertheless this did not happen in the 8 s of simulation after the pacing was stopped, where re-entrant waves travelled to the next SEP if they did not manage to excite the atrium through a certain one. The major cause of this unphysiologic behaviour is the too low conduction velocity in the exit pathways, as it will be discussed in the limitation section below. Longer simulations after the pacing was stopped were not performed to check if the re-entrant circuits were abolished after a certain time and if this time was different in the two set-ups. In the rabbit *hc* condition in fact, heterogeneity showed a tendency to limit re-entry duration (Figure 5.6).

5.4.4 Heart rate modulation by heterogeneity and fibrosis

In the uniform condition, both the rabbit and the human models showed *CL*s equal to single cell values (355 ms and 814 ms, respectively). For human, this is shorter than previous computational works (vs. 883 ± 1.7 ms [191] and 999 ms [200]), but perfectly inside the range of human heart rates (74 vs. $60 - 100$ bpm).

In rabbits, heterogeneity significantly shortens the *CL* in the *lc* configuration, but in humans the occurrence of exit blocks determines a large atrial σ_{CL} and average values close to the uniform condition. Interestingly, the simultaneous presence of heterogeneity and fibrosis determines opposite results: lower *CL* and σ_{CL} for humans, higher values and dispersion for rabbits. Differently from what happens in human single cell simulations indeed (Figure B.5), when SAN cells are hyperpolarized by the atrium, the time during which their membrane voltage is below the fibroblasts' resting potential (-50 mV) is increased. Thus, the fibroblasts act as current sources for a bigger portion of the *DD* phase, accelerating it. In addition, due to their depolarized resting potential, fibroblasts 1) soften intrinsic rate differences due to parameter randomization among cells by pushing them towards similar beating frequencies (Figure C.2) and 2) provide enough current to avoid exit blocks from the SEPs, supporting the hypothesis of Chapter 4 of a protective action of fibrosis over the SAN.

Why the opposite happens with rabbit might be due to the amount of fibrosis tested (40%), to the absence of a gradient of fibrosis, to the fibroblast model

used (human atrial [255]) or to a combination of the three. To the best of our knowledge, no rabbit-specific estimates of fibroblasts count in the SAN exist in literature, but other mammals (e.g., mice, cats and dogs) show lower physiological amounts than humans (20-30% vs. ∼45% [314]). While driving failure was obtained by Oren and Clancy with 50% fibrosis [184], all UF and HF *lc* rabbit models showed a pace and drive behaviour, highlighting how 40% may still represent a physiological fibrosis amount for rabbit. Otherwise, the different fibroblasts modelling approaches (active vs. passive models or resistive barriers [184]) may account for the difference. By itself, the presence of fibrosis minimally prolongs the *CL* (Figure 5.5), even if to a significant level in humans given the small variability across simulations (Figure 5.7). This small effect is consistent with the work by Karpaev and colleagues [190] but contrasts with the results by Oren and Clancy [184], with experimental data [289], [314] and with the results of Chapter 4 in the isolated human SAN. This discrepancy may be explained by the difference in voltage between the resting potential of the fibroblasts and the *MDP* of SAN cells when they are also coupled to the atrium, according to the mechanism described above.

Interestingly, when ACh is applied, the combination of heterogeneity and fibroblasts prevents the exit blocks occurring in the H model (CL = 1489±287 ms) and shortens the CL of the U condition (1448 ms, slightly longer than in [200]), avoiding bradycardia (991±76 ms, equal to 61 bpm) and reducing *CL* variability (Figure 5.9). During ISO administration, the HF set-up also shows a tendency to limit the tachycardia (109 vs. 113 bpm) achieved in the H condition (Figure 5.11), in agreement with the lower average heart rates obtained with fibroblasts alone (90 bpm). Therefore, under this point of view, fibrosis provides robustness to driving but at the same time reduces heart rate flexibility.

In the "full" model, a heart rate of 50 bpm was obtained. This slight bradycardia was the consequence of the reduced R_{gap} of both SAN cells and fibroblasts, needed to achieve a physiological atrial activation time. Also, considering the simultaneous simulated infusion of ACh and ISO, it reports the predominance of cholinergic over adrenergic effects, in line with experimental observations that the intrinsic rate (e.g., in denervated hearts) is higher than the *in vivo* rate due to the absence of the large basal parasympathetic tone [328], [329].

5.4.5 Heterogeneity and fibrosis shift the leading pacemaker location

Depending on the randomized ionic properties, on the fibroblasts distribution or on their interaction, clusters with different intrinsic properties (e.g., beating rate) form inside rabbit tissue and become dominant. The activation sequence, even if

consistent and stable in time, appears to be originating according to the location of these clusters (Figure 5.4) more than distally from the atrium as in the uniform model.

Thus, physiological levels of heterogeneity ($\sigma = 0.2$ for the log-normal distribution [33], [34], [291]) and fibrosis ([61], [315], [317]) can overcome the atrial sink effect and shift the leading pacemaker (LPM) location, at least at the coupling values adopted. In the human model, interventions that decrease the strength of the source or increase the sink – such as reducing R_gap in the full model, administering 25 nM ACh administration or blocking I_f – all brought the LPM away from the SEP exits. Consequently, the electrical excitation followed a more regular pattern of activation, propagating from the left part of the SAN towards the atrium (Figure C.6).

Interestingly, keeping fixed the diffused fibrosis distribution while changing the heterogeneity one resulted in atrial activation always from the same SEP (not shown), suggesting that fibroblasts may guide propagation. This is further strengthened by symmetrical simulations in which the distribution of cellular heterogeneity was fixed but the fibroblast one was changed, which resulted in atrial activation via different SEPs.

5.4.6 Gradients in gap junctional conductivity are necessary to achieve atrial driving

The SF computation in the rabbit model suggests that the *lc* configuration is safer than the *hc* one since, by isolating the SAN, it avoids hyperpolarization by the atrium and consequently allows the SAN to deliver more charge (Figure 5.5). Similarly, a steep gradient in gap junctional coupling was found to be necessary in order to obtain driving in the human model. This suggests that the most important parameter in order to achieve a robust atrial driving is inter-cellular coupling, as highlighted in previous works [186], [187], [191]. Indeed, the slope, half value and shape of transition inside and outside the SEPs were seen to deeply affect propagation, with only a fine balance of these parameters, as reported in the Methods section, allowing it to happen in the human model.

With rabbit, both the *lc* and *hc* conditions allowed the stimulus to propagate in the atrium, showing advantages and disadvantages. For example, no re-entry was shown in the *lc* condition, while *hc* one allowed driving with 25% I_{CaL} block). However, the *hc* condition seems rather unlikely if compared to gap junctional resistance experimental values (0.6-25 nS [186]). Also, no atrial depolarization is obtained in this configuration when 40% fibrosis is added to the tissue.

5.4.7 Effect of exit pathways width and number

In the rabbit model the number of SEPs does not influence the average *CL* or the *SF*, suggesting that, with the designed coupling gradient, the SAN represents a strong enough source that does not get affected by an increased sink [204]. Concerning SEP width, the simulations show that with both the human K [20] and MBS [27] models there is an inferior limit in the number of cells that has to compose the exit pathways for the crista terminalis to be excited, as found in the 3D detailed model by Amsaleg and colleagues [191]. However, Li et al. [200] managed to achieve SAN-atrial propagation with one SEP as narrow as 3 cells (modelled as pieces of tissue 30x30 µm with a membrane capacitance of 30 pF), even in the context of simulated heart failure (20% I_f block and I_{Na} blocks in the SAN, non-conductive fibrosis in SAN and SEP, 5% I_{Na} block in atrium). An explanation for this difference could be the fact that they scaled the maximal conductance of the sodium current in the SEP by a factor 5, increasing the ability of the pathway to capture the atrium.

With growing SEP widths, a slight increase in conduction velocity (and consequent reduction in conduction time) was obtained in the K and MBS models (Table 5.3). However, the *CL* did not appear to be affected by SEP width, contrarily to the 3D model [191]. This indeed showed that enlarging the SEPs led to loss of driving due to excessive hyperpolarization coming from a larger sink seen by the SEPs. This agrees with a previous study [206] reporting a *CL* prolongation up to SAN suppression with wider SEPs, while narrower SEPs allowed instead pacing and driving on a larger range of conductivities. This discrepancies might be ascribed to different aspects. Firstly, in a 2D setting like the one considered in this work, the interface between SAN and crista terminalis grows linearly upon increasing SEP width, but quadratically in 3D. Second, in [206] the SEPs are opened on both sides of the SAN. Third, the K model has a membrane capacitance of 50 pF, lower than the ones used in [191] (100 pF) and in [206] (81 pF). All these factors could lower the sink effect in the present model, limiting the *CL* modulation effect by SEP width.

5.4.8 The mosaic configuration helps to achieve atrial driving

In the last set of simulations, the MBS model resulted to be less easily excitable than the K one. The reason for this is that in the present work we only used the 29 equations describing the action potential of the atrial cell, removing the ones devoted to model the mechano-electric feedback and calmoduline-kinase activity. While the AP features were still in accordance to experimental values (Table C.1), the equations used were not optimized by themselves to describe the electrophysiology of a single atrial cell. The maximal upstroke velocity was for example

lower than in the original MBS model (dV/dt_{max} = 177 vs 199 $\mathrm{mV\,ms^{-1}}$). Thus, even when the maximal conductance of the fast sodium current was doubled to reproduce experimental values of conduction velocity in the crista terminalis, the atrial tissue composed by MBS model cells struggled to depolarize.

If further refinements are needed in order to use the electrophysiology equations of the MBS model as a stand-alone, these simulations provided some useful information on atrial driving. First of all, atrial cells interspersed in the exit pathways (so-called mosaic model) actually helped propagation compared to a flat interface. While this set-up was not needed with the K model, its addition to gradients in gap junctional coupling might represent a more robust – thus more likely – anatomical architecture of the SAN [190], [191]. Second, if SAN heterogeneity increases the amount of charge delivered to atrial cells (as shown above), this is not enough to overcome gaps that only coupling or anatomical aspects (such as indeed gradients and mosaic configurations) can. Indeed, without the addition of the mosaic set-up, only one SAN heterogeneous distribution managed to drive the atrium (and to an unphysiologically low rate due to exit blocks).

5.4.9 Limitations

It is important to take into account the several shortcomings of the present study.

The rabbit model had the advantage of featuring a SAN single cell model that was developed from a larger amount of experimental data. However, the availability of optical or electrical mapping data to validate the rabbit tissue model is more limited than for the human SAN. As mentioned above, no rabbit-specific SAN fibroblast model is present in literature, and the human atrial one was used. This is a limitation also for the human model, since to the best of the authors' knowledge no SAN-specific fibroblast model exist for humans or any other species. In this work we chose to use the Morgan et al. model [255] also for rabbits since we privileged the similarity of cellular phenotype (atrial vs. sinoatrial) rather than that of species (e.g. mice [250]). Other human fibroblast models [249], [330], [331] were not taken into consideration. Here fibroblasts were distributed diffusely according to a "concentration" gradient, with higher amounts distally from the crista terminalis which lower approaching the end of the SEPs. However, histological sections of the SAN of different species of mammals [245], [332], [333] showed that fibroblasts actually form a structural network that supports and protects different clusters of SAN myocytes. Additionally, mechanical aspects were neglected despite the fact that mechanics is known to have a profound modulatory role on SAN activity ([52], [258], [259] and Section 1.6.1).

Both rabbit and human models share limitations in anatomical aspects. Indeed, the 2D geometry adopted here represents a rough simplification of the SAN complex structure described in Chapter 1 [60], [61], [211]. In particular for the

human case, our model is anatomically more simple than the 3D one by Amsaleg et al. [191] which considered fiber direction, too. Considering that in an elaborated structure such as the SAN the anatomy has a clear impact on its function [48], our stylized model geometry quantitatively affects the results. For example, a conical shape of the SEPs may increase the strength of driving and limit the occurrence of reentry by providing a less favorable source-sink mismatch for the excitations entering the SAN. Also, we did not consider the presence of spatially-dependent distributions of ACh receptors [267] (or of the maximal conductance of the ACh-activated potassium current) or the presence of clusters of SAN cells with different intrinsic pacemaking properties [268], [280] and consequently we did not investigate the known effect of pacemaker shift following autonomic modulation. We only noted that cellular heterogeneity, fibrosis, acetylcholine or high frequency pacing modified the location of the earliest activation site (e.g., Figure C.5), which could be found closer to the atrium and even in the center of the SEPs, wuthout investigating it quantitatively. This is different from the uniform SAN, in which the beat originates distally from the atrium because of sink/source effects, in agreement with the 3D model [191].

The main shortcoming of the model is represented by the slow conduction inside the exit pathways. Considering a SAN cell length of 67 µm, average conduction velocity in the SAN was $\sim$1 cm s^{-1} (lower than experimental values of 5 cm s^{-1} [211]) which dropped to $<$0.5 cm s^{-1} in the SEPs. These velocities correspond to conduction times in the SEP of more than 300 ms (Table 5.3). Therefore, atrial activation was achieved on average more than 500 ms after the stimulus originates in the SAN, a value much higher than in other models ($<$100 ms [191], [200]) and outside experimental ranges (82$\pm$17 ms [211]). The slow sequence of activation sets the stage for re-entrant activity, as it happens in the H configuration in control conditions. Amsaleg et al. [191] reported velocities as low as 1 cm s^{-1} at the beginning of the gap junctional gradient in the SEP, but these sharply increased along the SEP. When we used the mosaic architecture with the MBS model, the limited width of the 2D SEP did not allow to have enough cells for a smooth transition, thus also in this case the conduction velocity showed an increase from $<$1 cm s^{-1} to 100 cm s^{-1} in a few cells span.

We did not consider the presence of a transitional cell phenotype, even though they were reported in several experimental works [61], [176]–[179] and used in previous mathematical models [76], [77], [184], [185], [334]. While this could have helped achieve higher CVs in the SEPs, early attempts in the rabbit model using scaling parameters for the SDiF model by Ly and Weinberg [185], resulted in an unphysiological activation sequence from the right part of the SEPs, similar to what was obtained by Oren and Clancy in 1D [184].

Another important limitation is that, as a first approach, all the conditions tested in this work only regarded the SAN. This is reasonable regarding the pres-

ence of fibrosis and vagal tone, which are considered to be minimal in the right atrium in physiological conditions. However, it neglects the heterogeneity in ionic properties of atrial tissue and its response to sympathetic stimulation, which likely have a role in modulating the ability of the SAN in driving the atrium. In addition, the number of *in silico* experiments run in this work appears to be limited compared to the model parameter space. For example, besides testing only one level of fibrosis, single values of I_f and I_{CaL} blocks were applied, as well as ACh or ISO concentrations (the FWS model does not feature dose-dependent ISO effects) and pacing frequencies. A full-scale sensitivity analysis, even if important for validating the model, would be computationally really expensive taking into account all the degrees of freedom of the model (e.g., geometry, gap junctional values, different amounts of fibrosis, different levels of autonomic modulations, etc...) and was outside the aim of this work. Nevertheless, a total of 187 simulations (76 for rabbit and 111 for human) of cardiac tissues composed of 40000 cells were run even with this more limited aim.

5.4.10 Future perspectives

Considering these limitations, future efforts will be directed particularly to overcome the shortcomings in the description of fibrosis. For example, it would be interesting to implement a network configuration of fibroblasts encircling clusters of SAN cells, each with different electrophysiological properties according to their location inside the SAN (e.g., head vs. tail [268], [280]). Would the fibroblasts act on homogenizing these properties – as they showed in the present work – or on the opposite would they contribute on keeping the different clusters separated? One could speculate that in the second scenario the autonomic nervous system would select one of these clusters to become the leading pacemaker site according to systemic needs [280].

As discussed above, all current blocks and neurotransmitter administration were only applied in the SAN (both K and MBS models do not model autonomic modulations effects), so it will be important in the future to study their effect in right atrial tissue as well. Also, checking if fibrosis – alone or together with heterogeneity – increases the chances of driving with the MBS model, as it did with the K model when I_{CaL} was blocked, would further support the idea of its beneficial effect on atrial driving.

Finally, other future developments might be represented by the reproduction of leading pacemaker shifts in a variety of conditions (autonomic modulation, ionic concentrations or pH changes), as well as the investigation of pathological conditions such as sinus node dysfunction and atrial fibrillation. Since the previous Chapter (e.g., Figure 4.1) showed that the isolated SAN is robust to higher levels of fibrosis (60%) it would be informative to test them in the context of SAN-atrial

coupling. With these models, the hypothesis [61] that SND is caused by localized fibrosis in the SEPs, more than by the overall amount of fibroblasts in the SAN, could be evaluated in detail.

5.5 Conclusions

While further work is needed to overcome the model's limitations and to describe in more detail the underlying mechanisms, this study suggests that physiological levels of SAN cellular heterogeneity and fibrosis, and most of all their synergistic action, enlarge the parametric space for which the SAN is able to effectively drive the atrium in 2D rabbit and human models. In a real setting, this could mean that the role of heterogeneity and fibrosis is that of increasing the robustness of propagation from the sinoatrial node to atrial tissue, ensuring sinus rhythm is guaranteed even in pathological conditions. Still, in agreement with previous literature, anatomical aspects such as SEP width but most of all gap junctional coupling, resulted of uttermost importance in allowing atrial excitation.

Adding on other hypothesis such as the role of fibroblasts in mechanical protection, these model predictions – if validated in experimental studies – represent a quantitative explanation to the extraordinary heterogeneity and fibrosis seen in sinoatrial tissue.

Chapter 6

Chronic Vagal Nerve Stimulation Stabilizes Autonomic Input in Infarcted Pigs

The content of this chapter is the result of part of the work carried out during the research visit at the

Cardiac Arrhythmia Center, University of California, Los Angeles (UCLA)
June 3rd - December 2nd, 2022

in the context of the project
Geometric and Harmonic Analysis with Interdisciplinary Applications (GHAIA)

in fulfillment of the research stay requirement of the PhD program.

Abstract

Chronic vagal nerve stimulation (cVNS) is emerging as an effective therapy in a number of cardiovascular diseases such as myocardial infarction and heart failure. However, its mechanisms of action and its therapeutic potential is still largely unexplored.

In this work, we adopted heart rate variability analysis to assess the role of cVNS in post-infarction recovery. Electrocardiographic telemetry data from ten pigs divided in two groups (myocardial infarction and myocardial infarction with cVNS), were acquired and analyzed along a time span of six weeks.

The results show that cVNS reduces the frequency-domain metrics variability across pigs in 4-6 weeks and significantly increases the powers in the very-low and low frequency bands in less than 4 weeks. The average heart rate is decreased and the low-frequency on high-frequency power ratio is increased, suggesting improved health and better prognosis of the cVNS group, but without reaching statistical significance.

Taken together, these findings report of a beneficial role of cVNS in counteracting maladaptive remodelling and in promoting better outcomes in the progress of infarction.

6.1 Introduction

The heart undergoes a tight control by the autonomic nervous system: chronotropy (rate), inotropy (contraction), dromotropy (conduction) and lusitropy (relaxation) – that is, every aspect of cardiac actvity – are all regulated by autonomic input. However, not all portions of the heart are equally modulated. Indeed, the sinoatrial node area is particularly rich in parasympathetic nerve terminals compared to the right atrium [269]. These neurons are collected in the right-atrial ganglionated plexus (RAGP), which contains adrenergic neurons too [269]. Both neuron types release neurotransmitters such as ACh and NE, eliciting the second messenger cascades described in Section 1.7.

From an anatomical perspective, the RAGP is part of the Intrinsic Cardiac Nervous System (ICNS), which is the lowest level (closer to the heart) of a complex hierarchical structure also composed by the Intrathoracic Extracardiac Ganglia in the middle and by the Central Nervous System (CNS) at the top [335], [336]. The ICNS connects in afferent and efferent manners with the other levels, but also possesses intrinsic connections that create Local Circuit Neurons (LCN) to process information without the involvement of the higher centers [335]. Figure 6.1 shows a simplified scheme of the whole hierarchy of cardiac innervation.

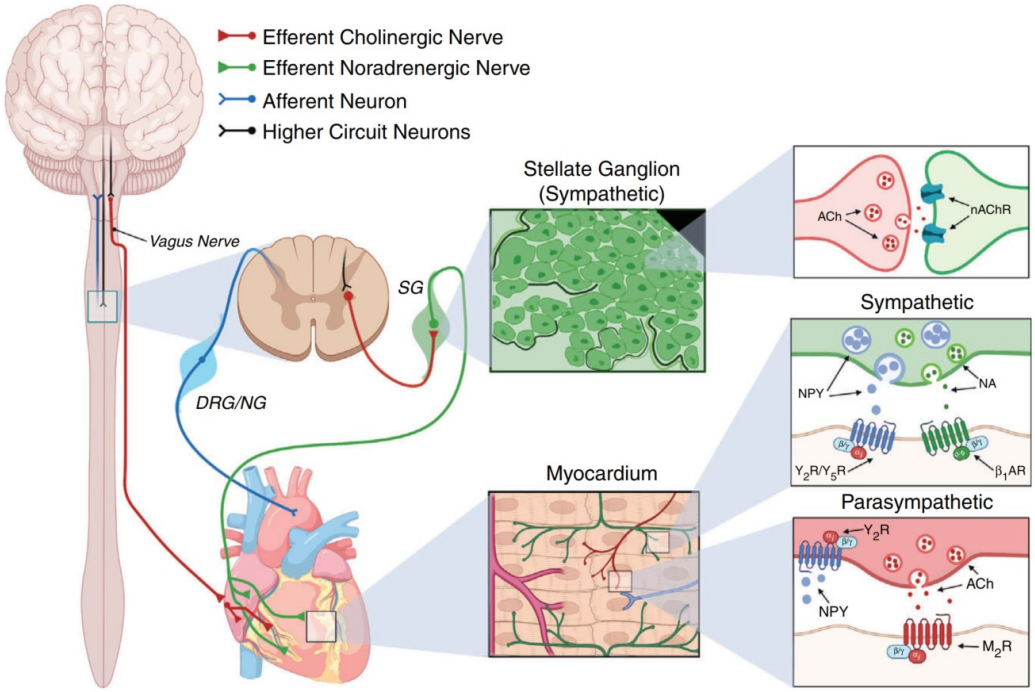

Figure 6.1: (Caption in next page).

Figure 6.1: ▲ ***Schematic of the innervation of the heart****. From Clyburn et al. [337]. The higher centers in the CNS connect to the cholinergic branch of the ANS in the medulla, from which the vagus nerve departs and directly synapses the RAGP. Differently, the adrenergic branch receives efferent input in the spinal chord where efferent cholinergic nerves exit to connect in the stellate ganglia (SG) to post-ganglionic noradrenergic nerves that in turn innervate the heart. Afferent information to the CNS travels through Dorsal Root (DRG) and Nodose Ganglia (NG). (ACh) acetylcholine, (naACh) nicotinic acetylcholine receptors, (NPY) neuropeptide Y, (NA) noradrenaline, (Y_2R/Y_5R) Y2 and Y5 NPY receptors, (β_1AR) $\beta 1$ adrenergic receptors, (M_2R) muscarinic receptors.*

This brief intorduction overlooks many aspects of the elaborate anatomy of the connections and of the complex function of the different cellular phenotypes. However, the way the nervous system controls heart function is still largely unknown, especially in diseased conditions [337], [338]. In recent years the field of neurocardiology [339] has seen a stark rise in interest and exciting results [340]–[342], providing promising therapies and new approaches to unresolved problems such as cardiac remodeling after injury [337], [343]–[345]. Sympathetic hyperactivation and parasympathetic withdrawal are frequent consequences of cardiac insults, such as myocardial infarction [336], [337]. The imbalance of the ANS in favour of a higher adrenergic tone leads to maladaptive tissue remodeling with consequent poorer prognosis, as shown by the lower rate of survival in patients showing markers of sympathetic activation (e.g., higher heart rate) following MI [346], [347]. In this context, actions that would reduce sympathetic hyperactivity and re-impose a parasympathetic dominance, would be beneficial at the clinical level.

Vagal Nerve Stimulation (VNS) has demonstrated in recent years to be able to serve this role, proving to be effective in counteracting remodelling [341], [348] and in mitigating arrhythmias (neurally-induced AF [340] and ventricular tachycardia/fibrillation after MI [348]) in mammals and in improving clinical markers (e.g., mean heart rate, heart rate variability, left ventricular ejection fraction) in heart failure clinical trials [344], [345]. This innovative technique is based on the delivery of electrical stimuli to the vagus nerve through a surgically implanted electrode. The stimulation is done at the *fulcrum*, that is the combination of stimulus frequency, amplitude and pulse width that allows to obtain parasympathetic activation while not affecting the heart rate [349]. The subjects undergo a titration procedure to determine this operating point and to get accustomed to the therapy. The fulcrum, which is subject-dependent, is reached when the afferent and efferent components of the vagus nerve – characterized by different activation thresholds – are stimulated with an intensity that allows to obtain equal but opposite effects on the heart rate. A phenomenological mathematical model of this system [350]

showed that increasing the stimulation amplitude first induces tachycardia because of a reduced afferent-mediated central parasympathetic control. However, when the amplitude is further increased, the heart rate is progressively reduced up to a net bradycardic effect due to direct efferent effects of parasympathetic nerves on the heart [350]. When the effect on the heart rate is balanced (at the fulcrum), but also when the stimulus is below the threshold for a net sympathetic effect, the models shows that neural activity is different from baseline. This tells that there is the possibility for remodeling without in fact directly affecting the heart rate.

The objective of this Chapter is that of investigating the effects of cVNS therapy in the recovery from myocardial infarction in pigs. To do this, Heart Rate Variability (HRV) analysis was employed as a non-invasive tool of assessment, in order to set the stage for future clinical investigation of cVNS efficacy. HRV is indeed a widely used technique in clinical practice for its low cost, easy of use and standardization [171], even if controversies remain in the meaning of spectral indices (e.g., what determines the very-low and low frequency components of the RR intervals spectrum [351]).

The hypothesis expressed in this work is that the beneficial effects that cVNS was shown to have in pigs in terms of tissue remodelling, cardiovascular indices improvement and arrhythmia inducibility reduction after MI [348], is also quantifiable with HRV methods. In particular, myocardial infarction was reported to: 1) increase the low-frequency and decrease the high-frequency components of the RR intervals spectrum [352], [353]; 2) have a strong correlation between mortality and reduced ultra- and very-low frequency components, and less to low- and high-frequency ones [354]; 3) be a risk factor for sudden cardiac death, especially with low respiratory sinus arrhythmia [355], [356] or low and very-low frequency components and standard deviation of the RR intervals [346], [347]. Therefore, if cVNS acts on counteracting maladaptive remodeling following MI, it is expected to ameliorate these (and maybe others) HRV markers.

The next sections will illustrate the methodology adopted and the results obtained, to conclude with a discussion of the main findings and of the possible future developments.

6.2 Methods

6.2.1 Study Design

10 Yucatan mini-pigs (Sus scrofa, S&S Farms) were used for the present analysis, divided in 2 groups: untreated myocardial infarction (MI, n = 5) and MI + chronic vagal nerve stimulation (MI+cVNS, n = 5). MI induction, cVNS administration and telemetry acquisition were performed as in previous works [348]. In

this study, we employed heart rate variability (HRV) analysis to assess the effects of cVNS in the recovery from MI. To do this, telemetry data were acquired at different time points (Figure 6.2) and analyzed at: baseline (BL), 2 days post-MI (week 1), 1 week post-MI (week 2), 3 weeks post-MI (week 4), 5 weeks post-MI (week 6). Since sinus rhythm was not stable during the first 24 hours after MI was induced (due to the great presence of extrasystoles and arrhythmic episodes), only the second day of acquisition was selected and analyzed. For better comparisons, only the second 24h of each recording were consequently analyzed. One MI pig died before reaching week 6, so only 4 pigs were used for this group at this time point.

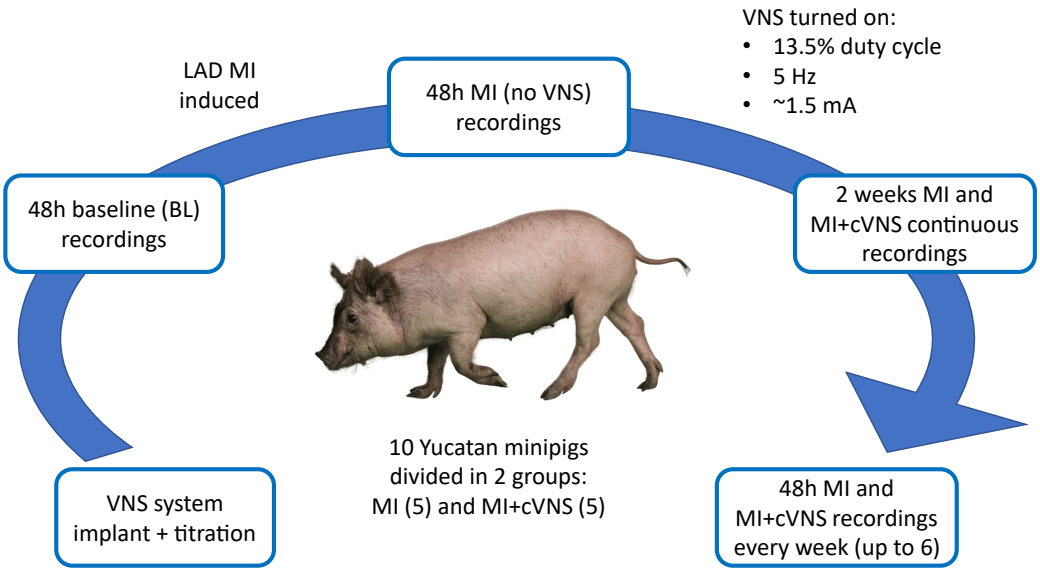

Figure 6.2: ***Design of the present study****. In the specific group, the cVNS device was implanted and titrated to determine the fulcrum. 48h baseline recordings were acquired and then a myocardial infarction was induced via Left Anterior Descending Coronary Artery (LAD) occlusion in all pigs. A 48h recording was acquired and then the cVNS system was turned in the MI+cVNS group. At this point, two weeks continuous recording followed by 48h recordings at week 3,4,5 and 6 were acquired.*

6.2.2 Heart rate variability analysis

For each time point, the 24-hour long unipolar electrograms (EGMs) were exported from the acquisition system (Data Science International) using Ponemah software (Data Science International). Files were converted to a .mat format using Spike2 software (Cambridge Electronic Design Limited) and analyzed in Matlab

R2019b (The Mathworks Inc.). Considering an average 100 bpm heart rate for pigs, this database included roughly 7.2 million R peaks.

The PhysioZoo opensource software platform [357] was used to detect the R peaks from the pig EGMs as well as to compute the HRV metrics. The source code of the platform was modified to avoid using the software GUI (thus improving computational times with long recordings), to automate data analysis and to work with pig atrial EGMs. The *jqrs* algorithm [357] was indeed modified to better discern between the similar-amplitude atrial P waves and ventricular R waves seen in the EGMs. Pig-dependent thresholds were necessary for R waves recognition due to the huge heterogeneity in telemetry data morphology across different pigs. R peaks annotations were additionally randomly selected and manually inspected to verify the method's accuracy. See Figure 6.3 for an example of ECG trace and R peak detection.

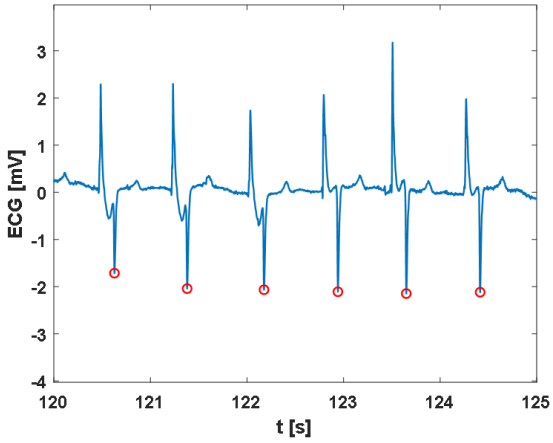

Figure 6.3: ***Example of ECG signal****. 5 s baseline recording from pig #24594 (MI group, blue line) and detected R peaks (red circles).*

The RR intervals, obtained as the difference in time between identified R peaks, were filtered by removing outliers and replacing them by linear interpolation. The outliers were defined as: 1) intervals simultaneously 15% shorter and 15% longer than the previous and the subsequent one; 2) intervals 30% shorter than the previous one and 3) intervals 50% longer than the previous one. This method empirically proved to be effective in removing premature ventricular contractions (PVCs) and artifacts (e.g., amplifier saturation, Figure D.1). Then, the 24-hour long tachograms were split into 5-minutes long, 80%-overlapping windows on which HRV metrics were computed. Windows containing more than 2 outliers were excluded from the analysis (Figure D.2) in order to perform HRV analysis only when the pigs where in sinus rhythm, according to clinical guide-

lines [171]. In addition, the 5-minutes windows were randomly inspected to check for stationarity and were removed if this requirement was not met.

Figure D.3 reports the obtained circadian variations in RR intervals for each pig of the two groups at baseline, averaged over the 5-minutes windows. Four types of HRV measures were computed and analysed: time-domain, frequency domain, fragmentation and non-linear domain metrics. The former included *AVNN*, *SDNN*, *RMSSD* and pNN_{50}, respectively the average, the standard deviation and the root mean square error of the intervals between normal R peaks as well as the percentage of RR intervals exceeding the previous one by 50 ms. These metrics all arguably represent the activation levels of the parasympathetic branch of the ANS [171]. The second included the ratio between the power in the low and high frequency bands of the power spectral density of the tachogram (LF/HF ratio) and the powers in the very low, low and high frequency bands normalized to the total power (VLF_n, LF_n, HF_n). Spectral bands were chosen as reported in literature for pigs [358], [359]: VLF = 0.003-0.01 Hz, LF = 0.01-0.07 Hz and HF = 0.07-0.3 Hz. Fragmentation metrics included the percentage of inflection points (*PIP*), the inverse average length of the acceleration/deceleration segments (*IALS*), the percentage of short segments (*PSS*) and the percentage of RR intervals in alternation segments (*PAS*) [360]. The last group consisted of 5 measures: RR interval standard deviation along the long axis of the Poincaré plot (*SD*1), RR interval standard deviation along the short axis of the Poincaré plot (*SD*2), slope coefficients α_1 (short range RR interval correlation), α_2 (long range RR interval correlation) of Detrended Fluctuation Analysis and finally Sample Entropy (*Samp.en.*). All metrics were computed using the PhysioZoo implementation [357]. See [360] for a summary of definitions of all the measures used in this study.

Averages and standard deviations were obtained for all metrics across the selected 5-minutes windows, obtaining 1 value for each pig at each time point for every HRV measure. The spectral indices VLF_n, LF_n and HF_n were adjusted to take into account the effect of the average heart rate by multiplying them for the ratio between *AVNN* at each time point and *AVNN* at week 1 (where the heart rate was maximal due to MI). Statistical analysis was performed using a two-way repeated measures ANOVA test to study the interaction effect of time and treatment (cVNS) in the progress of MI. Data normality and sphericity were checked using Shapiro-Wilk and Mauchly tests, respectively. If data normality was not met, the non-parametric Friedman test was adopted. If sphericity was not met, the Greenhouse-Geisser correction method was employed to adjust the P value. Finally, the Tukey-Kramer method was adopted as a post-hoc test. All statistical tests were performed in Matlab R2019b using built-in functions. P values < 0.05 were considered statistically significant.

6.3 Results

Figure 6.4 and 6.6 report the results for the frequency-domain and fragmentation, time-domain and non-linear metrics, respectively. There is a general tendency in time-domain metrics reduction following MI, with a consequent recovery in the last weeks (4 and 6) in both groups. However, no effect of treatment can be appreciated and statistical significance is not met even with respect to time in either groups (1 way ANOVA, p = 0.0512 for $AVNN$ of the MI+cVNS groups).

All frequency metrics – with the exception of HF_n which shows the biphasic trend of time-domain metrics – undergo a progressive increase over time, which becomes significant in the case of LF_n and VLF_n of the MI+cVNS (1 way ANOVA, p = 0.0220, p = $2.43 \cdot 10^{-5}$, respectively). Importantly, for these two metrics significance is met with respect to the interaction between time and treatment (2 way ANOVA, p = 0.0228 and p = $8.76 \cdot 10^{-5}$), highlighting a role of the chronic vagal nerve stimulation treatment. Post-hoc analysis reports a significant difference for both LF_n and VLF_n metrics at week 4 (p = 0.00281 and p = 0.00440) and week 6 (p = $3.88 \cdot 10^{-4}$ and p = 0.00310, respectively). Interestingly, the LF/HF ratio also results significant from the Tukey-Kramer test (p = 0.00410 at week 6), but does not reach significance in the ANOVA (p = 0.134).

No other metric (fragmentation or non-linear) resulted in positive outcomes of the statistical tests, even though $SD1$ ans $SD2$ showed biphasic trends (similar to time-domain metrics).

Nevertheless, an important trend is shown by the standard deviations of the frequency-domain measures of Figure 6.4. Indeed, after MI is induced (week 1) the dispersion of the metrics increases up to a maximum (between week 3 and 4, Figure D.4) for both groups. After reaching this maximum, the metrics variability across pigs undergoes a reduction at week 6, which is particularly marked for the frequency measures of the MI+cVNS group, compared to the control MI pigs.

6.4 Discussion

The main finding of this study is represented by the fact that chronic application of cVNS results in a reduction of frequency metrics dispersion across pigs. As it can be appreciated in Figures 6.6 and D.4, weeks 2 and 4 see an increase in dispersion in both MI and MI+cVNS groups, but only the latter shows lower standard deviations at week 6. This means that the cardiac innervation remodeling imparted by cVNS is going on with different dynamics across the pigs, but it is complete after 4-6 weeks for all animals in this group. Furthermore, since every MI+cVNS subject shows equal frequency components, the action of cVNS appears to be that of stabilizing neural input, providing robust control of the insulted tissues, instead

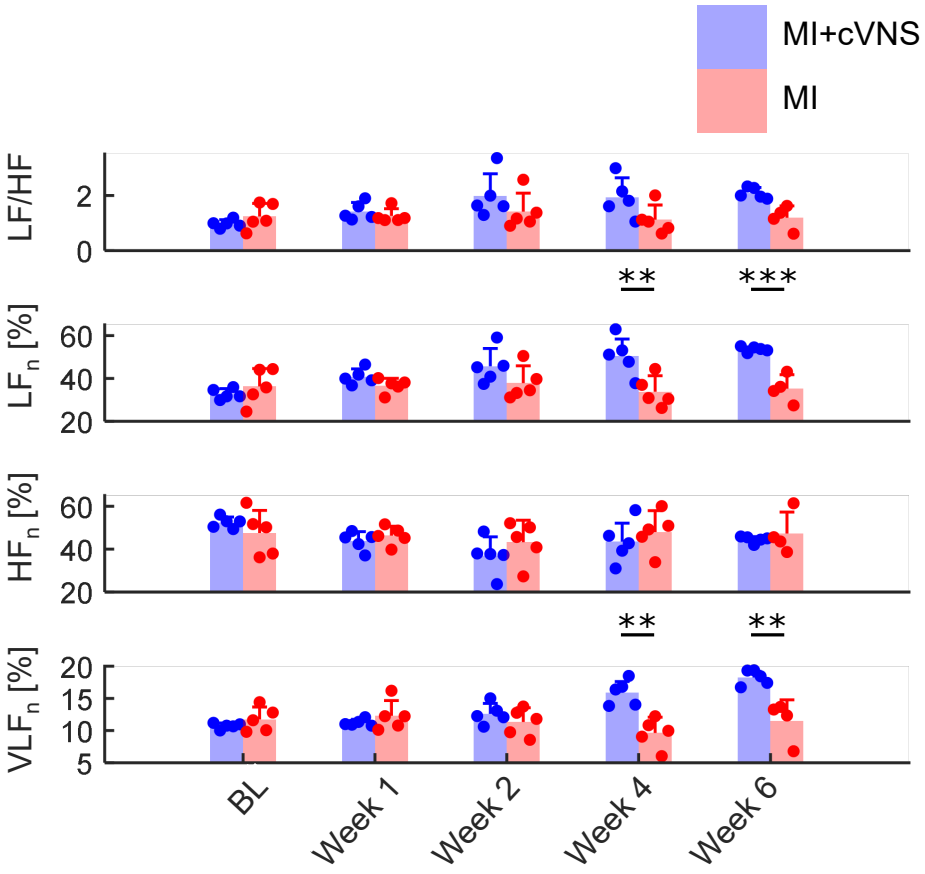

Figure 6.4: ***Frequency-domain HRV metrics results****. Dots represent values for single pigs, averaged between the selected 5-minutes windows out of the 24h at each time point. Bars and intervals represent mean±std values across different pigs at each time point. *p < 0.05, **p < 0.01, ***p < 0.001.*

of determining a sympathetic withdrawal in favour of parasympathetic activity.

The second result is indeed the significant increase in VLF_n and LF_n in time (week 4 and 6, Figure 6.6) compared to the control MI group. Both adrenergic and cholinergic activation seem to contribute to LF power [351], fact that blurs the traditional distinction between a LF component being due to sympathetic activity and a HF one being given by parasympathetic activation. Here, despite the fact that spectral band thresholds were chosen according to literature values for pigs, and were visually checked to correctly identify respiratory sinus arrhythmia power in the HF band, a parasympathetic contribution in the LF band can not be ruled out and may explain the discrepancy with reported reductions in LF power with post-MI recovery [352]. Therefore, an increase in LF_n may be interpreted as

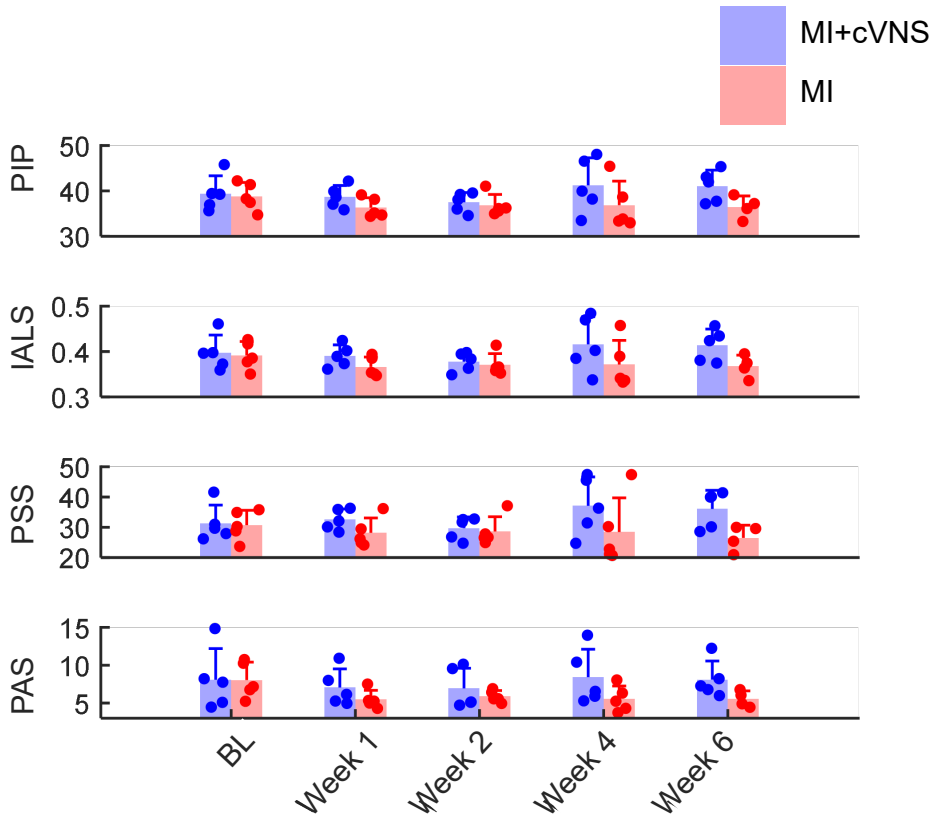

Figure 6.5: ***Fragmentation HRV metrics results****. Dots represent values for single pigs, averaged between the selected 5-minutes windows out of the 24h at each time point. Bars and intervals represent mean±std values across different pigs at each time point.*

a measure of an enlarged total autonomic activity, reflecting a healthier brain-heart axis. This is also suggested by the increase in the LF/HF ratio which, even if it does not meet statistical significance, is in agreement with previous works showing *"a better total ANS activity and better patient prognosis"* (quoted from Chang et al. [361]). That is, cVNS is acting on determining a more stable and stronger global ANS activity more than downregulating the relative adrenergic contribution. VLF power seems instead to be originated by intrinsic rhythms of the heart, in particular due to stimulation of afferent sensory neurons [351], [362], [363]. This agrees with the role cVNS has in stimulating the heart, promoting ICNS activity and the general health of the organ. Indeed, low VLF levels have been associated with: 1) a higher sudden cardiac death risk after MI [347], [354], [364]; 2) inflammation [365], [366]; 3) higher risk of adverse cardiovascular events and hospitalization [367] and higher mortality [361] in chronic hemodialysis patients; 4) higher mortality in kidney disease patients [368]. Even if almost none of these

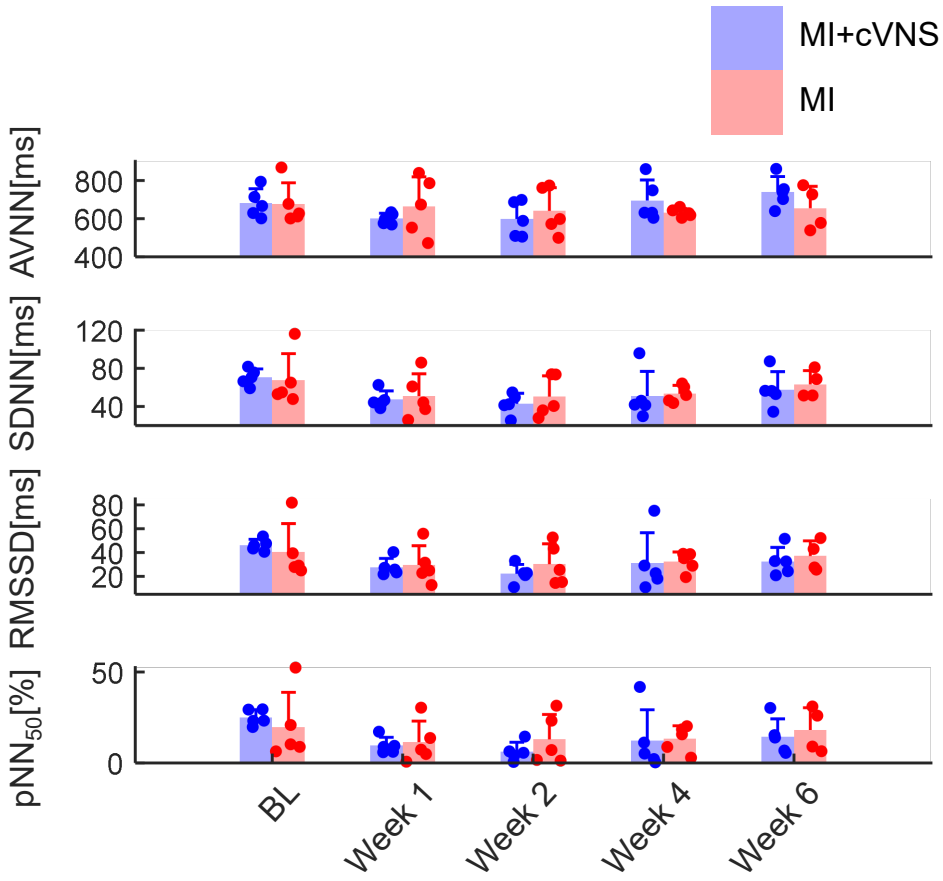

Figure 6.6: ***Time-domain HRV metrics results****. Dots represent values for single pigs, averaged between the selected 5-minutes windows out of the 24h at each time point. Bars and intervals represent mean±std values across different pigs at each time point.*

studies reported normalized VLF power values, and some even omitted to report the average heart rate, questioning the robustness of the results, our findings are in line with most of the available literature. However, there are also contradictory works, reporting that VLF is a risk factor for all-cause mortality in hemodialysis patients [369] and is upregulated in patients suffering from obstructive sleep apnea [370].

The third resuls is represented by the biphasic trends shown by the time and non-linear metrics, which would likely reach significance with a larger number of pigs. In particular, $AVNN$, $SDNN$, $RMSSD$, pNN_{50} and to a lesser extent $SD1$ and $SD2$ show an initial shrinking, with lowest values at week 2, similarly to what HF_n does (in accordance with previous reports [352]). After reaching the minimum, these indices tend to recover the initial values at week 6, with $AVNN$ even showing

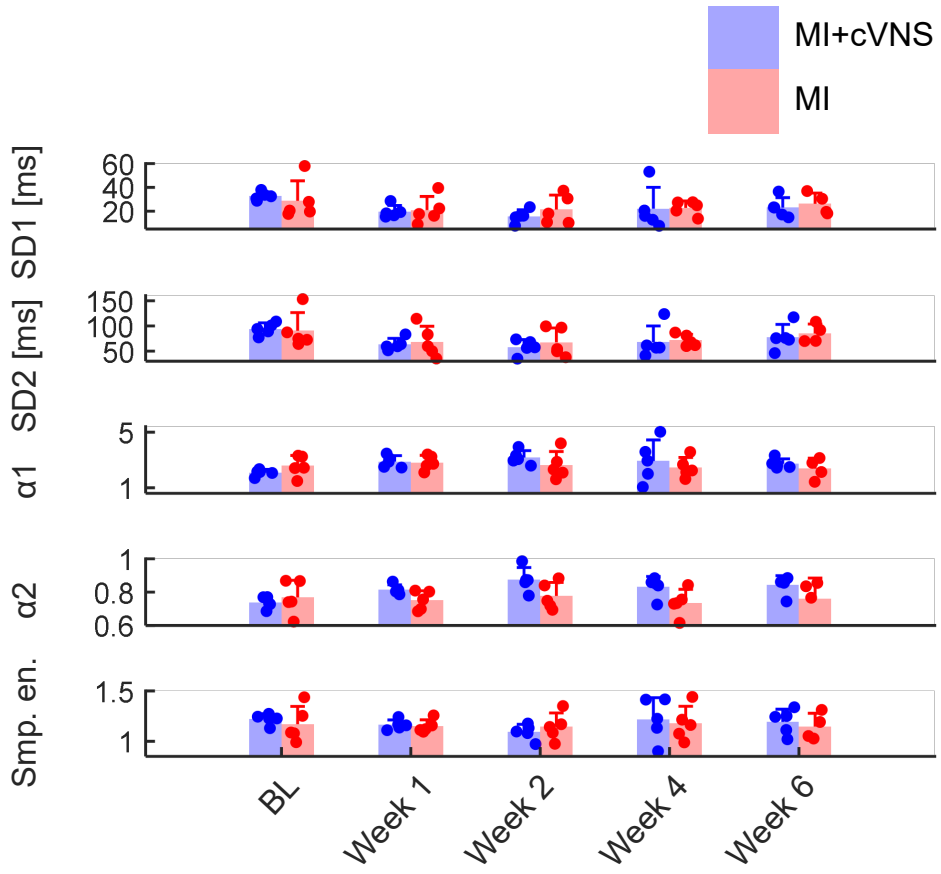

Figure 6.7: ***Non-linear HRV metrics results****. Dots represent values for single pigs, averaged between the selected 5-minutes windows out of the 24h at each time point. Bars and intervals represent mean±std values across different pigs at each time point.*

an increase compared to *BL*. This shows that cVNS, if on one hand is calibrated to leave the heart rate unaltered in the short term, it is able to promote neural and cardiac remodelling that has long-term effects such as reducing the average heart rate. The change in *SDNN*, *RMSSD*, *pNN*50 seems instead to be entirely attributable to natural recovery, given that no appreciable differences can be seen between the two groups.

The fragmentation and non-linear metrics do not produce significant results either, but show a tendency to be increased by VNS at weeks 4 and 6 compared to MI, with the exception of *SD*1 and *SD*2. Upregulation of these metrics was reported to be associated with poorer survival in humans [371] and with aging in mice [360]. However, they also represent measures of complexity and information content of the signal and, as it is known, a too regular cardiac beat is a sign of

diseases [372]. So, further investigation is needed to determine if these trends may weaken the vision of cVNS as a promoter of cardiac health.

This study has other limitations, such as the limited number of pigs employed which, as discussed above, may have reduced the power of the statistical tests. In addition, the implants have been performed by different surgeons at different timings, possibly contributing to intra- and inter-operator errors adding to the noticeable HRV measures variability between the animals. Concerning HRV analysis, the automatic discarding of single RR beats longer or shorter than a certain percentage compared to previous beats has long been recognized as having poor outcomes with respect to manual annotation [171]. However, given the amplitude of the employed database, it was necessary to adopt an automatic procedure and perform human supervision only in small samples. More robust implementations, such as deep learning approaches, are left for future investigations. These may also account for the identification of arrhythmic episodes and extrasystoles to quantify the post-MI arrhythmia burden and the possible beneficial effects of cVNS from this point of view. Besides the largeness of the database, another strength of this study is represented by the long term analysis, spanning from baseline conditions to acute MI up to recovery 5 weeks after MI. This allowed to assess the effects of cVNS during a long period of time, along which which vagal nerve stimulation was shown to act. As reported by the results in this chapter indeed, the VNS effects on HRV indices tend to saturate between week 4 and 6.

Understanding the mechanisms behind such complex phenomena will require great effort in terms of experiment but also modelling [373]. There is still a huge gap between what was shown in the previous chapter, where ANS control is phenomenologically modelled as dose-dependent neurotransmitter effects at the ion-channel or intracellular-calcium level, and the complex interactions inside the hierarchy of structure between the ANS and the heart.

If a proof-of-concept of biophysically-detailed multiscale model of ANS control over the heart has been recently proposed [374], and mathematical descriptions of neural network and VNS functioning are well established [350], [362], [363], much work has still to be done to give a general description of cardiac neural control. Inspiration from neuroscience (Section 1.8) will likely give a major contribution in developing sinoatrial node computational models, as it has already started doing [280], [375]. In the short term, these models will help in reproducing and explaining intriguing phenomena such as leading pacemaker shifts seen in a variety of experimental conditions.

6.5 Conclusions

To sum up, in this Chapter EGM data of infarcted pigs was analyzed using heart rate variability techniques to investigate the therapeutic effects of chronic vagal nerve stimulation. The results suggest that cVNS is effective in counteracting maladaptive remodelling following MI by stabilizing autonomic input and control of the heart. This is shown by the reduced dispersion in HRV frequency metrics in the MI+cVNS group compared to the control MI group at week 6. cVNS also increases normalized VLF and LF powers while tends to reduce the average heart rate, all indices of better health and prognosis after MI. Future studies are warranted to enlarge the sample size and to understand the mechanism of action and other possible beneficial effects of cVNS.

General conclusions

In recent times, computational models have become a consolidated tool for basic research and have warranted promising clinical applications [42]. Compared to animal experimentation or clinical trials, modelling studies show reduced costs, times and ethical issues. Still, experiments are needed to give data in input to models, creating a paradigm where the feedback between experimental data and model predictions provide the best framework for cardiovascular research [376]. A fundamental strength of biophysically detailed models is that they allow the investigation of the mechanisms underlying phenomena in a direct and controllable way. Taking this dissertation as an example, the conditional removal of specific intracellular processes (e.g., sarcoplasmic calcium release, Chapter 2), perfectly selective ion currents block (e.g., I_f and I_{CaL}, Chapters 3 and 5), the addition of desired amounts of different cellular phenotypes inside cardiac tissues (e.g., Chapters 4 and 5), are all conditions hardly reproducible in the wet lab. This kind of sensitivity analyses are enabled by the development of computational power and high performance computing techniques, which provide reasonable simulation times even when large populations of models or whole organs are studied.

The main limitation of mathematical models remains their validation [377]–[379]. Due to their high non-linearity, springing from the extraordinary complexity of biological organisms, the constant comparison and interaction with experimental data is essential. This is especially true for human cardiac electrophysiology, and even more regarding the sinoatrial node for which the scarcity of data is particularly critical. While mathematical approaches such as automatic parameter optimizations provide some workarounds, these necessitate stricter inspection of their veracity. Experimental data can additionally have flaws that can propagate into the models, even when they are performed according to state-of-the-art methods [380].

Keeping these considerations in mind, some key points can be extracted from the present work. First of all, the simulations with the spatial model of rabbit single sinoatrial node cell (Chapter 2) suggest that the contribution of local calcium releases from ryanodine receptors to the diastolic period depends on the inter-

play between the membrane and the calcium clocks. In fact, blocking LCRs has resulted in both shortening and prolongations of the DD phase according to the relative protein expressions of membrane ion channels and SERCA pump. Interestingly, the presence of LCRs allowed to achieve a wider range of beating rates in both single and coupled cells, in accordance with a recently proposed theory [39]. However, in coupled cells simulations this came at the price of reduced driving ability of the dormant cell by the spontaneous one.

Chapter 3 highlights the remarkable robustness of the isolated SAN towards a number of challenging conditions. Coupled SAN cells are indeed able to synchronize their pacing frequency at physiological rates for human and rabbits despite increasing amounts of heterogeneity, which causes a growing amount of cells to become dormant when isolated. The addition of 50% I_{CaL} block determines a pronounced increase in this amount, bringing the SAN tissue to failure of automaticity. Still, there are protective gap junctional resistivity values that allow few dozens of cells to drive a tissue of thousands. Grouping together these few cells enlarges the range of gap junctional coupling for which the whole tissue rhythmically depolarizes.

The substitution of SAN cells with different numbers of non myocytes (i.e., fibroblasts and connective, fat or scar tissue) was shown in Chapter 4 to not prevent it from reaching synchronization, again highlighting its robustness. Nevertheless, high presence (60% of the tissue) of dormant cells with low heterogeneity or of patchy fibrosis resulted in spontaneous sinus tachycardia.

In Chapter 5 SAN robustness was investigated with respect to atrial driving. In this context, the models showed that heterogeneity, gradients and fibrosis represent fundamental tools to achieve propagation of the heartbeat. This is a fascinating concept since, usually, they are deemed as detrimental while speaking of the working myocardium. For example, heterogeneity in ventricular repolarization times has been recognized as a mechanism of arrhythmia and an underlying cause of sudden cardiac death [381]. Similarly, both fibroblasts proliferation and fibrosis have been shown to serve as a substrate for both ventricular and atrial arrhythmias [255], [300], [304], [382]. Fibrosis is also thought to have a role in sinus node dysfunction [187], [196], [219], [222], [327], [383], [384], even if no clear correlation between the amount of fibrosis and SND onset has been demonstrated [314]. Therefore, thinking that the simulations carried out throughout this work predict that heterogeneity and fibrosis are actually beneficial to SAN physiology, surely requires experimental validation but also warrants further exciting insights. One reason for which previous computational works obtained a hampered SAN function when simulating the presence of non-myocardial tissue is that resistive barriers (fibrosis) or passive loads were used as modelling approaches [184], [187], opposed to the presence of fibroblast-myocyte coupling evaluated in this work. This overlooks their ability to act as current sources when

the SAN cells' membrane voltage is below their resting potential, feature that allows them to actually be beneficial to pacemaking activity ([190] and Chapter 5), as reported in ventricular tissue cultures [325]. Only high amounts of patchy fibrosis – where the active fibroblasts work as functional blocks similar to resistive barriers – favour arrhythmic conditions (Chapter 4).

At present, the only way to effectively treat patients with sinus node dysfunction [40], [54] is the implantation of an electronic pacemaker [41], [53], [61], [213], [294]. These have several shortcomings, among which limited biocompatibility of the materials, battery duration and heart rate modulation can be listed. The results presented in this work can be useful for the design and development of biological pacemakers (BPs), which could overcome the drawbacks of the electronic ones [385]–[387]. For example, the BPs could be tuned to show desired levels of heterogeneity (close to the $\sigma = 0.2$ used in this thesis) and include fibroblasts in SAN hiPSCs-CM (human-induced pluripotent stem cells derived cardiomyocytes) cultures. Further, BPs could enable the reestablishment of autonomic control over the sinoatrial node.

As the results of Chapter 6 contribute to underline, the nervous system is indeed crucial for cardiovascular function. The heart rate variability analysis performed in this work substantiates the hypothesis that vagal nerve stimulation counteracts maladaptive remodelling due to sympathetic over-activation following myocardial infarction. In particular, VNS stabilizes the activity of both branches of the autonomic nervous system, as shown by the reduced variability of the normalized powers in the different spectral bands. Thus, VNS appears a valuable technique that could be applied to the treatment of a variety of cardiac pathology (e.g., myocardial infarction, neurally-induced atrial fibrillation). Being the sinoatrial node the main target of parasympathetic innervation to the heart [269], [388], it constitutes a fundamental part of this treatment. The approach used here to study VNS effectiveness in shaping the pig's recovery from infarction does not allow to investigate the mechanism by which this action in achieved (e.g., what is driving the changes undergoing in the SAN). On the opposite side, there is still a huge gap between computational models like the one used in Chapter 5 and such complex organism-level processes, which has just started to be addressed [374]. The biophysically-detailed multiscale approach – adopted in this dissertation – still appears as the most powerful instrument to unravel the intricate relationship between the heart and the brain.

To conclude, the work carried out in this dissertation will hopefully foster further research on the electrifying sinoatrial node.

Appendices

Appendix A

Table A.1: ***Parameters of the baseline model and 5 randomized cells.***

Parameter	Baseline model	Cell #1	Cell #2	Cell #3	Cell #4	Cell #5
$\mathbf{P_{CaL}}$	0.36036	0.442601	0.345661	0.419823	0.36638	0.403361
$\mathbf{P_{CaT}}$	0.808023	0.8721	1.160421	0.831228	1.172885	0.941354
$\mathbf{g_{Kr}}$	0.056798	0.0561	0.055484	0.083523	0.058341	0.071164
$\mathbf{g_{Ks}}$	0.083711	0.091581	0.106977	0.095727	0.061447	0.086115
$\mathbf{g_{Na}}$	0.631268	0.608277	0.696954	0.617518	0.688411	0.928302
$\mathbf{g_{fNa}}$	1.010029	1.241765	1.211304	1.087815	1.031041	1.155007
$\mathbf{g_{fK}}$	2.020057	1.478146	1.603649	2.515432	1.802287	1.976057
$\mathbf{g_{to}}$	0.101003	0.16199	0.129886	0.093272	0.111471	0.108781
$\mathbf{I_{NaKmax}}$	3.18159	3.014186	4.254118	3.127671	2.761788	3.961806
$\mathbf{I_{NaCamax}}$	0.013013	0.010171	0.00859	0.020918	0.009938	0.012017
$\mathbf{P_{up}}$	0.014	0.011135	0.013514	0.012734	0.009857	0.013763

Table A.2: ***AP features of the baseline model and 5 heterogeneous cells with and without LCRs in diastole****. Cycle length (CL), Maximum Diastolic Potential (MDP), Action Potential Amplitude (APA), Overshoot (OS), Action Potential Duration at 50% repolarization (APD_{50}), Maximum Upstroke Velocity (dV/dt_{max}), Take-off potential (TOP), and ratio between charges fluxes during DD: sodium-calcium exchanger (Q_{NaCa}), funny channels charge (Q_f) and total charge (Q_{tot}). Data is shown as mean $\pm$ standard deviation; values were averaged on the last 2 s of 20 s simulation for the baseline simulation; the first cycle was used in all other simulations to see acute effects of LCRs switch-off. The first rows represent control conditions, the second rows in italic represent the condition with no LCRs.*

Feature	Baseline model	Cell #1	Cell #2	Cell #3	Cell #4	Cell #5
DD(ms)	193±1	129	112	278	218	168
	308	*168*	*166*	*151*	*158*	*187*
MDP(mV)	-61±0.1	-61	-59	-65	-62	-63
	-58.5	*-63*	*-62*	*-63*	*-63*	*-63*
APA(mV)	78±0.8	75	76	85	74	77
	67	*81*	*80*	*81*	*81*	*81*
OS(mV)	19±0.7	14	17	20	12	14
	8	*18*	*18*	*18*	*18*	*18*
APD_{50}(ms)	131±0.4	126	125	120	107	103
	118	*126*	*125*	*125*	*125*	*125*
dV/dt_{max}(V/s)	6.4±0.2	6.3	6.1	8.8	6.5	7.4
	3.7	*8.8*	*8.7*	*8.8*	*8.7*	*8.7*
TOP(mV)	-34.9	-36.3	-34.7	-32.2	-33.5	-33.8
	-34.2	*-31.3*	*-31*	*-31.4*	*-31.4*	*-31.6*
Q_{NaCa}/Q_f(%)	87.2	62.5	163	66.1	51.7	59.5
	55	*39.5*	*53.5*	*26.4*	*32.8*	*42.7*
Q_{NaCa}/Q_{tot}(%)	111	84	100	119.4	99.4	93
	111.3	*61.6*	*72*	*36.8*	*46.5*	*66.1*
Q_f/Q_{tot}(%)	127.3	134.5	61.1	180.5	192.4	156.3
	202.3	*155.8*	*134.9*	*139.7*	*141.8*	*154.6*

Appendix B

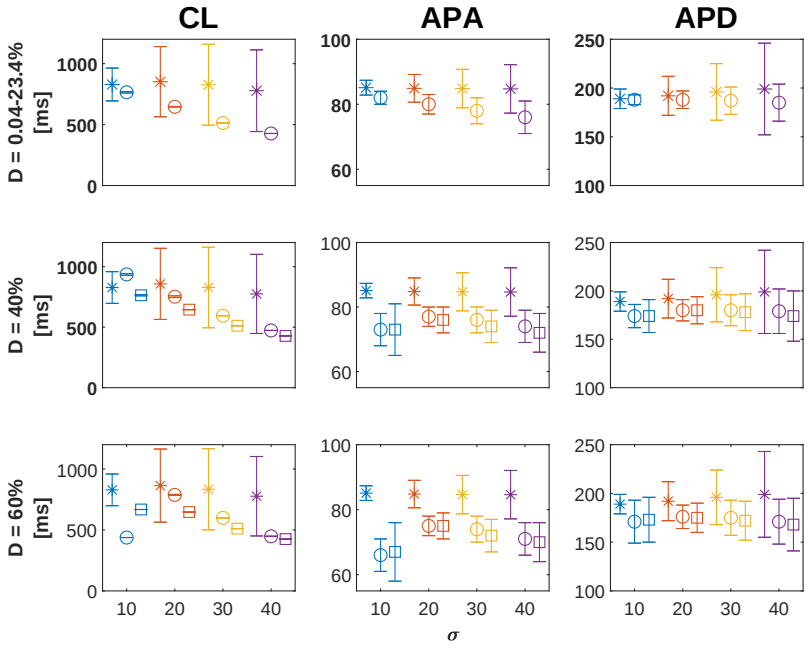

Figure B.1: ***AP features of the tissue containing dormant cells at different densities (D) and SAN heterogeneity levels (σ).*** *Asterisks (∗) identify simulations with uncoupled cells, whereas circles (○) and squares (□) identify simulations with random and cluster distributions, respectively. Mean±std.*

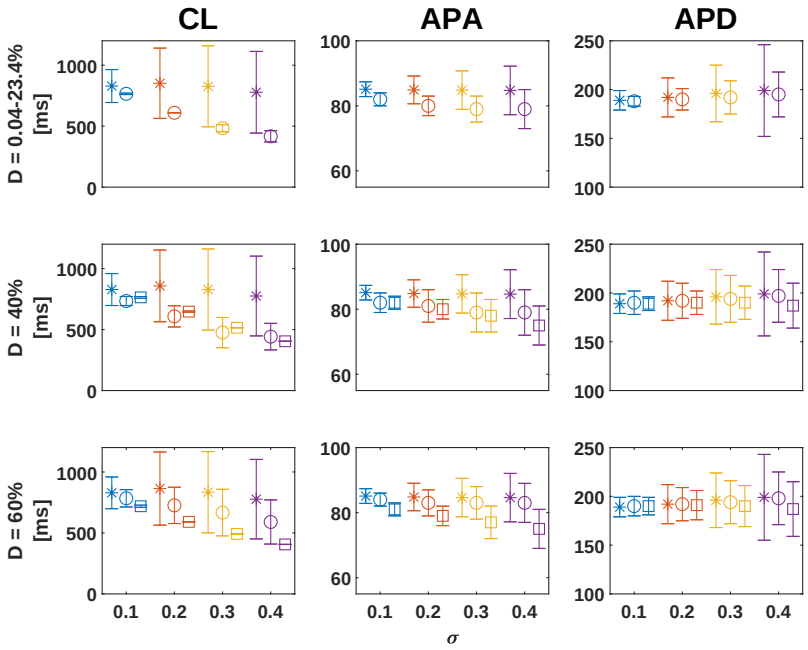

Figure B.2: ***AP features of the tissue containing scars at different densities*** *(D)* ***and SAN heterogeneity levels*** *(σ). Asterisks (∗) identify simulations with uncoupled cells, whereas circles (○) and squares (□) identify simulations with random and cluster distributions, respectively. Mean±std.*

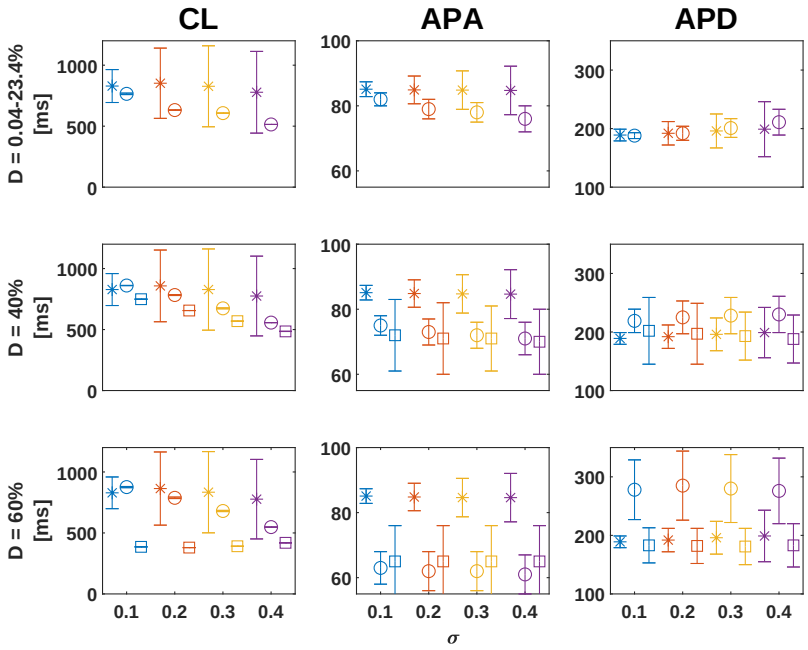

Figure B.3: ***AP features of the tissue containing fibroblasts at different densities*** *(D)* ***and SAN heterogeneity levels*** *(σ). Asterisks (∗) identify simulations with uncoupled cells, whereas circles (○) and squares (□) identify simulations with random and cluster distributions, respectively. Mean±std.*

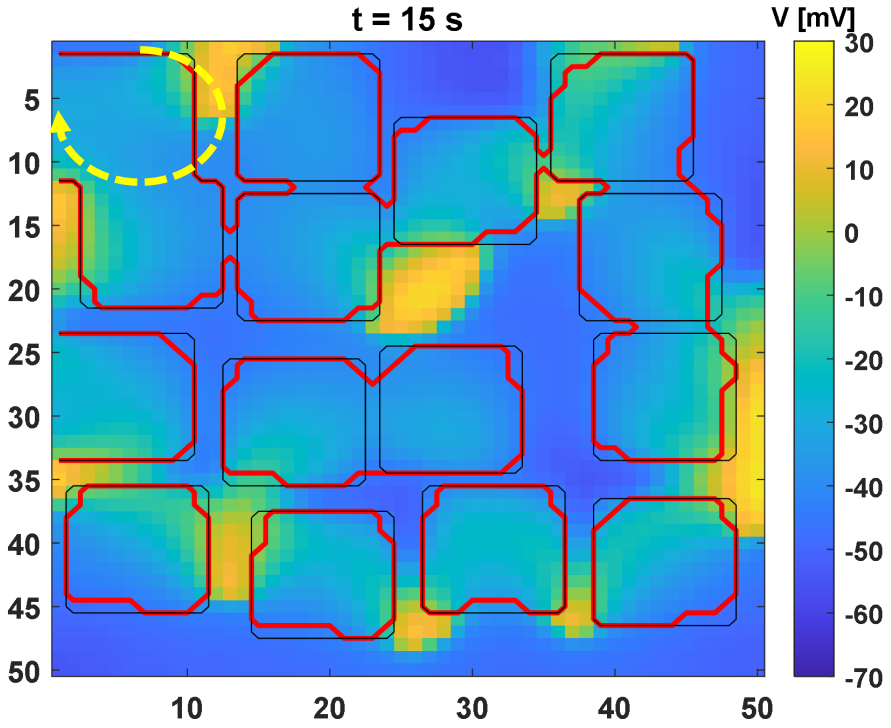

Figure B.4: ***Voltage map showing the electrical activity of the 2D tissue with fibroblasts distributed in clusters (black rectangles),*** $D = 60\%$, $\sigma = 0.1$. *The red lines encircle cells not reaching 0 mV, while the yellow dashed arrow shows the reentrant pathway around one cluster determining the tachycardia seen in this condition (*$CL = 438\,\text{ms}$*).*

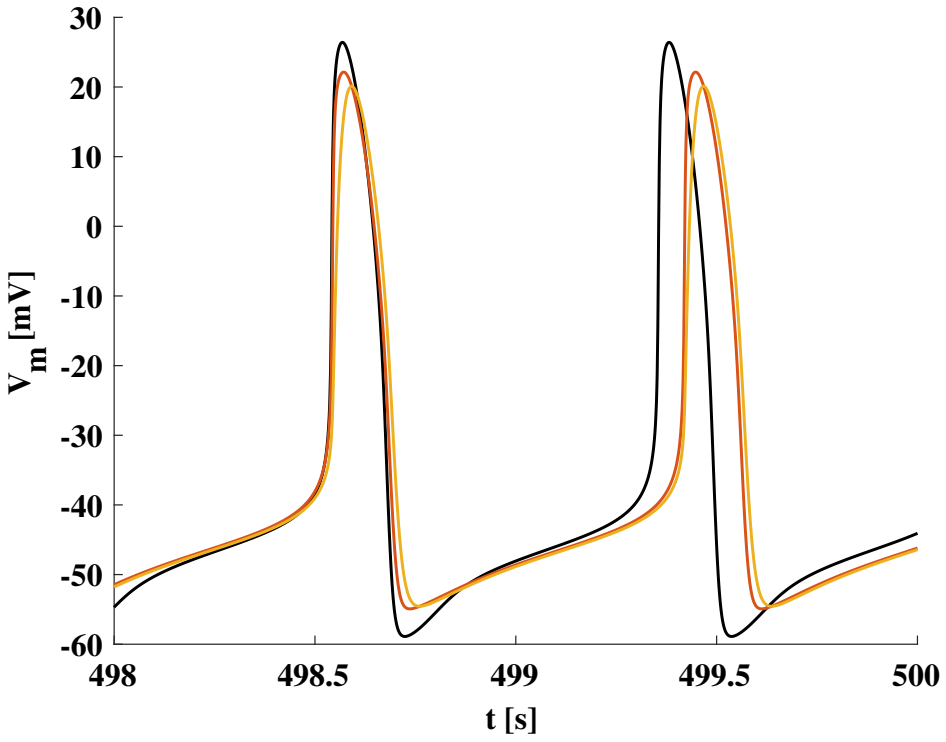

Figure B.5: ***Effect of one fibroblast on a single human SAN cell model AP****. The black trace represent the AP of the isolated single human cell FWS model [25], while the orange and yellow ones represent respectively the APs of the SAN cell and fibroblast (Morgan model [255]) when coupled together with* $R_{gap} = 1\,\mathrm{G}\Omega$.

Appendix C

Supplemental Methods

In order to simulate simultaneous administration of ACh and ISO, the FWS model [25] was modified to take into account their effects in an additive manner. In the model, the only target shared by parasympathetic and sympathetic stimulation is the parameter b_{up}, the basal uptake rate of the SERCA pump. Its dependence on ACh and ISO concentrations was thus according to the following equation:

$$b_{up} = \frac{0.7 * [ACh]}{0.0009 + [ACh]} - 0.25$$

where the first term represents the dose-dependent ACh response and the second one a fixed reduction due to ISO at a fixed concentration of 1 μM.

Supplemental Figures and Tables

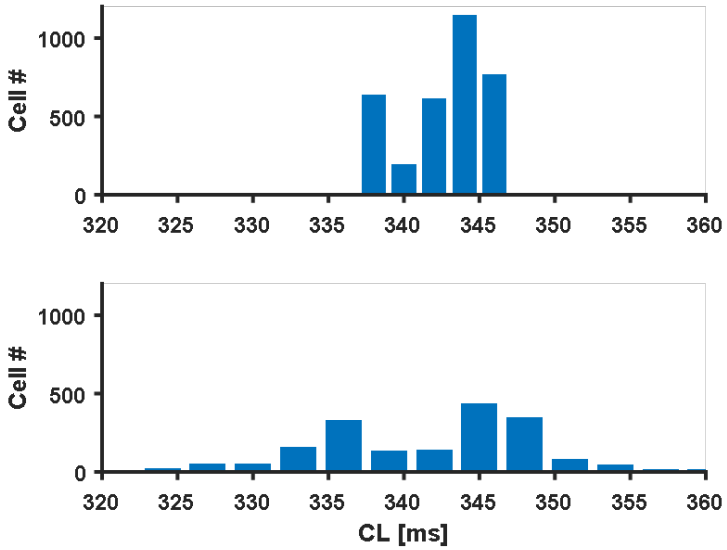

Figure C.1: ***Example of cycle length distributions in rabbit SAN during atrial driving****. (Top) heterogeneous condition and (bottom) heterogeneous and fibrosis condition of central and right panel of Figure 5.4, respectively.*

Table C.1: ***Biomarkers of the reduced MBS model.*** *Experimental data is reported as mean and range [lower bound, upper bound]. APD: action potential duration at 90, 50 and 30% of repolarization; V_{amp}: voltage difference between overshoot and resting membrane potential; $V : diast$: resting membrane potential; dV/dt_{max}: maximal upstroke velocity; Ca_{sys}: systolic calcium concentration in the cytosol; Ca_{dias}: diastolic calcium concentration in the cytosol; ttp_{ca}: time to calcium concentration peak in the cytosol; rt_{50Ca}: rise time to 50% calcium concentration peak in the cytosol; TT_{Ca}: total transient duration. Definitions as in [27].*

Biomarker	*Experimental data*	*Original MBS*	*Reduced MBS*
Action potential			
APD_{90} [ms]	263 [202, 332]	225	238
APD_{50} [ms]	50 [25, 94]	45	50
APD_{30} [ms]	8 [5, 14]	8	14
V_{amp} [mV]	103 [83 130]	120	112
V_{rest} [mV]	-75 [-68, -75]	-75	-76
dV/dt_{max} [mV ms^{-1}]	179 [159, 232]	199	177
Ca^{2+} transient			
Ca_{sys} [µM]	0.268 [0.18, 0.4]	0.221	0.519
Ca_{dias} [µM]	0.223 [0.2, 0.25]	0.187	0.172
ttp_{Ca} [ms]	53 [49, 56]	94	53
rt_{50Ca} [ms]	178 [169, 187]	173	106
TT_{Ca} [ms]	539 [508, 570]	690	404

Table C.2: ***Action potential features in the SAN in different configurations in basal conditions.*** *The H, F and HF configuration reported are for tissue #1.*

Feature	**U**	**H**	**UF**	**HF**
Whole SAN				
CL [ms]	810±52.5	624±9.3	815±32.5	639±0.7
MDP [mV]	-58.5±1.6	-56±2.5	-55.8±2.6	-54.4±6.4
dV/dt_{max} [mV ms^{-1}]	7.4±1.3	8.5±1.9	7.9±2.2	8.4±2.6
Leading SEP only				
CL [ms]	814±0.1	624±1.9	817±0.1	639±0.1
MDP [mV]	-55.7±2.2	-56.1±2.4	-57.8±5.3	-59±6.4
dV/dt_{max} [mV ms^{-1}]	7.7±4.4	7.6±3.7	9.3±5.6	10.4+6.9

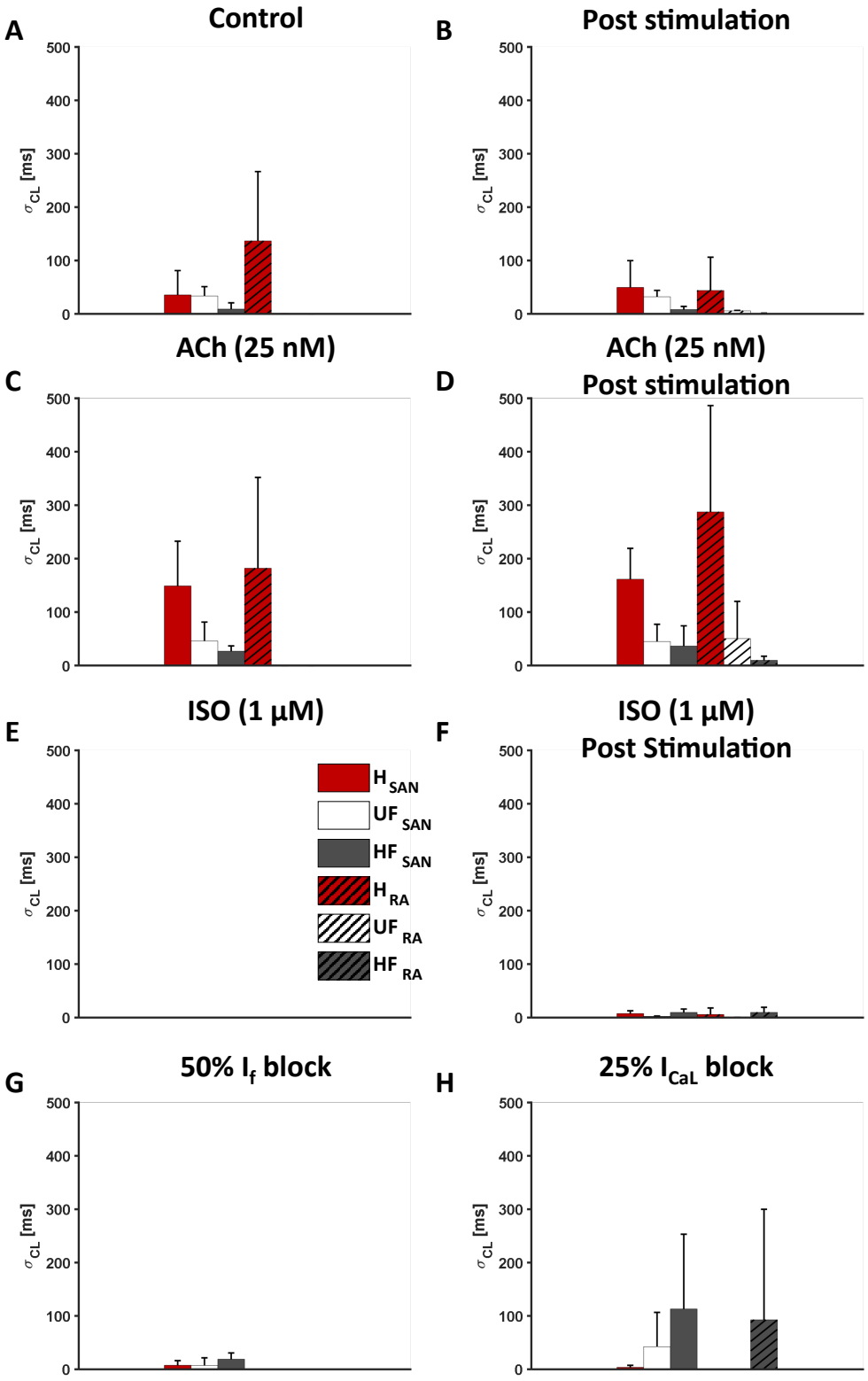

Figure C.2: ***SAN and RA CL standard deviation of the human model in different conditions****. In the SAN, σ_{CL} reports SAN myocytes synchronization; in the RA (hatched bars), it can inform on the presence of SEP alternans or exit blocks. H: heterogeneity; UF: fibroblasts; HF: heterogeneity and fibroblasts.*

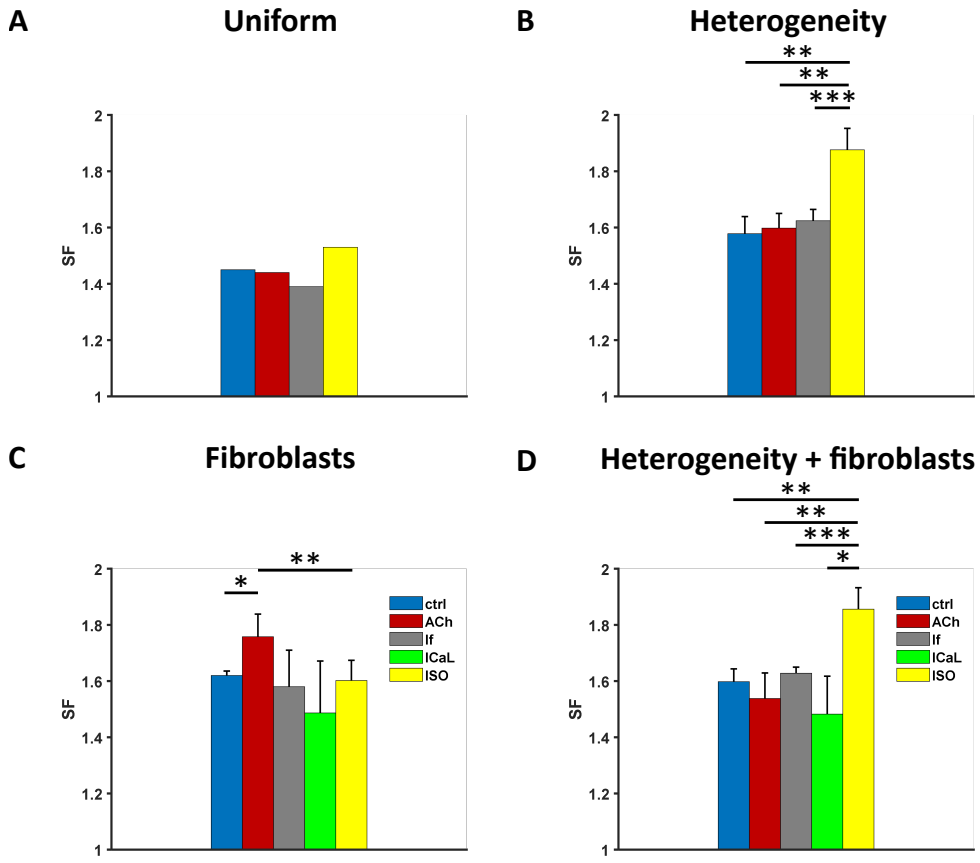

Figure C.3: ***Comparisons of safety factor values in the human model in different conditions****. A) Uniform condition. B) Presence of heterogeneity. C) Presence of fibroblasts. D) Presence of heterogeneity and fibrosis. No atrial driving was achieved with 25% I_{CaL} block in the A) and B).*

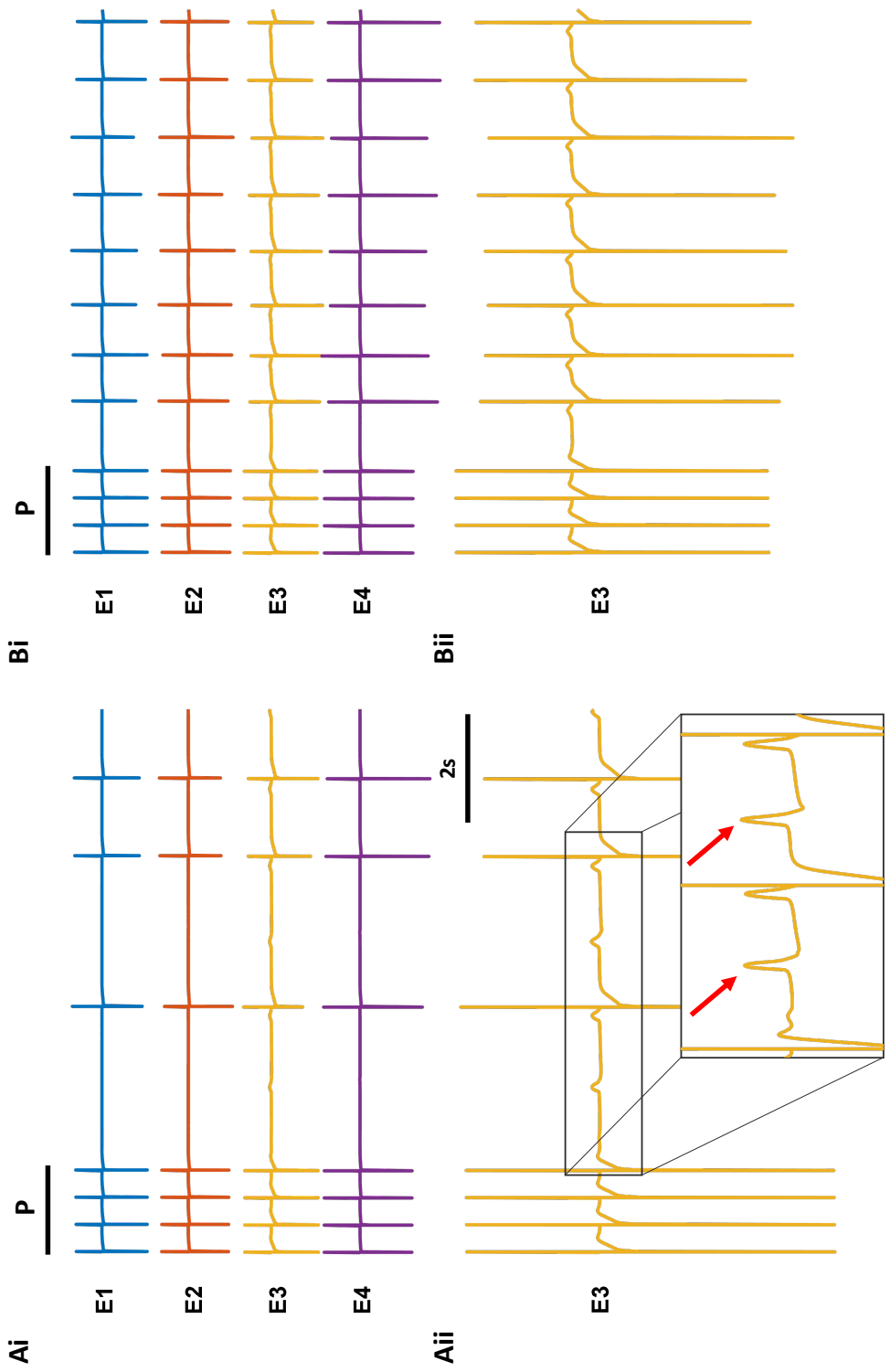

Figure C.4: ***Electromiograms in the tissue with ACh administration during and after pacing****. Ai) Uniform SAN tissue recordings with the 4 electrodes of Figure 5.3; Aii) Electrode #3 signal with zooming on activity after pacing is stopped. The red arrow indicate SAN activity not follow by the atrial spike (exit blocks). Bi) HF model #1 recordings and Bii) zoom on electrode #3. P: pacing.*

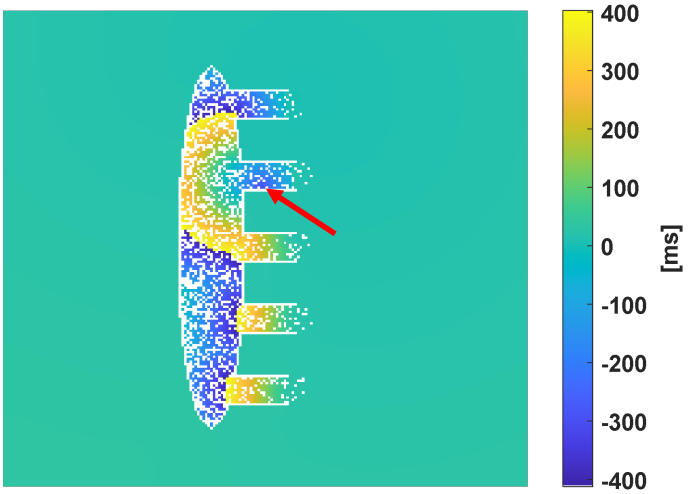

Figure C.5: ***Activation time map of model #2 of the HF condition with 25% I_{CaL} block.*** *Atrial activation at the SEP interface is taken as the reference instant. As pointed by the red arrow, activation start in SEP #2 and travels both retrograde inside the SAN and forward to excite the atrium. White picels represent the fibroblasts.*

Table C.3: ***Action potential features in the SAN in different configurations with 25% I_{CaL} block.*** *The H and HF configuration reported are for tissue #1.*

Feature	U	H	UF	HF
Whole SAN				
CL [ms]	1131±0.1	884±1.9	1073±155	805±24.9
MDP [mV]	-58.5±2.1	-55.7±2.5	-54.9±1.9	-53.6±3
dV/dt_{max} [mV ms^{-1}]	5.4±0.6	6.1±1.2	5.5±0.7	6.5±2.4
Leading SEP only				
CL [ms]	1131±0.1	883±4.1	1296±433	806±0.1
MDP [mV]	-59.1±5.2	-58.9±5.2	-55.8±3.9	-55.1±3.4
dV/dt_{max} [mV ms^{-1}]	5.4±1.5	5.8±1.7	5.1±1.8	7.2±4.6

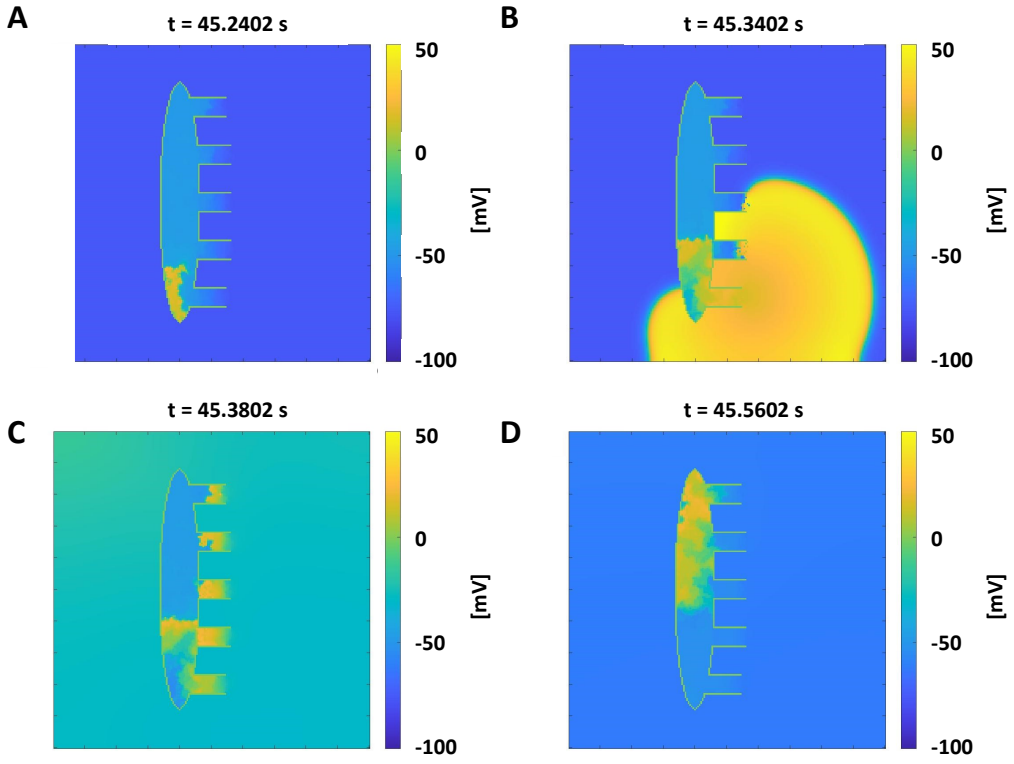

Figure C.6: ***Activation sequence in the "full" model with heterogeneity and fibrosis plus 25 nM acetylcholine and 1 µM isoproterenol administration.*** *Here R_{gap} of the fibroblast is equal to 1 GΩ. A, B C and D represent sequential frames of the activation: the beat originates in the SAN tail, exits from SEP #5 and re-enters from SEPs #1-4 reaching SAN center and head in $\sim$ 300 ms.*

Appendix D

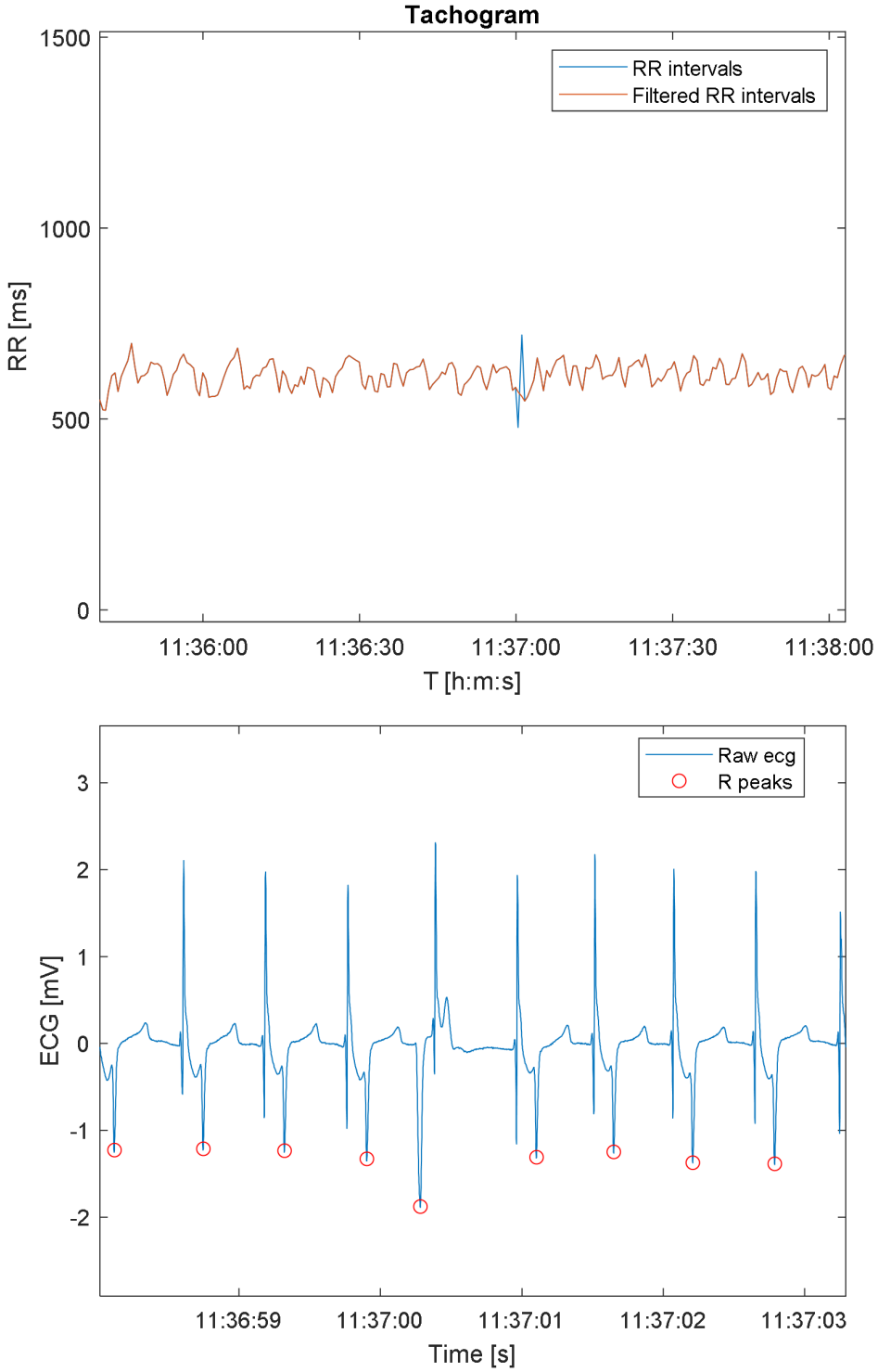

Figure D.1: ***PVC filtering****. Original and filtered (i.e. with removed PVC) tachograms (top) and corresponding raw ECG signal (bottom).*

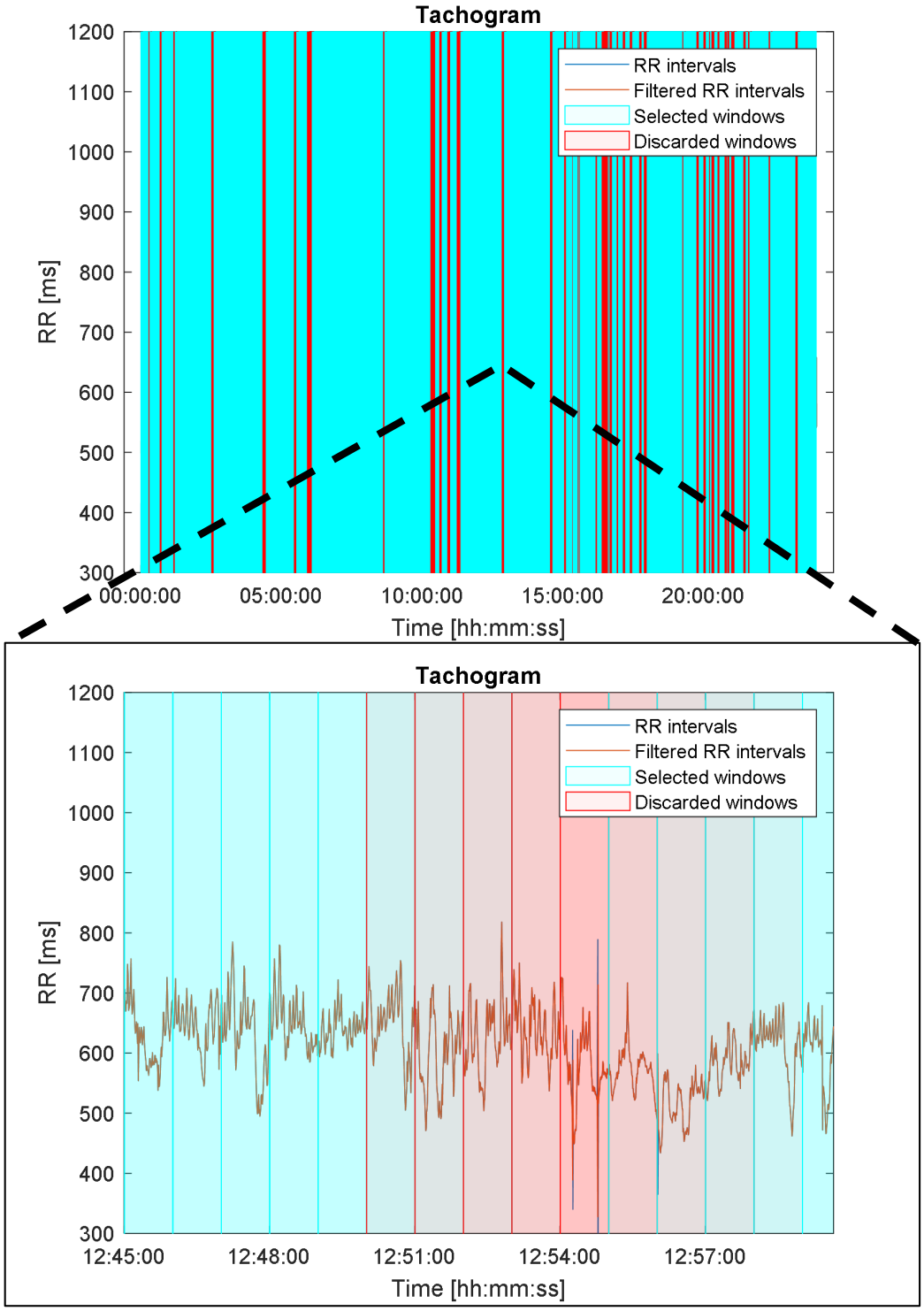

Figure D.2: ***PVC filtering and noisy 5-minutes tachogram windows removal.*** *24h tachogram (top) and close-up inspection of removed 5-minutes windows due to artifacts presence (bottom).*

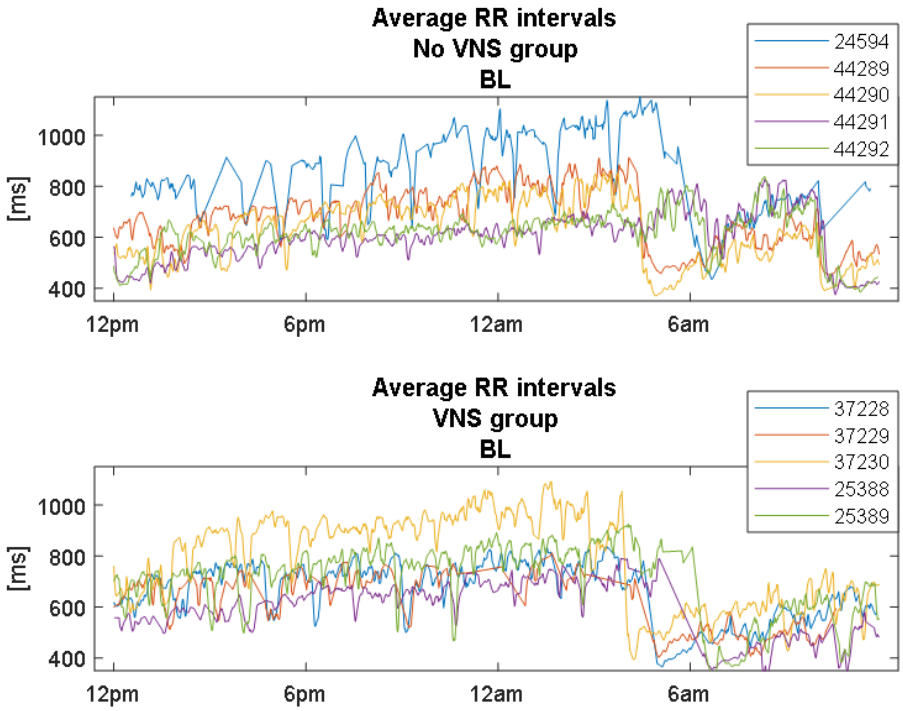

Figure D.3: ***Circadian variations of average RR intervals****. RR intervals were averaged over 5-minutes window and plotted against time during the day for all pigs at baseline. MI group (top) and MI+cVNS group (bottom).*

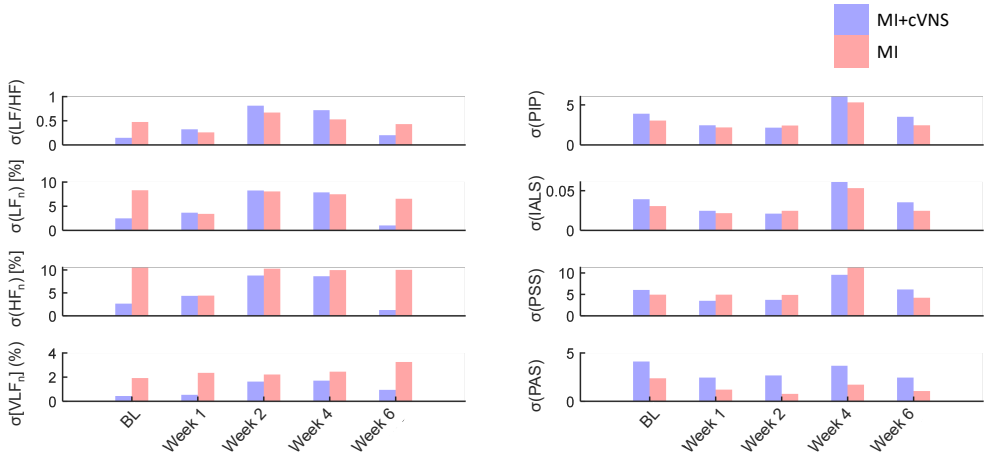

Figure D.4: ***Standard deviation of frequency-domain (left) and fragmentation (right) HRV metrics****.*

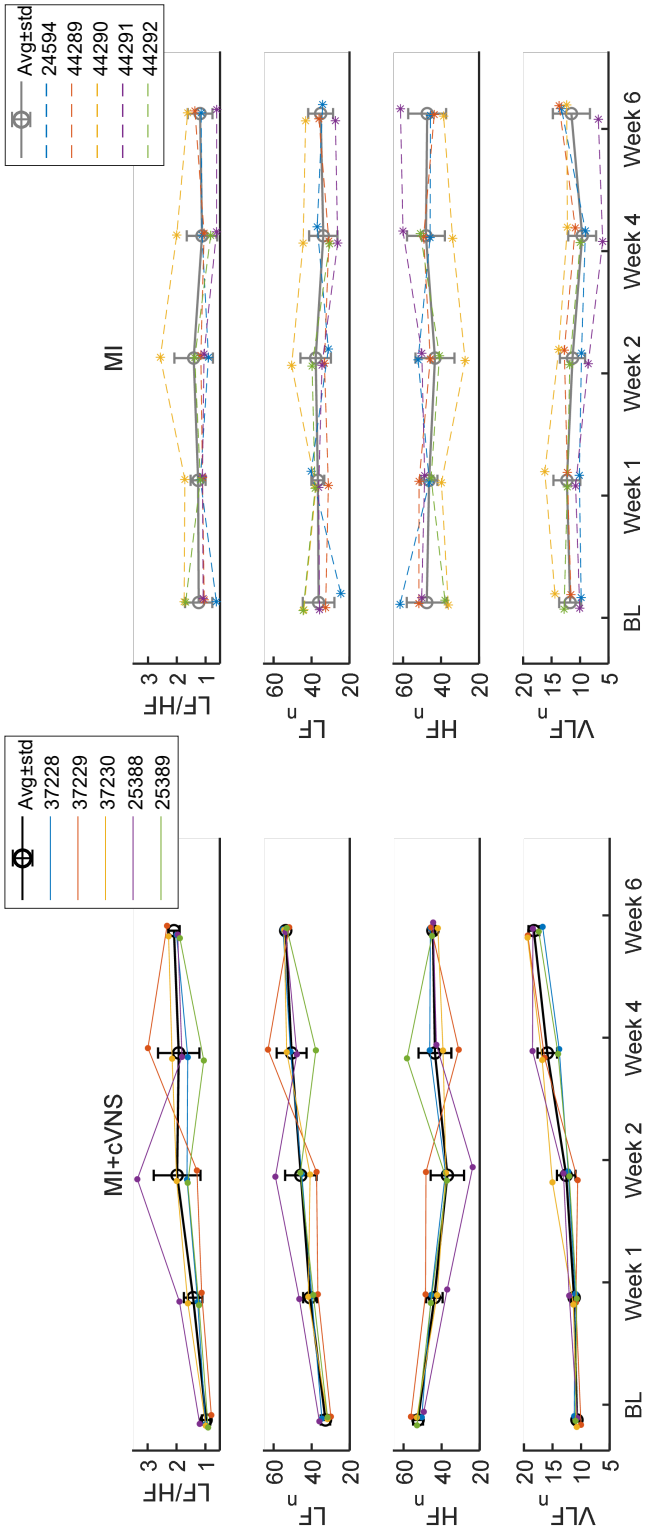

Figure D.5: ***Frequency-domain HRV metrics results disaggregated by pig****. Black and gray solid lines and dots show mean±std values for MI+cVNS and MI groups (as reported in Figure 6.4). Colored lines show trends for individual pigs for both MI+cVNS (left, solid lines and dots) and MI (right, dashed lines and asterisks) groups, respectively.*

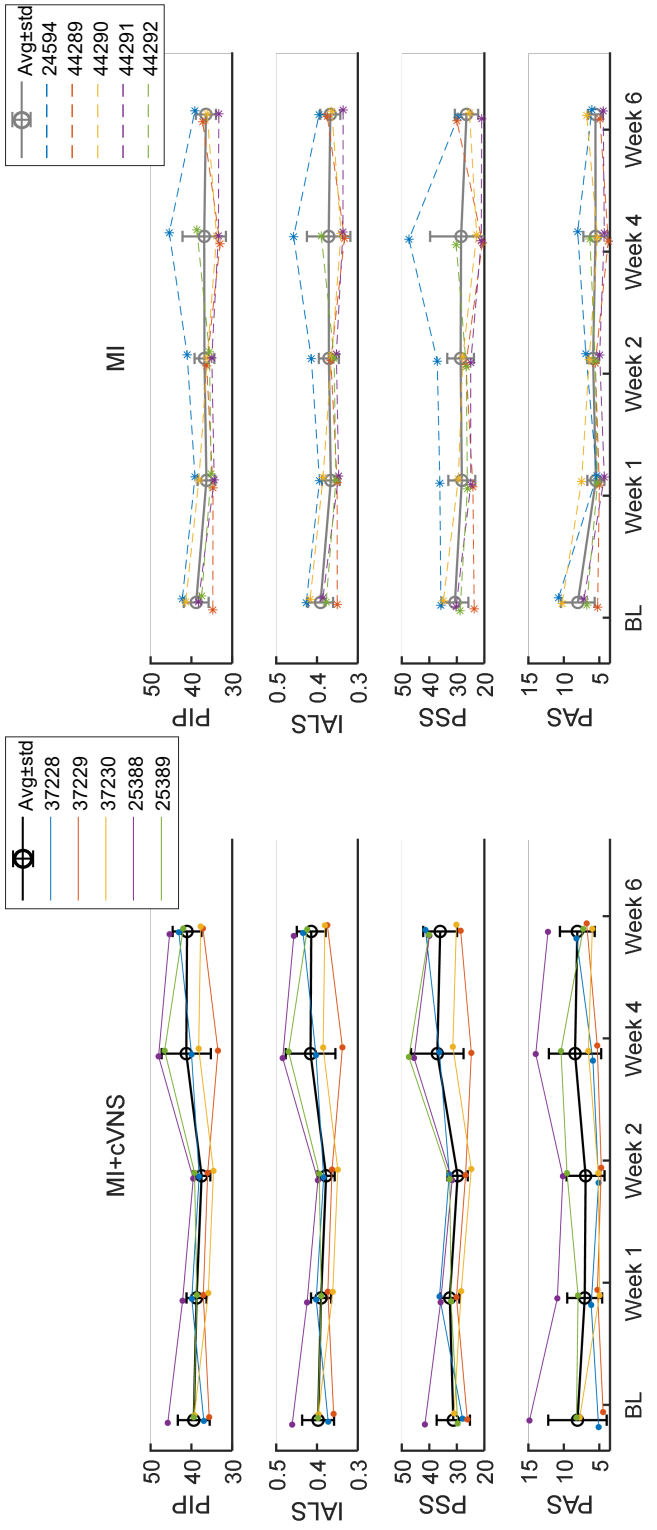

Figure D.6: ***Fragmentation HRV metrics results disaggregated by pig****. Black and gray solid lines and open dots show mean±std values for MI+cVNS and MI groups (as reported in Figure 6.4). Colored lines show trends for individual pigs for both MI+cVNS (left, solid lines abd dots) and MI (right, dashed lines and asterisks) groups, respectively.*

Bibliography

[1] M. Boyett, H. Honjo, and I. Kodama, "The sinoatrial node, a heterogeneous pacemaker structure," *Cardiovascular Research*, pp. 658–687, Sep. 2000. DOI: 10.1016/S0008-6363(00)00135-8.

[2] M. E. Mangoni and J. Nargeot, "Genesis and Regulation of the Heart Automaticity," en, *Physiological Reviews*, pp. 919–982, Jul. 2008. DOI: 10.1152/physrev.00018.2007.

[3] O. Monfredi, H. Dobrzynski, T. Mondal, M. R. Boyett, and G. M. Morris, "The Anatomy and Physiology of the Sinoatrial Node—A Contemporary Review," en, *Pacing and Clinical Electrophysiology*, pp. 1392–1406, 2010. DOI: 10.1111/j.1540-8159.2010.02838.x.

[4] H. Dobrzynski, R. H. Anderson, A. Atkinson, *et al.*, "Structure, function and clinical relevance of the cardiac conduction system, including the atrioventricular ring and outflow tract tissues," en, *Pharmacology & Therapeutics*, pp. 260–288, Aug. 2013. DOI: 10.1016/j.pharmthera.2013.04.010.

[5] S. D. Unudurthi, R. M. Wolf, and T. J. Hund, "Role of sinoatrial node architecture in maintaining a balanced source-sink relationship and synchronous cardiac pacemaking," en, *Frontiers in Physiology*, Nov. 2014. DOI: 10.3389/fphys.2014.00446.

[6] M. Easterling, S. Rossi, A. J. Mazzella, and M. Bressan, "Assembly of the Cardiac Pacemaking Complex: Electrogenic Principles of Sinoatrial Node Morphogenesis," en, *Journal of Cardiovascular Development and Disease*, p. 40, Apr. 2021. DOI: 10.3390/jcdd8040040.

[7] T. Kurian, C. Ambrosi, W. Hucker, V. V. Fedorov, and I. R. Efimov, "Anatomy and Electrophysiology of the Human AV Node: FUNCTIONAL ANATOMY OF AV NODE," en, *Pacing and Clinical Electrophysiology*, pp. 754–762, Feb. 2010. DOI: 10.1111/j.1540-8159.2010.02699.x.

[8] J. Billette and R. Tadros, "An integrated overview of AV node physiology," en, *Pacing and Clinical Electrophysiology*, pp. 805–820, Jul. 2019. DOI: 10.1111/pace.13734.

[9] S. M. Markowitz and B. B. Lerman, "A contemporary view of atrioventricular nodal physiology," en, *Journal of Interventional Cardiac Electrophysiology*, pp. 271–279, Aug. 2018. DOI: 10.1007/s10840-018-0392-5.

[10] D. Noble, "A modification of the Hodgkin-Huxley equations applicable to Purkinje fibre action and pacemaker potentials," en, *The Journal of Physiology*, pp. 317–352, Feb. 1962. DOI: 10.1113/jphysiol.1962.sp006849.

[11] R. E. McAllister, D. Noble, and R. W. Tsien, "Reconstruction of the electrical activity of cardiac Purkinje fibres," eng, *The Journal of Physiology*, pp. 1–59, Sep. 1975. DOI: 10.1113/jphysiol.1975.sp011080.

[12] G. W. Beeler and H. Reuter, "Reconstruction of the action potential of ventricular myocardial fibres," en, *The Journal of Physiology*, pp. 177–210, 1977. DOI: 10.1113/jphysiol.1977.sp011853.

[13] D. DiFrancesco and D. Noble, "A model of cardiac electrical activity incorporating ionic pumps and concentration changes," en, *Philosophical Transactions of the Royal Society of London. B, Biological Sciences*, pp. 353–398, Jan. 1985. DOI: 10.1098/rstb.1985.0001.

[14] D. W. Hilgemann and D. Noble, "Excitation-contraction coupling and extracellular calcium transients in rabbit atrium: Reconstruction of basic cellular mechanisms," eng, *Proceedings of the Royal Society of London. Series B, Biological Sciences*, pp. 163–205, Mar. 1987. DOI: 10.1098/rspb.1987.0015.

[15] C. H. Luo and Y. Rudy, "A dynamic model of the cardiac ventricular action potential. I. Simulations of ionic currents and concentration changes.," *Circulation Research*, pp. 1071–1096, Jun. 1994, Publisher: American Heart Association. DOI: 10.1161/01.RES.74.6.1071.

[16] T. O'Hara, L. Virág, A. Varró, and Y. Rudy, "Simulation of the Undiseased Human Cardiac Ventricular Action Potential: Model Formulation and Experimental Validation," en, *PLoS Computational Biology*, A. D. McCulloch, Ed., e1002061, May 2011. DOI: 10.1371/journal.pcbi.1002061.

[17] M. Courtemanche, R. J. Ramirez, and S. Nattel, "Ionic mechanisms underlying human atrial action potential properties: Insights from a mathematical model," eng, *The American Journal of Physiology*, H301–321, Jul. 1998. DOI: 10.1152/ajpheart.1998.275.1.H301.

[18] K. H. W. J. ten Tusscher, D. Noble, P. J. Noble, and A. V. Panfilov, "A model for human ventricular tissue," *American Journal of Physiology-Heart and Circulatory Physiology*, H1573–H1589, Apr. 2004, Publisher: American Physiological Society. DOI: 10.1152/ajpheart.00794.2003.

[19] E. Grandi, S. V. Pandit, N. Voigt, *et al.*, "Human Atrial Action Potential and Ca2+ Model," *Circulation Research*, pp. 1055–1066, Oct. 2011, Publisher: American Heart Association. DOI: 10.1161/CIRCRESAHA.111.253955.

[20] J. T. Koivumäki, T. Korhonen, and P. Tavi, "Impact of Sarcoplasmic Reticulum Calcium Release on Calcium Dynamics and Action Potential Morphology in Human Atrial Myocytes: A Computational Study," en, *PLOS Computational Biology*, e1001067, Jan. 2011, Publisher: Public Library of Science. DOI: 10.1371/journal.pcbi.1001067.

[21] Y. Kurata, I. Hisatome, S. Imanishi, and T. Shibamoto, "Dynamical description of sinoatrial node pacemaking: Improved mathematical model for primary pacemaker cell," en, *American Journal of Physiology-Heart and Circulatory Physiology*, H2074–H2101, Nov. 2002. DOI: 10.1152/ajpheart.00900.2001.

[22] V. A. Maltsev and E. G. Lakatta, "Synergism of coupled subsarcolemmal Ca $^{2+}$ clocks and sarcolemmal voltage clocks confers robust and flexible pacemaker function in a novel pacemaker cell model," en, *American Journal of Physiology-Heart and Circulatory Physiology*, H594–H615, Mar. 2009. DOI: 10.1152/ajpheart.01118.2008.

[23] S. Kharche, J. Yu, M. Lei, and H. Zhang, "A mathematical model of action potentials of mouse sinoatrial node cells with molecular bases," en, *American Journal of Physiology-Heart and Circulatory Physiology*, H945–H963, Sep. 2011. DOI: 10.1152/ajpheart.00143.2010.

[24] S. Severi, M. Fantini, L. A. Charawi, and D. DiFrancesco, "An updated computational model of rabbit sinoatrial action potential to investigate the mechanisms of heart rate modulation: Model of SAN action potential," en, *The Journal of Physiology*, pp. 4483–4499, Sep. 2012. DOI: 10.1113/jphysiol.2012.229435.

[25] A. Fabbri, M. Fantini, R. Wilders, and S. Severi, "Computational analysis of the human sinus node action potential: Model development and effects of mutations: Model of the human sinoatrial AP," en, *The Journal of Physiology*, pp. 2365–2396, Apr. 2017. DOI: 10.1113/JP273259.

[26] C. Bartolucci, E. Passini, J. Hyttinen, M. Paci, and S. Severi, "Simulation of the Effects of Extracellular Calcium Changes Leads to a Novel Computational Model of Human Ventricular Action Potential With a Revised Calcium Handling," en, *Frontiers in Physiology*, p. 314, Apr. 2020. DOI: 10.3389/fphys.2020.00314.

[27] F. Mazhar, C. Bartolucci, F. Regazzoni, *et al.*, "A detailed mathematical model of the human atrial cardiomyocyte: Integration of electrophysiology and cardiomechanics," en, *The Journal of Physiology*, 2023. DOI: 10.1113/JP283974.

[28] A. Muszkiewicz, O. J. Britton, P. Gemmell, *et al.*, "Variability in cardiac electrophysiology: Using experimentally-calibrated populations of models to move beyond the single virtual physiological human paradigm," *Progress in Biophysics and Molecular Biology*, Recent Developments in Biophysics & Molecular Biology of Heart Rhythm, pp. 115–127, Jan. 2016. DOI: 10.1016/j.pbiomolbio.2015.12.002.

[29] O. J. Britton, A. Bueno-Orovio, K. Van Ammel, *et al.*, "Experimentally calibrated population of models predicts and explains intersubject variability in cardiac cellular electrophysiology," *Proceedings of the National Academy of Sciences*, E2098–E2105, Jun. 2013, Publisher: Proceedings of the National Academy of Sciences. DOI: 10.1073/pnas.1304382110.

[30] W. Groenendaal, F. A. Ortega, A. R. Kherlopian, A. C. Zygmunt, T. Krogh-Madsen, and D. J. Christini, "Cell-Specific Cardiac Electrophysiology Models," en, *PLOS Computational Biology*, e1004242, Apr. 2015, Publisher: Public Library of Science. DOI: 10.1371/journal.pcbi.1004242.

[31] A. Carusi, K. Burrage, and B. Rodríguez, "Bridging experiments, models and simulations: An integrative approach to validation in computational cardiac electrophysiology," en, *American Journal of Physiology-Heart and Circulatory Physiology*, H144–H155, Jul. 2012. DOI: 10.1152/ajpheart.01151.2011.

[32] J. Q. X. Gong and E. A. Sobie, "Population-based mechanistic modeling allows for quantitative predictions of drug responses across cell types," en, *npj Systems Biology and Applications*, pp. 1–11, Feb. 2018, Number: 1 Publisher: Nature Publishing Group. DOI: 10.1038/s41540-018-0047-2.

[33] A. V. Maltsev, M. D. Stern, E. G. Lakatta, and V. A. Maltsev, "Functional Heterogeneity of Cell Populations Increases Robustness of Pacemaker Function in a Numerical Model of the Sinoatrial Node Tissue," eng, *Frontiers in Physiology*, p. 845 634, 2022. DOI: 10.3389/fphys.2022.845634.

[34] C. Campana, E. Ricci, C. Bartolucci, S. Severi, and E. A. Sobie, "Coupling and heterogeneity modulate pacemaking capability in healthy and diseased two-dimensional sinoatrial node tissue models," en, *PLOS Computational Biology*, e1010098, Nov. 2022, Publisher: Public Library of Science. DOI: 10.1371/journal.pcbi.1010098.

[35] A. V. Maltsev, M. D. Stern, and V. A. Maltsev, "Disorder in Ca2+ release unit locations confers robustness but cuts flexibility of heart pacemaking," *Journal of General Physiology*, e202113061, Aug. 2022. DOI: 10.1085/jgp.202113061.

[36] Y. Himeno, N. Sarai, S. Matsuoka, and A. Noma, "Ionic Mechanisms Underlying the Positive Chronotropy Induced by β1-Adrenergic Stimulation in Guinea Pig Sinoatrial Node Cells: A Simulation Study," en, *The Journal of Physiological Sciences*, pp. 53–65, 2008. DOI: 10.2170/physiolsci.RP015207.

[37] A. Keith and M. Flack, "The Form and Nature of the Muscular Connections between the Primary Divisions of the Vertebrate Heart," *Journal of Anatomy and Physiology*, pp. 172–189, Apr. 1907.

[38] E. G. Lakatta and D. DiFrancesco, "What keeps us ticking: A funny current, a calcium clock, or both?" en, *Journal of Molecular and Cellular Cardiology*, pp. 157–170, Aug. 2009. DOI: 10.1016/j.yjmcc.2009.03.022.

[39] J. N. Weiss and Z. Qu, "The Sinus Node," en, *JACC: Clinical Electrophysiology*, S2405500X20309622, Nov. 2020. DOI: 10.1016/j.jacep.2020.09.017.

[40] P. Mesirca, V. V. Fedorov, T. J. Hund, *et al.*, "Pharmacologic Approach to Sinoatrial Node Dysfunction," en, *Annual Review of Pharmacology and Toxicology*, annurev–pharmtox–031120–115 815, Jan. 2021. DOI: 10.1146/annurev-pharmtox-031120-115815.

[41] O. Monfredi and M. Boyett, "Sick sinus syndrome and atrial fibrillation in older persons — A view from the sinoatrial nodal myocyte," en, *Journal of Molecular and Cellular Cardiology*, pp. 88–100, Jun. 2015. DOI: 10.1016/j.yjmcc.2015.02.003.

[42] P. T. Sager, G. Gintant, J. R. Turner, S. Pettit, and N. Stockbridge, "Rechanneling the cardiac proarrhythmia safety paradigm: A meeting report from the Cardiac Safety Research Consortium," en, *American Heart Journal*, pp. 292–300, Mar. 2014. DOI: 10.1016/j.ahj.2013.11.004.

[43] B. Amuzescu, R. Airini, F. B. Epureanu, S. A. Mann, T. Knott, and B. M. Radu, "Evolution of mathematical models of cardiomyocyte electrophysiology," en, *Mathematical Biosciences*, p. 108 567, Apr. 2021. DOI: 10.1016/j.mbs.2021.108567.

[44] J. Corral-Acero, F. Margara, M. Marciniak, *et al.*, "The 'Digital Twin' to enable the vision of precision cardiology," en, *European Heart Journal*, ehaa159, Mar. 2020. DOI: 10.1093/eurheartj/ehaa159.

[45] E. G. Lakatta, V. A. Maltsev, and T. M. Vinogradova, "A Coupled SYSTEM of Intracellular Ca2+ Clocks and Surface Membrane Voltage Clocks Controls the Timekeeping Mechanism of the Heart's Pacemaker," *Circulation Research*, pp. 659–673, Mar. 2010, Publisher: American Heart Association. DOI: 10.1161/CIRCRESAHA.109.206078.

[46] V. A. Maltsev, Y. Yaniv, A. V. Maltsev, M. D. Stern, and E. G. Lakatta, "Modern Perspectives on Numerical Modeling of Cardiac Pacemaker Cell," *Journal of Pharmacological Sciences*, pp. 6–38, 2014. DOI: 10.1254/jphs.13R04CR.

[47] Y. Yaniv, E. Lakatta, and V. Maltsev, "From two competing oscillators to one coupled-clock pacemaker cell system," *Frontiers in Physiology*, 2015. DOI: 10.3389/fphys.2015.00028.

[48] T. Nikolaidou, O. V. Aslanidi, H. Zhang, and I. R. Efimov, "Structure–Function Relationship in the Sinus and Atrioventricular Nodes," en, *Pediatric Cardiology*, pp. 890–899, Aug. 2012. DOI: 10.1007/s00246-012-0249-0.

[49] D. Lang and A. V. Glukhov, "Cellular and Molecular Mechanisms of Functional Hierarchy of Pacemaker Clusters in the Sinoatrial Node: New Insights into Sick Sinus Syndrome," eng, *Journal of Cardiovascular Development and Disease*, Apr. 2021. DOI: 10.3390/jcdd8040043.

[50] T. A. Quinn and P. Kohl, "Mechano-sensitivity of cardiac pacemaker function: Pathophysiological relevance, experimental implications, and conceptual integration with other mechanisms of rhythmicity," en, *Progress in Biophysics and Molecular Biology*, pp. 257–268, Oct. 2012. DOI: 10.1016/j.pbiomolbio.2012.08.008.

[51] T. A. Quinn, P. Camelliti, E. A. Rog-Zielinska, *et al.*, "Electrotonic coupling of excitable and nonexcitable cells in the heart revealed by optogenetics," *Proceedings of the National Academy of Sciences*, pp. 14 852–14 857, Dec. 2016, Publisher: Proceedings of the National Academy of Sciences. DOI: 10.1073/pnas.1611184114.

[52] T. A. Quinn and P. Kohl, "Cardiac Mechano-Electric Coupling: Acute Effects of Mechanical Stimulation on Heart Rate and Rhythm," *Physiological Reviews*, pp. 37–92, May 2020, Publisher: American Physiological Society. DOI: 10.1152/physrev.00036.2019.

[53] M. Choudhury, Institute of Cardiovascular Sciences, University of Manchester, Manchester, UK, M. R. Boyett, Institute of Cardiovascular Sciences, University of Manchester, Manchester, UK, G. M. Morris, and Institute of Cardiovascular Sciences, University of Manchester, 46 Grafton Street, Manchester, M13 9NT, UK. E: Gwilym.Morris@manchester.ac.uk, "Biology of the Sinus Node and its Disease," en, *Arrhythmia & Electrophysiology Review*, p. 28, 2015. DOI: 10.15420/aer.2015.4.1.28.

[54] L. R. Jackson, B. Rathakrishnan, K. Campbell, *et al.*, "Sinus Node Dysfunction and Atrial Fibrillation: A Reversible Phenomenon?: SINUS NODE DYSFUNCTION AND ATRIAL FIBRILLATION," en, *Pacing and Clinical Electrophysiology*, pp. 442–450, Apr. 2017. DOI: 10.1111/pace.13030.

[55] D. Noble, A. Garny, and P. J. Noble, "How the HodgkinHuxley equations inspired the Cardiac Physiome Project," en, *J Physiol*, p. 16, 2012.

[56] A. Varró, J. Tomek, N. Nagy, *et al.*, "Cardiac Transmembrane Ion Channels and Action Potentials: Cellular Physiology and Arrhythmogenic Behavior," en, *Physiological Reviews*, physrev.00024.2019, Oct. 2020. DOI: 10.1152/physrev.00024.2019.

[57] P. Li, G. T. Lines, M. M. Maleckar, and A. Tveito, "Mathematical models of cardiac pacemaking function," en, *Frontiers in Physics*, 2013. DOI: 10.3389/fphy.2013.00020.

[58] Z. Kohajda, A. Loewe, N. Tóth, A. Varró, and N. Nagy, "The Cardiac Pacemaker Story—Fundamental Role of the Na+/Ca2+ Exchanger in Spontaneous Automaticity," en, *Frontiers in Pharmacology*, p. 516, Apr. 2020. DOI: 10.3389/fphar.2020.00516.

[59] R. Wilders, "Computer modelling of the sinoatrial node," en, *Medical & Biological Engineering & Computing*, pp. 189–207, Feb. 2007. DOI: 10.1007/s11517-006-0127-0.

[60] N. Chandler, O. Aslanidi, D. Buckley, *et al.*, "Computer Three-Dimensional Anatomical Reconstruction of the Human Sinus Node and a Novel Paranodal Area," en, p. 10, 2011.

[61] T. A. Csepe, J. Zhao, B. J. Hansen, *et al.*, "Human sinoatrial node structure: 3D microanatomy of sinoatrial conduction pathways," en, *Progress in Biophysics and Molecular Biology*, pp. 164–178, Jan. 2016. DOI: 10.1016/j.pbiomolbio.2015.12.011.

[62] V. Maltsev and E. Lakatta, "Dynamic interactions of an intracellular Ca2+ clock and membrane ion channel clock underlie robust initiation and regulation of cardiac pacemaker function," *Cardiovascular Research*, pp. 274–284, 2008. DOI: 10.1093/cvr/cvm058.

[63] D. DiFrancesco, "A Brief History of Pacemaking," en, *Frontiers in Physiology*, p. 1599, Jan. 2020. DOI: 10.3389/fphys.2019.01599.

[64] A. Noma, M. Morad, and H. Irisawa, "Does the "pacemaker current" generate the diastolic depolarization in the rabbit SA node cells?" en, *Pflügers Archiv*, pp. 190–194, May 1983. DOI: 10.1007/BF00584356.

[65] D. DiFrancesco, A. Ferroni, M. Mazzanti, and C. Tromba, "Properties of the hyperpolarizing-activated current (if) in cells isolated from the rabbit sino-atrial node," eng, *The Journal of Physiology*, pp. 61–88, Aug. 1986. DOI: 10.1113/jphysiol.1986.sp016177.

[66] J. C. Denyer and H. F. Brown, "Pacemaking in rabbit isolated sino-atrial node cells during Cs+ block of the hyperpolarization-activated current if.," *The Journal of Physiology*, pp. 401–409, Oct. 1990.

[67] A. C. v. Ginneken and W. Giles, "Voltage clamp measurements of the hyperpolarization-activated inward current I(f) in single cells from rabbit sino-atrial node.," en, *The Journal of Physiology*, pp. 57–83, 1991. DOI: https://doi.org/10.1113/jphysiol.1991.sp018459.

[68] C. Thollon, C. Cambarrat, J. Vian, J. F. Prost, J. L. Peglion, and J. P. Vilaine, "Electrophysiological effects of S 16257, a novel sino-atrial node modulator, on rabbit and guinea-pig cardiac preparations: Comparison with UL-FS 49," eng, *British Journal of Pharmacology*, pp. 37–42, May 1994. DOI: 10.1111/j.1476-5381.1994.tb13025.x.

[69] P. Bois, J. Bescond, B. Renaudon, and J. Lenfant, "Mode of action of bradycardic agent, S 16257, on ionic currents of rabbit sinoatrial node cells," eng, *British Journal of Pharmacology*, pp. 1051–1057, Jun. 1996. DOI: 10.1111/j.1476-5381.1996.tb15505.x.

[70] M. R. Nikmaram, M. R. Boyett, I. Kodama, R. Suzuki, and H. Honjo, "Variation in effects of Cs+, UL-FS-49, and ZD-7288 within sinoatrial node," *American Journal of Physiology-Heart and Circulatory Physiology*, H2782–H2792, Jun. 1997, Publisher: American Physiological Society. DOI: 10.1152/ajpheart.1997.272.6.H2782.

[71] H. S. Choi, D. Y. Wang, D. Noble, and C. O. Lee, "Effect of isoprenaline, carbachol, and Cs+ on Na+ activity and pacemaker potential in rabbit SA node cells," *American Journal of Physiology-Heart and Circulatory Physiology*, H205–H214, Jan. 1999, Publisher: American Physiological Society. DOI: 10.1152/ajpheart.1999.276.1.H205.

[72] T. M. Vinogradova, K. Y. Bogdanov, and E. G. Lakatta, "Beta-Adrenergic stimulation modulates ryanodine receptor Ca(2+) release during diastolic depolarization to accelerate pacemaker activity in rabbit sinoatrial nodal cells," eng, *Circulation Research*, pp. 73–79, Jan. 2002. DOI: 10.1161/hh0102.102271.

[73] A. Bucchi, M. Baruscotti, and D. DiFrancesco, "Current-dependent block of rabbit sino-atrial node I(f) channels by ivabradine," eng, *The Journal of General Physiology*, pp. 1–13, Jul. 2002. DOI: 10.1085/jgp.20028593.

[74] A. Bucchi, M. Baruscotti, R. B. Robinson, and D. DiFrancesco, "Modulation of rate by autonomic agonists in SAN cells involves changes in diastolic depolarization and the pacemaker current," eng, *Journal of Molecular and Cellular Cardiology*, pp. 39–48, Jul. 2007. DOI: 10.1016/j.yjmcc.2007.04.017.

[75] M. L. DiFrancesco, P. Mesirca, I. Bidaud, D. Isbrandt, and M. E. Mangoni, "The funny current in genetically modified mice," en, *Progress in Biophysics and Molecular Biology*, pp. 39–50, Nov. 2021. DOI: 10.1016/j.pbiomolbio.2021.06.003.

[76] Y. Kurata, H. Matsuda, I. Hisatome, and T. Shibamoto, "Regional Difference in Dynamical Property of Sinoatrial Node Pacemaking: Role of Na+ Channel Current," en, *Biophysical Journal*, pp. 951–977, Jul. 2008. DOI: 10.1529/biophysj.107.112854.

[77] H. Zhang, A. V. Holden, I. Kodama, *et al.*, "Mathematical models of action potentials in the periphery and center of the rabbit sinoatrial node," en, *American Journal of Physiology-Heart and Circulatory Physiology*, H397–H421, Jul. 2000. DOI: 10.1152/ajpheart.2000.279.1.H397.

[78] T. Tao, D. J. Paterson, and N. P. Smith, "A model of cellular cardiac-neural coupling that captures the sympathetic control of sinoatrial node excitability in normotensive and hypertensive rats," eng, *Biophysical Journal*, pp. 594–602, Aug. 2011. DOI: 10.1016/j.bpj.2011.05.069.

[79] A. V. Maltsev, V. A. Maltsev, M. Mikheev, *et al.*, "Synchronization of Stochastic Ca2+ Release Units Creates a Rhythmic Ca2+ Clock in Cardiac Pacemaker Cells," en, *Biophysical Journal*, pp. 271–283, Jan. 2011. DOI: 10.1016/j.bpj.2010.11.081.

[80] A. V. Maltsev, Y. Yaniv, M. D. Stern, E. G. Lakatta, and V. A. Maltsev, "RyR-NCX-SERCA Local Cross-Talk Ensures Pacemaker Cell Function at Rest and During the Fight-or-Flight Reflex," en, *Circulation Research*, Oct. 2013. DOI: 10.1161/CIRCRESAHA.113.302465.

[81] M. D. Stern, L. A. Maltseva, M. Juhaszova, S. J. Sollott, E. G. Lakatta, and V. A. Maltsev, "Hierarchical clustering of ryanodine receptors enables emergence of a calcium clock in sinoatrial node cells," en, *Journal of General Physiology*, pp. 577–604, May 2014. DOI: 10.1085/jgp.201311123.

[82] G. Seemann, C. Höper, F. B. Sachse, O. Dössel, A. V. Holden, and H. Zhang, "Heterogeneous three-dimensional anatomical and electrophysiological model of human atria," en, *Philosophical Transactions of the Royal Society A: Mathematical, Physical and Engineering Sciences*, pp. 1465–1481, Jun. 2006. DOI: 10.1098/rsta.2006.1781.

[83] N. J. Chandler, I. D. Greener, J. O. Tellez, *et al.*, "Molecular Architecture of the Human Sinus Node: Insights Into the Function of the Cardiac Pacemaker," en, *Circulation*, pp. 1562–1575, Mar. 2009. DOI: 10.1161/CIRCULATIONAHA.108.804369.

[84] A. Pohl, A. Wachter, N. Hatam, and S. Leonhardt, "A computational model of a human single sinoatrial node cell," en, *Biomedical Physics & Engineering Express*, p. 035 006, Apr. 2016. DOI: 10.1088/2057-1976/2/3/035006.

[85] S. Dokos, B. Celler, and N. Lovell, "Ion Currents Underlying Sinoatrial Node Pacemaker Activity: A New Single Cell Mathematical Model," en, *Journal of Theoretical Biology*, pp. 245–272, Aug. 1996. DOI: 10.1006/jtbi.1996.0129.

[86] A. O. Verkerk, R. Wilders, M. M. van Borren, *et al.*, "Pacemaker current (If) in the human sinoatrial node," en, *European Heart Journal*, pp. 2472–2478, Sep. 2007. DOI: 10.1093/eurheartj/ehm339.

[87] M. S. Imtiaz, P.-Y. von der Weid, D. R. Laver, and D. F. van Helden, "SR Ca2+ store refill—a key factor in cardiac pacemaking," en, *Journal of Molecular and Cellular Cardiology*, pp. 412–426, Sep. 2010. DOI: 10.1016/j.yjmcc.2010.03.015.

[88] N. Sarai, S. Matsuoka, S. Kuratomi, K. Ono, and A. Noma, "Role of Individual Ionic Current Systems in the SA Node Hypothesized by a Model Study," en, *The Japanese Journal of Physiology*, pp. 125–134, 2003. DOI: 10.2170/jjphysiol.53.125.

[89] V. A. Maltsev and E. G. Lakatta, "A novel quantitative explanation for the autonomic modulation of cardiac pacemaker cell automaticity via a dynamic system of sarcolemmal and intracellular proteins," en, p. 14, 2010.

[90] Y. Yaniv, H. A. Spurgeon, A. E. Lyashkov, *et al.*, "Crosstalk between Mitochondrial and Sarcoplasmic Reticulum Ca2+ Cycling Modulates Cardiac Pacemaker Cell Automaticity," en, *PLoS ONE*, A. Leri, Ed., e37582, May 2012. DOI: 10.1371/journal.pone.0037582.

[91] Y. Yaniv, S. Sirenko, B. D. Ziman, H. A. Spurgeon, V. A. Maltsev, and E. G. Lakatta, "New evidence for coupled clock regulation of the normal automaticity of sinoatrial nodal pacemaker cells: Bradycardic effects of ivabradine are linked to suppression of intracellular Ca2+ cycling," en, *Journal of Molecular and Cellular Cardiology*, pp. 80–89, Sep. 2013. DOI: 10.1016/j.yjmcc.2013.04.026.

[92] Y. Yaniv, M. D. Stern, E. G. Lakatta, and V. A. Maltsev, "Mechanisms of Beat-to-Beat Regulation of Cardiac Pacemaker Cell Function by Ca2+ Cycling Dynamics," en, *Biophysical Journal*, pp. 1551–1561, Oct. 2013. DOI: 10.1016/j.bpj.2013.08.024.

[93] Y. Yaniv, A. Ganesan, D. Yang, *et al.*, "Real-time relationship between PKA biochemical signal network dynamics and increased action potential firing rate in heart pacemaker cells," en, *Journal of Molecular and Cellular Cardiology*, p. 11, 2015.

[94] J. Behar, A. Ganesan, J. Zhang, and Y. Yaniv, "The Autonomic Nervous System Regulates the Heart Rate through cAMP-PKA Dependent and Independent Coupled-Clock Pacemaker Cell Mechanisms," en, *Frontiers in Physiology*, Sep. 2016. DOI: 10.3389/fphys.2016.00419.

[95] J. Behar and Y. Yaniv, "Age-related pacemaker deterioration is due to impaired intracellular and membrane mechanisms: Insights from numerical modeling," *Journal of General Physiology*, pp. 935–949, Sep. 2017. DOI: 10.1085/jgp.201711792.

[96] S. Morotti, H. Ni, C. H. Peters, *et al.*, "Intracellular Na+ Modulates Pacemaking Activity in Murine Sinoatrial Node Myocytes: An In Silico Analysis," eng, *International Journal of Molecular Sciences*, May 2021. DOI: 10.3390/ijms22115645.

[97] A. M. Alghamdi, M. R. Boyett, J. C. Hancox, and H. Zhang, "Cardiac Pacemaker Dysfunction Arising From Different Studies of Ion Channel Remodeling in the Aging Rat Heart," English, *Frontiers in Physiology*, Mar. 2020, Publisher: Frontiers. DOI: 10.3389/fphys.2020.546508.

[98] C. J. Christel, N. Cardona, P. Mesirca, *et al.*, "Distinct localization and modulation of Cav1.2 and Cav1.3 L-type Ca2+ channels in mouse sinoatrial node," *The Journal of Physiology*, pp. 6327–6341, Dec. 2012. DOI: 10.1113/jphysiol.2012.239954.

[99] M. E. Mangoni, A. Traboulsie, A.-L. Leoni, *et al.*, "Bradycardia and Slowing of the Atrioventricular Conduction in Mice Lacking CaV3.1/α1G T-Type Calcium Channels," *Circulation Research*, pp. 1422–1430, Jun. 2006, Publisher: American Heart Association. DOI: 10.1161/01.RES.0000225862.14314.49.

[100] A. Loewe, Y. Lutz, D. Nairn, *et al.*, "Hypocalcemia-Induced Slowing of Human Sinus Node Pacemaking," en, *Biophysical Journal*, pp. 2244–2254, Dec. 2019. DOI: 10.1016/j.bpj.2019.07.037.

[101] M. Hoekstra, A. C. van Ginneken, R. Wilders, and A. O. Verkerk, "HCN4 current during human sinoatrial node-like action potentials," en, *Progress in Biophysics and Molecular Biology*, S007961072100050X, Jun. 2021. DOI: 10.1016/j.pbiomolbio.2021.05.006.

[102] A. M. Alghamdi, C. P. Testrow, D. G. Whittaker, M. R. Boyett, J. C. Hancox, and H. Zhang, "Mechanistic Insights Into the Reduced Pacemaking Rate of the Rabbit Sinoatrial Node During Postnatal Development: A Simulation Study," en, *Frontiers in Physiology*, p. 547 577, Nov. 2020. DOI: 10.3389/fphys.2020.547577.

[103] D. Noble and Y. Rudy, "Models of cardiac ventricular action potentials: Iterative interaction between experiment and simulation," en, *Philosophical Transactions of the Royal Society of London. Series A: Mathematical, Physical and Engineering Sciences*, pp. 1127–1142, Jun. 2001. DOI: 10.1098/rsta.2001.0820.

[104] M. Vassalle, "The vicissitudes of the pacemaker current I Kdd of cardiac purkinje fibers," en, *Journal of Biomedical Science*, pp. 699–716, Nov. 2007. DOI: 10.1007/s11373-007-9182-2.

[105] R. A. Capel and D. A. Terrar, "The importance of Ca2+-dependent mechanisms for the initiation of the heartbeat," *Frontiers in Physiology*, p. 80, 2015. DOI: 10.3389/fphys.2015.00080.

[106] W. Shi, R. Wymore, H. Yu, *et al.*, "Distribution and Prevalence of Hyperpolarization - Activated Cation Channel (HCN) mRNA Expression in Cardiac Tissues," *Circulation Research*, e1–e6, Jul. 1999, Publisher: American Heart Association. DOI: 10.1161/01.RES.85.1.e1.

[107] C. Brioschi, S. Micheloni, J. O. Tellez, *et al.*, "Distribution of the pacemaker HCN4 channel mRNA and protein in the rabbit sinoatrial node," en, *Journal of Molecular and Cellular Cardiology*, pp. 221–227, Aug. 2009. DOI: 10.1016/j.yjmcc.2009.04.009.

[108] S. Moosmang, J. Stieber, X. Zong, M. Biel, F. Hofmann, and A. Ludwig, "Cellular expression and functional characterization of four hyperpolarization - activated pacemaker channels in cardiac and neuronal tissues," en, *European Journal of Biochemistry*, pp. 1646–1652, 2001. DOI: 10.1046/j.1432-1327.2001.02036.x.

[109] N. Linscheid, S. J. R. J. Logantha, P. C. Poulsen, *et al.*, "Quantitative proteomics and single-nucleus transcriptomics of the sinus node elucidates the foundation of cardiac pacemaking," en, *Nature Communications*, p. 2889, Dec. 2019. DOI: 10.1038/s41467-019-10709-9.

[110] C. Altomare, B. Terragni, C. Brioschi, *et al.*, "Heteromeric HCN1-HCN4 Channels: A Comparison with Native Pacemaker Channels from the Rabbit Sinoatrial Node," en, *The Journal of Physiology*, pp. 347–359, Jun. 2003. DOI: 10.1113/jphysiol.2002.027698.

[111] D. DiFrancesco, "Considerations on the size of currents required for pacemaking," en, *Journal of Molecular and Cellular Cardiology*, pp. 802–803, Apr. 2010. DOI: 10.1016/j.yjmcc.2009.11.022.

[112] V. A. Maltsev and E. G. Lakatta, "Numerical models based on a minimal set of sarcolemmal electrogenic proteins and an intracellular Ca2+ clock generate robust, flexible, and energy-efficient cardiac pacemaking," en, *Journal of Molecular and Cellular Cardiology*, pp. 181–195, Jun. 2013. DOI: 10.1016/j.yjmcc.2013.03.004.

[113] O. Monfredi, K. Tsutsui, B. Ziman, M. D. Stern, E. G. Lakatta, and V. A. Maltsev, "Electrophysiological heterogeneity of pacemaker cells in the rabbit intercaval region, including the SA node: Insights from recording multiple ion currents in each cell," *American Journal of Physiology-Heart and Circulatory Physiology*, H403–H414, Mar. 2018, Publisher: American Physiological Society. DOI: 10.1152/ajpheart.00253.2016.

[114] A. O. Verkerk and R. Wilders, "Hyperpolarization-Activated Current, , in Mathematical Models of Rabbit Sinoatrial Node Pacemaker Cells," en, *BioMed Research International*, pp. 1–18, 2013. DOI: 10.1155/2013/872454.

[115] A. O. Verkerk and R. Wilders, "Relative importance of funny current in human versus rabbit sinoatrial node," en, *Journal of Molecular and Cellular Cardiology*, pp. 799–801, Apr. 2010. DOI: 10.1016/j.yjmcc.2009.09.020.

[116] A. O. Verkerk, M. M. G. J. van Borren, and R. Wilders, "Calcium Transient and Sodium-Calcium Exchange Current in Human versus Rabbit Sinoatrial Node Pacemaker Cells," en, *The Scientific World Journal*, pp. 1–10, 2013. DOI: 10.1155/2013/507872.

[117] E. Ravagli, A. Bucchi, C. Bartolucci, *et al.*, "Cell-specific Dynamic Clamp analysis of the role of funny If current in cardiac pacemaking," en, *Progress in Biophysics and Molecular Biology*, pp. 50–66, Jan. 2016. DOI: 10.1016/j.pbiomolbio.2015.12.004.

[118] Z. Kohajda, N. Tóth, J. Szlovák, *et al.*, "Novel Na+/Ca2+ Exchanger Inhibitor ORM-10962 Supports Coupled Function of Funny-Current and Na+/Ca2+ Exchanger in Pacemaking of Rabbit Sinus Node Tissue," en, *Frontiers in Pharmacology*, p. 1632, Jan. 2020. DOI: 10.3389/fphar.2019.01632.

[119] Y. Kurata, H. Matsuda, I. Hisatome, and T. Shibamoto, "Roles of hyperpolarization - activated current I_f in sinoatrial node pacemaking: Insights from bifurcation analysis of mathematical models," en, *American Journal of Physiology-Heart and Circulatory Physiology*, H1748–H1760, Jun. 2010. DOI: 10.1152/ajpheart.00729.2009.

[120] Y. Kurata, I. Hisatome, S. Imanishi, and T. Shibamoto, "Roles of L-type Ca^{2+} and delayed-rectifier K^+ currents in sinoatrial node pacemaking: Insights from stability and bifurcation analyses of a mathematical model," en, *American Journal of Physiology-Heart and Circulatory Physiology*, H2804–H2819, Dec. 2003. DOI: 10.1152/ajpheart.01050.2002.

[121] Y. Kurata, I. Hisatome, M. Tanida, and T. Shibamoto, "Effect of hyperpolarization - activated current I_f on robustness of sinoatrial node pacemaking: Theoretical study on influence of intracellular Na^+ concentration," en, *American Journal of Physiology-Heart and Circulatory Physiology*, H1337–H1351, May 2013. DOI: 10.1152/ajpheart.00777.2012.

[122] A. O. Verkerk and R. Wilders, "Pacemaker activity of the human sinoatrial node: Effects of HCN4 mutations on the hyperpolarization-activated current," en, *EP Europace*, pp. 384–395, Mar. 2014. DOI: 10.1093/europace/eut348.

[123] A. Verkerk and R. Wilders, "Pacemaker Activity of the Human Sinoatrial Node: An Update on the Effects of Mutations in HCN4 on the Hyperpolarization - Activated Current," en, *International Journal of Molecular Sciences*, pp. 3071–3094, Jan. 2015. DOI: 10.3390/ijms16023071.

[124] M. Schlepper, J. Thormann, and V. Mitrovic, "Cardiovascular effects of forskolin and phosphodiesterase-III inhibitors," eng, *Basic Research in Cardiology*, pp. 197–212, 1989. DOI: 10.1007/BF02650360.

[125] C. H. Peters, P. W. Liu, S. Morotti, *et al.*, "Bidirectional flow of the funny current (If) during the pacemaking cycle in murine sinoatrial node myocytes," eng, *Proceedings of the National Academy of Sciences of the United States of America*, e2104668118, Jul. 2021. DOI: 10.1073/pnas.2104668118.

[126] D. A. Kass, J. M. Hare, and D. Georgakopoulos, "Murine Cardiac Function," *Circulation Research*, pp. 519–522, Mar. 1998, Publisher: American Heart Association. DOI: 10.1161/01.RES.82.4.519.

[127] Y. Kurata, I. Hisatome, and T. Shibamoto, "Roles of sarcoplasmic reticulum Ca2+ cycling and Na+/Ca2+ exchanger in sinoatrial node pacemaking: Insights from bifurcation analysis of mathematical models," *American Journal of Physiology-Heart and Circulatory Physiology*, H2285–H2300, Mar. 2012, Publisher: American Physiological Society. DOI: 10.1152/ajpheart.00221.2011.

[128] Z. Gao, T. P. Rasmussen, Y. Li, *et al.*, "Genetic Inhibition of Na+-Ca2+ Exchanger Current Disables Fight or Flight Sinoatrial Node Activity Without Affecting Resting Heart Rate," *Circulation Research*, pp. 309–317, Jan. 2013, Publisher: American Heart Association. DOI: 10.1161/CIRCRESAHA.111.300193.

[129] S. Groenke, E. D. Larson, S. Alber, *et al.*, "Complete Atrial-Specific Knockout of Sodium-Calcium Exchange Eliminates Sinoatrial Node Pacemaker Activity," en, *PLOS ONE*, e81633, Nov. 2013, Publisher: Public Library of Science. DOI: 10.1371/journal.pone.0081633.

[130] S. J. R. J. Logantha, M. K. Stokke, A. J. Atkinson, *et al.*, "Ca2+-Clock-Dependent Pacemaking in the Sinus Node Is Impaired in Mice with a Cardiac Specific Reduction in SERCA2 Abundance," en, *Frontiers in Physiology*, Jun. 2016. DOI: 10.3389/fphys.2016.00197.

[131] A. V. Maltsev, V. A. Maltsev, and M. D. Stern, "Stabilization of diastolic calcium signal via calcium pump regulation of complex local calcium releases and transient decay in a computational model of cardiac pacemaker cell with individual release channels," en, *PLOS Computational Biology*, A. D. McCulloch, Ed., e1005675, Aug. 2017. DOI: 10.1371/journal.pcbi.1005675.

[132] Y. Himeno, F. Toyoda, H. Satoh, *et al.*, "Minor contribution of cytosolic Ca $^{2+}$ transients to the pacemaker rhythm in guinea pig sinoatrial node cells," en, *American Journal of Physiology-Heart and Circulatory Physiology*, H251–H261, Jan. 2011. DOI: 10.1152/ajpheart.00764.2010.

[133] H. Zhang, T. Butters, I. Adeniran, *et al.*, "Modeling the Chronotropic Effect of Isoprenaline on Rabbit Sinoatrial Node," en, *Frontiers in Physiology*, 2012. DOI: 10.3389/fphys.2012.00241.

[134] J. Behar and Y. Yaniv, "Dynamics of PKA phosphorylation and gain of function in cardiac pacemaker cells: A computational model analysis," en, *American Journal of Physiology-Heart and Circulatory Physiology*, H1259–H1266, May 2016. DOI: 10.1152/ajpheart.00076.2016.

[135] S. G. Sirenko, V. A. Maltsev, Y. Yaniv, *et al.*, "Electrochemical Na $^{+}$ and Ca $^{2+}$ gradients drive coupled-clock regulation of automaticity of isolated rabbit sinoatrial nodal pacemaker cells," en, *American Journal of Physiology-Heart and Circulatory Physiology*, H251–H267, Jul. 2016. DOI: 10.1152/ajpheart.00667.2015.

[136] M. S. Kim, A. V. Maltsev, O. Monfredi, *et al.*, "Heterogeneity of calcium clock functions in dormant, dysrhythmically and rhythmically firing single pacemaker cells isolated from SA node," en, *Cell Calcium*, pp. 168–179, Sep. 2018. DOI: 10.1016/j.ceca.2018.07.002.

[137] M. E. Mangoni, B. Couette, E. Bourinet, *et al.*, "Functional role of L-type Cav1.3 Ca2+ channels in cardiac pacemaker activity," *Proceedings of the National Academy of Sciences*, pp. 5543–5548, Apr. 2003, Publisher: Proceedings of the National Academy of Sciences. DOI: 10.1073/pnas.0935295100.

[138] A. E. Lyashkov, J. Behar, E. G. Lakatta, Y. Yaniv, and V. A. Maltsev, "Positive Feedback Mechanisms among Local Ca Releases, NCX, and ICaL Ignite Pacemaker Action Potentials," en, *Biophysical Journal*, pp. 1176–1189, Mar. 2018. DOI: 10.1016/j.bpj.2017.12.043.

[139] Z. Zhou and S. L. Lipsius, "T-Type Calcium Current in Latent Pacemaker Cells Isolated from Cat Right Atrium," English, *Journal of Molecular and Cellular Cardiology*, pp. 1211–1219, Sep. 1994, Publisher: Elsevier. DOI: 10.1006/jmcc.1994.1139.

[140] H. Zhang, B. Joung, T. Shinohara, X. Mei, P.-S. Chen, and S.-F. Lin, "Synergistic Dual Automaticity in Sinoatrial Node Cell and Tissue Models," en, *Circulation Journal*, pp. 2079–2088, 2010. DOI: 10.1253/circj.CJ-10-0265.

[141] A. G. Torrente, P. Mesirca, P. Neco, *et al.*, "L-type Cav1.3 channels regulate ryanodine receptor-dependent Ca2+ release during sino-atrial node pacemaker activity," *Cardiovascular Research*, pp. 451–461, Mar. 2016. DOI: 10.1093/cvr/cvw006.

[142] M. Baudot, E. Torre, I. Bidaud, *et al.*, "Concomitant genetic ablation of L-type Cav1.3 (α1D) and T-type Cav3.1 (α1G) Ca2+ channels disrupts heart automaticity," en, *Scientific Reports*, p. 18 906, Nov. 2020, Number: 1 Publisher: Nature Publishing Group. DOI: 10.1038/s41598-020-76049-7.

[143] J. Louradour, O. Bortolotti, E. Torre, *et al.*, "L-Type Cav1.3 Calcium Channels Are Required for Beta-Adrenergic Triggered Automaticity in Dormant Mouse Sinoatrial Pacemaker Cells," eng, *Cells*, p. 1114, Mar. 2022. DOI: 10.3390/cells11071114.

[144] W. Shen, *Development of a biophysically detailed mathematical model of a mouse atrial cell for the study of cellular proarrhythmic mechanisms*. The University of Manchester (United Kingdom), 2016.

[145] T. M. Vinogradova, A. E. Lyashkov, W. Zhu, *et al.*, "High Basal Protein Kinase A–Dependent Phosphorylation Drives Rhythmic Internal Ca2+ Store Oscillations and Spontaneous Beating of Cardiac Pacemaker Cells," *Circulation Research*, pp. 505–514, Mar. 2006, Publisher: American Heart Association. DOI: 10.1161/01.RES.0000204575.94040.d1.

[146] H. J. Levine, "Rest Heart rate and life expectancy," en, *Journal of the American College of Cardiology*, pp. 1104–1106, Oct. 1997. DOI: 10.1016/S0735-1097(97)00246-5.

[147] D. C. Michaels, E. P. Matyas, and J. Jalife, "Dynamic interactions and mutual synchronization of sinoatrial node pacemaker cells. A mathematical model," eng, *Circulation Research*, pp. 706–720, May 1986. DOI: 10.1161/01.res.58.5.706.

[148] D. Michaels, E. Matyas, and J. Jalife, "Mechanisms of sinoatrial pacemaker synchronization: A new hypothesis," *Circulation Research*, pp. 704–714, 1987. DOI: 10.1161/01.RES.61.5.704.

[149] A. T. Winfree, "Biological rhythms and the behavior of populations of coupled oscillators," en, *Journal of Theoretical Biology*, pp. 15–42, Jul. 1967. DOI: 10.1016/0022-5193(67)90051-3.

[150] A. T. Winfree, *The Geometry of Biological Time*. Springer, Berlin, 1980. DOI: 10.1007/978-3-662-22492-2.

[151] D. Cai, R. Winslow, and D. Noble, "Effects of gap junction conductance on dynamics of sinoatrial node cells: Two-cell and large-scale network models," *IEEE Transactions on Biomedical Engineering*, pp. 217–231, Mar. 1994, Conference Name: IEEE Transactions on Biomedical Engineering. DOI: 10.1109/10.284940.

[152] E. Verheijck, R. Wilders, R. Joyner, *et al.*, "Pacemaker synchronization of electrically coupled rabbit sinoatrial node cells," *Journal of General Physiology*, pp. 95–112, 1998. DOI: 10.1085/jgp.111.1.95.

[153] R. Wilders, E. E. Verheijck, R. Kumar, *et al.*, "Model clamp and its application to synchronization of rabbit sinoatrial node cells," *American Journal of Physiology-Heart and Circulatory Physiology*, H2168–H2182, Nov. 1996, Publisher: American Physiological Society. DOI: 10.1152/ajpheart.1996.271.5.H2168.

[154] K. W. Spitzer, N. Sato, H. Tanaka, L. Firek, M. Zaniboni, and W. R. Giles, "Electrotonic modulation of electrical activity in rabbit atrioventricular node myocytes," eng, *The American Journal of Physiology*, H767–776, Aug. 1997. DOI: 10.1152/ajpheart.1997.273.2.H767.

[155] A. N. Mata, G. R. Alonso, G. L. Garza, J. R. G. Fernández, M. A. C. García, and N. P. C. Ábrego, "Parallel simulation of the synchronization of heterogeneous cells in the sinoatrial node," en, *Concurrency and Computation: Practice and Experience*, e5317, 2020. DOI: https://doi.org/10.1002/cpe.5317.

[156] D. Gratz, B. Onal, A. Dalic, and T. J. Hund, "Synchronization of Pacemaking in the Sinoatrial Node: A Mathematical Modeling Study," en, *Frontiers in Physics*, p. 63, Jun. 2018. DOI: 10.3389/fphy.2018.00063.

[157] Campana, "A 2-Dimensional Computational Model to Analyze the Effects of Cellular Heterogeneity on Cardiac Pacemaking," eng, Ph.D. dissertation, University of Bologna, 2015.

[158] E. Ricci, S. Severi, F. Cona, and A. Fabbri, "Multiscale analysis of an HCN4 channel double mutation in a human sinoatrial computational model," en, p. 111, 2020.

[159] J. Anumonwo, M. Delmar, A. Vinet, D. Michaels, and J. Jalife, "Phase resetting and entrainment of pacemaker activity in single sinus nodal cells," *Circulation Research*, pp. 1138–1153, 1991. DOI: 10.1161/01.RES.68.4.1138.

[160] D. Tsalikakis, H. Zhang, D. Fotiadis, G. Kremmydas, and Ł. Michalis, "Phase response characteristics of sinoatrial node cells," en, *Computers in Biology and Medicine*, pp. 8–20, Jan. 2007. DOI: 10.1016/j.compbiomed.2005.09.011.

[161] K. Li, Z. Chu, and X. Huang, "Annihilation of the pacemaking activity in the sinoatrial node cell and tissue," *AIP Advances*, p. 125 319, 2018, Publisher: American Institute of Physics. DOI: 10.1063/1.5051509.

[162] X. Huang, Y. Mi, Y. Qian, and G. Hu, "Phase-locking behaviors in an ionic model of sinoatrial node cell and tissue," en, *Physical Review E*, p. 061 917, Jun. 2011. DOI: 10.1103/PhysRevE.83.061917.

[163] P. Glynn, B. Onal, and T. J. Hund, "Cycle Length Restitution in Sinoatrial Node Cells: A Theory for Understanding Spontaneous Action Potential Dynamics," en, *PLoS ONE*, X. Ai, Ed., e89049, Feb. 2014. DOI: 10.1371/journal.pone.0089049.

[164] S. Fenske, K. Hennis, R. D. Rötzer, *et al.*, "cAMP-dependent regulation of HCN4 controls the tonic entrainment process in sinoatrial node pacemaker cells," eng, *Nature Communications*, p. 5555, Nov. 2020. DOI: 10.1038/s41467-020-19304-9.

[165] H. Dvir and S. Zlochiver, "Interbeat Interval Modulation in the Sinoatrial Node as a Result of Membrane Current Stochasticity - A Theoretical and Numerical Study," *Biophysical Journal*, pp. 1281–1292, 2015. DOI: 10.1016/j.bpj.2015.01.010.

[166] J. G. C. Ponard, A. A. Kondratyev, and J. P. Kucera, "Mechanisms of Intrinsic Beating Variability in Cardiac Cell Cultures and Model Pacemaker Networks," en, *Biophysical Journal*, pp. 3734–3752, May 2007. DOI: 10.1529/biophysj.106.091892.

[167] M. Zaniboni, F. Cacciani, and R. L. Lux, "Beat-to-Beat Cycle Length Variability of Spontaneously Beating Guinea Pig Sinoatrial Cells: Relative Contributions of the Membrane and Calcium Clocks," en, *PLOS ONE*, e100242, Jun. 2014, Publisher: Public Library of Science. DOI: 10.1371/journal.pone.0100242.

[168] Monfredi, Oliver, Lyashkov Alexey E., Johnsen Anne-Berit, *et al.*, "Biophysical Characterization of the Underappreciated and Important Relationship Between Heart Rate Variability and Heart Rate," *Hypertension*, pp. 1334–1343, Dec. 2014, Publisher: American Heart Association. DOI: 10.1161/HYPERTENSIONAHA.114.03782.

[169] M. Rocchetti, G. Malfatto, F. Lombardi, and A. Zaza, "Role of the Input/Output Relation of Sinoatrial Myocytes in Cholinergic Modulation of Heart Rate Variability," en, *Journal of Cardiovascular Electrophysiology*, pp. 522–530, 2000. DOI: 10.1111/j.1540-8167.2000.tb00005.x.

[170] A. Zaza and F. Lombardi, "Autonomic indexes based on the analysis of heart rate variability: A view from the sinus node," *Cardiovascular Research*, pp. 434–442, 2001. DOI: 10.1016/S0008-6363(01)00240-1.

[171] T. Force, "Heart Rate Variability," *Circulation*, pp. 1043–1065, Mar. 1996, Publisher: American Heart Association. DOI: 10.1161/01.CIR.93.5.1043.

[172] M. Malik, K. Hnatkova, H. V. Huikuri, F. Lombardi, G. Schmidt, and M. Zabel, "CrossTalk proposal: Heart rate variability is a valid measure of cardiac autonomic responsiveness," en, *The Journal of Physiology*, pp. 2595–2598, 2019. DOI: 10.1113/JP277500.

[173] M. R. Boyett, H. Zhang, A. Garny, and A. V. Holden, "Control of the pacemaker activity of the sinoatrial node by intracellular Ca $^{2+}$. Experiments and modelling," en, *Philosophical Transactions of the Royal Society of London. Series A: Mathematical, Physical and Engineering Sciences*, pp. 1091–1110, Jun. 2001. DOI: 10.1098/rsta.2001.0818.

[174] A. Garny, P. Kohl, and M. R. Boyett, "One-Dimensional Rabbit Sinoatrial Node Models:" en, p. 12, 2003.

[175] R. Joyner and F. van Capelle, "Propagation through electrically coupled cells. How a small SA node drives a large atrium," en, *Biophysical Journal*, pp. 1157–1164, Dec. 1986. DOI: 10.1016/S0006-3495(86)83559-7.

[176] W. K. Bleeker, A. J. Mackaay, M. Masson-Pévet, L. N. Bouman, and A. E. Becker, "Functional and morphological organization of the rabbit sinus node.," en, *Circulation Research*, pp. 11–22, Jan. 1980. DOI: 10.1161/01.RES.46.1.11.

[177] I. Kodama and M. R. Boyett, "Regional differences in the electrical activity of the rabbit sinus node," en, *Pflügers Archiv*, pp. 214–226, Jul. 1985. DOI: 10.1007/BF00581242.

[178] M. R. Boyett, H. Honjo, M. Yamamoto, M. R. Nikmaram, R. Niwa, and I. Kodama, "Downward gradient in action potential duration along conduction path in and around the sinoatrial node," *American Journal of Physiology-Heart and Circulatory Physiology*, H686–H698, Feb. 1999, Publisher: American Physiological Society. DOI: 10.1152/ajpheart.1999.276.2.H686.

[179] E. Verheijck, M. J. van Kempen, M. Veereschild, J. Lurvink, H. J. Jongsma, and L. N. Bouman, "Electrophysiological features of the mouse sinoatrial node in relation to connexin distribution," *Cardiovascular Research*, pp. 40–50, Oct. 2001. DOI: 10.1016/S0008-6363(01)00364-9.

[180] S. Cloherty, S. Dokos, and N. Lovell, "A Comparison of 1-D Models of Cardiac Pacemaker Heterogeneity," en, *IEEE Transactions on Biomedical Engineering*, pp. 164–177, Feb. 2006. DOI: 10.1109/TBME.2005.862538.

[181] G. López Garza, N. P. Castellanos, and R. Godínez, "Cell-to-cell modeling of the interface between atrial and sinoatrial anisotropic heterogeneous nets," en, *Computational Biology and Chemistry*, pp. 245–259, Jun. 2017. DOI: 10.1016/j.compbiolchem.2017.04.008.

[182] M. A. Muñoz, J. Kaur, and E. J. Vigmond, "Onset of atrial arrhythmias elicited by autonomic modulation of rabbit sinoatrial node activity: A modeling study," *American Journal of Physiology-Heart and Circulatory Physiology*, H1974–H1983, Aug. 2011, Publisher: American Physiological Society. DOI: 10.1152/ajpheart.00059.2011.

[183] A. Al Abed, T. Guo, N. H. Lovell, and S. Dokos, "Optimisation of Ionic Models to Fit Tissue Action Potentials: Application to 3D Atrial Modelling," *Computational and Mathematical Methods in Medicine*, pp. 1–16, 2013. DOI: 10.1155/2013/951234.

[184] R. V. Oren and C. E. Clancy, "Determinants of Heterogeneity, Excitation and Conduction in the Sinoatrial Node: A Model Study," en, *PLoS Computational Biology*, W. Giles, Ed., e1001041, Dec. 2010. DOI: 10.1371/journal.pcbi.1001041.

[185] C. Ly and S. H. Weinberg, "Analysis of heterogeneous cardiac pacemaker tissue models and traveling wave dynamics," en, *Journal of Theoretical Biology*, pp. 18–35, Dec. 2018. DOI: 10.1016/j.jtbi.2018.09.023.

[186] S. Inada, H. Zhang, J. O. Tellez, *et al.*, "Importance of Gradients in Membrane Properties and Electrical Coupling in Sinoatrial Node Pacing," en, *PLoS ONE*, A. V. Panfilov, Ed., e94565, Apr. 2014. DOI: 10.1371/journal.pone.0094565.

[187] S. R. Kharche, E. Vigmond, I. R. Efimov, and H. Dobrzynski, "Computational assessment of the functional role of sinoatrial node exit pathways in the human heart," en, *PLOS ONE*, A. V. Panfilov, Ed., e0183727, Sep. 2017. DOI: 10.1371/journal.pone.0183727.

[188] S. Verheule, M. J. A. van Kempen, P. H. J. A. t. Welscher, B. R. Kwak, and H. J. Jongsma, "Characterization of Gap Junction Channels in Adult Rabbit Atrial and Ventricular Myocardium," *Circulation Research*, pp. 673–681, 1997, Publisher: American Heart Association. DOI: 10.1161/01.RES.80.5.673.

[189] D. S. Lindblad, C. R. Murphey, J. W. Clark, and W. R. Giles, "A model of the action potential and underlying membrane currents in a rabbit atrial cell," en, *American Journal of Physiology-Heart and Circulatory Physiology*, H1666–H1696, Oct. 1996. DOI: 10.1152/ajpheart.1996.271.4.H1666.

[190] A. A. Karpaev, R. A. Syunyaev, and R. R. Aliev, "Effects of fibroblast-myocyte coupling on the sinoatrial node activity: A computational study," eng, *International Journal for Numerical Methods in Biomedical Engineering*, e2966, May 2018. DOI: 10.1002/cnm.2966.

[191] A. Amsaleg, J. Sánchez, R. Mikut, and A. Loewe, "Characterization of the pace-and-drive capacity of the human sinoatrial node: A 3D in silico study," en, *Biophysical Journal*, pp. 4247–4259, Nov. 2022. DOI: 10.1016/j.bpj.2022.10.020.

[192] J. O. Tellez, H. Dobrzynski, I. D. Greener, *et al.*, "Differential Expression of Ion Channel Transcripts in Atrial Muscle and Sinoatrial Node in Rabbit," *Circulation Research*, pp. 1384–1393, Dec. 2006, Publisher: American Heart Association. DOI: 10.1161/01.RES.0000251717.98379.69.

[193] H. Zhang, Y. Zhao, M. Lei, *et al.*, "Computational evaluation of the roles of Na+ current, iNa, and cell death in cardiac pacemaking and driving," *American Journal of Physiology-Heart and Circulatory Physiology*, H165–H174, Jan. 2007, Publisher: American Physiological Society. DOI: 10.1152/ajpheart.01101.2005.

[194] L. Protas, R. Oren, C. Clancy, and R. Robinson, "Age-dependent changes in Na current magnitude and TTX-sensitivity in the canine sinoatrial node," *Journal of Molecular and Cellular Cardiology*, pp. 172–180, 2010. DOI: 10.1016/j.yjmcc.2009.07.028.

[195] A. O. Verkerk, R. Wilders, M. M. van Borren, and H. L. Tan, "Is sodium current present in human sinoatrial node cells?" en, *International Journal of Biological Sciences*, pp. 201–204, 2009. DOI: 10.7150/ijbs.5.201.

[196] X. Hao, Y. Zhang, X. Zhang, *et al.*, "TGF-β1-mediated fibrosis and ion channel remodeling are key mechanisms in producing the sinus node dysfunction associated with SCN5A deficiency and aging," eng, *Circulation. Arrhythmia and Electrophysiology*, pp. 397–406, Jun. 2011. DOI: 10.1161/CIRCEP.110.960807.

[197] R. Wilders, "Sinus Bradycardia in Carriers of the SCN5A-1795insD Mutation: Unraveling the Mechanism through Computer Simulations," en, *International Journal of Molecular Sciences*, p. 634, Feb. 2018. DOI: 10.3390/ijms19020634.

[198] X. Li, J.-q. Zhang, and J.-w. Shuai, "Isoprenaline: A Potential Contributor in Sick Sinus Syndrome—Insights from a Mathematical Model of the Rabbit Sinoatrial Node," en, *The Scientific World Journal*, pp. 1–11, 2014. DOI: 10.1155/2014/540496.

[199] R. Wilders, "Cellular Mechanisms of Sinus Node Dysfunction in Carriers of the SCN5A-E161K Mutation and Role of the H558R Polymorphism," en, *Frontiers in Physiology*, p. 1795, Dec. 2018. DOI: 10.3389/fphys.2018.01795.

[200] N. Li, A. Kalyanasundaram, B. J. Hansen, *et al.*, "Impaired neuronal sodium channels cause intranodal conduction failure and reentrant arrhythmias in human sinoatrial node," en, *Nature Communications*, p. 512, Dec. 2020. DOI: 10.1038/s41467-019-14039-8.

[201] R. M. Shaw and Y. Rudy, "Ionic Mechanisms of Propagation in Cardiac Tissue: Roles of the Sodium and L-type Calcium Currents During Reduced Excitability and Decreased Gap Junction Coupling," en, *Circulation Research*, pp. 727–741, Nov. 1997. DOI: 10.1161/01.RES.81.5.727.

[202] T. D. Butters, O. V. Aslanidi, S. Inada, *et al.*, "Mechanistic Links Between Na^+ Channel (SCN5A) Mutations and Impaired Cardiac Pacemaking in Sick Sinus Syndrome," en, *Circulation Research*, pp. 126–137, Jul. 2010. DOI: 10.1161/CIRCRESAHA.110.219949.

[203] F. Cacciani and M. Zaniboni, "Chronotropic Modulation of the Source-Sink Relationship of Sinoatrial-Atrial Impulse Conduction and Its Significance to Initiation of AF: A One-Dimensional Model Study," en, *BioMed Research International*, pp. 1–18, 2015. DOI: 10.1155/2015/496418.

[204] A. Fabbri, A. Loewe, R. Wilders, and S. Severi, "Pace-and-drive of the human sinoatrial node — A preliminary computational investigation," in *2017 Computing in Cardiology (CinC)*, ISSN: 2325-887X, Sep. 2017, pp. 1–4. DOI: 10.22489/CinC.2017.120-218.

[205] V. V. Fedorov, R. Chang, A. V. Glukhov, *et al.*, "Complex Interactions Between the Sinoatrial Node and Atrium During Reentrant Arrhythmias in the Canine Heart," en, *Circulation*, pp. 782–789, Aug. 2010. DOI: 10.1161/CIRCULATIONAHA.109.935288.

[206] Zyantekorov D.A., Syunyaev R.A., Kharche S.R., *et al.*, "Is insulating border necessary for human SAN?," 2018.

[207] S. Inada, J. Hancox, H. Zhang, and M. Boyett, "One-Dimensional Mathematical Model of the Atrioventricular Node Including Atrio-Nodal, Nodal, and Nodal-His Cells," *Biophysical Journal*, pp. 2117–2127, Oct. 2009. DOI: 10.1016/j.bpj.2009.06.056.

[208] P. Podziemski, "A simple model of the right atrium of the human heart with the sinoatrial and atrioventricular nodes included," en, *J Clin Monit Comput*, p. 18, 2013.

[209] J. Li, S. Inada, J. E. Schneider, H. Zhang, H. Dobrzynski, and M. R. Boyett, "Three-Dimensional Computer Model of the Right Atrium Including the Sinoatrial and Atrioventricular Nodes Predicts Classical Nodal Behaviours," en, *PLoS ONE*, A. V. Panfilov, Ed., e112547, Nov. 2014. DOI: 10.1371/journal.pone.0112547.

[210] H. Dobrzynski, J. Li, J. Tellez, *et al.*, "Computer Three-Dimensional Reconstruction of the Sinoatrial Node," en, *Circulation*, pp. 846–854, Feb. 2005. DOI: 10.1161/01.CIR.0000152100.04087.DB.

[211] V. V. Fedorov, A. V. Glukhov, R. Chang, *et al.*, "Optical Mapping of the Isolated Coronary-Perfused Human Sinus Node," en, *Journal of the American College of Cardiology*, pp. 1386–1394, Oct. 2010. DOI: 10.1016/j.jacc.2010.03.098.

[212] N. Li, B. J. Hansen, T. A. Csepe, *et al.*, "Redundant and diverse intranodal pacemakers and conduction pathways protect the human sinoatrial node from failure," en, *Science Translational Medicine*, eaam5607, Jul. 2017. DOI: 10.1126/scitranslmed.aam5607.

[213] M. Semelka, J. Gera, and S. Usman, "Sick Sinus Syndrome: A Review," en, p. 6, 2013.

[214] J. Wu, Y. Zhang, X. Zhang, *et al.*, "Altered sinoatrial node function and intra-atrial conduction in murine gain-of-function *Scn5a* +/δKPQ hearts suggest an overlap syndrome," en, *American Journal of Physiology-Heart and Circulatory Physiology*, H1510–H1523, Apr. 2012. DOI: 10.1152/ajpheart.00357.2011.

[215] C.-S. Ki, C. L. Jung, H.-j. Kim, *et al.*, "A KCNQ1 mutation causes age-dependant bradycardia and persistent atrial fibrillation," en, *Pflügers Archiv - European Journal of Physiology*, pp. 529–540, Mar. 2014. DOI: 10.1007/s00424-013-1337-6.

[216] D. G. Whittaker, M. A. Colman, H. Ni, J. C. Hancox, and H. Zhang, "Human Atrial Arrhythmogenesis and Sinus Bradycardia in KCNQ1-Linked Short QT Syndrome: Insights From Computational Modelling," en, *Frontiers in Physiology*, p. 1402, Oct. 2018. DOI: 10.3389/fphys.2018.01402.

[217] X. Zhou, A. Bueno-Orovio, R. J. Schilling, *et al.*, "Investigating the Complex Arrhythmic Phenotype Caused by the Gain-of-Function Mutation KCNQ1-G229D," en, *Frontiers in Physiology*, p. 259, Mar. 2019. DOI: 10.3389/fphys.2019.00259.

[218] L. Arbel-Ganon, J. A. Behar, A. M. Gómez, and Y. Yaniv, "Distinct mechanisms mediate pacemaker dysfunction associated with catecholaminergic polymorphic ventricular tachycardia mutations: Insights from computational modeling," en, *Journal of Molecular and Cellular Cardiology*, pp. 85–95, Jun. 2020. DOI: 10.1016/j.yjmcc.2020.04.017.

[219] R. M. Wolf, P. Glynn, S. Hashemi, *et al.*, "Atrial fibrillation and sinus node dysfunction in human ankyrin-B syndrome: A computational analysis," en, *American Journal of Physiology-Heart and Circulatory Physiology*, H1253–H1266, May 2013. DOI: 10.1152/ajpheart.00734.2012.

[220] J. Bai, Y. Lu, R. Sharma, and J. Zhao, "In Silico Screening of the Key Electrical Remodelling Targets in Atrial Fibrillation-induced Sinoatrial Node Dysfunction," en, Dec. 2019. DOI: 10.22489/CinC.2019.001.

[221] P. D. Swaminathan, A. Purohit, S. Soni, *et al.*, "Oxidized CaMKII causes cardiac sinus node dysfunction in mice," en, *Journal of Clinical Investigation*, pp. 3277–3288, Aug. 2011. DOI: 10.1172/JCI57833.

[222] M. Luo, X. Guan, E. D. Luczak, *et al.*, "Diabetes increases mortality after myocardial infarction by oxidizing CaMKII," en, *The Journal of Clinical Investigation*, pp. 1262–1274, Mar. 2013, Publisher: American Society for Clinical Investigation. DOI: 10.1172/JCI65268.

[223] A. Loewe, Y. Lutz, N. Nagy, *et al.*, "Inter-Species Differences in the Response of Sinus Node Cellular Pacemaking to Changes of Extracellular Calcium," en, p. 4, 2019.

[224] X. Bai, K. Wang, Y. Yuan, *et al.*, "Mechanism underlying impaired cardiac pacemaking rhythm during ischemia: A simulation study," en, *Chaos: An Interdisciplinary Journal of Nonlinear Science*, p. 093 934, Sep. 2017. DOI: 10.1063/1.5002664.

[225] W.-C. Tong, I. Ghouri, and M. J. Taggart, "Computational modeling of inhibition of voltage-gated Ca channels: Identification of different effects on uterine and cardiac action potentials," en, *Frontiers in Physiology*, Oct. 2014. DOI: 10.3389/fphys.2014.00399.

[226] A. Kojima, H. Kitagawa, M. Omatsu-Kanbe, H. Matsuura, and S. Nosaka, "Inhibitory effects of sevoflurane on pacemaking activity of sinoatrial node cells in guinea-pig heart," en, *British Journal of Pharmacology*, pp. 2117–2135, 2012. DOI: https://doi.org/10.1111/j.1476-5381.2012.01914.x.

[227] A. Kojima, Y. Ito, H. Kitagawa, H. Matsuura, and S. Nosaka, "Direct Negative Chronotropic Action of Desflurane on Sinoatrial Node Pacemaker Activity in the Guinea Pig Heart," *Anesthesiology*, pp. 1400–1413, Jun. 2014. DOI: 10.1097/ALN.0000000000000165.

[228] A. Kojima, Y. Ito, H. Kitagawa, and H. Matsuura, "Ionic mechanisms underlying the negative chronotropic action of propofol on sinoatrial node automaticity in guinea pig heart: Inhibition of sinoatrial node activity by propofol," en, *British Journal of Pharmacology*, pp. 799–814, Feb. 2015. DOI: 10.1111/bph.12936.

[229] A. Kojima and H. Matsuura, "Ionic mechanisms of the action of anaesthetics on sinoatrial node automaticity," en, *European Journal of Pharmacology*, pp. 63–72, Nov. 2017. DOI: 10.1016/j.ejphar.2017.08.006.

[230] J. Bai, Y. Lu, and H. Zhang, "In silico study of the effects of anti-arrhythmic drug treatment on sinoatrial node function for patients with atrial fibrillation," en, *Scientific Reports*, p. 305, Dec. 2020. DOI: 10.1038/s41598-019-57246-5.

[231] I. Bidaud, A. D'Souza, G. Forte, *et al.*, "Genetic Ablation of G Protein-Gated Inwardly Rectifying K+ Channels Prevents Training-Induced Sinus Bradycardia," *Frontiers in Physiology*, 2021. DOI: 10.3389/fphys.2020.519382.

[232] M. Baruscotti, A. Bucchi, R. Milanesi, *et al.*, "A gain-of-function mutation in the cardiac pacemaker HCN4 channel increasing cAMP sensitivity is associated with familial Inappropriate Sinus Tachycardia," eng, *European Heart Journal*, pp. 280–288, Jan. 2017. DOI: 10.1093/eurheartj/ehv582.

[233] J. Zhao, T. Liu, and G. Li, "Relationship Between Two Arrhythmias: Sinus Node Dysfunction and Atrial Fibrillation," en, *Archives of Medical Research*, pp. 351–355, May 2014. DOI: 10.1016/j.arcmed.2014.04.005.

[234] T. Mesquita, R. Zhang, J. H. Cho, *et al.*, "Mechanisms of Sinoatrial Node Dysfunction in Heart Failure With Preserved Ejection Fraction," *Circulation*, pp. 45–60, 2022, Publisher: American Heart Association. DOI: 10.1161/CIRCULATIONAHA.121.054976.

[235] R. Cappato, S. Castelvecchio, C. Ricci, *et al.*, "Clinical Efficacy of Ivabradine in Patients With Inappropriate Sinus Tachycardia," en, *Journal of the American College of Cardiology*, pp. 1323–1329, Oct. 2012. DOI: 10.1016/j.jacc.2012.06.031.

[236] C. M. Janson, R. B. Tan, V. R. Iyer, R. L. Vogel, V. L. Vetter, and M. J. Shah, "Ivabradine for treatment of tachyarrhythmias in children and young adults," *HeartRhythm Case Reports*, pp. 333–337, Mar. 2019. DOI: 10.1016/j.hrcr.2019.03.007.

[237] M. R. Boyett, Y. Wang, S. Nakao, *et al.*, "Point: Exercise training-induced bradycardia is caused by changes in intrinsic sinus node function," *Journal of Applied Physiology*, pp. 684–685, Sep. 2017, Publisher: American Physiological Society. DOI: 10.1152/japplphysiol.00604.2017.

[238] G. E. Billman, "Counterpoint: Exercise training-induced bradycardia: The case for enhanced parasympathetic regulation," *Journal of Applied Physiology*, pp. 686–688, Sep. 2017, Publisher: American Physiological Society. DOI: 10.1152/japplphysiol.00605.2017.

[239] A. D'Souza, A. Bucchi, A. B. Johnsen, *et al.*, "Exercise training reduces resting heart rate via downregulation of the funny channel HCN4," en, *Nature Communications*, p. 3775, May 2014, Number: 1 Publisher: Nature Publishing Group. DOI: 10.1038/ncomms4775.

[240] G. E. Billman, K. L. Cagnoli, T. Csepe, *et al.*, "Exercise training-induced bradycardia: Evidence for enhanced parasympathetic regulation without changes in intrinsic sinoatrial node function," en, *Journal of Applied Physiology*, pp. 1344–1355, Jun. 2015. DOI: 10.1152/japplphysiol.01111.2014.

[241] A. Bernjak, A. Iqbal, S. R. Heller, and R. H. Clayton, "Hypoglycaemia combined with mild hypokalaemia reduces the heart rate and causes abnormal pacemaker activity in a computational model of a human sinoatrial cell," *Journal of The Royal Society Interface*, p. 20 210 612, Nov. 2021, Publisher: Royal Society. DOI: 10.1098/rsif.2021.0612.

[242] P. Kohl, P. Camelliti, F. L. Burton, and G. L. Smith, "Electrical coupling of fibroblasts and myocytes: Relevance for cardiac propagation," en, *Journal of Electrocardiology*, pp. 45–50, Oct. 2005. DOI: 10.1016/j.jelectrocard.2005.06.096.

[243] U. Doris, S. Kharche, M. Petkova, H. Dobrzynski, and J. Yanni, "A sexy approach to pacemaking: Differences in function and molecular make up of the sinoatrial node," en, *Histology and Histopathology*, pp. 1255–1268, Nov. 2019. DOI: 10.14670/HH-18-115.

[244] T. A. Csepe, J. Zhao, L. V. Sul, *et al.*, "Novel application of 3D contrast-enhanced CMR to define fibrotic structure of the human sinoatrial node in vivo," en, *European Heart Journal - Cardiovascular Imaging*, pp. 862–869, Aug. 2017. DOI: 10.1093/ehjci/jew304.

[245] P. Camelliti, C. R. Green, I. LeGrice, and P. Kohl, "Fibroblast network in rabbit sinoatrial node: Structural and functional identification of homogeneous and heterogeneous cell coupling," eng, *Circulation Research*, pp. 828–835, Apr. 2004. DOI: 10.1161/01.RES.0000122382.19400.14.

[246] T. R. Brown, T. Krogh-Madsen, and D. J. Christini, "Computational Approaches to Understanding the Role of Fibroblast-Myocyte Interactions in Cardiac Arrhythmogenesis," en, *BioMed Research International*, pp. 1–12, 2015. DOI: 10.1155/2015/465714.

[247] A. C. Zeigler, W. J. Richardson, J. W. Holmes, and J. J. Saucerman, "Computational modeling of cardiac fibroblasts and fibrosis," en, *Journal of Molecular and Cellular Cardiology*, pp. 73–83, Apr. 2016. DOI: 10.1016/j.yjmcc.2015.11.020.

[248] V. Jacquemet and C. S. Henriquez, "Modelling cardiac fibroblasts: Interactions with myocytes and their impact on impulse propagation," en, *EP Europace*, pp. vi29–vi37, Nov. 2007. DOI: 10.1093/europace/eum207.

[249] F. Liu, H. Wu, X. Yang, *et al.*, "A new model of myofibroblast-cardiomyocyte interactions and their differences across species," *Biophysical Journal*, pp. 3764–3775, Sep. 2021. DOI: 10.1016/j.bpj.2021.06.040.

[250] K. Andrew MacCannell, H. Bazzazi, L. Chilton, Y. Shibukawa, R. B. Clark, and W. R. Giles, "A Mathematical Model of Electrotonic Interactions between Ventricular Myocytes and Fibroblasts," *Biophysical Journal*, pp. 4121–4132, Jun. 2007. DOI: 10.1529/biophysj.106.101410.

[251] A. Greisas and S. Zlochiver, "Modulation of Cardiac Pacemaker Inter Beat Intervals by Sinoatrial Fibroblasts - a Numerical Study," en, p. 4, 2016.

[252] M. B. Rook, A. C. van Ginneken, B. de Jonge, A. el Aoumari, D. Gros, and H. J. Jongsma, "Differences in gap junction channels between cardiac myocytes, fibroblasts, and heterologous pairs," *American Journal of Physiology-Cell Physiology*, pp. C959–C977, Nov. 1992, Publisher: American Physiological Society. DOI: 10.1152/ajpcell.1992.263.5.C959.

[253] P. Kohl, A. Kamkin, I. Kiseleva, and D. Noble, "Mechanosensitive fibroblasts in the sino-atrial node region of rat heart: Interaction with cardiomyocytes and possible role," en, *Experimental Physiology*, pp. 943–956, Nov. 1994. DOI: 10.1113/expphysiol.1994.sp003819.

[254] E. Ricci, C. Bartolucci, and S. Severi, "Effects of Density and Distribution of Non-Spontaneous Myocytes, Scars and Fibroblasts Inside the Human Sinoatrial Node," in *2021 Computing in Cardiology (CinC)*, ISSN: 2325-887X, Sep. 2021, pp. 1–4. DOI: 10.23919/CinC53138.2021.9662905.

[255] R. Morgan, M. A. Colman, H. Chubb, G. Seemann, and O. V. Aslanidi, "Slow Conduction in the Border Zones of Patchy Fibrosis Stabilizes the Drivers for Atrial Fibrillation: Insights from Multi-Scale Human Atrial Modeling," English, *Frontiers in Physiology*, 2016, Publisher: Frontiers. DOI: 10.3389/fphys.2016.00474.

[256] V. V. Galanin, "Similitude Methods and Three-Dimensional Simulation of the Electrical Activity of the Rabbit Sinoatrial Node and Adjacent Atrial Myocardium," en, *Biophysics*, pp. 142–148, Jan. 2021. DOI: 10.1134/S000635092101019X.

[257] E. A. MacDonald, J. Madl, J. Greiner, *et al.*, "Sinoatrial Node Structure, Mechanics, Electrophysiology and the Chronotropic Response to Stretch in Rabbit and Mouse," en, *Frontiers in Physiology*, p. 809, Jul. 2020. DOI: 10.3389/fphys.2020.00809.

[258] E. A. MacDonald and T. A. Quinn, "What keeps us ticking? Sinoatrial node mechano-sensitivity: The grandfather clock of cardiac rhythm," en, *Biophysical Reviews*, pp. 707–716, Oct. 2021. DOI: 10.1007/s12551-021-00831-8.

[259] D. Turner, C. Kang, P. Mesirca, *et al.*, "Electrophysiological and Molecular Mechanisms of Sinoatrial Node Mechanosensitivity," *Frontiers in Cardiovascular Medicine*, 2021.

[260] S. Dokos, B. Celler, and N. Lovell, "Vagal Control of Sinoatrial Rhythm: A Mathematical Model," en, *Journal of Theoretical Biology*, pp. 21–44, Sep. 1996. DOI: 10.1006/jtbi.1996.0141.

[261] S. S. Demir, J. W. Clark, and W. R. Giles, "Parasympathetic modulation of sinoatrial node pacemaker activity in rabbit heart: A unifying model," en, *American Journal of Physiology-Heart and Circulatory Physiology*, H2221–H2244, Jun. 1999. DOI: 10.1152/ajpheart.1999.276.6.H2221.

[262] H. Zhang, A. V. Holden, D. Noble, and M. R. Boyett, "Analysis of the Chronotropic Effect of Acetylcholine on Sinoatrial Node Cells," en, *Journal of Cardiovascular Electrophysiology*, pp. 465–474, May 2002. DOI: 10.1046/j.1540-8167.2002.00465.x.

[263] N. P. Castellanos and R. Godinez, "Simulating the extrinsic regulation of the sinoatrial node cells using a unified computational model," en, *Biomedical Physics & Engineering Express*, p. 035 009, May 2017, Publisher: IOP Publishing. DOI: 10.1088/2057-1976/aa6bff.

[264] R. Moss, F. B. Sachse, E. G. Moreno-Galindo, R. A. Navarro-Polanco, M. Tristani-Firouzi, and G. Seemann, "Modeling effects of voltage dependent properties of the cardiac muscarinic receptor on human sinus node function," en, *PLOS Computational Biology*, A. L. Marsden, Ed., e1006438, Oct. 2018. DOI: 10.1371/journal.pcbi.1006438.

[265] D. S. Rubenstein and S. L. Lipsius, "Mechanisms of automaticity in subsidiary pacemakers from cat right atrium.," *Circulation Research*, pp. 648–657, Apr. 1989, Publisher: American Heart Association. DOI: 10.1161/01.RES.64.4.648.

[266] D. (R.) Šćepanović, "A model of sinoatrial node cell regulation by the autonomic nervous system," eng, Accepted: 2012-01-12T19:29:19Z, Thesis, Massachusetts Institute of Technology, 2011.

[267] D. Lang, "Spatiotemporal control of heart rate in a rabbit heart," en, *Journal of Electrocardiology*, p. 9, 2011.

[268] J. A. Brennan, Q. Chen, A. Gams, *et al.*, "Evidence of Superior and Inferior Sinoatrial Nodes in the Mammalian Heart," en, *JACC: Clinical Electrophysiology*, pp. 1827–1840, Dec. 2020. DOI: 10.1016/j.jacep.2020.09.012.

[269] P. Hanna, M. J. Dacey, J. Brennan, *et al.*, "Innervation and Neuronal Control of the Mammalian Sinoatrial Node a Comprehensive Atlas," en, *Circulation Research*, pp. 1279–1296, Apr. 2021. DOI: 10.1161/CIRCRESAHA.120.318458.

[270] D. Lang and A. V. Glukhov, "Functional Microdomains in Heart's Pacemaker: A Step Beyond Classical Electrophysiology and Remodeling," en, *Frontiers in Physiology*, p. 1686, Nov. 2018. DOI: 10.3389/fphys.2018.01686.

[271] R. Bychkov, M. Juhaszova, K. Tsutsui, *et al.*, "Synchronized Cardiac Impulses Emerge From Heterogeneous Local Calcium Signals Within and Among Cells of Pacemaker Tissue," en, *JACC: Clinical Electrophysiology*, pp. 907–931, Aug. 2020. DOI: 10.1016/j.jacep.2020.06.022.

[272] D. Liang, Z. Xue, J. Xue, *et al.*, "Sinoatrial node pacemaker cells share dominant biological properties with glutamatergic neurons," eng, *Protein & Cell*, Feb. 2021. DOI: 10.1007/s13238-020-00820-9.

[273] R. Bychkov, M. Juhaszova, M. Calvo-Rubio Barrera, *et al.*, "The Heart's Pacemaker Mimics Brain Cytoarchitecture and Function: Novel Interstitial Cells Expose Complexity of the SAN," en, *JACC: Clinical Electrophysiology*, pp. 1191–1215, Oct. 2022. DOI: 10.1016/j.jacep.2022.07.003.

[274] T. Mäki-Marttunen, G. T. Lines, A. G. Edwards, *et al.*, "Pleiotropic effects of schizophrenia-associated genetic variants in neuron firing and cardiac pacemaking revealed by computational modeling," en, *Translational Psychiatry*, p. 5, Nov. 2017. DOI: 10.1038/s41398-017-0007-4.

[275] E. A. MacDonald, R. A. Rose, and T. A. Quinn, "Neurohumoral Control of Sinoatrial Node Activity and Heart Rate: Insight From Experimental Models and Findings From Humans," en, *Frontiers in Physiology*, p. 170, Mar. 2020. DOI: 10.3389/fphys.2020.00170.

[276] "CellML," DOI: https://www.cellml.org/.

[277] G. Plank, A. Loewe, A. Neic, *et al.*, "The openCARP simulation environment for cardiac electrophysiology," en, *Computer Methods and Programs in Biomedicine*, p. 106 223, Sep. 2021. DOI: 10.1016/j.cmpb.2021.106223.

[278] M. Clerx, P. Collins, E. de Lange, and P. G. Volders, "Myokit: A simple interface to cardiac cellular electrophysiology," en, *Progress in Biophysics and Molecular Biology*, pp. 100–114, Jan. 2016. DOI: 10.1016/j.pbiomolbio.2015.12.008.

[279] C. Rickert and C. Proenza, "ParamAP: Standardized Parameterization of Sinoatrial Node Myocyte Action Potentials," en, *Biophysical Journal*, pp. 765–769, Aug. 2017. DOI: 10.1016/j.bpj.2017.07.001.

[280] A. V. Maltsev, M. D. Stern, E. G. Lakatta, and V. A. Maltsev, "A novel conceptual model of heart rate autonomic modulation based on a small-world modular structure of the sinoatrial node," English, *Frontiers in Physiology*, Dec. 2023, Publisher: Frontiers. DOI: 10.3389/fphys.2023.1276023.

[281] A. G. Torrente, R. Zhang, H. Wang, *et al.*, "Contribution of small conductance K+ channels to sinoatrial node pacemaker activity: Insights from atrial-specific Na+/Ca2+ exchange knockout mice," *The Journal of Physiology*, pp. 3847–3865, Jun. 2017. DOI: 10.1113/JP274249.

[282] J. Jalife, "Mutual entrainment and electrical coupling as mechanisms for synchronous firing of rabbit sino-atrial pace-maker cells.," en, *The Journal of Physiology*, pp. 221–243, 1984. DOI: https://doi.org/10.1113/jphysiol.1984.sp015461.

[283] D. L. Ypey, D. E. Clapham, and R. L. DeHaan, "Development of electrical coupling and action potential synchrony between paired aggregates of embryonic heart cells," en, *The Journal of Membrane Biology*, pp. 75–96, Mar. 1979. DOI: 10.1007/BF01869344.

[284] M. Kim, O. Monfredi, L. Maltseva, E. Lakatta, and V. Maltsev, "β-Adrenergic Stimulation Synchronizes a Broad Spectrum of Action Potential Firing Rates of Cardiac Pacemaker Cells toward a Higher Population Average," English, *Cells*, 2021. DOI: 10.3390/cells10082124.

[285] M. A. Cummins, P. J. Dalal, M. Bugana, S. Severi, and E. A. Sobie, "Comprehensive analyses of ventricular myocyte models identify targets exhibiting favorable rate dependence," eng, *PLoS computational biology*, e1003543, Mar. 2014. DOI: 10.1371/journal.pcbi.1003543.

[286] J. D. Moreno, P.-C. Yang, J. R. Bankston, *et al.*, "Ranolazine for congenital and acquired late INa-linked arrhythmias: In silico pharmacological screening," eng, *Circulation Research*, e50–e61, Sep. 2013. DOI: 10.1161/CIRCRESAHA.113.301971.

[287] S. A. Mann, M. Imtiaz, A. Winbo, *et al.*, "Convergence of models of human ventricular myocyte electrophysiology after global optimization to recapitulate clinical long QT phenotypes," eng, *Journal of Molecular and Cellular Cardiology*, pp. 25–34, Nov. 2016. DOI: 10.1016/j.yjmcc.2016.09.011.

[288] M. R. Boyett, S. Inada, S. Yoo, *et al.*, "Connexins in the sinoatrial and atrioventricular nodes," eng, *Advances in Cardiology*, pp. 175–197, 2006. DOI: 10.1159/000092569.

[289] J. P. Fahrenbach, R. Mejia-Alvarez, and K. Banach, "The relevance of non-excitable cells for cardiac pacemaker function: Non-excitable cells and cardiac pacemaker function," en, *The Journal of Physiology*, pp. 565–578, Dec. 2007. DOI: 10.1113/jphysiol.2007.144121.

[290] A. X. Sarkar and E. A. Sobie, "Quantification of repolarization reserve to understand interpatient variability in the response to proarrhythmic drugs: A computational analysis," *Heart Rhythm*, pp. 1749–1755, Nov. 2011. DOI: 10.1016/j.hrthm.2011.05.023.

[291] E. A. Sobie, "Parameter Sensitivity Analysis in Electrophysiological Models Using Multivariable Regression," en, *Biophysical Journal*, pp. 1264–1274, Feb. 2009. DOI: 10.1016/j.bpj.2008.10.056.

[292] Y.-S. Lee, O. Z. Liu, H. S. Hwang, B. C. Knollmann, and E. A. Sobie, "Parameter Sensitivity Analysis of Stochastic Models Provides Insights into Cardiac Calcium Sparks," *Biophysical Journal*, pp. 1142–1150, Mar. 2013. DOI: 10.1016/j.bpj.2012.12.055.

[293] S. Morotti and E. Grandi, "Logistic regression analysis of populations of electrophysiological models to assess proarrythmic risk," *MethodsX*, pp. 25–34, Jan. 2017. DOI: 10.1016/j.mex.2016.12.002.

[294] M. J. Wallace, M. El Refaey, P. Mesirca, T. J. Hund, M. E. Mangoni, and P. J. Mohler, "Genetic Complexity of Sinoatrial Node Dysfunction," English, *Frontiers in Genetics*, 2021, Publisher: Frontiers. DOI: 10.3389/fgene.2021.654925.

[295] A. M. W. Alings and L. N. Bouman, "Electrophysiology of the ageing rabbit and cat sinoatrial node - a comparative study," *European Heart Journal*, pp. 1278–1288, Sep. 1993. DOI: 10.1093/eurheartj/14.9.1278.

[296] J. O. Tellez, M. Mączewski, J. Yanni, *et al.*, "Ageing-dependent remodelling of ion channel and Ca2+ clock genes underlying sino-atrial node pacemaking," en, *Experimental Physiology*, pp. 1163–1178, 2011. DOI: 10.1113/expphysiol.2011.057752.

[297] S. A. Jones, M. K. Lancaster, and M. R. Boyett, "Ageing-related changes of connexins and conduction within the sinoatrial node," en, *The Journal of Physiology*, pp. 429–437, 2004. DOI: 10.1113/jphysiol.2004.072108.

[298] Anumonwo J M, Wang H Z, Trabka-Janik E, *et al.*, "Gap junctional channels in adult mammalian sinus nodal cells. Immunolocalization and electrophysiology.," *Circulation Research*, pp. 229–239, Aug. 1992, Publisher: American Heart Association. DOI: 10.1161/01.RES.71.2.229.

[299] Y. Xie, D. Sato, A. Garfinkel, Z. Qu, and J. N. Weiss, "So Little Source, So Much Sink: Requirements for Afterdepolarizations to Propagate in Tissue," en, *Biophysical Journal*, pp. 1408–1415, Sep. 2010. DOI: 10.1016/j.bpj.2010.06.042.

[300] T. P. Nguyen, Z. Qu, and J. N. Weiss, "Cardiac fibrosis and arrhythmogenesis: The road to repair is paved with perils," *Journal of Molecular and Cellular Cardiology*, Myocyte - Fibroblast Signalling in Myocardium, pp. 83–91, May 2014. DOI: 10.1016/j.yjmcc.2013.10.018.

[301] M. R. Boyett, J. Yanni, J. Tellez, *et al.*, "Regulation of sinus node pacemaking and atrioventricular node conduction by HCN channels in health and disease," en, *Progress in Biophysics and Molecular Biology*, pp. 61–85, Nov. 2021. DOI: 10.1016/j.pbiomolbio.2021.06.008.

[302] R. M. John and S. Kumar, "Sinus Node and Atrial Arrhythmias," en, *Circulation*, pp. 1892–1900, May 2016. DOI: 10.1161/CIRCULATIONAHA.116.018011.

[303] K. Tsutsui, O. J. Monfredi, S. G. Sirenko-Tagirova, *et al.*, "A coupled-clock system drives the automaticity of human sinoatrial nodal pacemaker cells," en, *Science Signaling*, eaap7608, Jun. 2018. DOI: 10.1126/scisignal.aap7608.

[304] J. Pellman, J. Zhang, and F. Sheikh, "Myocyte-fibroblast communication in cardiac fibrosis and arrhythmias: Mechanisms and model systems," en, *Journal of Molecular and Cellular Cardiology*, pp. 22–31, May 2016. DOI: 10.1016/j.yjmcc.2016.03.005.

[305] Y. Wang, Q. Li, B. Tao, *et al.*, "Fibroblasts in heart scar tissue directly regulate cardiac excitability and arrhythmogenesis," *Science*, pp. 1480–1487, Sep. 2023, Publisher: American Association for the Advancement of Science. DOI: 10.1126/science.adh9925.

[306] K. Tsutsui, M. Florio, A. Yang, *et al.*, "cAMP-Dependent Signaling Restores AP Firing in Dormant SA Node Cells via Enhancement of Surface Membrane Currents and Calcium Coupling," English, *Frontiers in Physiology*, 2021. DOI: 10.3389/fphys.2021.596832.

[307] J. Zhao, R. Sharma, A. Kalyanasundaram, *et al.*, "Mechanistic insight into the functional role of human sinoatrial node conduction pathways and pacemaker compartments heterogeneity: A computer model analysis," en, *PLOS Computational Biology*, e1011708, Dec. 2023, Publisher: Public Library of Science. DOI: 10.1371/journal.pcbi.1011708.

[308] K. H. Jæger and A. Tveito, "The simplified Kirchhoff network model (SKNM): A cell-based reaction–diffusion model of excitable tissue," *Scientific Reports*, p. 16 434, Sep. 2023. DOI: 10.1038/s41598-023-43444-9.

[309] S. Verheule, M. J. A. van Kempen, S. Postma, M. B. Rook, and H. J. Jongsma, "Gap junctions in the rabbit sinoatrial node," en, *American Journal of Physiology-Heart and Circulatory Physiology*, H2103–H2115, May 2001. DOI: 10.1152/ajpheart.2001.280.5.H2103.

[310] O. V. Aslanidi, M. R. Boyett, H. Dobrzynski, J. Li, and H. Zhang, "Mechanisms of Transition from Normal to Reentrant Electrical Activity in a Model of Rabbit Atrial Tissue: Interaction of Tissue Heterogeneity and Anisotropy," en, *Biophysical Journal*, pp. 798–817, Feb. 2009. DOI: 10.1016/j.bpj.2008.09.057.

[311] M. Yamamoto, H. Honjo, R. Niwa, and I. Kodama, "Low-frequency extracellular potentials recorded from the sinoatrial node," *Cardiovascular Research*, pp. 360–372, Aug. 1998. DOI: 10.1016/S0008-6363(98)00091-1.

[312] W. H. Litchenberg, L. W. Norman, A. K. Holwell, K. L. Martin, K. W. Hewett, and R. G. Gourdie, "The rate and anisotropy of impulse propagation in the postnatal terminal crest are correlated with remodeling of Cx43 gap junction pattern," eng, *Cardiovascular Research*, pp. 379–387, Jan. 2000. DOI: 10.1016/s0008-6363(99)00363-6.

[313] J. R. de Groot, T. Veenstra, A. O. Verkerk, *et al.*, "Conduction slowing by the gap junctional uncoupler carbenoxolone," eng, *Cardiovascular Research*, pp. 288–297, Nov. 2003. DOI: 10.1016/j.cardiores.2003.07.004.

[314] T. A. Csepe, A. Kalyanasundaram, B. J. Hansen, J. Zhao, and V. V. Fedorov, "Fibrosis: A structural modulator of sinoatrial node physiology and dysfunction," en, *Frontiers in Physiology*, Feb. 2015. DOI: 10.3389/fphys.2015.00037.

[315] T. A. Csepe, B. J. Hansen, and V. V. Fedorov, "Atrial fibrillation driver mechanisms: Insight from the isolated human heart," en, *Trends in Cardiovascular Medicine*, pp. 1–11, Jan. 2017. DOI: 10.1016/j.tcm.2016.05.008.

[316] A. Kalyanasundaram, N. Li, M. L. Gardner, *et al.*, "Fibroblast-Specific Proteotranscriptomes Reveal Distinct Fibrotic Signatures of Human Sinoatrial Node in Nonfailing and Failing Hearts," *Circulation*, pp. 126–143,

Jul. 2021, Publisher: American Heart Association. DOI: 10.1161/CIRCULATIONAHA.120.051583.

[317] N. Li, B. J. Hansen, J. Kennelly, *et al.*, "High-Resolution 3-Dimensional Multimodality Imaging to Resolve Intramural Human Sinoatrial Node Pacemakers and Epicardial-Endocardial Atrial Exit Sites," *Circulation: Arrhythmia and Electrophysiology*, e011528, Apr. 2023, Publisher: American Heart Association. DOI: 10.1161/CIRCEP.122.011528.

[318] F. Ravelli, M. Masè, M. Del Greco, M. Marini, and M. Disertori, "Acute Atrial Dilatation Slows Conduction and Increases AF Vulnerability in the Human Atrium," en, *Journal of Cardiovascular Electrophysiology*, pp. 394–401, 2011, _eprint: https://onlinelibrary.wiley.com/doi/pdf/10.1111/j.1540-8167.2010.01939.x. DOI: 10.1111/j.1540-8167.2010.01939.x.

[319] P. Kojodjojo, P. Kanagaratnam, V. Markides, D. W. Davies, and N. Peters, "Age-related changes in human left and right atrial conduction," eng, *Journal of Cardiovascular Electrophysiology*, pp. 120–127, Feb. 2006. DOI: 10.1111/j.1540-8167.2005.00293.x.

[320] A. Ferrer, R. Sebastián, D. Sánchez-Quintana, *et al.*, "Detailed Anatomical and Electrophysiological Models of Human Atria and Torso for the Simulation of Atrial Activation," en, *PLOS ONE*, e0141573, Nov. 2015, Publisher: Public Library of Science. DOI: 10.1371/journal.pone.0141573.

[321] P. M. Boyle and E. J. Vigmond, "An Intuitive Safety Factor for Cardiac Propagation," en, *Biophysical Journal*, pp. L57–L59, Jun. 2010. DOI: 10.1016/j.bpj.2010.03.018.

[322] C. Bartolucci, C. Fabbri, C. Tomasi, P. Sabbatani, S. Severi, and C. Corsi, "Computational Analysis of Mapping Catheter Geometry and Contact Quality Effects on Rotor Detection in Atrial Fibrillation," *Frontiers in Physiology*, 2021.

[323] K. E. Shillieto, P. Ganesan, A. J. Salmin, E. M. Cherry, A. M. Pertsov, and B. Ghoraani, "Catheter simulator software tool to generate electrograms of any multi-polar diagnostic catheter from 3D atrial tissue," in *2016 38th Annual International Conference of the IEEE Engineering in Medicine and Biology Society (EMBC)*, ISSN: 1558-4615, Aug. 2016, pp. 2741–2744. DOI: 10.1109/EMBC.2016.7591297.

[324] Y. Xie, A. Garfinkel, P. Camelliti, P. Kohl, J. N. Weiss, and Z. Qu, "Effects of fibroblast-myocyte coupling on cardiac conduction and vulnerability to reentry: A computational study," *Heart Rhythm*, pp. 1641–1649, Nov. 2009. DOI: 10.1016/j.hrthm.2009.08.003.

[325] M. Miragoli, N. Salvarani, and S. Rohr, "Myofibroblasts Induce Ectopic Activity in Cardiac Tissue," *Circulation Research*, pp. 755–758, Oct. 2007, Publisher: American Heart Association. DOI: 10.1161/CIRCRESAHA.107.160549.

[326] Q. Lou, A. V. Glukhov, B. Hansen, *et al.*, "Tachy-brady arrhythmias: The critical role of adenosine-induced sinoatrial conduction block in post-tachycardia pauses," *Heart Rhythm*, pp. 110–118, Jan. 2013. DOI: 10.1016/j.hrthm.2012.09.012.

[327] Q. Lou, B. J. Hansen, O. Fedorenko, *et al.*, "Upregulation of Adenosine A1 Receptors Facilitates Sinoatrial Node Dysfunction in Chronic Canine Heart Failure by Exacerbating Nodal Conduction Abnormalities Revealed by Novel Dual-Sided Intramural Optical Mapping," en, *Circulation*, pp. 315–324, Jul. 2014. DOI: 10.1161/CIRCULATIONAHA.113.007086.

[328] T. Opthof, "The normal range and determinants of the intrinsic heart rate in manq," en, *Cardiovascular Research*, 1970.

[329] C. H. Peters, E. J. Sharpe, and C. Proenza, "Cardiac Pacemaker Activity and Aging," en, *Annual Review of Physiology*, pp. 21–43, Feb. 2020. DOI: 10.1146/annurev-physiol-021119-034453.

[330] F. B. Sachse, A. P. Moreno, and J. A. Abildskov, "Electrophysiological Modeling of Fibroblasts and their Interaction with Myocytes," en, *Annals of Biomedical Engineering*, pp. 41–56, Jan. 2008. DOI: 10.1007/s10439-007-9405-8.

[331] M. M. Maleckar, J. L. Greenstein, W. R. Giles, and N. A. Trayanova, "Electrotonic Coupling between Human Atrial Myocytes and Fibroblasts Alters Myocyte Excitability and Repolarization," *Biophysical Journal*, pp. 2179–2190, Oct. 2009. DOI: 10.1016/j.bpj.2009.07.054.

[332] D. Sánchez-Quintana, R. H. Anderson, J. A. Cabrera, *et al.*, "The terminal crest: Morphological features relevant to electrophysiology," en, *Heart*, pp. 406–411, Oct. 2002. DOI: 10.1136/heart.88.4.406.

[333] R. L. Smithers, H. K. Kao, S. Zeigler, *et al.*, "Making Heads or Tails of the Large Mammalian Sinoatrial Node Micro-Organization," *Circulation: Arrhythmia and Electrophysiology*, e010465, Dec. 2021, Publisher: American Heart Association. DOI: 10.1161/CIRCEP.121.010465.

[334] N. H. Lovell, S. L. Cloherty, B. G. Celler, and S. Dokos, "A gradient model of cardiac pacemaker myocytes," en, *Progress in Biophysics and Molecular Biology*, pp. 301–323, Jun. 2004. DOI: 10.1016/j.pbiomolbio.2003.12.001.

[335] J. L. Ardell and J. A. Armour, "Neurocardiology: Structure-Based Function," en, in *Comprehensive Physiology*, R. Terjung, Ed., 1st ed., Wiley, Sep. 2016, pp. 1635–1653. DOI: 10.1002/cphy.c150046.

[336] J. Hadaya and J. L. Ardell, "Autonomic Modulation for Cardiovascular Disease," en, *Frontiers in Physiology*, p. 617 459, Dec. 2020. DOI: 10.3389/fphys.2020.617459.

[337] C. Clyburn, J. J. Sepe, and B. A. Habecker, "What gets on the nerves of cardiac patients? Pathophysiological changes in cardiac innervation," eng, *The Journal of Physiology*, pp. 451–461, Feb. 2022. DOI: 10.1113/JP281118.

[338] R. Mehra, O. A. Tjurmina, O. A. Ajijola, *et al.*, "Research Opportunities in Autonomic Neural Mechanisms of Cardiopulmonary Regulation: A Report From the National Heart, Lung, and Blood Institute and the National Institutes of Health Office of the Director Workshop," en, *JACC: Basic to Translational Science*, pp. 265–293, Mar. 2022. DOI: 10.1016/j.jacbts.2021.11.003.

[339] K. Shivkumar, O. A. Ajijola, I. Anand, *et al.*, "Clinical neurocardiology defining the value of neuroscience-based cardiovascular therapeutics," *The Journal of Physiology*, pp. 3911–3954, Jul. 2016. DOI: 10.1113/JP271870.

[340] S. Salavatian, E. Beaumont, J.-P. Longpré, *et al.*, "Vagal stimulation targets select populations of intrinsic cardiac neurons to control neurally induced atrial fibrillation," *American Journal of Physiology-Heart and Circulatory Physiology*, H1311–H1320, Nov. 2016, Publisher: American Physiological Society. DOI: 10.1152/ajpheart.00443.2016.

[341] E. Beaumont, E. M. Southerland, J. C. Hardwick, *et al.*, "Vagus nerve stimulation mitigates intrinsic cardiac neuronal and adverse myocyte remodeling postmyocardial infarction," *American Journal of Physiology-Heart and Circulatory Physiology*, H1198–H1206, Oct. 2015, Publisher: American Physiological Society. DOI: 10.1152/ajpheart.00393.2015.

[342] E. Beaumont, G. L. Wright, E. M. Southerland, *et al.*, "Vagus nerve stimulation mitigates intrinsic cardiac neuronal remodeling and cardiac hypertrophy induced by chronic pressure overload in guinea pig," *American Journal of Physiology-Heart and Circulatory Physiology*, H1349–H1359, May 2016, Publisher: American Physiological Society. DOI: 10.1152/ajpheart.00939.2015.

[343] M. A. Konstam, D. L. Mann, J. J. E. Udelson, *et al.*, "Advances in Our Clinical Understanding of Autonomic Regulation Therapy Using Vagal Nerve Stimulation in Patients Living With Heart Failure," *Frontiers in Physiology*, 2022.

[344] I. S. Anand, M. A. Konstam, H. U. Klein, *et al.*, "Comparison of symptomatic and functional responses to vagus nerve stimulation in ANTHEM-HF, INOVATE-HF, and NECTAR-HF," en, *ESC Heart Failure*, pp. 76–84, 2020, _eprint: https://onlinelibrary.wiley.com/doi/pdf/10.1002/ehf2.12592. DOI: 10.1002/ehf2.12592.

[345] R. K. Premchand, K. Sharma, S. Mittal, *et al.*, "Autonomic regulation therapy via left or right cervical vagus nerve stimulation in patients with chronic heart failure: Results of the ANTHEM-HF trial," eng, *Journal of Cardiac Failure*, pp. 808–816, Nov. 2014. DOI: 10.1016/j.cardfail.2014.08.009.

[346] J. Hayano, N. Ueda, M. Kisohara, E. Yuda, R. M. Carney, and J. A. Blumenthal, "Survival Predictors of Heart Rate Variability After Myocardial Infarction With and Without Low Left Ventricular Ejection Fraction," *Frontiers in Neuroscience*, 2021.

[347] X. Liu, L. Xiang, and G. Tong, "Predictive values of heart rate variability, deceleration and acceleration capacity of heart rate in post-infarction patients with LVEF $\geq$35%," *Annals of Noninvasive Electrocardiology*, e12771, Jul. 2020. DOI: 10.1111/anec.12771.

[348] J. Hadaya, A.-H. Dajani, S. Cha, *et al.*, "Vagal Nerve Stimulation Reduces Ventricular Arrhythmias and Mitigates Adverse Neural Cardiac Remodeling Post–Myocardial Infarction," en, *JACC: Basic to Translational Science*, S2452302X23001560, Jun. 2023. DOI: 10.1016/j.jacbts.2023.03.025.

[349] J. L. Ardell, H. Nier, M. Hammer, *et al.*, "Defining the neural fulcrum for chronic vagus nerve stimulation: Implications for integrated cardiac control," en, *The Journal of Physiology*, pp. 6887–6903, 2017, _eprint: https://onlinelibrary.wiley.com/doi/pdf/10.1113/JP274678. DOI: 10.1113/JP274678.

[350] G. Kember, J. L. Ardell, J. A. Armour, and M. Zamir, "Vagal Nerve Stimulation Therapy: What Is Being Stimulated?" en, *PLOS ONE*, e114498, Dec. 2014, Publisher: Public Library of Science. DOI: 10.1371/journal.pone.0114498.

[351] F. Shaffer and J. P. Ginsberg, "An Overview of Heart Rate Variability Metrics and Norms," eng, *Frontiers in Public Health*, p. 258, 2017. DOI: 10.3389/fpubh.2017.00258.

[352] F. Lombardi, G. Sandrone, S. Pernpruner, *et al.*, "Heart rate variability as an index of sympathovagal interaction after acute myocardial infarction," en, *The American Journal of Cardiology*, pp. 1239–1245, Dec. 1987. DOI: 10.1016/0002-9149(87)90601-1.

[353] F. Lombardi, G. Sandrone, M. T. Spinnler, *et al.*, "Heart rate variability in the early hours of an acute myocardial infarction," English, *American Journal of Cardiology*, pp. 1037–1044, May 1996, Publisher: Elsevier. DOI: 10.1016/S0002-9149(96)00127-0.

[354] J. T. Bigger, J. L. Fleiss, R. C. Steinman, L. M. Rolnitzky, R. E. Kleiger, and J. N. Rottman, "Frequency domain measures of heart period variability and mortality after myocardial infarction.," *Circulation*, pp. 164–171, Jan. 1992, Publisher: American Heart Association. DOI: 10.1161/01.CIR.85.1.164.

[355] M. Peltola, M. P. Tulppo, A. Kiviniemi, *et al.*, "Respiratory sinus arrhythmia as a predictor of sudden cardiac death after myocardial infarction," *Annals of Medicine*, pp. 376–382, Jan. 2008, Publisher: Taylor & Francis _eprint: https://doi.org/10.1080/07853890701884659. DOI: 10.1080/07853890701884659.

[356] D. Sinnecker, M. Dommasch, A. Steger, *et al.*, "Expiration-Triggered Sinus Arrhythmia Predicts Outcome in Survivors of Acute Myocardial Infarction," en, *Journal of the American College of Cardiology*, pp. 2213–2220, May 2016. DOI: 10.1016/j.jacc.2016.03.484.

[357] J. A. Behar, A. A. Rosenberg, I. Weiser-Bitoun, *et al.*, "PhysioZoo: A Novel Open Access Platform for Heart Rate Variability Analysis of Mammalian Electrocardiographic Data," *Frontiers in Physiology*, 2018.

[358] M. Kuwahara, A. Suzuki, H. Tsutsumi, M. Tanigawa, H. Tsubone, and S. Sugano, "Power Spectral Analysis of Heart Rate Variability for Assessment of Diurnal Variation of Autonomic Nervous Activity in Miniature Swine," en, *Laboratory Animal Science*, p. 7, 1999.

[359] R. M. Marchant-Forde, D. J. Marlin, and J. N. Marchant, "Validation of a cardiac monitor for measuring heart rate variability in adult female pigs: Accuracy, artefacts and editing," eng, *Physiology & Behavior*, pp. 449–458, Jan. 2004. DOI: 10.1016/j.physbeh.2003.09.007.

[360] J. M. Moen, C. H. Morrell, M. G. Matt, *et al.*, "Emergence of heartbeat frailty in advanced age I: Perspectives from life-long EKG recordings in adult mice," en, *GeroScience*, Jun. 2022. DOI: 10.1007/s11357-022-00605-4.

[361] Y.-M. Chang, Y.-T. Huang, I.-L. Chen, *et al.*, "Heart rate variability as an independent predictor for 8-year mortality among chronic hemodialysis patients," en, *Scientific Reports*, p. 881, Jan. 2020, Number: 1 Publisher: Nature Publishing Group. DOI: 10.1038/s41598-020-57792-3.

[362] G. C. Kember, G. A. Fenton, K. Collier, and J. A. Armour, "Aperiodic stochastic resonance in a hysteretic population of cardiac neurons," *Physical Review E*, pp. 1816–1824, Feb. 2000, Publisher: American Physical Society. DOI: 10.1103/PhysRevE.61.1816.

[363] G. C. Kember, G. A. Fenton, J. A. Armour, and N. Kalyaniwalla, "Competition model for aperiodic stochastic resonance in a Fitzhugh-Nagumo model of cardiac sensory neurons," *Physical Review E*, p. 041 911, Mar. 2001, Publisher: American Physical Society. DOI: 10.1103/PhysRevE.63.041911.

[364] T. H. Mäkikallio, P. Barthel, R. Schneider, *et al.*, "Prediction of sudden cardiac death after acute myocardial infarction: Role of Holter monitoring in the modern treatment era," *European Heart Journal*, pp. 762–769, Apr. 2005. DOI: 10.1093/eurheartj/ehi188.

[365] R. Lampert, J. D. Bremner, S. Su, *et al.*, "Decreased heart rate variability is associated with higher levels of inflammation in middle-aged men," *American heart journal*, 759.e1–759.e7, Oct. 2008. DOI: 10.1016/j.ahj.2008.07.009.

[366] R. M. Carney, K. E. Freedland, P. K. Stein, *et al.*, "Heart Rate Variability and Markers of Inflammation and Coagulation in Depressed Patients with Coronary Heart Disease," *Journal of psychosomatic research*, pp. 463–467, Apr. 2007. DOI: 10.1016/j.jpsychores.2006.12.004.

[367] S.-Y. Huang, Y.-C. Chen, Y.-H. Kao, *et al.*, "Renal failure induces atrial arrhythmogenesis from discrepant electrophysiological remodeling and calcium regulation in pulmonary veins, sinoatrial node, and atria," eng, *International Journal of Cardiology*, pp. 846–857, Jan. 2016. DOI: 10.1016/j.ijcard.2015.10.004.

[368] N. Osataphan, W. Wongcharoen, A. Phrommintikul, P. Putchagarn, and K. Noppakun, "Predictive value of heart rate variability on long-term mortality in end-stage kidney disease on hemodialysis," *PLOS ONE*, e0282344, Feb. 2023. DOI: 10.1371/journal.pone.0282344.

[369] S. Badarau, D. Siriopol, D. Drugus, *et al.*, "Electrocardiogram abnormalities and heart rate variability in predicting mortality and cardiovascular events among hemodialyzed patients," en, *International Urology and Nephrology*, pp. 1703–1708, Oct. 2015. DOI: 10.1007/s11255-015-1063-4.

[370] Z. Wang, F. Jiang, J. Xiao, *et al.*, "Heart rate variability changes in patients with obstructive sleep apnea: A systematic review and meta-analysis," en, *Journal of Sleep Research*, e13708, 2023. DOI: 10.1111/jsr.13708.

[371] I. S. Lensen, O. J. Monfredi, R. T. Andris, D. E. Lake, and J. R. Moorman, "Heart rate fragmentation gives novel insights into non-autonomic mechanisms governing beat-to-beat control of the heart's rhythm," *JRSM Cardiovascular Disease*, p. 2 048 004 020 948 732, Aug. 2020. DOI: 10.1177/2048004020948732.

[372] F. Shaffer, R. McCraty, and C. L. Zerr, "A healthy heart is not a metronome: An integrative review of the heart's anatomy and heart rate variability," *Frontiers in Psychology*, 2014.

[373] N. Z. Gurel, K. B. Sudarshan, S. Tam, *et al.*, "Studying Cardiac Neural Network Dynamics: Challenges and Opportunities for Scientific Computing," *Frontiers in Physiology*, 2022.

[374] P.-C. Yang, A. Rose, K. R. DeMarco, *et al.*, "A multiscale predictive digital twin for neurocardiac modulation," en, *The Journal of Physiology*, pp. 3789–3812, 2023. DOI: 10.1113/JP284391.

[375] N. Moise and S. H. Weinberg, *Emergent Electrical Activity, Tissue Heterogeneity, and Robustness in a Calcium Feedback Regulatory Model of the Sinoatrial Node*, en, Pages: 2022.11.11.516175 Section: New Results, Nov. 2022. DOI: 10.1101/2022.11.11.516175.

[376] D. Noble, "Modelling the heart: Insights, failures and progress," en, *BioEssays*, pp. 1155–1163, 2002. DOI: 10.1002/bies.10186.

[377] R. H. Johnstone, E. T. Chang, R. Bardenet, *et al.*, "Uncertainty and variability in models of the cardiac action potential: Can we build trustworthy models?" en, *Journal of Molecular and Cellular Cardiology*, pp. 49–62, Jul. 2016. DOI: 10.1016/j.yjmcc.2015.11.018.

[378] G. R. Mirams, S. A. Niederer, and R. H. Clayton, "The fickle heart: Uncertainty quantification in cardiac and cardiovascular modelling and simulation," en, *Philosophical Transactions of the Royal Society A: Mathematical, Physical and Engineering Sciences*, p. 20 200 119, Jun. 2020. DOI: 10.1098/rsta.2020.0119.

[379] D. G. Whittaker, M. Clerx, C. L. Lei, D. J. Christini, and G. R. Mirams, "Calibration of ionic and cellular cardiac electrophysiology models," en, *WIREs Systems Biology and Medicine*, e1482, 2020, _eprint: https://onlinelibrary.wiley.com/doi/pdf/10.1002/wsbm.1482. DOI: 10.1002/wsbm.1482.

[380] A. P. Clark, M. Clerx, S. Wei, *et al.*, "Leak current, even with gigaohm seals, can cause misinterpretation of stem cell-derived cardiomyocyte action potential recordings," *EP Europace*, euad243, Sep. 2023. DOI: 10.1093/europace/euad243.

[381] M. Amoni, S. Ingelaere, J. Moeyersons, *et al.*, "Regional beat-to-beat variability of repolarization increases during ischemia and predicts imminent arrhythmias in a pig model of myocardial infarction," *American Journal of Physiology-Heart and Circulatory Physiology*, H54–H65, Jul. 2023, Publisher: American Physiological Society. DOI: 10.1152/ajpheart.00732.2022.

[382] H. Cochet, R. Dubois, S. Yamashita, *et al.*, "Relationship Between Fibrosis Detected on Late Gadolinium-Enhanced Cardiac Magnetic Resonance and Re-Entrant Activity Assessed With Electrocardiographic Imaging in Human Persistent Atrial Fibrillation," *JACC: Clinical Electrophysiology*, pp. 17–29, Jan. 2018. DOI: 10.1016/j.jacep.2017.07.019.

[383] A. V. Glukhov, L. T. Hage, B. J. Hansen, *et al.*, "Sinoatrial Node Reentry in a Canine Chronic Left Ventricular Infarct Model," *Circulation: Arrhythmia and Electrophysiology*, pp. 984–994, Oct. 2013, Publisher: American Heart Association. DOI: 10.1161/CIRCEP.113.000404.

[384] A. V. Glukhov, A. Kalyanasundaram, Q. Lou, *et al.*, "Calsequestrin 2 deletion causes sinoatrial node dysfunction and atrial arrhythmias associated with altered sarcoplasmic reticulum calcium cycling and degenerative fibrosis within the mouse atrial pacemaker complex1," en, *European Heart Journal*, pp. 686–697, Mar. 2015. DOI: 10.1093/eurheartj/eht452.

[385] S. I. Protze, J. Liu, U. Nussinovitch, *et al.*, "Sinoatrial node cardiomyocytes derived from human pluripotent cells function as a biological pacemaker," en, *Nature Biotechnology*, pp. 56–68, Jan. 2017. DOI: 10.1038/nbt.3745.

[386] S. Chauveau, P. R. Brink, and I. S. Cohen, "Stem cell–based biological pacemakers from proof of principle to therapy: A review," en, *Cytotherapy*, pp. 873–880, Jul. 2014. DOI: 10.1016/j.jcyt.2014.02.014.

[387] E. Cingolani, J. I. Goldhaber, and E. Marbán, "Next-generation pacemakers: From small devices to biological pacemakers," eng, *Nature Reviews. Cardiology*, pp. 139–150, Mar. 2018. DOI: 10.1038/nrcardio.2017.165.

[388] J. Wink, R. van Delft, R. Notenboom, *et al.*, "Human adult cardiac autonomic innervation: Controversies in anatomical knowledge and relevance for cardiac neuromodulation," en, *Autonomic Neuroscience*, p. 102 674, Sep. 2020. DOI: 10.1016/j.autneu.2020.102674.